Available online at www.sciencedirect.com

SCIENCE DIRECT®

Surface Science Reports 57 (2005) 157–298

surface science reports

www.elsevier.com/locate/surfrep

Molecular beam experiments on model catalysts

J. Libuda*, H.-J. Freund

Fritz-Haber-Institut der Max-Planck-Gesellschaft, Faradayweg 4-6, 14195 Berlin, Germany

Accepted 20 March 2005

Abstract

Heterogeneous catalysts are highly complex materials with respect to both their composition and structure. The reaction kinetics on their surfaces is known to depend sensitively on numerous structural and chemical factors including the particle size and structure, the support or the presence of poisons and promotors. At the microscopic level, however, little is known about the microscopic origin of these effects. The main reason for this lack of knowledge is the vast complexity of typical heterogeneous catalysts and several experimental difficulties related to the application of modern surface science techniques to these systems.

In this review, we summarize recent attempts to overcome these difficulties, based on the application of molecular beam methods to well-defined model catalysts. Using supported model catalysts, many aspects of the complex structural properties of real catalysts can be reproduced in a well-controlled manner. At the same time, the molecular beam approach allows quantitative and detailed investigations of the kinetics and dynamics of surface

---

Abbreviations: AES, Auger electron spectroscopy; AFM, atomic force microscopy; AIS, autoionization spectroscopy; ARUPS, angle-resolved ultraviolet photoelectron spectroscopy; DFT, density functional theory; DI, direct inelastic; EBL, electron beam lithography; EELS, electron energy loss spectroscopy; FEM, field electron microscopy; FIM, field ion microscopy; FT, Fourier transform; GCA, glass capillary array; HR-EELS, high resolution electron energy loss spectroscopy; IR, infrared; IRAS, infrared reflection absorption spectroscopy; ISS, ion scattering spectroscopy; KE, kinetic energy; KRE, kinetic rate quation; LEED, low energy electron diffraction; LH, Langmuir–Hinshelwood; MB, molecular beam; MBRS, molecular beam relaxation spectroscopy; MC, Monte-Carlo; ME, master equation; MF, mean field; MSSR, metal surface selection rule; PES, photoelectron spectroscopy; PVD, physical vapor deposition; QMS, quadrupole mass spectrometer; RHEED, reflection high energy electron diffraction; TD, trapping desorption; TOF, turnover frequency; TPD, temperature programmed desorption; TR, time-resolved; SEM, scanning electron microscopy; SIMS, secondary ion mass spectroscopy; SMSI, strong metal support interaction; SSITKA, steady-state isotopic transient kinetic analysis; SPA-LEED, spot profile analysis low energy electron diffraction; STM, scanning tunneling microscopy; STS, scanning tunneling spectroscopy; SXRD, surface X-ray diffraction; TEM, transmission electron spectroscopy; UHV, ultrahigh vacuum; XAS, X-ray absorption spectroscopy; XPS, X-ray photoelectron spectroscopy

* Corresponding author. Fax: +49 30 84134309.

E-mail address: libuda@fhi-berlin.mpg.de (J. Libuda).

doi:10.1016/j.surfrep.2005.03.002

reactions. The combined information on structure and kinetics provides detailed insights into the kinetic phenomena on complex catalyst surfaces at the microscopic level.

The processes studied so far include the kinetics of adsorption and desorption involving various adsorbates and the reaction kinetics of several simple surface reactions, such as, e.g. CO oxidation, NO dissociation, NO–CO reaction and methanol oxidation. Several kinetic phenomena have been identified which are specific to supported catalyst systems. These include, e.g. the role of the support in the reaction kinetics, the role of different types of adsorption and reaction sites on small active particles, the interplay of these sites via surface diffusion, the surface mobility of reactants, coverage fluctuations on small particles, local differences in catalytic activity and selectivity on active particles, as well as the role of co-adsorbates under reaction conditions. Special emphasis is put on the development of realistic microkinetics models based on experimentally determined structure and kinetics.

Keywords: Heterogeneous catalysis; Model catalysis; Surface reactions; Reaction kinetics; Molecular beams

---

Contents

1. Introduction . . . 159
    1.1. Reaction kinetics in heterogeneous catalysis . . . 159
    1.2. Reaction kinetics on supported catalysts . . . 161
    1.3. Molecular beams and model catalysts . . . 164
2. The molecular beam approach . . . 166
    2.1. Molecular beams in surface kinetics and dynamics . . . 166
    2.2. Generation and properties of molecular beams . . . 171
        2.2.1. Supersonic beam sources . . . 171
        2.2.2. Effusive beam sources . . . 175
    2.3. Some design considerations for MB experiments in model catalysis . . . 176
3. Supported model catalysts . . . 179
    3.1. Development of supported model catalysts . . . 179
    3.2. Supported model catalysts used in molecular beam studies . . . 184
        3.2.1. Preparation by physical metal deposition and growth . . . 184
        3.2.2. Preparation by electron beam lithography . . . 193
        3.2.3. Other preparation methods . . . 194
4. Molecular beam studies in catalysis . . . 196
    4.1. Experiments on single crystal surfaces . . . 196
    4.2. Experiments on supported model catalysts . . . 197
5. Adsorption and desorption kinetics . . . 198
    5.1. Sticking coefficient measurements and capture zone effects . . . 198
        5.1.1. Capture zones—general remark . . . 199
        5.1.2. CO adsorption . . . 200
        5.1.3. O_2 adsorption . . . 204
        5.1.4. NO adsorption . . . 204
        5.1.5. CH_3OH adsorption . . . 206
        5.1.6. Microkinetic models . . . 207
    5.2. Other adsorption–desorption experiments . . . 208
6. CO oxidation . . . 209
    6.1. General remarks . . . 209
    6.2. Steady-state and transient kinetics . . . 212
        6.2.1. Experiments on supported Pd model catalysts . . . 212
        6.2.2. Microkinetic simulations . . . 222

6.3. Angle-resolved experiments and surface diffusion 227
6.3.1. Experimental results 229
6.3.2. Microkinetic simulations 230
6.4. Kinetic bistabilities and coverage fluctuations 236
6.4.1. Experimental results 236
6.4.2. Microkinetic simulations 238
7. Methanol decomposition and oxidation 242
7.1. Methanol decomposition on Pd surfaces—general remarks 242
7.2. Mechanism 245
7.3. Dehydrogenation and oxidation under transient and steady-state conditions 247
7.4. Specific reaction sites 255
7.5. Microkinetic simulations 259
8. NO decomposition and reduction 261
8.1. NO decomposition on Pd surfaces—general remarks 261
8.2. NO interaction with the model support 262
8.3. NO adsorption on supported model catalysts 264
8.4. NO dissociation 270
8.5. NO–CO reaction 275
8.6. Microkinetic simulations 280
9. Summary and outlook 282
Acknowledgements 284
References 285

1. Introduction

1.1. Reaction kinetics in heterogeneous catalysis

Catalytic processes at interfaces occupy a pivotal position in many fields of applied chemistry, ranging from chemical manufacturing to the rapidly developing areas of environmental technology and energy generation and storage. In the chemical industry, heterogeneous catalysis has been utilized for a long time and today catalytic steps are involved in most manufacturing processes. The development of new catalysts, which exhibit enhanced performance, has led to sudden improvements in many fields of application. A list of major catalytic inventions of the last century has been compiled in the literature [1,2]. More recently, the development of catalytic converters has helped to drastically decrease pollutant emissions from mobile and stationary sources. In future applications, catalytic processes may be involved in various emerging fields such as fuel cell technology. Our present understanding of heterogeneous catalysis has been summarized in a large number of monographs, ranging from Rideal's classic 'Concepts in Catalysis' [3] to several modern comprehensive treatments (see, e.g. [1,4]).

Catalysis is – by definition – a kinetic phenomenon. For practical reasons, the reaction kinetics is typically described using global terms such as, e.g. *activity*, *selectivity* or *stability*: the activity describes the increase in reaction rate toward the desired product upon use of the catalytic material. Typically, the global rate is the result of a more or less complex sequence of microscopic steps with different degree of rate control. Besides the pure reaction kinetics on the catalyst's surface, factors such as heat or mass transport may also play an important role under realistic conditions. *Selectivity* is, in general, one of the most important characteristics, as it determines the nature and quantity of side products and, therefore, the efficient use of the reactants as well as possible purification requirements. From a kinetic point of view, selectivity is related to the ratio of reaction rates related to desired and undesired pathways in the reaction network. Naturally, such ratios are determined by small differences in activation energy, making investigations of selectivity a rather delicate issue, both from an experimental and from a theoretical point of view. For practical reactions, *stability* is a very important aspect. The stability of the catalyst is related to slow changes of the rate of one or more steps in a reaction network as a function of time. Such changes may be, for example, the result of morphological changes or poisoning processes.

For practical applications, kinetic modeling of catalytic processes typically focuses on the quantitative description of the global kinetics as a function of the reaction parameters. From the microscopic point of view, the corresponding models are rather coarse and the relation of global kinetics to the elementary reaction steps is generally unclear or speculative. The ultimate goal of fundamental research in catalysis would be a well-founded microkinetic model, in which all elementary processes of the reaction network are properly described (see, e.g. [5]). This would include an accurate description of the kinetics of all elementary adsorption, diffusion, reaction and desorption steps including their coverage and temperature dependencies, which should be individually determined by kinetic experiments or theoretical calculations. In particular, a true microscopic understanding of the kinetics may require effects to be taken into account which are beyond the kinetic rate equation (KRE) approach typically used in microkinetic modeling, e.g. including the presence and distribution of non-equivalent reaction and adsorption sites, surface diffusion processes or adsorbate interactions leading to islanding or non-homogeneous adsorbate distributions.

In practice, such detailed models are hardly available. Only for very few and simple reaction systems, such as the CO oxidation, the CO–NO reaction or the ammonia synthesis on simple single crystal surfaces, more or less detailed microkinetic description have been developed (see, e.g. [6,7]). Even for these simple cases, a number of open questions remain. Despite this fact, however, combined surface science and kinetic investigations provide a route toward increasingly detailed insights into the microscopic reaction kinetics on single crystal surfaces.

For real catalyst materials, however, the situation is significantly more complicated. Few catalysts are simple elements or homogeneous compounds. Instead, most systems are based on *complex materials* such as multicomponent mixtures of different oxides or combined metal/oxide systems. Often, their surfaces exhibit specific structural properties on the nanometer scale or chemical species, which critically depend on the preparation procedures. In order to illustrate this point, two examples are considered, which are related to most of the work presented in this review:

(i) The first example is the automotive catalytic converter, which was first introduced in 1975 and is still under development (for a comprehensive introduction see [8,9]). In principle, the system removes hazardous pollutants from exhaust gases by oxidizing CO and hydrocarbons to CO_2 and H_2O and by reducing nitrogen oxides to N_2. The construction of the converter is based on a ceramic or metallic monolith, which is traversed by several thousand straight channels. These channels are covered by a high surface area oxide washcoat, consisting of a mixture of aluminium oxide, cerium oxide and zirconium oxide, but may also contain various alkaline earth metals, transition metals and rare earth oxides. Finally, the washcoat is loaded with mixtures of precious metals, specifically palladium, rhodium and platinum, which typically form three-dimensional particles with a diameter of a few nanometers. One of the reactions, the CO oxidation, has been in the center of academic interest for a long time, as an example of a surface reaction, which is mechanistically simple and easy to study (see, e.g. [10]). For practical reasons, the nitric oxide reduction is much more relevant to environmental catalysis. The reason is that modern lean-burn engines produce oxygen-rich exhaust gas conditions, under which the reduction of nitrogen oxides might not be efficient [11,12].

(ii) The second example of a heterogeneously catalyzed reaction system is related to methanol synthesis, which was first commercialized by BASF in 1923, using a zinc oxide/chromium oxide catalyst. Forty years later, it was finally replaced by the ICI catalyst, containing copper, zinc oxide (ZnO) and alumina (Al_2O_3) (for an introduction, see [1,13]). Alternative catalytic materials for methanol synthesis have been developed, which are based on palladium particles supported by silica (SiO_2) (see [14], also [15] and references therein). Their performance, however, was shown to critically depend on the presence of certain basic metal–oxides as promoters, such as CaO [16].

Both examples represent typical supported catalysts, consisting of one or more active components highly dispersed on a surface-rich and thermally stable support material. The compositional and structural complexity of these systems is their principal advantage. Apparently, it is this feature which allows us to tune surface properties in order to optimize selectivity and activity with respect to a specific reaction.

At the same time, however, complexity is also the dilemma of research in catalysis: at a molecular level, an understanding of reaction kinetics at heterogeneous and porous interfaces is difficult to achieve. In addition, many modern methods of surface chemistry, which hold the potential to provide detailed information about surface structure and properties, cannot be applied to commercial catalysts. As a consequence, our microscopic level knowledge about reaction kinetics on heterogeneous catalysts is scarce and there are only a few cases, where the microscopic origins of specific catalytic properties of complex surfaces have been identified unambiguously.

1.2. Reaction kinetics on supported catalysts

In this review, we focus on the reaction kinetics on complex catalyst surfaces and on attempts to approach a microscopic understanding of the related kinetic phenomena. Specifically, we discuss the differences, which are observed in comparison to the kinetics on single crystal surfaces.

As an important class of heterogeneous catalysts, we consider *supported metal catalysts*, which are used in many practical applications (see Section 1.1). A typical supported metal catalyst is based on a thermally stable and surface-rich oxide support material, such as, e.g. alumina (Al_2O_3) or silica (SiO_2). On these oxides, well-dispersed metal particles – typically in the size range of a few nanometers – are prepared, e.g. through impregnation with a precursor followed by suitable chemical and thermal treatment or via alternative methods.

In Fig. 1, a schematic model of a supported catalyst particle is displayed. It is noteworthy that even for the simplest systems, a large number of non-equivalent sites are exposed, the nature and density of which depends on various structural parameters: on the support itself, we typically find *regular oxide areas* as well as a large number of characteristic *oxide defects sites* or *chemically modified oxide structures* (e.g. hydroxyl groups or promotors). The reaction sites exposed by the supported metal particle depend on its *orientation*, *size*, *shape* and *structure*. Typically, we find majority and minority facet sites (generally different low index crystal planes), but also a large number of defects, such as edges, corners, interfaces, kinks and steps. In addition, the geometric and electronic structure of the active particles depend on their size and their interaction with the support. The latter has an influence on the *metal–oxide interface* as

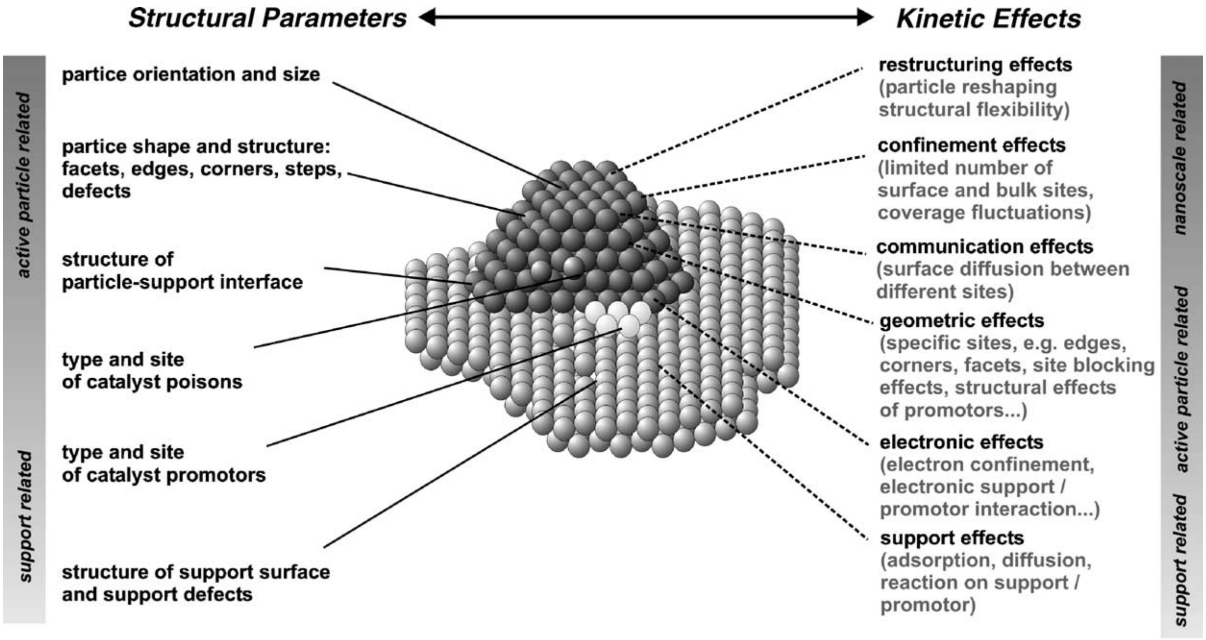

Fig. 1. Structural parameters and kinetic effects on supported metal catalysts (adapted from [73]).

well, at which specific interface sites may be available. In addition, the properties of specific sites on the particles and on the support may be modified by *poisons* and *promotors* under reaction conditions.

It was recognized early on that a support does not only help to stabilize the high dispersion of the catalytically active metal, but that particle size and support may have a drastic influence on the catalytic performance itself (see [17–20] and references therein). Apparently, it is the specific properties of the many sites exposed, as well as their interplay that determines the overall catalytic activity of the surface. But how can the large number of structural parameters be related to reaction kinetics? Here, several different concepts have been put forward, which can be briefly classified as follows (see Fig. 1):

(i) *Support effects*: there are many cases in which the reaction network directly involves the support (see, e.g. [21–23] for the case of NO reduction catalysts). Alternatively, adsorption processes on the support and elementary steps on the active particle can be coupled by surface diffusion. In case of activated adsorption, such processes are referred to as *spillover* or *reverse-spillover*, respectively [24,25]. In the case on non-activated adsorption surface diffusion between the support and the supported particle may give rise to *capture zone effects*, which in specific cases may have an effect on the reaction kinetics as well (see [19,26,27]) and references therein). In addition to the support effects, there are *support interactions*, which lead to a modification of the reaction and adsorption properties of the supported particles and may have both structural and electronic origins. Here, the most prominent example is the case of the *strong metal support interaction* for metals on reducible oxides (see [28] and references therein).

(ii) *Electronic effects*: the electronic structure of a supported particle may differ from an extended metal surface, for example, due to its limited size leading to *electron confinement*, due to *lattice distortions* induced by the reduced dimensions or due to *electronic influences of the support*. These kinds of effects are expected to be strong only for very small particles (see, e.g. [29–31]). In addition, *promotors* located on the active particle may lead to a modification of the adsorption properties via their electronic influence (e.g. [32]). In a similar fashion, a specific role is often attributed to *interface sites* between the particle and the support, the specific properties of which may also be the result of a local electronic effect [33].

(iii) *Geometric effects*: it is apparent that a metal particle exposes specific sites, such as particle edges or corners, which are not present on a perfect single crystal surface. Their density depends on the particle size and is substantial in the practically relevant size range of a few nanometers. Additional irregular sites such as steps may occur, in particular, if the equilibrium shape of the particle is not fully established. It should be noted that in many cases the properties of particle specific sites cannot be simulated by the simple use of stepped or defect-rich single crystals and, therefore, they represent an inherent property of particles in the nanometer size regime. These specific sites may exhibit specific activities with respect to a given reaction (see, e.g. [19] and references therein).

Most effects from groups (i) to (iii) are the result of a direct modification of the adsorption or reaction properties of specific adsorption or reaction sites on supported particle system as compared to the ideal single crystal surface. In addition, there a kinetic phenomena which arise from the complex structure of the catalyst surface (typically on the length scale of few nanometers), without any direct modification of the properties of individual reaction or adsorption sites:

(iv) *Communication effects*: communication effects can result from a coupling of small surface regions with different adsorption and reaction properties via fast surface diffusion. Such regions could, for example, be different facets of a crystalline particle or various defect sites. As a result, the reaction rate in the coupled system may strongly differ from a simple linear combination of the individual regions [20,27,34,35]. The capture zone and spillover effects, discussed in (i), can be classified as specific cases of communication effects, involving transport between the active particles and the support.

(v) *Confinement phenomena*: modifications of the kinetics can arise as a result of the fact that the mobility of reactants is limited due to the structure of the catalyst. Reactants may, for example, be confined on the active metal particles, with surface diffusion to other parts of the surface being inhibited. There are different consequences of this effect: for example, bulk diffusion, which is easily possible for some reactants such as hydrogen, may be restricted, leading to changes in the related kinetics [36]. Another consequence of the reactant confinement are coverage fluctuations, which occur on sufficiently small catalyst particles, and which may have an influence on the reaction kinetics [37–39].

(vi) *Restructuring effects*: adsorbate induced reconstructions or faceting are well-known effects on extended single crystal surfaces. On small particles, reactant induced restructuring is expected to represent an even more frequent and versatile phenomenon, with large potential impact on the reaction kinetics. Adsorbate induced restructuring effects may range from changes of the particle equilibrium shape (e.g. [40]) or restructuring induced by bulk phase transformation (e.g. oxidation) via the adsorbate induced disrupture of small particles (e.g. [41] and references therein) to the structural flexibility of small clusters in the presence of reactants [42].

Despite these numerous ideas about the reactivity of supported catalyst systems, the actual number of examples, in which such effects have been directly linked to the kinetics of catalytic reactions at the microscopic level, is small.

1.3. Molecular beams and model catalysts

From the discussion in the preceding sections, it is apparent that any understanding of reaction kinetics on catalysts at the microscopic level requires two basic difficulties two be overcome (see Fig. 2).

The first problem is related to the vast *structural complexity* of most heterogeneous catalysts, which complicates the microscopic interpretation of kinetic data. In addition, experimental difficulties arise due to the porosity and limited electrical and thermal conductivity of these systems if modern surface science methods are to be applied. This problem is frequently denoted as the *materials gap* between surface science and catalysis (see, e.g. [43,44]).

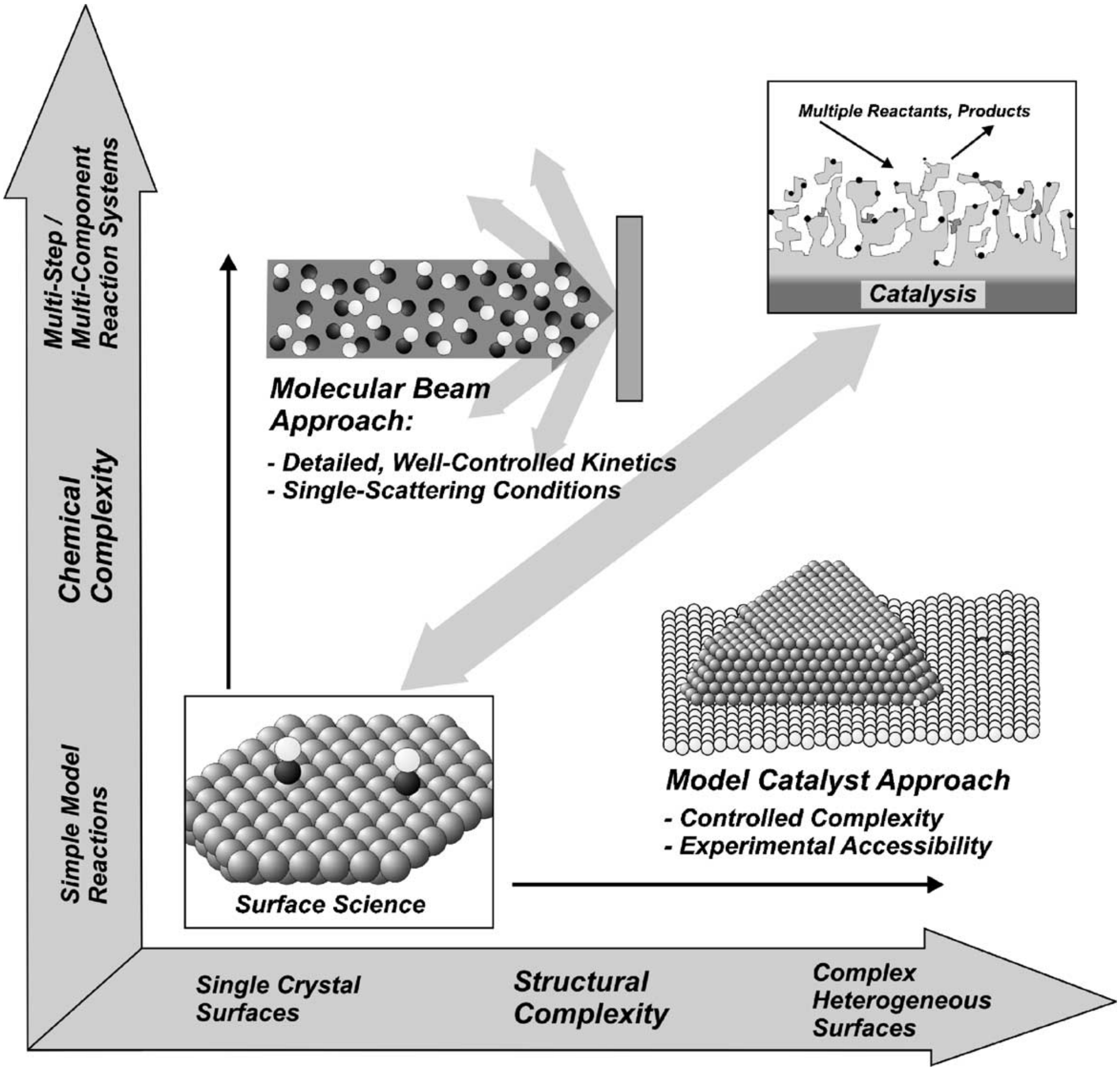

Fig. 2. Schematic representation of the topic of this report: model catalysts are combined with molecular beam experiments in order to provide detailed information on the kinetics of catalytic reactions.

One strategy to overcome this problem is the use of *model catalysts*. Over the last decade, a broad spectrum of *model catalysts* has been developed by several groups (see, e.g. [19,45–50] and references therein). The most important feature of these model systems is that they allow us to introduce certain structural features of a catalyst surface in a well-controlled manner, simultaneously avoiding the full complexity of the real system. In addition, surface science can be applied to most model catalysts in a straightforward fashion. For the special case of supported catalysts, model systems have been developed on the basis of oxide single crystals [47,49,51,52] and thin films [45,46,48,53] onto which metals are deposited under exactly controlled conditions in ultrahigh vacuum (UHV). Here, the thermal and electrical conductivity of thin oxide films allows the unrestricted use of surface analytical tools, such as, for example, scanning tunneling microscopy (STM), photoelectron spectroscopies or electron diffraction and provides good control of the temperature. As a result, it is possible to characterize the geometric and electronic structure of these systems in great detail [45,46,54–62].

Once the foundations have been laid with respect to a structural characterization of the model catalysts, the second problem is to identify the actual *correlations between microscopic structure and microscopic kinetics*. Aiming at the understanding of real catalytic processes, the problem is further complicated by the fact that under realistic conditions most catalytic processes are characterized by a substantial degree of *chemical complexity*, in the sense that typically many-component mixtures of reactants and products interact with the catalyst surface (e.g. for the case of the automotive emission control catalysts the exhaust gas contains CO_2, N_2, H_2O, CO, O_2, nitrogen oxides, various hydrocarbons, etc.) or the process involves intricate reaction networks with multiple steps and pathways (see, e.g. the case of methanol oxidation discussed in Section 7).

One approach used to establish these correlations is based on *molecular beam* (*MB*) *techniques*. The application of molecular beams provides a unique way of performing detailed, quantitative and systematic experiments on the kinetics and dynamics of surface reactions (see, e.g. [63–70]). On single crystal surfaces, MB methods have helped to elucidate many aspects of the dynamics and kinetics of adsorption, reaction and desorption processes in great detail. The application of MB techniques to more complex surfaces is still in its infancy, however.

This review provides an overview of recent work, which aims to integrate the two approaches, i.e. *model catalysts* and *molecular beams*. Certain specific aspects related to the field have been subject to brief reviews recently [71–75], and an overview of work performed before 1997 can be found in the review on supported model catalysts by Henry [19].

In Section 2, we review the experimental issues related to the application of molecular beams in studies of surface kinetics and dynamics. An overview is given of previous experimental setups developed and used in this field and we discuss the specific design considerations for kinetic beam experiments on model catalysts.

A brief overview of the field of supported model catalysts is provided in Section 3. Different preparation methods are compared and some examples are given, which are of relevance for the experiments discussed in the following sections. Moreover, the type of information, which is available on the geometric and electronic structure is illustrated as well as information on the adsorption properties of these systems.

In the remaining sections, we review specific experimental results obtained by application of MB methods to model catalysts. A general overview of the systems studied is given in Section 4. Subsequently, specific questions are addressed, including the adsorption and desorption kinetics on model catalysts (Section 5) and the kinetics of specific surface reactions including the CO oxidation

(Section 6), reactions of methanol (Section 7) and the dissociation and reduction of NO (Section 8). Here, the central point is the identification of kinetic phenomena, which are specific to supported particle systems. As microkinetic simulations typically prove to be very helpful in the interpretation of the MB data, we put a special focus on kinetic models, wherever available.

Although the systems and kinetic phenomena discussed may seem rather complex from the point of view of surface science, the still appear rather simplistic when compared to real catalytic processes. Possible future developments, which might help to close the gap between these two worlds will be briefly touched upon in Section 9.

2. The molecular beam approach

2.1. Molecular beams in surface kinetics and dynamics

MB techniques are well-established among the major tools to study the dynamics and kinetics of surface reactions. The experimental pre-requisites, various types of beam experiments, the kind of information derived from these, as well as a large number of case studies have been subject to several reviews over the last decades (see, e.g. [63,64,66–70] and references therein). A general overview over atomic and molecular beams techniques including beam-surface experiments is available elsewhere [76,77].

A MB is a spatially well-defined, directed and collision-free flow of molecules. Typically, it is generated in a beam source such as displayed in Fig. 3: the first step is an expansion of gas from a so-called stagnation state (p_0, T_0) into the vacuum. The dynamic properties of the molecules in this expansion depend on the specific conditions of the experiment. From a small solid angle of this expansion, molecules are extracted by means of an aerodynamic skimmer or an aperture. In this manner, a directed beam is formed, which can be further modified in many ways. Typically, the desired temporal structure is prepared by modulation, using a mechanical chopper or shutter. For dynamical studies, the distribution of energy over the different external and internal degrees of freedom can be controlled via the

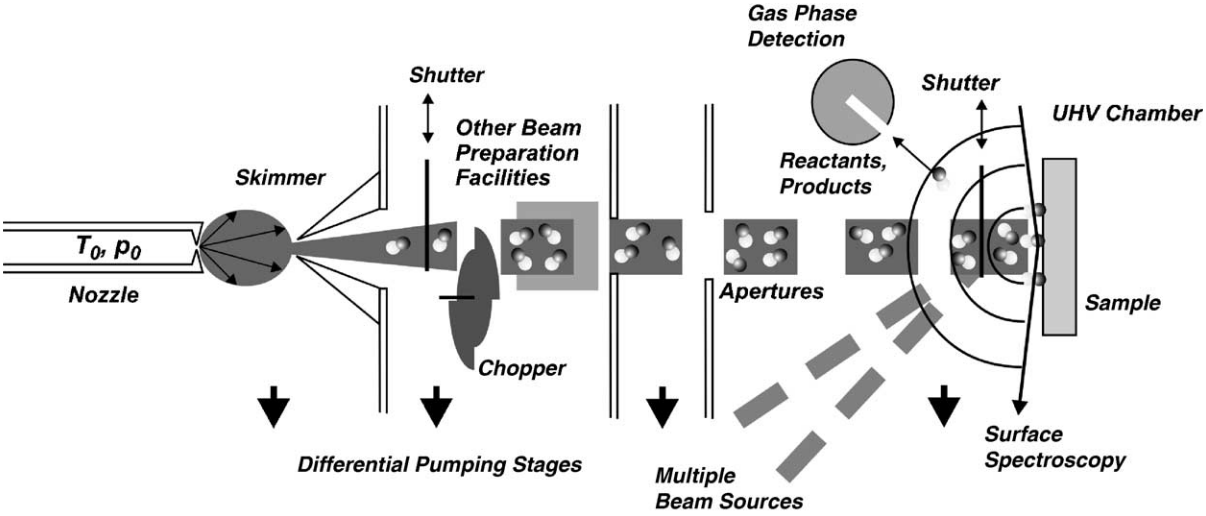

Fig. 3. Schematic representation of a molecular beam experiment for the study of gas–surface interactions (from [74]).

stagnation state or 'in flight' by state selection or excitation. These methods benefit from the fact that the beam itself represents a collision-free environment, i.e. the energy distribution prepared is largely preserved until collision with the surface. An essential feature of any beam source is the fact that the direct beam has to be separated from the effusive background of molecules by implementing several differential pumping stages. From the last differential pumping stage, the beam enters the scattering chamber and finally collides with the sample at the desired angle of incidence.

If a reaction is studied, which involves several reactants, these can either be introduced via the background gas or by crossing several beams on the sample surface. The latter possibility is advantageous due to the lager degree of control over these reactants and the lower background pressure during the experiment. In principle, two types of detection can be coupled with the beam setup. Classically, gas phase detection provides information on the scattered or desorbing reactants, as well as on desorbing reaction products. Experimentally, detection of gas phase molecules is realized either in an angular-integrated mode or in an angle-resolved mode by means of quadrupole mass spectrometry, bolometric detection or laser spectroscopy. Alternatively, time-resolved surface spectroscopies can applied in order to obtain information on adsorbed species.

In the literature, numerous MB setups of different complexity have been described, most of which were optimized to study specific aspects of gas–surface interactions (see, e.g. [42,64,65,67,78–97]). In general, we can subdivide these machines into two categories.

The first group of experiments was specifically designed in order to study the dynamics of gas–surface interaction (see, e.g. [64,67,78,86,88–90,96]). Such investigations basically require one supersonic beam source with a maximum of control over its dynamic parameters and an optimized angular and time-resolved detection of the scattered beam. In general, the incidence angle, the kinetic energy (KE), the vibrational or rotational energy distribution or the orientation of the incident molecules can be varied and the sticking probability, the angular distribution, the velocity distribution or the vibrational or rotational energy distribution of desorbing or scattered species can be detected.

In this report, we mainly focus on the second category of beam experiments, which primarily aim at the kinetics and mechanism of surface reactions (see, e.g. [78,79,84,85,89–95,97]).

The complexity of these systems differs widely. The simplest setups are based on MB dosers without differential pumping [42,91,93]. In spite of their simplicity, these setups already provide many of the characteristic advantages of typical beam experiments. Sophisticated MB machines, e.g. such as the systems described by Sibener and coworkers [89,90,98], Ceyer and coworkers [65,78] or by the authors [97], include multiple, differentially pumped sources, allowing several reactant beams to be crossed on the sample surface. In most cases, quadrupole mass spectrometers (QMS) are used for gas phase detection, either in non-line-of-sight geometry for global rate measurements or in a differentially pumped line-of-sight setup for time and angle-resolved work.

Comparing the MB approach over simple reactor studies, the main differences arise from the fact that a MB experiment is performed under *single collision conditions*, meaning that there is essentially a single interaction of the reactant molecules with the surface in an otherwise collision-free environment. The experimental advantages arising, arise from this fact, can be summarized as follows:

(i) *Determination of absolute reaction probabilities*: the fact that the incident flux is known makes it possible to determine absolute probabilities for different types of reactive processes, i.e. sticking coefficients in the case of adsorption or reactive sticking probabilities for surface reactions. Typically, the measurements are performed in an experiment based on a procedure originally proposed by King and Wells [99], detecting the relative pressure change in the background gas. Reaction probabilities are determined in a similar fashion, detecting the partial pressures of the reactants and/or the products. The experimental procedure can be extended to determine absolute sticking probability at desorption temperature [100]. The King and Wells method relies on a sufficiently fast response of the vacuum system. For reactive gases, the system response may be slow, however, due to interaction of the molecules with the chamber walls and, therefore, has to be taken into account in the analysis [101]. The King and Wells method is typically suitable for detecting sticking probabilities in the range between about 10^{-2} and 1. Lower sticking probabilities require the detection of surface species formed upon adsorption or reaction. The latter method is purely limited by the time-scale on which contamination of the surface occurs, either due to contaminations present in the beam or originating from the background gas.

For heterogeneous and nanostructured surfaces, the determination of absolute adsorption and reaction probabilities is particularly interesting, not only because it opens up the possibility to directly compare reaction rates as a function of surface structure, but also due to the possible investigation of coupling effects between coexisting surface areas via surface diffusion. The corresponding experiments are reviewed in Section 5.

(ii) *Fast and flexible reactant flux modulation*: the temporal modulation of reactant fluxes is one of the key issues in kinetics and dynamics. Essential information is available from transient experiments, which provide valuable input information for a microkinetic analysis. Coupled with mass spectrometry and periodic modulation of the beam, the method is often referred to as MB relaxation spectroscopy (MBRS) (see, e.g. [63] and references therein). A specific case is transient isotopic exchange experiments, which permit acquisition of transient data under steady-state conditions (equivalent to the steady-state isotopic transient kinetic analysis method, SSITKA, frequently employed in heterogeneous catalysis, see, e.g. [102]).

Already at an early stage of surface MB experiments, the analysis of modulated beam data have been discussed in terms of linear response theory (see, e.g. [103], see also [104–107]). It is useful to reconsider briefly the foundations of this approach (for earlier experimental results and theory, we refer to the review by D'Evelyn and Madix [63]): naturally, the detected flux depends on the modulation of the incident beam $J_{\mathrm{mod}}(t)$ by the chopper or shutter. The response of the detector can be described as the convolution of the modulation function $J_{\mathrm{mod}}(t)$ and a transfer function $T(t)$, providing a full description of the response of the system:

$$J(t) = T(t) \otimes J_{\mathrm{mod}}(t)$$

The total transfer function $T(t)$ contains several contributions such as, e.g. (1) the flight time from the chopper to the surface ($T_{\mathrm{in}}(t)$, typically in the order of 10^{-3} to 10^{-4} s), (2) the surface residence time ($T_{\mathrm{surf}}(t)$), (3) the flight time from the surface to the detector ($T_{\mathrm{out}}(t)$, typically similar to T_{in}) and (4) the response time of the detector ($T_{\mathrm{det}}(t)$, for QMS detection typically in the order of 10^{-5} s), yielding:

$$T(t) = T_{\mathrm{in}}(t) \otimes T_{\mathrm{surf}}(t) \otimes T_{\mathrm{out}}(t) \otimes T_{\mathrm{det}}(t).$$

Here, $T_{\mathrm{surf}}(t)$ contains the desired information on the surface kinetics and $T_{\mathrm{out}}(t)$ holds the information on the velocity distribution of the products. If the experimental conditions cannot be chosen such that the desired transfer function dominates the total response, the individual contributions have to be determined by means of deconvolution or fitting procedures [103]. In practice, most kinetic experiments are performed under conditions, where the surface reaction typically dominates the transient response (see Sections 6–8). For experiments which are based on detection of the background partial pressure (i.e. sticking coefficient measurements, integral transient rate measurements), $T_{\text{out}}(t)$ is replaced by the response of the vacuum system $T_{\text{vac}}(t)$ (typically $>10^{-2}$ s) and $T_{\text{in}}(t)$ and $T_{\text{det}}(t)$ can be neglected:

$$T(t) = T_{\text{surf}}(t) \otimes T_{\text{vac}}(t).$$

It is noteworthy that the restrictions due to $T_{\text{vac}}(t)$ (or $T_{\text{out}}(t)$ and $T_{\text{det}}(t)$) do not apply for direct surface detection, e.g. via fast infrared reflection absorption spectroscopy (IRAS) or photoelectron spectroscopy (PES), which in principle opens up the possibility of investigating faster processes. Here, the limiting factors are the sensitivity of the spectroscopic methods available and the achievable beam intensities (see Section 2.1).

In spite of the elegance of this type of analysis in simple cases, it should be noted that in the case of non-linear kinetics, the analysis becomes significantly more complex. Such non-linearities are common and arise, e.g. from the reaction mechanism or from coverage dependencies of sticking coefficients or rate constants. A possible experimental approach to this problem is to choose specific reaction conditions so that the flux modulation only induces small pertubations of the steady-state (see, e.g. [63,98,108]). Alternatively, the transient response of the non-linear system can be directly simulated via microkinetic modeling (see Section 6.1).

(iii) *Control over dynamic properties of incident molecules*: in a MB, the particles approach the surface in a largely collision-free environment. Thus, it is, for example, possible to prepare molecules in a particular state before collision with the surface. This opens up the possibility of studying the dynamics of gas–surface interaction and to obtain detailed information on the potential energy surfaces, which determine reactive and non-reactive processes.

Among the parameters which can be controlled are the angle of incidence and the KE (via the temperature in the stagnation state, by means of seeding or by velocity selection), the rotational and vibrational state (by means of state selection via laser excitation or to a certain degree via the temperature in the stagnation state), and in some cases even the molecular orientation. As dynamic experiments are not in the focus of this review, we refer to the corresponding reviews and monographs for an overview over the field [64,67,68,76,77,88,109,110].

As a consequence of the complexity of dynamic experiments and their interpretation, most studies in this field are limited to single crystal surfaces and simple adsorbates. Work on more complex surfaces is still in its infancy. Nonetheless, it should be kept in mind that the gas–surface dynamics governs important elementary processes in catalysis and a deeper understanding of the corresponding phenomena remains an important challenge for future work.

(iv) *Collision-free detection of scattered and desorbing molecules*: while at the sample position, local pressures up to 10^{-2} Pa can be obtained in a MB experiment, the background pressure is typically several orders of magnitude lower. Therefore, molecules scattered or desorbing from the sample can be detected in a collision-free fashion, even at large sample–detector distances. Among the types of information available from direct detection are, for example, the angular distribution of reactant molecules, their KE and their vibrational or rotational energy distribution (see [64,67,68,109,111] and references therein). Careful studies of this type reveal many details on the potential energy surfaces, which determine desorption and reaction events or scattering processes.

For the study of more complex catalyst surface, the angular and velocity distributions of the reaction products are of particular interest. The latter may sensitively depend on the reaction site and surface structure, as shown by Matsushima and coworkers (see, e.g. [112–115], for a review see [116]). For heterogeneous surfaces, an analysis of the angular or velocity distribution may potentially provide information on reaction rates on specific surface sites (see Section 6.2). Other applications of measurements of angular and velocity distributions involve the characterization of trapping and direct scattering processes of adsorbates on planar model supports (see Section 5.1).

Taking advantage of these opportunities, numerous MB studies have been performed addressing the dynamics and kinetics of surface reactions on single crystal surfaces (see Section 4.1). It should be noted, however, that most experimental efforts so far have exclusively focused on gas phase detection methods. Very few attempts have been made to incorporate time-resolved in situ surface spectroscopies. However, combined information on reaction rates and surface species becomes crucial in studies on more complex surfaces, which expose a large number of different adsorption sites.

Sibener et al. have pointed out that He reflectivity measurements provide a natural and very sensitive method of providing additional in situ data in an MBRS experiment [98], e.g. on surface coverages. The technique fails, however, for most heterogeneous or nanostructured surfaces as a result of their large surface corrugation. Other surface detection methods, which have been combined with MB experiments are electron energy loss spectroscopy (EELS) [81,117] and Auger electron spectroscopy (AES) (see, e.g. [117,118]). Bowker et al. have described an apparatus, which combines a simple effusive MB source and IRAS [119]. Recently, significant progress has been made toward combining MB experiments and high resolution photoelectron spectroscopy using synchrotron radiation by Denecke and coworkers [95,120–123].

A large fraction of the experimental data discussed in the following was acquired using a MB apparatus combining multiple beam sources and IRAS [97] (see Section 2.3). Surface IR spectroscopy is of the most specific and sensitive tools to study adsorption of molecules on surfaces, including aspects such as, e.g. the nature of adsorbates, the interaction with the substrate, the adsorption site or intermolecular interactions [124,125] and provides a natural connection to real heterogeneous catalysis, where vibrational spectroscopy represents one of the standard characterization methods (see, e.g. [126]). Depending on the requirements of the system, surface IR spectroscopy can be performed in various modes including transmission, reflection, diffuse reflectance or internal reflection. For supported model catalysts based on oxide single crystals, studies have been performed mainly in transmission (e.g. [127,128]) or reflection (e.g. [58,129–131]) mode (IRAS). If thin oxide films on metal substrates are used, relatively high signal intensities are obtained in IRAS due to the optical properties of the metal. Here, two aspects have to be kept in mind (see, e.g. [125,132]): first, the metal surface selection rule (MSSR) generally applies for these systems. This limits the range of active vibrational modes to those which have a non-zero component of the dynamic dipole moment perpendicular to the surface. The second point is that often there are strong dipole coupling effects between neighboring adsorbate molecules, resulting in intensity transfer between bands. Both effects contribute to the difficulties related to a quantitative analysis of IRAS data. To some extent, the problem can be surmounted by calibration procedures (see Section 7).

Although time-resolved FTIR spectroscopy with temporal resolution up to the ns region is routinely used in gas or liquid phase work, examples for TR-IR spectroscopy studies on surfaces with high temporal resolution are extremely rare. Mainly, this is due to the low signal intensity in single reflection IR spectroscopy requiring data accumulation in a periodically driven surface process. Based on the fluxes which are obtained in a molecular beam experiment (see Section 2.2), the required temporal resolution is estimated to fall in the millisecond range and can be easily achieved via conventional rapid scan techniques. Higher resolution is obtained via record-in-flight-techniques (e.g. [133–135]) or with step-scan spectroscopy (e.g. [136,137]).

An example for a combined molecular beam TR-IRAS experiment with millisecond time resolution is shown is shown in Fig. 4. The adsorption–desorption kinetics of CO on Pd particles on Al_2O_3/NiAl(1 1 0) (see Section 5) is probed using a CO beam modulated at a frequency of 0.877 Hz and at a temporal resolution of 38 ms (see [97] for details). During the experiment, which is performed below the main desorption temperature of CO, the coverage remains high and the spectral changes detected are mainly due to shifts in the CO stretching bands upon compression and expansion of the CO layer (see Section 5 for details). The example illustrates the remarkable sensitivity of the method in this type of experiment.

2.2. *Generation and properties of molecular beams*

If we consider the types of molecular beam sources in gas–surface studies, we can distinguish between two limiting cases: *effusive sources* and *supersonic sources*. The differences between the two categories are related to the expansion conditions, giving rise to specific types of energy distribution of the molecules in the beam (see, e.g. [138,139]).

2.2.1. *Supersonic beam sources*

The expansion conditions are classified via the so-called Knudsen number $Kn = \lambda/d$ (λ is the mean free path of the gas molecules and d is the source aperture dimension). Supersonic sources operate at low Knudsen numbers [138]. Schematically, the source setup is displayed in Fig. 5. Starting from the stagnation state (Mach number $\mathbf{M} \ll 1$), a pressure difference accelerates the gas flow, which, under

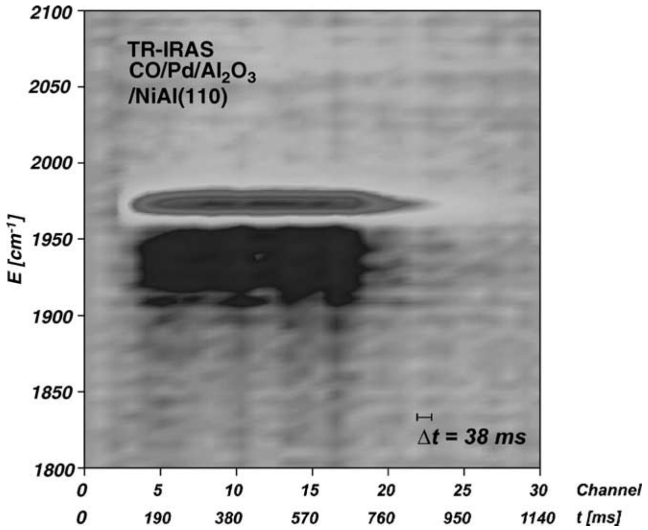

Fig. 4. Time-resolved IR reflection absorption spectra for CO adsorbed on a Pd/alumina model catalyst at $T_{\text{Surface}} = 330$ K, during modulation of the CO flux via an effusive source.

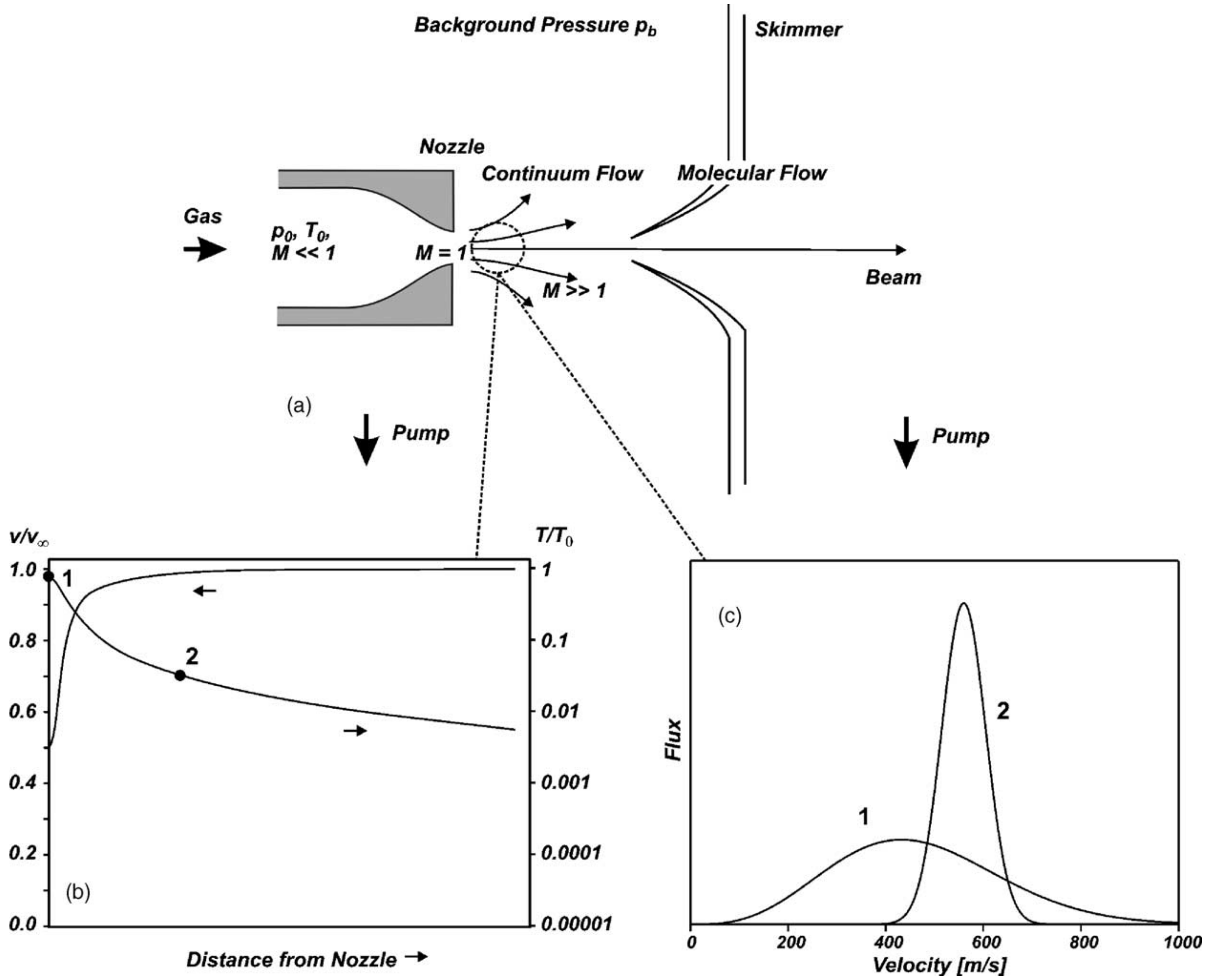

Fig. 5. Characteristic features of a molecular beam sources based on a free-jet expansion: (a) schematic setup of the beam source; (b) velocity and temperature as a function of the distance from the nozzle; (c) velocity distribution before (1) and in (2) the expansion (the example shows the velocity distribution for Ar at $T_0 = 300$ K (1) and for $T = 10$ K (2), respectively).

sufficiently extreme conditions, reaches sonic speed ($\mathbf{M} = 1$) as it exits the nozzle and supersonic speed ($\mathbf{M} > 1$) upon further expansion. A small solid angle of the expansion is extracted by means of a skimmer, before the expanding gas flow can readjust to the boundary conditions. Inside the expansion, frequent collisions between the molecules result in an efficient cooling (see Fig. 5). As a result the velocity υ of the molecules rapidly approaches an asymptotic value and the translational temperature decreases until there is a transition to molecular flow. The (parallel) translational temperature $T_{||}$ characterizes the width of the parallel velocity distribution for the flux $I_{||}$, which is generally modeled by a shifted Boltzmann distribution ($\upsilon_{||}$ is the parallel velocity and M is the molecular mass):

$$I_{||} \propto \upsilon^3 \exp\left(-\frac{M(\upsilon - \upsilon_{||})^2}{2kT_{||}} \right).$$

A simple estimate of the parallel velocity can be obtained by means of a thermodynamic analysis, assuming an ideal gas, constant heat capacity C_p, constant $\gamma = C_p/C_v$ and efficient cooling ($T_{||} \ll T_0$, $\upsilon_{||} \approx \upsilon_\infty$), where we obtain a maximum or terminal velocity υ_∞ ($\langle M \rangle$ is the average molecular mass):

$$\upsilon_\infty = \left(\frac{2RT_0}{\langle M \rangle} \left(\frac{\gamma}{\gamma - 1} \right) \right)^{0.5}.$$

The fact that all species in the expanding gas mixture have the same velocity (disregarding 'slip effects', see [138] and references therein) provides some degree of control over the KE of the species of interest by preparing gas mixtures with inert gases ('seeding'). It should be noted that, in practice, the relaxation of internal energy depends on the number of molecular collisions in the expansion (determined by the expansion conditions) and the energy transfer between the degrees of freedom. In general, there is efficient cooling of translational and rotational motion, whereas this is not necessarily the case for vibrational degrees of freedom, in particular for small molecules.

In summary, the main advantages of a supersonic beam source are: (a) *narrow velocity distribution*, (b) *variable kinetic energy* and (c) a large degree of *control over the internal energy*. Moreover, a broad scope of methods exists, which allow the modification of the energy distribution or selection of specific excited states in flight, i.e. after preparation of the beam. These features are essential in studies of the *gas–surface dynamics*, of *surface scattering and diffraction* or of *fast transient kinetics*.

The design of supersonic sources is well-documented in the literature ([76] and references therein), and typically involves two to three differential pumping stages, with the pumping speed in the expansion chamber limiting the gas throughput and, therefore, the beam intensity. Intensity modulation is typically provided by pulsed nozzle sources and mechanical choppers. Time-of-flight spectra are taken with a differentially pumped QMS operating in pulse counting mode and a multichannel scaler. Some characteristic features and experiments are displayed in Fig. 6 (see [97] for details). In the limit of short opening times, pulsed solenoid source (Fig. 6a) typically produce irregular pulse shapes (see, e.g. [140,141]) and have to be synchronized with a chopper in order to obtain well-defined short gas pulses, suitable for velocity measurements. From the corresponding time-of-flight spectra, it is straightforward to derive the KE distribution of the species (see, e.g. [66,111]), taking into account the experimental geometry and several instrumental contributions and delays (chopper function, QMS response time, etc.).

Some basic scattering experiments are illustrated in Fig. 6c–f involving (i) scattering of Ar from an ice multilayer and (ii) scattering of O_2 from an Al_2O_3 model support (see Section 3) [97]. To a first approximation, we can generally divide the flux of impinging molecules into a fraction which is trapped in a physisorbed state followed by later desorption (trapping desorption component, TD), and a part which is more or less directly scattered back into the gas phase (direct inelastic scattering, DI) (see, e.g. [67] and references therein). Both channels can be distinguished via their angular (Fig. 6c and d) and KE distribution (Fig. 6e and f). The fraction of molecules trapped upon impingement depends on the KE and internal energy distribution and incidence angle of the molecules in the beam, as well as on the dynamics of the molecule surface interaction and surface temperature. For O_2 scattering from Al_2O_3, partial trapping is expected, whereas in the case of Ar scattering from ice layers, energy transfer is very efficient, resulting in nearly complete trapping (except at very high KE) [142]. An important implication, which follows from the behavior in the latter case is that on the basis of the principle of detailed balance, the angular distribution of desorbing Ar molecules from the ice layer should follow a cosine law and the velocity distribution should correspond to a Maxwell–Boltzmann distribution with $T = T_{\text{Surface}}$.

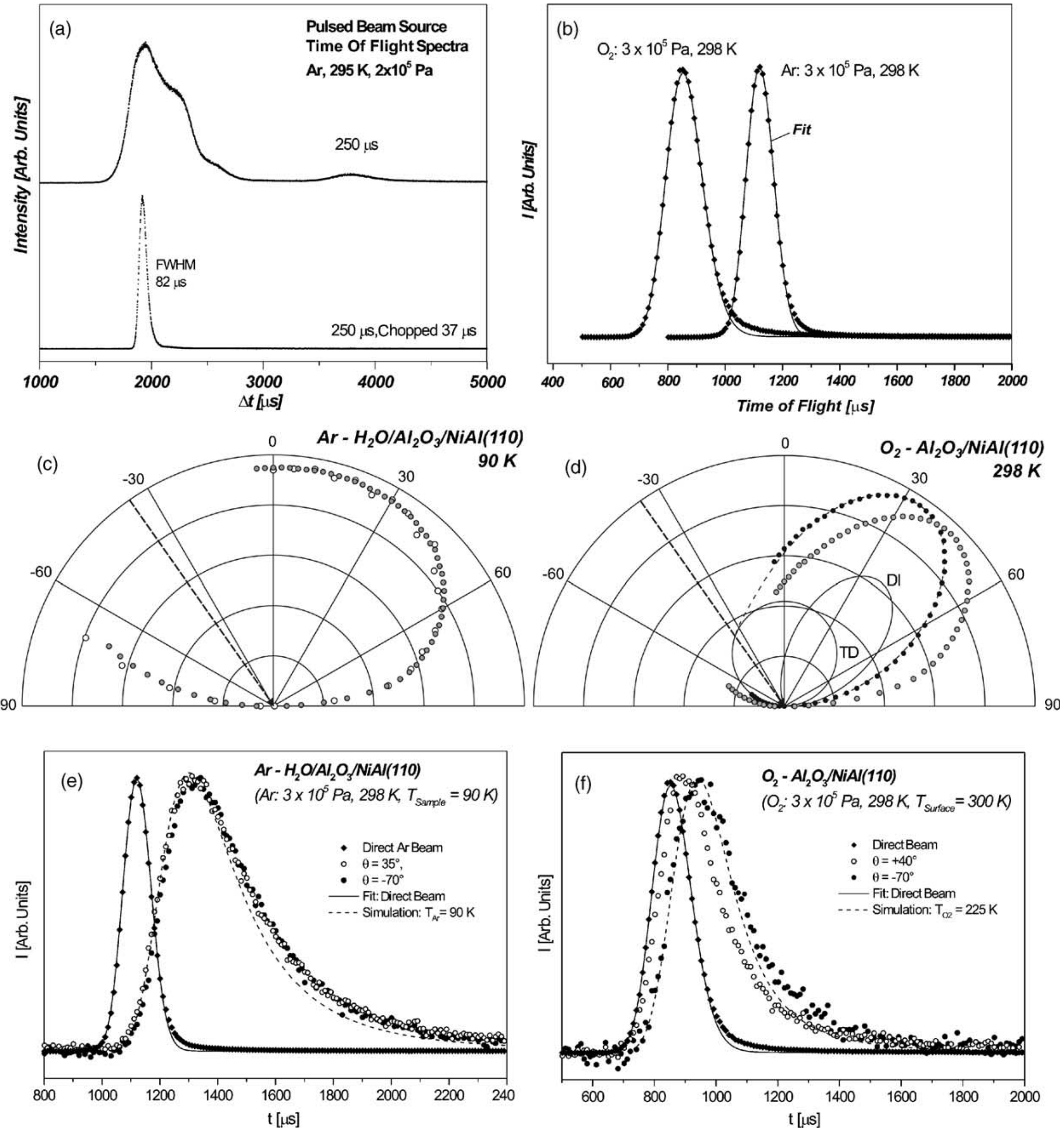

Fig. 6. Time and angle-resolved scattering experiments: (a) time-of-flight spectra for a direct pulsed and pulsed/chopped Ar beam; (b) time-of-flight spectra and fits for an Ar and an O_2 beam; (c) angular distribution for Ar scattered from an ice multilayer; (d) angular distribution for O_2 scattered from an alumina model support; (e) time-of-flight spectra for Ar scattering from an ice multilayer; (f) time-of-flight spectra for O_2 scattering from an alumina model support, from [97].

The differentially pumped angle-resolved QMS detector provides two methods to determine this angular distribution of scattered molecules: (1) the time-of-flight spectra for a pulsed beam are acquired and integrated (Fig. 6c, open circles) or (2) the partial pressure of the scattered gas in detector compartment is measured using a continuous beam (Fig. 6a, filled circles). The principal difference between the two methods is that, in the latter case, the signal is dominated by thermalized molecules, whereas the time-of-flight method involves ionization in flight, leading to a detection efficiency depending on the KE distribution. Both methods yield identical distributions in the Ar–ice case due to the angle independent KE distribution expected for complete trapping. The fact that in this case the angular distribution $I(\theta)_{\text{Ar–ice}}$ follows a cosine law allows a simple correction of angle-resolved data $I_{\text{exp}}(\theta)$ for the detector acceptance function according to:

$$I(\theta) = \cos(\theta)\frac{I_{\text{exp}}(\theta)}{I_{\text{Ar-ice}}(\theta)}$$

The procedure is illustrated for O_2 scattering from clean Al_2O_3/NiAl(1 1 0), where an asymmetric distribution is indicative of a pronounced DI component (Fig. 6d, gray circles). The distribution is corrected for the angular acceptance of the detector (Fig. 6d, black circles) and subsequently can be decomposed into a lobular DI component and a symmetric TD component (possibly including some diffuse scattering from defects). Corresponding time-of-flight spectra are shown in Fig. 6e and f. As expected we find a Maxwell–Boltzmann velocity distribution corresponding to the surface temperature for the complete trapping case (Ar–ice), whereas for the partial trapping case (O_2–Al_2O_3/NiAl) the KE depends on the detection angle, due to the different contributions of the DI and the TD components.

2.2.2. Effusive beam sources

The second class of beam sources is so-called effusive sources, which operate at large Knudsen numbers. Under such expansion conditions, there is only a negligible number of intermolecular collision between the gas molecules exiting the source. Thus, the energy distribution in all degrees of freedom is described by the temperature of the stagnation state T_0, and specifically, the velocity of the gas molecules follows a Maxwell–Boltzmann distribution for the flux:

$$I = N\upsilon^3 \exp\left(-\frac{M\upsilon^2}{2kT_0}\right)$$

The simplest effusive source is based on a thin-walled orifice, which produces a cosine angular flux distribution. Formation of a beam requires the extraction of a small solid angle element from this flux and, therefore, removal of most of the gas by differential pumping. As the background pressure has to be kept sufficiently low to avoid distraction of the beam, the maximum beam intensity is typically limited by the pumping speed in the expansion chamber. The situation can be improved by using long channels instead of thin-walled orifices, which show a strongly angle dependent transmission probability and allow a collimation of the flux (Fig. 7). Corresponding angular distributions are displayed in Fig. 7c as a function of the length to radius ratio L/r of the channels (low pressure limit [143], see also [139] and references therein).

Usually, the collimation effect is described via a peaking factor κ, which represents the ratio of the centerline intensity of the actual distribution $I(0)$ and a cosine distribution at identical total flux $\dot{N}$. In the low pressure limit and for sufficiently long channels, κ can be approximated as (see also [139] and references therein):

$$\kappa = \frac{\pi}{\dot{N}} I(0) = \frac{3L}{8r}$$

Thus, at typical L/r values of around 40, peaking factors of $\kappa \approx 15$ can be obtained. For comparison, it should be noted that, depending on the type of gas used, the peaking factors for supersonic expansions are in the range between 1.1 and 2.0 only [144].

As the pressure increases, the mean free path of the gas molecules approaches the channel length. In this pressure region, molecular collisions lead to a broadening of the angular distribution and to deviations from the Maxwell–Boltzmann velocity distribution ([145–149], see also [139] and references therein). It follows that a collimation effect at high total flux and high stagnation pressure can be achieved by using parallel arrays of small channels (glass capillary arrays, GCAs, Fig. 7).

In summary, the main advantages of GCA effusive sources are: (a) *high maximum intensity* at reduced pumping requirements, (b) *variable beam flux* over several orders of magnitude without changes in the beam properties, (c) *low stagnation state pressure* which allows easy beam generation for reactants with low vapor pressure and (d) *reduced gas consumption*, which is advantageous in case of experiments with rare or expensive (e.g. isotopically labeled) reactants. It follows that the use of effusive sources is advantageous in most studies of *surface kinetics*, provided the broad KE distribution does not represent crucial limitation for the experiment under consideration.

Focusing on GCA based beam setups previously used in kinetic studies on surfaces, it should be pointed out that in most cases simple dosers without any differential pumping were designed and used (see, e.g. [91,145–156]). This type of source requires either very short source–sample distances or leads to high gas loads due to the diffuse part of the angular distribution.

The setup of an effusive source is shown in Fig. 8a, which combines the application of a GCA and two differential pumping stages in order to reduce the background gas load (see [97] for details). Typical centerline intensities and beam profiles generated by the source are displayed in Fig. 8b. The most useful feature for quantitative kinetic experiments is the fact that the stagnation state pressure and beam intensity are exactly proportional over several orders of magnitude. In the high pressure limit, scattering losses (mainly intrabeam collisions due to the velocity and directional spread in front of the source) result in a decreasing flux and define an upper boundary for the intensities that can be obtained.

With respect to quantitative reactivity measurements, a second important aspect is the homogeneity of the beam flux over the sample surface. In contrast to the supersonic source, which can be treated as a point source, the GCA source has a finite size and, therefore, the beam profile sensitively depends on the details of constructions. For the above-mentioned source type typical 2D intensity profiles are displayed in Fig. 8b, resulting in intensity variations over the sample area on the order of few percent of the total intensity [97].

2.3. Some design considerations for MB experiments in model catalysis

In order to illustrate some design considerations for MB experiments in model catalysis we briefly review the setup of an apparatus, which has recently been built for this type of application (see Fig. 9) [97]. The primary requirements are the following:

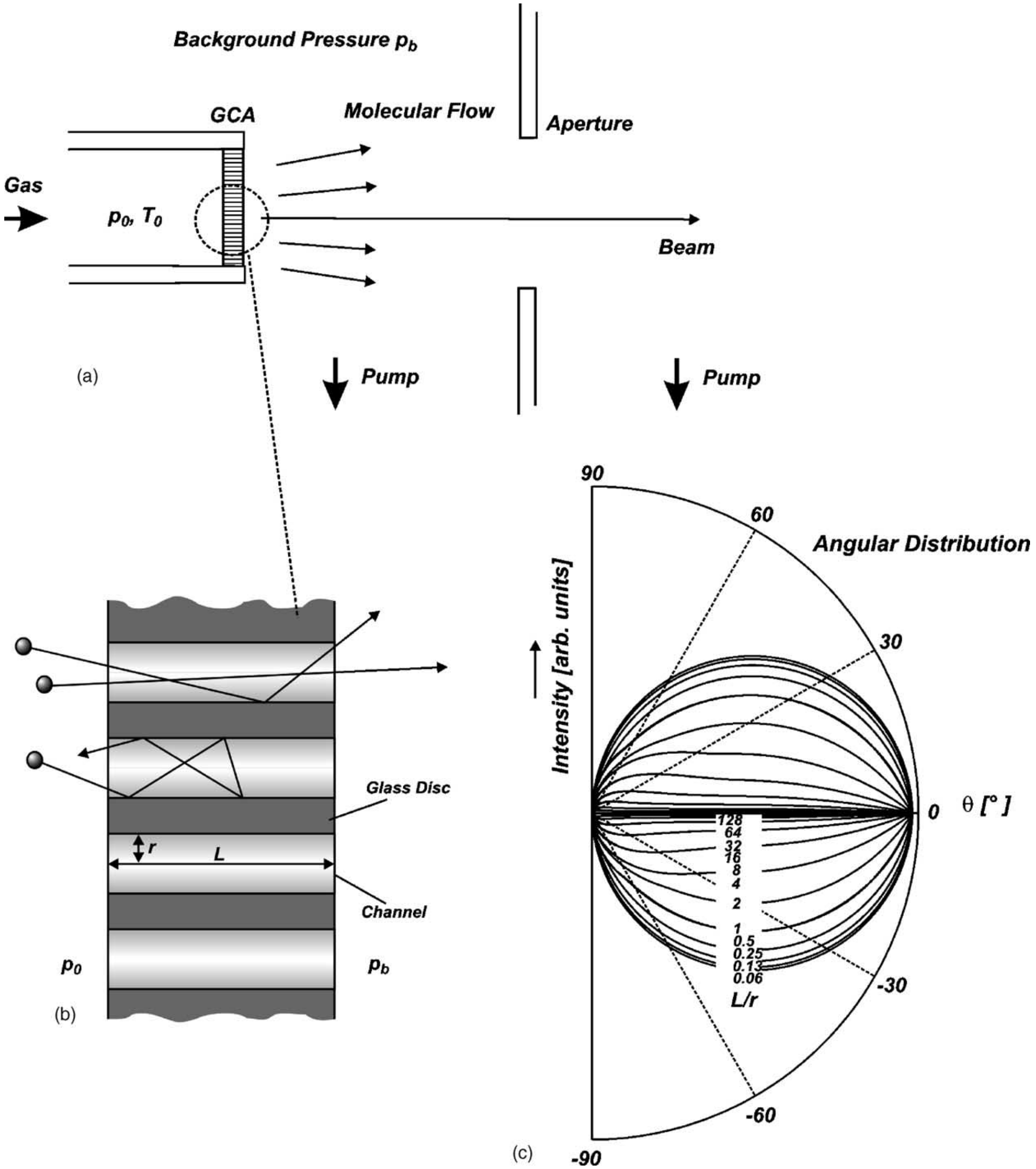

Fig. 7. (a) Schematic setup of a effusive beam source based on a glass capillary array (GCA); (b) schematic representation of the GCA focussing effect; (c) calculated angular distributions of the gas flux through a GCA in the limit of high Knudsen numbers as a function of the length-to-radius ratio.

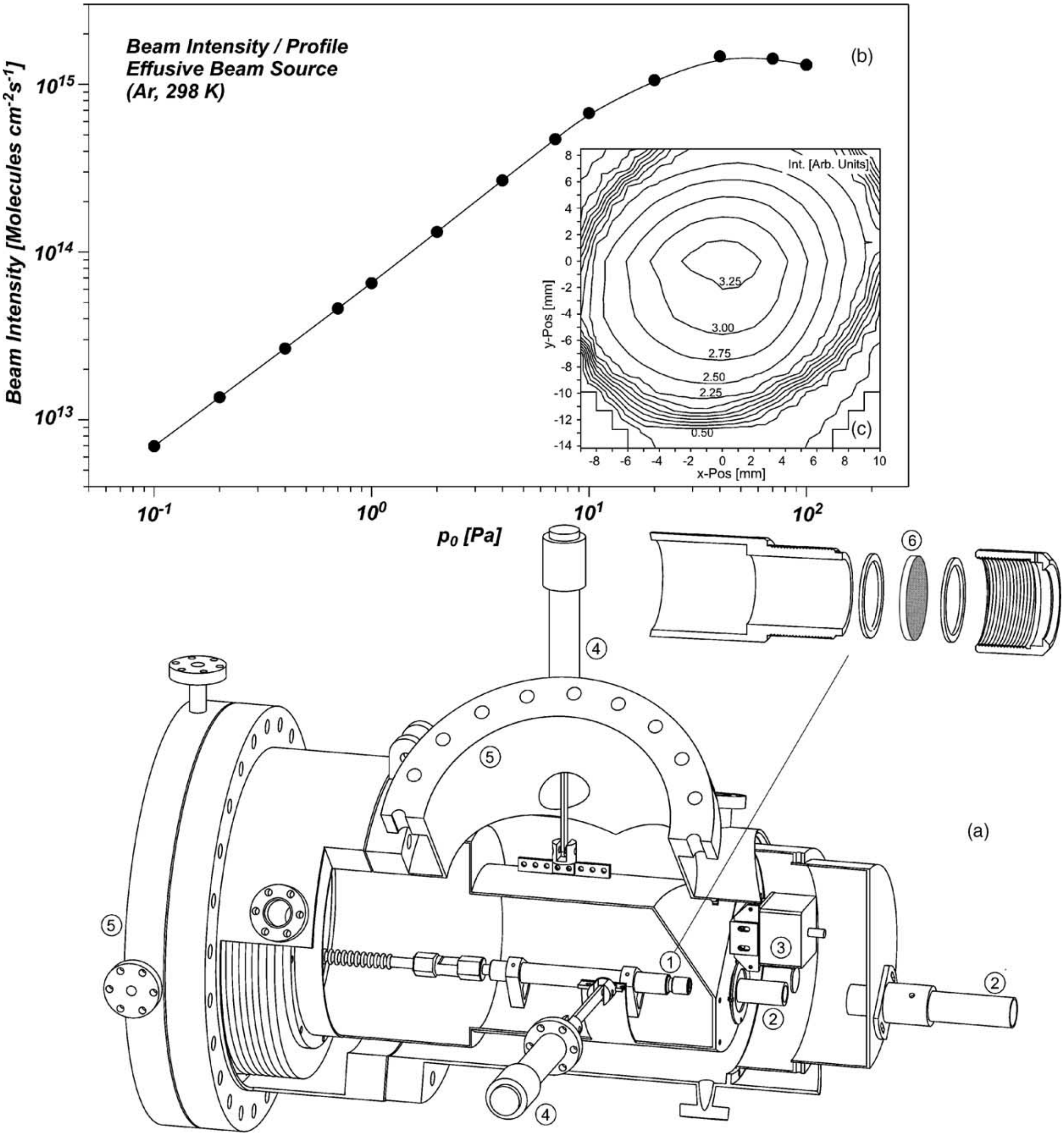

Fig. 8. (a) Differentially pumped effusive GCA source ((1) source tube; (2) apertures; (3) shutter; (4) alignment; (5) TMP; (6) GCA); (b) beam intensity as a function of backing pressure; (c) beam profile (Ar, 10 Pa), from [97].

(i) A combination of *beam sources* should allow flux modulation (a) with multiple reactants, (b) over a broad range of frequencies, (c) with maximal long-term stability and, finally, (d) should provide the highest purity of the gases.

In the setup shown in Fig. 9, up to three molecular beams can be crossed on the sample surface. An arrangement involving supersonic and effusive sources combines the advantages of both techniques and provides flexible modulation capabilities.

(ii) The *gas phase detection* facilities (a) should be applicable to a broad range of reactants and products and (b) should provide temporal resolution on the time-scale of both transient reactivity and/or (reactive) scattering experiments (typically 10^{-6} to 10^{3} s). Here, quadrupole mass spectrometry is the most universal method, but provides an intrinsically low sensitivity (e.g. as compared to bolometric detection or photoionization). Therefore, angle-resolved studies typically require differential pumping of the detector region. In addition non-line-of-sight mass spectrometry is required to measure integral reaction or adsorption rates (see Fig. 9).

(iii) As discussed above a key issue in connection with complex surfaces is time-resolved *surface spectroscopy*: here, the main requirements are (a) high specificity with respect to chemical species and adsorption site, (b) compatibility with rough and nanostructured surfaces, (c) temporal resolution on the time-scale of beam induced concentration changes (typically $>10^{-3}$ s) and (d) high sensitivity and low data acquisition times.

A detection method, which fulfils most of these requirements is Fourier transform IR reflection absorption spectroscopy (FT-IRAS). Moreover, the grazing reflection geometry used simplifies the design of the MB system (see Fig. 9). The main drawback of the method is the difficulty related to the quantitative analysis of surface IR spectra (see section discussion below).

Finally, two more aspects are noteworthy. The first concerns the alignment of the beam sources and detectors, being one of the most critical during operation. The corresponding alignment procedures have to be planned and taken into account during design of the apparatus. A discussion of some details can be found in the literature [97].

The second point concerns the data acquisition procedures, communication and synchronization of the different components. Here, more complex kinetic experiments often involve specific sequences of beam pulses and acquisition schemes. If such experiments are to be performed in a quantitative and reproducible fashion, a high level of automation is required (i.e. full remote control capabilities of beam sources, modulation and detectors). Usually, implementation of this type of experiments is straightforward, if the corresponding capabilities (motor driven shutters, valves, etc.) are included in the design of the apparatus [97].

3. Supported model catalysts

3.1. Development of supported model catalysts

Since modern surface science emerged, the understanding of heterogeneous catalysis has been one of the main driving forces for studies in this field. Over the years, the complexity of surfaces employed in experimental work has increased dramatically (see Fig. 10). As this review mainly focuses on the kinetics

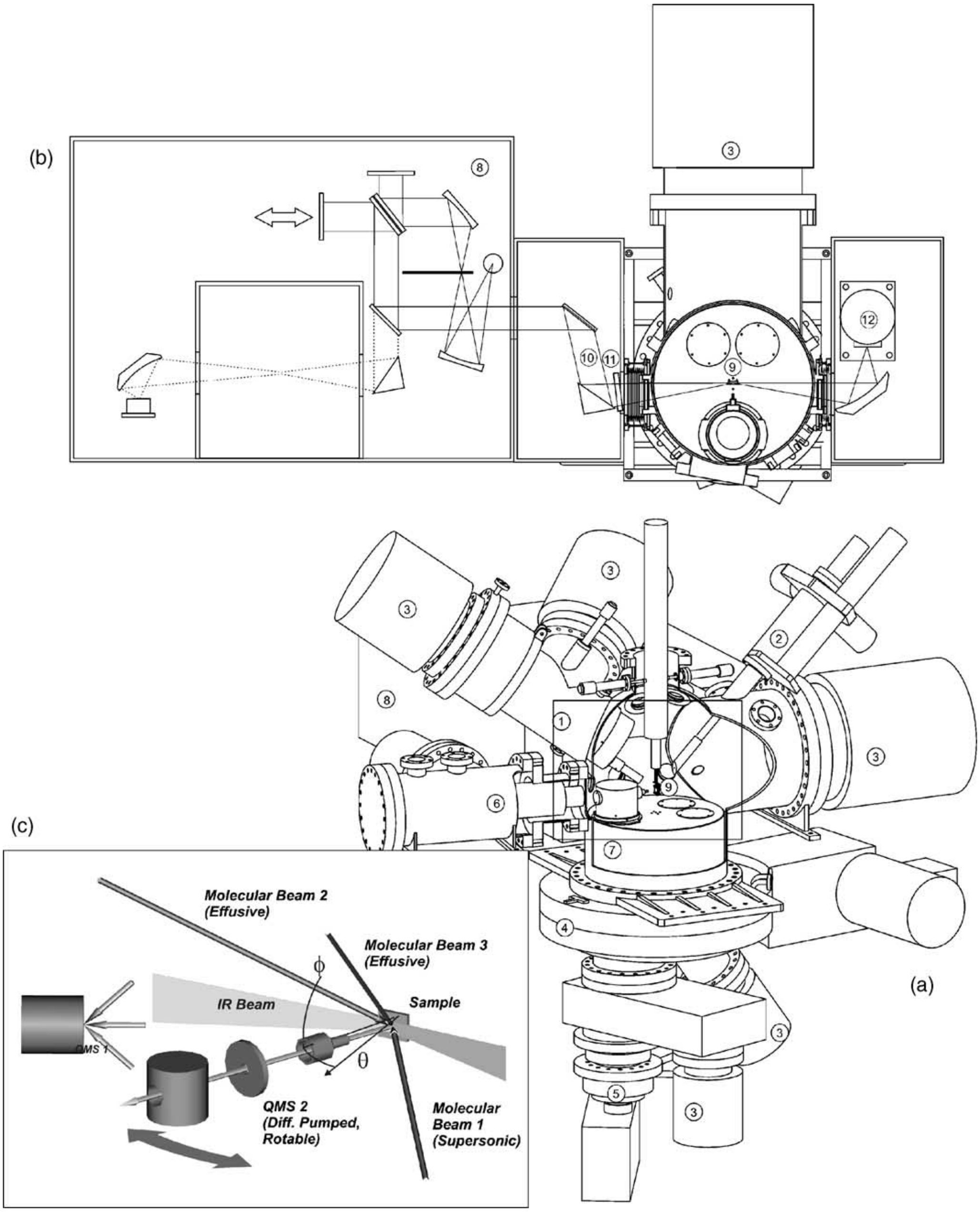

Fig. 9. Molecular beam apparatus for the study of surface kinetics on model catalysts: (a) scattering chamber; (b) IR reflection absorption (IRAS) setup; (c) schematic representation of the experimental setup ((1) effusive beam source; (2) beam monitor; (3) TMP; (4) rotating platform; (5) rotating QMS; (6) stationary QMS; (7) differential pumping stages; (8) FT-IR spectrometer; (9) sample; (10) IR beam; (11) MIR polarizer; (12) MCT detector), from [97].

on model catalysts, we restrict ourselves to a brief general introduction to the field and put a special focus on those systems, which have actually been used in MB studies. For a more exhaustive overview over the field of model catalyst preparation and characterization, we refer to several reviews that have appeared over the last decade [19,20,46,157–160].

Early work in surface kinetics and model catalysis mainly focussed on the chemistry of metal single crystal surfaces, providing important reference data on the reactivity of ideal surfaces and possible reaction mechanisms (see, e.g. [161,162]). Natural limitations arise with respect to the study of effects, which result from deviations from these ideal structures. Here, studies on stepped or defect-rich single crystals provide some insights. However, these surfaces may only poorly resemble the properties of real catalyst surfaces. The reason is that, as pointed out in Section 1, most real catalyst are relatively complex materials, often based on metal oxides or oxide supported metal particles, with a broad range of very specific structural properties and kinetic phenomena.

As a result, great efforts have been made to apply surface science methods to oxide surfaces. For the preparation of oxide surfaces, there are two general methods: (i) the use of bulk oxide crystals or (ii) the use of thin oxide films:

(i) We consider the bulk oxide approach first. The most perfect oxide surfaces can be prepared via cleavage of oxide single crystals (see [19] and references therein for an overview). Their quality

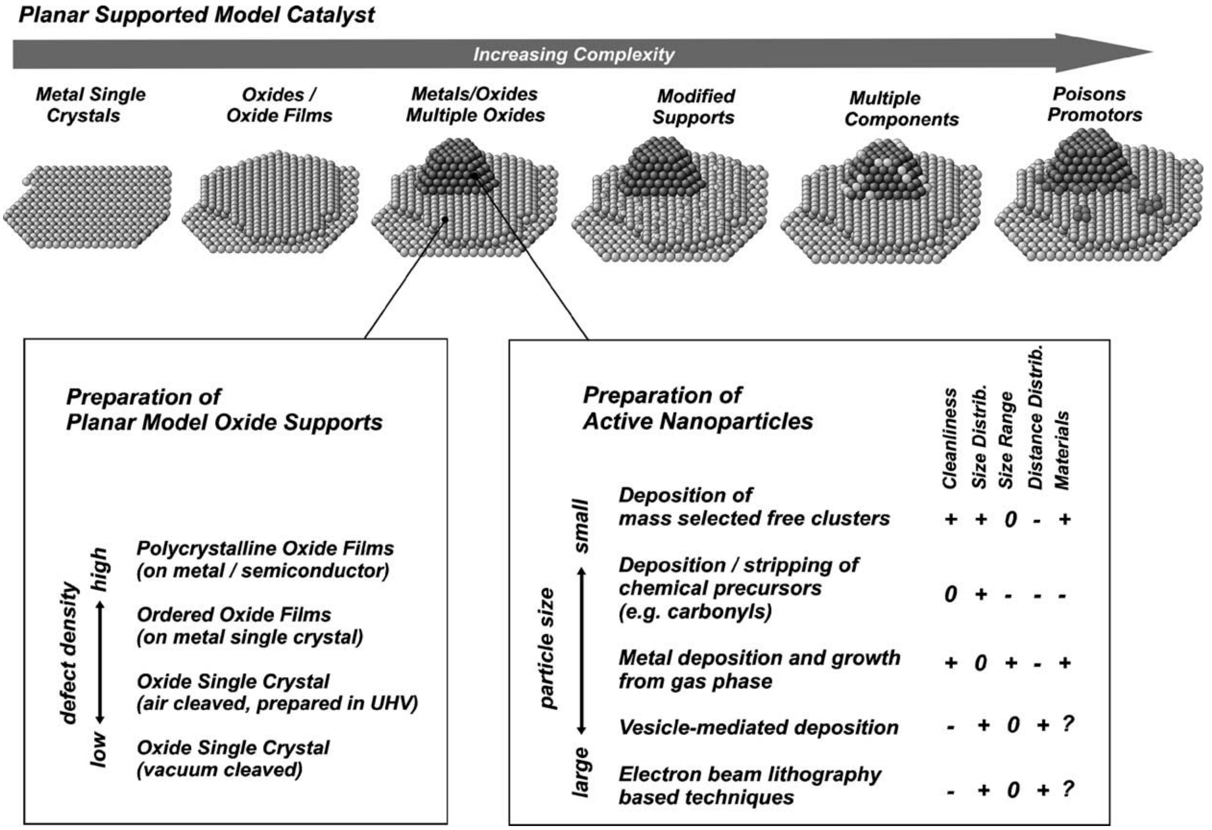

	Cleanliness	Size Distrib.	Size Range	Distance Distrib.	Materials
Deposition of mass selected free clusters	+	+	0	-	+
Deposition / stripping of chemical precursors (e.g. carbonyls)	0	+	-	-	-
Metal deposition and growth from gas phase	+	0	+	-	+
Vesicle-mediated deposition	-	+	0	+	?
Electron beam lithography based techniques	-	+	0	+	?

Fig. 10. Development of supported model catalysts and comparison of preparation techniques, from [73].

critically depends on whether cleavage is carried out in air with subsequent cleaning in ultrahigh vacuum or directly under UHV conditions. Significantly, lower defect densities are achieved in the latter case. The control over the defect properties is one of the key issues in the preparation of oxide surface. The reason is that these defects often have a major influence or even fully control their reactivity of the surface and the growth of metal deposits. Another general advantage of single crystals based supported model catalysts is their good thermal stability, i.e. limitations due changes of particle size and morphology arise from thermal reshaping and ripening processes only. Restructuring processes during reaction can often be avoided by pre-treating the systems under appropriate conditions. Those supported model catalysts, which are based on bulk oxides and have been used in kinetic MB studies are reviewed in more detail in Section 3.2.1.1.

(ii) The second approach is the preparation of oxide thin films. From the experimental point of view, the main advantages of these systems result from their enhanced electrical and thermal conductivity. Whereas the low electrical and thermal conductivity of bulk oxides may lead to severe experimental restriction, e.g. with respect to the application of electron spectroscopies, scanning tunneling microscopy and other experimental methods, these problems are avoided if thin or ultrathin oxide films on metallic supports are employed. In addition, the high thermal conductivity of the metallic support simplifies exact temperature measurements. One less obvious advantage is that in some cases surface structures can be prepared, which are not accessible on macroscopic single crystal surfaces. Often, the price to pay for these advantages is a reduced thermal stability, arising from the fact that mobility of the oxide ions increases at higher temperature. As a result, metal diffusion through the oxide layer may occur under severe reaction conditions. Nevertheless, numerous oxide thin films have been successfully used in model studies and substantial efforts have been undertaken to develop suitable preparation procedures and to characterize structure, defects and defect densities of their surface. Some experiments in this field have made use of polycrystalline oxides and oxide films (see, e.g. [94,163–165]), which, however, are associated with the drawback that their surfaces expose high defect densities and poorly defined structures. To a large extent, these problems are avoided by the use of ordered oxide films. As a consequence, large efforts have been undertaken by various groups to develop preparation procedures for different types of ordered oxide films on metallic supports. Today, numerous recipes are available for the preparation of ordered oxide films including, e.g. Al_2O_3, SiO_2, MgO, NiO, Cr_2O_3, $Fe_{3x}O_y$ and many others (see, e.g. [166–171] and references therein). Their preparation is typically based (a) on the direct oxidation of a metal (or semiconductor) single crystal (e.g. [172,173]), (b) on the oxidation of an alloy single crystal (e.g. [166,174]) or (c) on the deposition and oxidation of a metal on an inert substrate single crystal ([167,170,175]). In spite of the quality of these surfaces, it should be pointed out that the defect densities of typical ordered oxide thin films are in general significantly higher than those of UHV-cleaved single crystals. This fact has in many consequences for the nucleation behavior of metal particles [46]. Thin film based model catalysts, which have been used in MB work are reviewed in Section 3.2.1.2.

After preparation and characterization of the model support, the next step is the preparation of the active particles. In most cases, these active particles are metal or oxide aggregates in the nanometer size range. Ideally, these particles are characterized by: (i) a clean and contamination-free surface, (ii) by a well-defined size and structure and (iii) by a well-defined spatial distribution of the active particles on the support. In addition, the preparation procedure should provide a maximum of control over these parameters and should be applicable to a broad range of materials. In practice, several preparation procedures have been developed, all of which, however, only partially fulfil the above criteria and all techniques have certain advantages and disadvantages. Some current methods, which have been used or, at least, may potentially be used in surface science studies are briefly summarized in Fig. 10. In addition, there are other preparation techniques in catalysis and model catalysis, mainly based on deposition from solution, e.g. impregnation methods typically used in the preparation of real catalysts [4]. These methods are rarely used in surface science due to the problems related to contamination and less well-defined structural and chemical properties. For this reason, they are not considered further here.

For surface science studies on supported model catalysts, the most common preparation method is metal vapor deposition and growth from the gas phase (*physical vapor deposition*, *PVD*) [19,160,171]. The main advantages of PVD are its applicability to most materials and the cleanliness of the samples prepared. In addition, a broad range of particle sizes can be obtained by carefully controlling the preparation conditions. One inherent drawback is the fact that samples are characterized by a more or less broad distribution of particle sizes and shapes. Moreover, the position and distance of the particles on the surface cannot be controlled externally, but in most cases is determined by the nucleation behavior, depending on the specific combination of metal and oxide surface and, in many cases, on the type and distribution of surface defects on the model support. It is important to note that the type of defect, which is active for nucleation processes, can be chosen via the growth temperature. As a result, the particle density and size can often be varied over a large range of values by choosing the appropriate growth conditions. Typically, particle sizes in the order of 1 to approximately 10 nm are easily accessible. In Section 3.2.1, those systems, which have been used in MB work, will be considered in more detail.

Some alternative preparation methods have been suggested to overcome these drawbacks, but there are much fewer studies which have actually made use of these approaches in model studies. Most of these techniques aim at the formation of well-defined chemical entities or of aggregates of well-defined size, which are subsequently deposited on the surface. An example is *chemical vapor deposition*, i.e. the preparation of complexes with well-defined stoichiometry and sufficiently high vapor pressure, which can be deposited on the surface via the gas phase (see, e.g. [176,177]). Here, the main restrictions are given by the availability of suitable precursors and the lack of control over the distribution of the active aggregates on the surface. Moreover, problems may arise upon stripping of the ligands due to the reduced stability of the ligand-free aggregates or due to contaminants remaining on the particle surface upon decomposition of the ligands. A promising approach for the range of smaller aggregates, which avoids contamination due to incomplete removal of the ligand shell, is the formation and *deposition of free clusters from the gas phase*. Such aggregates can be mass-selected and subsequently soft-landed on the surface [42,178]. In a unique fashion, this method allows atom-by-atom control over the aggregate size. Also, cluster deposition without additional mass-selection has been tested [179]. The main drawback which remains is the fact that the distribution of the particles can only indirectly be controlled by the quality of the oxide surface via nucleation at defect sites. As a result, the particle distance distribution remains poorly defined and the experiments are limited to low nominal metal coverage in order to avoid coalescence. Recently, preparation methods have been developed which aim at a simultaneous control over particle size and distance. Here, one possibility is the *deposition of micelles filled with metal aggregates*. The distance of these entities on the surface can be selected via their shells, consisting, for example, of diblock copolymers [180,181]. An alternative approach is the use of ordered arrays of colloidal particles as a sputter mask (*colloidal lithography*) [182,183]. Not only the distance, but also the individual position of each particle can be controlled by the use of nanolithographic preparation methods such as *electron beam lithography* (EBL) [184–188]. Today, lithographic preparation techniques are capable of producing metal aggregates with sizes down to the order of 10 nm. Thus, the particle size range relevant for heterogeneous catalysis becomes accessible, but the methods are not yet applicable to the range of very small particles. In addition, the methods based on vesicles, colloids or lithographic techniques involve exposure of the sample to non-UHV environments and, therefore, have a inherent tendency to introduce contaminations into the model system. To what extent this fact limits the use of such systems in model studies is not clear, as only few attempts have been made to apply such preparation methods in surface science and MB studies (see Section 3.2.2).

Today, current research aims at the development of the next generation of model catalyst surfaces, including additional structural and chemical features such as modified [55] or mixed oxide systems [189,190], multiple component particles [191,192], poisons [193] or promoters. Such more complex model systems have not been used in MB experiments yet and corresponding studies are expected to provide a challenging and promising field for future work.

3.2. Supported model catalysts used in molecular beam studies

Most supported model catalyst used in MB studies have been prepared by PVD. In addition, some work has been performed on samples prepared by EBL and other methods. We will briefly revisit the structural properties of these systems in the following, using the results as a basis for the discussion of kinetic experiments in the following sections.

3.2.1. Preparation by physical metal deposition and growth

We divide supported model catalysts prepared by PVD, into two groups, depending on whether bulk oxides or thin films were used as a support. The advantages and disadvantages of both types of systems were discussed in the previous section.

3.2.1.1. On oxide single crystals. Pioneering work in the field was performed by Henry and coworkers, who studied various adsorption–desorption systems and surface reactions on Pd model catalysts, primarily based on MgO(1 0 0) single crystals [79,194–205]. Among the systems studied were the adsorption and desorption of CO and NO, the oxidation of CO and the CO–NO reaction. An overview over the specific reaction systems is given in Section 4.2.

In these studies, the growth and structure of the Pd particles were characterized in great detail by high resolution transmission electron microscopy (TEM) and, previously, by Helium diffraction [206,207] (see Fig. 11). As for most metal-on-oxide systems, Pd/MgO(1 0 0) shows a three-dimensional (Vollmer–Weber) growth mode. The most important feature is that the nucleation density of the Pd particles on UHV-cleaved single crystals is relatively low and can be continuously varied mainly via the sample temperature during deposition. Typical values fall in the range between 10^{10} and 10^{12} particles cm^{-2}. On air-cleaved MgO crystals the nucleation density is significantly higher [19], due to contaminations, which are present even after brief exposure to air. This contamination gives rise to the formation of point defects upon post-cleaning procedures in UHV, resulting in significantly higher particle densities and possible coalescence at lower nominal metal exposures [205]. The distribution of nucleation sites and coalescence is an important parameter for the width of the particle size distribution obtained. If the nucleation sites are well-distributed and coalescence is avoided, relatively narrow size distribution can be obtained (see

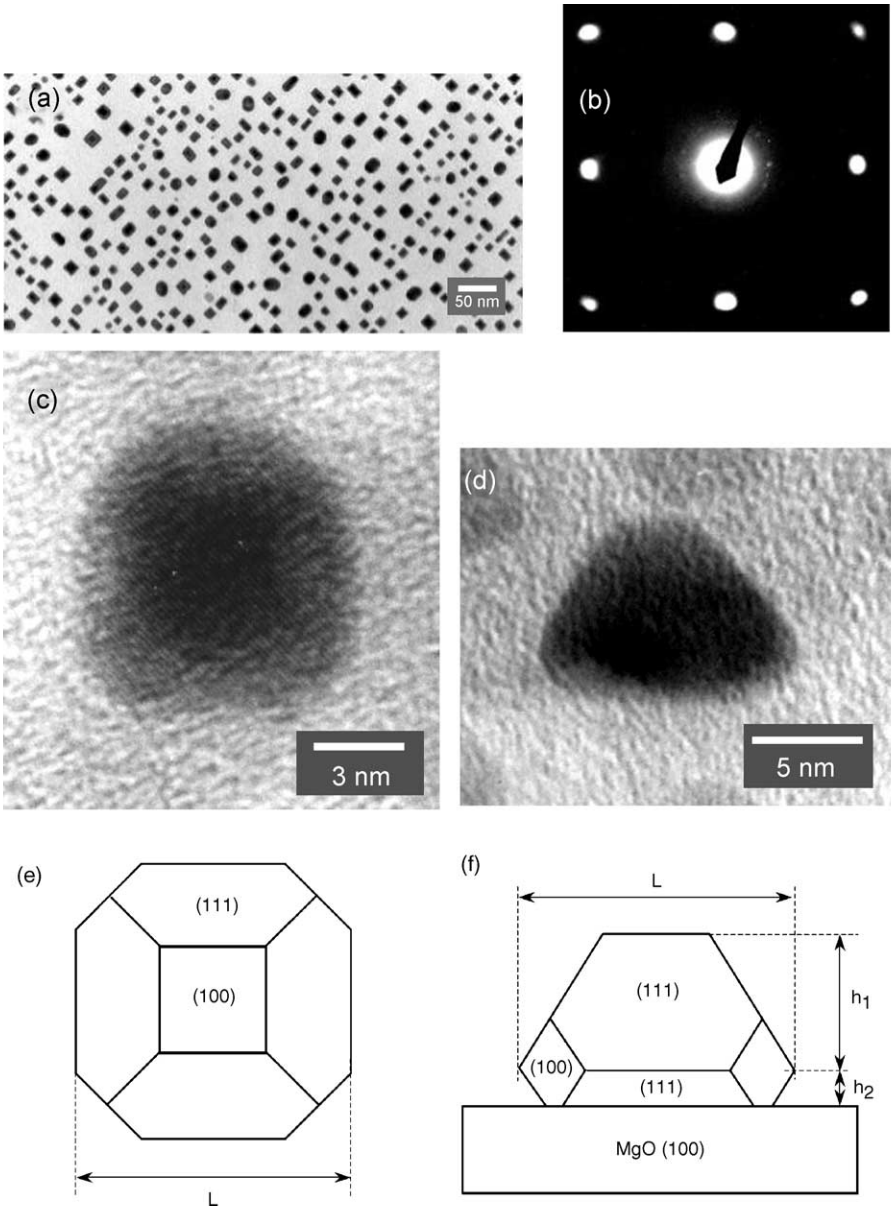

Fig. 11. Characterization of a Pd model catalyst based on UHV-cleaved MgO(1 0 0) by transmission electron microscopy (TEM): (a) overview; (b) electron diffraction diagram; (c) top view of individual Pd particle; (d) profile view; (e) schematic representation of top view; (f) schematic representation of side view, from [205].

Fig. 11). Coalescence and irregular distributions of nucleations sites, on the other hand may lead to significantly broader distributions.

A second very important aspect is the structural characterization of the individual particles (see Fig. 11). Typically, treatment at elevated sample temperatures is employed in order to obtain regular particle shapes. An important issue is the crystallographic orientation of the particle which typically depends on the support. On MgO(1 0 0), the Pd particles grow in (1 0 0) orientation and the particle shape corresponds to a cubo-octahedron, exposing (1 0 0) and (1 1 1) facets only. The precise shape of the particles, however, has been shown to depend on the growth conditions and on the particle size itself [208,209], and as a result, may be relatively difficult to control. One detail to be noticed is that TEM allows the particle shape to be investigated not only from top but also in a cross-section parallel to the support. This allows the exact particle size to be determined including the contact angle, which is important for the determination of the adhesion energy [205]. For the specific case of Pd/MgO(1 0 0), contact angles larger than 90° were found, indicating a weak interaction with the support.

Apart from the work by Henry et al., MB experiments on both model catalysts prepared on α-Al_2O_3 single crystals [49,52,210–214] and thick γ-Al_2O_3 films [94,210,212,215–218] were performed by Matolin and coworkers. In their studies on α-Al_2O_3 single crystals, three different crystallographic orientation (0 0 0 1), (1 −1 0 2) and (1 1 −2 0) were used. Different preparation conditions involving heating in air or in vacuum led to the formation of stoichiometric and reduced surfaces, respectively [219]. Pd and Rh particles were prepared and the reaction systems studied on those systems included the adsorption–desorption of CO and O_2 as well as CO oxidation. Typically, the particles were prepared at elevated temperature and the systems were stabilized by O_2 and CO treatment prior to use. Particle sizes and densities were determined by TEM. Typical particle sizes fell in the range between 2 and 20 nm and the particle densities between 10^{12} and 10^{13} cm^{-2}. In addition to these structural parameters, the authors determined the epitaxial relationship of the particles with respect to the support by reflection high energy electron diffraction (RHEED). It was found that the crystallographic orientation of the Pd particles depended on the orientation of the α-Al_2O_3 support, with (1 1 1) orientation on α-Al_2O_3(0 0 0 1) and (1 1 1) and (1 1 0) orientation on α-Al_2O_3(1 −1 0 2) [214].

So far, the only MB experiments on supported model catalyst based on a reducible bulk oxide were performed by Bowker et al., who investigated CO adsorption [220] as well as formic acid adsorption and decomposition [221] on Pd particles on TiO_2(1 1 0). The Pd particles were prepared at room temperature and post-annealed to 473 K before characterization by means of STM [222]. Vollmer–Weber growth was observed, with particle sizes around 4 nm and densities of around 8×10^{12} cm^{-2}, but the particles we found to exhibit low aspect ratios, indicating a relatively strong interaction with the support. Although STM indicated only moderate morphological changes upon annealing, a drastic decrease in the CO uptake and CO sticking coefficient was found upon heating above 573 K [220]. The effect was investigated by STM [223] and assigned to a strong metal support interaction-like (SMSI, see, e.g. [28] and references therein) phenomenon, i.e. formation of an encapsulation layer of TiO_x on the Pd particle [220].

3.2.1.2. On oxide thin films. In earlier work, Matolin and coworkers employed a thick polycrystalline γ-Al_2O_3 film on Al, prepared by thermal oxidation as a model support for Pd [94,210,212–216] and Rh [217,218] particles. In our group, we have recently studied several adsorption and reaction systems using MB methods, primarily employing Pd supported model catalysts based on ordered Al_2O_3 films on NiAl(1 1 0) [61,62,224–240]. The systems investigated include the adsorption and desorption of CO and O_2, the adsorption, dissociation, dehydrogenation and oxidation of methanol and the adsorption and dissociation of NO. In the following, we will review the experimental results on the characterization of the Al_2O_3/NiAl(1 1 0) model support and on the Pd deposits in more detail. The reason is two-fold: firstly, a large fraction of the MB experiments discussed in the following relies on the structural characterization of the Pd/Al_2O_3/NiAl(1 1 0) system. Secondly, the system represents one of best explored example of a supported model catalyst, showing how – by combination of numerous experimental methods – detailed insights into the surface structure and chemistry can be obtained, even on relatively complex surfaces of supported model catalysts. It should be noted that, in addition to the Pd/Al_2O_3/NiAl(1 1 0) system, Raval and coworkers have recently started to perform combined MB and IRAS experiments on supported Au [241] and Cu model [242] catalysts on the same support. Both types of metal deposits were characterized by STM [243] and the reactions investigated were the adsorption of CO in the case of the supported Au catalyst and the adsorption, dissociation and reduction of NO in the case of the supported Cu catalyst.

Returning to the model support Al_2O_3/NiAl(1 1 0), the formation of the corresponding low energy electron diffraction (LEED) pattern was initially described by Müller et al. [244], and the preparation procedure and detailed structural characterization was reported by Jaeger et al. ([166], see also [174]). An important detail is the use of an NiAl(1 1 0) alloy crystal instead of an Al single crystal. This experimental detail allows higher annealing temperatures than on pure Al substrates, which is an essential point for obtaining a high degree of order. Attempts to prepare suitable oxide films by oxidation of pure Al single crystals were only moderately successful (see, e.g. [245–247]). After development of the preparation procedure, the geometric and electronic properties of the film were explored using a wide range of techniques, such as, e.g. AES, LEED, spot profile analysis LEED (SPA-LEED), PES (including X-ray photoelectron spectroscopy, XPS, and angle-resolved photoelectron spectroscopy, ARUPS), STM, atomic force microscopy (AFM), TEM, EELS and high resolution electron energy loss spectroscopy (HR-EELS), IRAS, ion scattering spectroscopy (ISS), surface X-ray diffraction (SXRD) and temperature programmed desorption (TPD) [46,60,166,174,248–256]. Briefly, the essential insights from these studies can be summarized as follows:

(i) *Geometric structure*: the oxide film is characterized by a well-defined thickness of approximately 0.5 nm, corresponding to two atomic layers of aluminum and oxygen ions [248,251]. With respect to the use as a model support, it is most important to ensure that metal substrate is fully covered by the oxide film and no holes remain, which could distort reactivity measurements. Whether this is the case can be routinely checked after preparation by testing the CO adsorption behavior, see, e.g. [248,257]. As demonstrated by the SPA-LEED and STM studies [46,60,166,174], the oxide films are flat on an atomic scale and the degree of order is exceptionally high. This point is of particular importance with respect a structural characterization of supported metal particles by scanning probe or diffraction methods. The LEED pattern [174] indicates a large, nearly rectangular unit cell, which is rotated with respect to the NiAl(1 1 0) substrate (see Fig. 12), and is commensurate with the substrate along the [1 −1 0] direction, but not along [0 0 1]. Due to the symmetry of the substrate, two reflection domains exist. At an early stage, a schematic structure model was suggested on the basis of LEED, AES, ARUPS and TPD [166]. TPD and ISS results were interpreted in terms of a preferential termination by a layer of oxygen ions [166,248,249]. Here, it should be kept in mind, however, that large interlayer relaxations are expected for these systems, which may drastically reduce the interlayer distances (see. e.g. [258]). The oxygen ions were originally proposed to be arranged in a distorted hexagonal arrangement, whereas the Al ions were suggested to simultaneously occupy both tetrahedral and octahedral sites. Recently, SXRD experiments were performed by Stierle et al. [253], and the authors were able to derive a refined model from their experimental data, arriving at the conclusion that it is a κ-alumina-like film. In recent STM work, atomic resolution has been achieved on the alumina film (see, e.g. [255,256,259]). On the basis of DFT

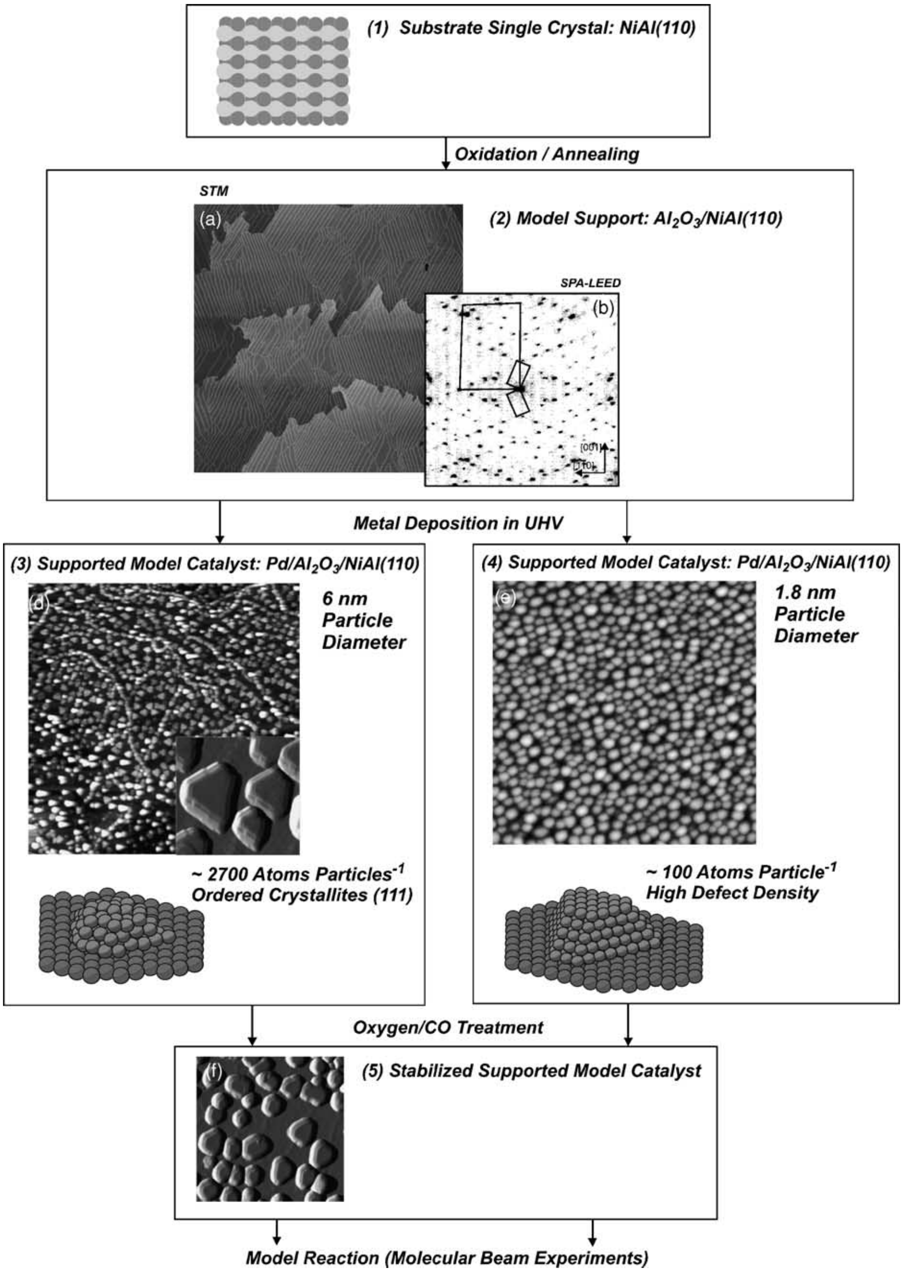

Fig. 12. Preparation of a Pd model catalyst based on an alumina thin film: (1) NiAl(1 1 0) substrate; (2) Al_2O_3/NiAl(1 1 0), (a) STM image (1 μm × 1 μm), (b) SPA-LEED pattern, dimension of the substrate and oxide unit cells indicated; (3) STM image (d, 300 nm × 300 nm, close-up: 20 × 20 nm), schematic model of the Pd particles; (4) STM image (e, 100 nm × 100 nm), schematic model of the Pd particles; (5) STM image after stabilization by oxygen treatment (f, STM, 50 nm × 50 nm), STM images from [61,264].

calculations, Kresse et al. refuted the SXRD-derived model and proposed a new structure, which is in full agreement with the STM data [259]. They suggested that the surface is composed of aluminium atoms pyramidally and tetrahedrally coordinated, a set of building blocks also found on the surface of reduced α-Al_2O_3(1 0 0 0) surfaces ([259], compare [260,261]).

(ii) *Electronic structure*: with respect to the interaction of molecules with the oxide film, an important question is whether the electronic properties of the film sufficiently resemble those of a bulk support. For the case of Al_2O_3/NiAl(1 1 0), the valence electronic structure, investigated by ARUPS, shows a well-developed parallel band structure suggesting a hexagonal arrangement of oxygen ions [166]. Moreover, EELS measurements show a band gap (~8 eV) [248], which agrees well with bulk values (see discussion in [46]). Related to the electronic structure is the question whether the oxide film gives rise to a sufficient decoupling of the metal particles from the metal support underneath. This issue was previously addressed by in a combined PES, X-ray absorption spectroscopy (XAS), AES and autoionization spectroscopy (AIS) study [56,252,262,263]. The results indicate that on the time-scale of the core hole lifetime the metal particles are completely decoupled from the metallic substrate.

(iii) *Defect structure*: as pointed out before, an essential factor with respect to the growth of metal deposits is the defect structure of the oxide film. In many cases, it is the defects on the support which determine the nucleation behavior of metal deposits and which, therefore, control the particle density and size. Different types of defects have been identified on the Al_2O_3 film mainly employing STM and SPA-LEED [46,60,174,254,255], but additional hints could also be derived from several other experiments (see, e.g. discussion in [46]). Among the one-dimensional defect structures are substrate steps and domain boundaries between the reflection domains. The dominating type of defects, however, are antiphase domain boundaries, which appear as straight lines at a preferential lateral distance in the STM image, from [264]) and lead to characteristic broadening effects in the intensity profile of the LEED reflections [174]. Recently, atomic scale information on the geometric and electronic structure of domain boundaries have been derived from STM and scanning tunneling spectroscopy (STS) [254,255] and SXRD [254]. In addition, indications were found that point defects or, more generally, specific adsorption sites on the domains can have an important influence in the nucleation behavior of metal particles, in particular at lower growth temperature [46]. For practical reasons, it is important to note that the reproducibility of the defect structure and defect density is high, if standardized preparation procedures are applied [46,174].

(iv) One of the most important points for reactivity studies is the interaction of reactants with the support. In general, it has been observed that the interaction of the film with many small molecules is weak for the pure oxide film (CO, O_2) [248]. There are exceptions to this rule, including, e.g. NO (see Section 8) [236].

After characterizing the model support, the next step is the deposition of active metal particles. For each type of metal deposit, the growth behavior, the geometric and electronic structure and the adsorption properties have to be studied individually. In the case of the Al_2O_3/NiAl(1 1 0) support, this has been accomplished in a series of studies for numerous metals, such as Pt, Pd, Rh, Ag, Ir, Co, Al, V, Au and Cu (see [44–46,59–61,192,243,265,266] and references therein). Most of the MB experiments have been performed on Pd particles and we review the corresponding results in more detail in the following. For with respect to two other systems used in MB work so far (Au/Al_2O_3/NiAl(1 1 0), Cu/Al_2O_3/NiAl(1 1 0) [241,243]) characterization by STM showed a Vollmer–Weber growth mode as for the Pd/Al_2O_3/

NiAl(1 1 0), but drastic differences with respect to the nucleation behavior, i.e. preferential nucleation at steps and domain boundaries for Cu, but no preferential nucleation at such sites for the case of Au. With respect to a detailed discussion of the growth behavior for different metals we refer to the review by Bäumer and Freund [46].

Returning to the case of Pd, from the point of view of its growth behavior there is one aspect which makes this system particularly interesting: as discussed before, in most cases metals on oxides follow a three-dimensional growth mode (Vollmer–Weber growth). Under a given set of conditions, there are drastic variations from metal to metal with respect to the nucleation density and the particle sizes. The latter critically depends on the metal–oxide interaction and the activation barriers for diffusion on the oxide. For the specific case of Pd, the nucleation densities strongly depend on the growth temperature and, as a consequence, the particle size can be varied over a very broad range (from aggregates of only few atoms up to islands containing more than 10^4 atoms [45,46,54,60]).

In the MB work, mainly two types of Pd/Al_2O_3/NiAl(1 1 0) model catalysts with rather dissimilar structural properties were used. The corresponding preparation conditions differ with respect to the growth temperature mainly. For both types of systems, information on the geometric and electronic structure and the adsorption properties was derived in previous studies [45,46,54,56–62,193,252, 257,262,263,267–269]. We briefly summarize the corresponding information, as far as it is of relevance for the discussion in the following sections:

(i) *Pd deposits prepared at room temperature (300 K) on Al_2O_3/NiAl(1 1 0)*: under these conditions, the diffusion of trapped Pd atoms on the Al_2O_3 domains is sufficiently fast that mainly line defects (antiphase domain boundaries, reflection domain boundaries and steps) act as preferential nucleation centers. As a consequence, the nucleation density is relatively low (in the order of 1.0×10^{12} cm^{-2}) and a preferential alignment of the Pd particles along these defects is observed. Three-dimensional particles (Vollmer–Weber growth) of well-defined crystalline shape (truncated cubo-octaheders) are formed. These crystallites grow in (1 1 1) orientation (in contrast to the Pd/MgO(1 0 0) system discussed in Section 3.2.1.1) and preferentially expose (1 1 1) facets as well as a small fraction of (1 0 0) facets. Moreover, STM and SPA-LEED investigations show an azimuthal alignment of the particles. The particle size depends on the amount of Pd deposited. For most MB experiments, particle sizes of approximately 6 nm were chosen (corresponding to approximately 3000 Pd atoms per particle). For this particular particle size about 20% of the metal atoms are located at the particle surface and, on the basis of SPA-LEED data, it was estimated that the particles cover about 20% of the alumina support. For more details, see [226,228] and references therein.

(ii) *Pd deposits prepared at low temperature (90 K) on Al_2O_3/NiAl(1 1 0)*: at this temperature, specific sites or point defects on the oxide domains become active as nucleation centers. As a consequence, Pd islands grow not only at the domain boundaries, but also on the domains themselves. In contrast to the larger particles of type I, STM and SPA-LEED studies reveal no indications for the formation of well-ordered facets. It is assumed that the surface of these particles is dominated by a broad range of defect sites. The higher nucleation density (up to 10^{13} cm^{-2}) results in smaller particles and higher dispersion. For most MB experiments, particle sizes of approximately 1.8 nm were chosen (corresponding to approximately 100 Pd atoms). For this particular size, about 60% of the metal atoms are located at the particle surface and the particles cover about 15% of the alumina support. For more details, see [226] and references therein.

In addition to the geometric structure and growth, the electronic structure of both adsorbate-free and adsorbate-covered Pd particles has been investigated by PES, XAS, AIS and AES [46,56,252,262,263]. Here, the development of a characteristic Pd(1 1 1) valence band structure could be observed as a function of size [252]. Moreover, the electronic decoupling of the supported particles from the metallic substrate by the oxide film has been tested [56].

The adsorption of different types of small molecules such as CO [45,46,56–58,62,193, 257,262,263,268], H_2 [267] or C_2H_4 [60,267,269] was studied as a function of particle size, employing a broad spectrum of methods, ranging from TPD to vibrational spectroscopies (HR-EELS and IRAS), STM, PES and XAS. In addition, simple reactions such as the dehydrogenation of C_2H_4 have been investigated [60,267]. With respect to many adsorption and reaction systems discussed in the following, CO adsorption and desorption is of critical importance. Among the possible reasons for size and structure dependent changes in the adsorption and reaction properties, the role of specific defect sites on the particles (such as, e.g. steps or edges) has attracted particular attention (see Sections 4 and 5). For Pd/Al_2O_3/NiAl(1 1 0), two effects could be identified as a function of particle size: whereas the TPD spectra from larger well-ordered particles closely resemble those of Pd(1 1 1) single crystals [46], slight shifts of the main desorption signal toward higher temperature with decreasing particle size indicate the presence of more strongly adsorbed CO [62]. In addition, the fraction of more weakly bound CO increases with decreasing particles size as well ([46,62] see also [46,56–58,60,262]). These observations can be summarized by concluding that the coverage dependence of the CO adsorption energy increases with decreasing particle size. This result will be taken into consideration in the discussion of particle size-dependent kinetic phenomena in adsorption and reaction processes in the following sections.

Before proceeding with the reactivity studies, a most critical point is to verify the stability of the supported model catalysts under reaction conditions. In the previous section, it was already pointed out that extended treatments at elevated temperature, possibly in a reactive atmosphere, were in many cases found to be necessary in order to stabilize the particles. This is the result of sintering and restructuring processes which are expected to occur, in particular under more extreme reaction conditions (see, e.g. [40,270]). For supported model catalysts based on oxide thin films, the situation may be further complicated by the fact that the oxide film may become instable at elevated temperature.

Again, we consider the system Pd/Al_2O_3/NiAl(1 1 0) as an example. In previous work, it was found that immediately after preparation the model system exhibits significant changes of the CO oxidation kinetics, even under the low pressure conditions and short time-scales of typical UHV reactivity experiments [61]. The origin of this effect could be identified in a combined MB, PES, STM, LEED and TPD study, some results of which are displayed in Fig. 13 [61,62]. MB oxygen sticking coefficient measurements revealed low uptakes in the temperature range between 100 and 250 K, compatible with molecular and dissociative surface adsorption on the Pd particles (compare [271–273]). Above 250 K, however, the oxygen uptake was observed to increase by nearly one order of magnitude. STM data taken before and after oxygen exposure neither showed changes in particle density nor in their morphology, basically excluding restructuring processes of the active metal particles as a possible reason for the effect.

Two possible reasons for the enhanced oxygen uptake can be invoked: (i) oxygen diffusion into subsurface and bulk regions of the three-dimensional Pd particles and oxidation or surface oxidation under more severe conditions and (ii) oxygen diffusion into or through the alumina film and thickening of the alumina layer.

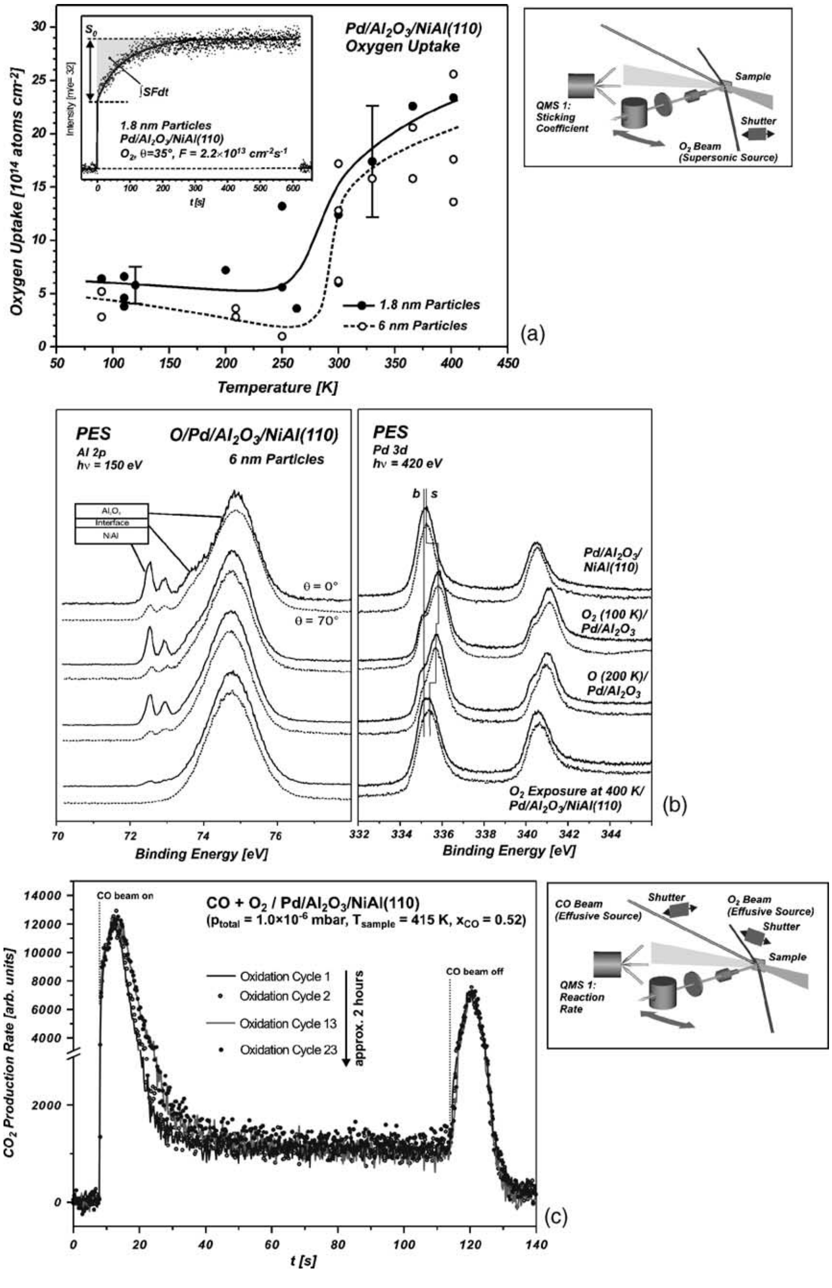

Fig. 13. On the stability of a supported Pd model catalyst based on an alumina thin film during thermal treatment and gas exposure: (a) oxygen uptake of $Pd/Al_2O_3/NiAl(1\,1\,0)$ as determined from sticking coefficient measurements, from [62]; (b) photoelectron spectra of $Pd/Al_2O_3/NiAl(1\,1\,0)$ before and after oxygen treatment at elevated temperature, from [62]; (c) stability of transient CO_2 production in CO oxidation experiment using a CO and an O_2 molecular beam crossed on the surface, from [226].

Both effects have been discussed in the literature, previously [61,62]. Slow formation of subsurface and bulk oxygen and oxide formation has been suggested and investigated in numerous studies on bulk Pd single crystals, both experimentally and theoretically [274–298]. However, for well-defined supported Pd model catalysts, no similar investigations have been conducted yet. For the Pd/Al_2O_3/NiAl(1 1 0) model catalyst a high resolution PES study [62] did not provide evidence for enhanced oxygen uptake under UHV conditions at temperatures up to 400 K (see Fig. 13b). In consideration of the single crystals experiments mentioned above, it is likely, however, that formation of surface oxides and subsurface oxygen species has an influence on the reaction kinetics under more severe condition.

With respect to the second effect, the stability of the thin oxide film, the PES experiments on Pd/Al_2O_3/NiAl(1 1 0) indicated a pronounced thickening of the alumina film upon oxygen exposure at elevated temperatures (see strong decrease of the NiAl substrate signal in Fig. 13b, compare [166]). The thickness of the additional oxide layer depends on the experimental conditions applied and its formation is likely to be the main reason for the enhanced oxygen uptake. In this respect, the following aspects are important to note: (i) formation of additional alumina occurs on the Pd-covered Al_2O_3/NiAl(1 1 0) only, whereas the pristine support film is completely inert to molecular oxygen. This behavior is attributed to activation of oxygen by adsorbate dissociation on the supported metal particles and subsequent spillover to the support. Similar effects have been observed before for vanadium on Al_2O_3/NiAl(1 1 0) [299] as well and, therefore, have to be considered in detail when investigating model catalysts based on ultrathin oxide films. As a result, detailed investigations of the adsorption behavior of the complete model catalyst system are essential before reactivity studies are performed. (ii) After extended oxygen exposure, the uptake becomes negligible and the kinetics of surface reactions performed on the system indeed becomes stable and reproducible on the time-scale of typical UHV experiments. As an example, a typical transient kinetic experiment is displayed in Fig. 13c (see Section 6 for discussion, see [62,226]). After stabilization treatment, structural characterization is required in order to identify possible changes in particle morphology. For the specific case of the Pd/Al_2O_3/NiAl(1 1 0) catalyst a STM study showed no significant changes of particle size, shape or density during this process [61].

3.2.2. Preparation by electron beam lithography

As pointed out in the previous sections, nucleation of metal particles prepared by physical vapor deposition is in many cases governed by the defect structure of the oxide support (with the exception of those cases in which there is a exceptionally strong interaction between the metal and the support surface). From an experimental point of view, there are two limitations, which arise from this fact. First, it is often difficult to vary the particle distance in a controlled fashion. A good control of particle distances would be highly desirable in all studies in which support related effects are investigated, such as, e.g. capture zone or spillover phenomena (see, e.g. Section 5). The second point is that there are certain limits with respect to the particle densities that can be prepared by simple nucleation and growth methods. The range of values over which the nucleation density can be varied also determines the range of accessible particle sizes. For a thin film based model system with rather high nucleation densities, this results in an upper limit for the particle size typically in the range of in the range of a few to several nanometers. For the specific case of Pd/Al_2O_3/NiAl(1 1 0) prepared by PVD, the largest particle sizes which can be prepared without severe distortions of the particle shape due to coalescence are in the order of 10 nm.

As has been pointed out in Section 3.1, new preparation methods are being developed in order to overcome these limitations. Here, we describe only one new method, being the preparation of particle arrays by EBL, as explored by Kasemo and coworkers [184,185,300–304] and Somorjai and coworkers [186–188,305–313]. With respect to kinetic studies in catalysis, the main advantages of EBL preparation are the high level of control which is provided over particle sizes (including a narrow size distribution and variable aspect ratios) and over particle distances and positions. Another important point is that in combination with model catalysts prepared by PVD, a much larger range of particle sizes becomes accessible for studies of kinetic phenomena (see Section 6).

Schematically, the EBL preparation method is depicted in Fig. 14a. It is a serial technique in which an electron beam is rastered across the surface of an electron sensitive polymeric resist, thus creating a computer-generated pattern in this film. After dissolving the exposed polymer, the active metal is vapor deposited onto the surface. The remaining resist is lifted-off in a suitable solvent, leaving the active metal particle in the prescribed pattern.

Recently, the first MB studies have been performed on model catalysts prepared by EBL [239,240,314,315]. The EBL model catalysts in this work were based on a thick polycrystalline SiO_2 film on Si(1 0 0), on which large three-dimensional Pd particles were prepared. The particle diameter and height in these studies was 500 nm and particle density was 5×10^7 cm^{-2}, with the particle being arranged on a hexagonal array. The only reaction system studied so far by MB methods is the oxidation of CO (see Section 6).

It should be pointed out that the most critical aspect with respect to EBL as a preparation method is the removal of contaminations which may remain on the surface from the fabrication process or from handling in non-UHV environments. Different cleaning procedures have been described in the literature involving oxidation and reduction cycles at high or low pressures or ion bombardment (see, e.g. [187,188,301,311]). The latter procedure, however, was found to lead to irreversible morphological changes of the system [187]. An effective cleaning procedure aiming at the removal of carbonaceous overlayers by NO_2 treatment and subsequent reduction was recently suggested by Grunes et al. [188]. For the Pd/SiO_2 model system used in the MB experiments, a two-step cleaning procedure was employed involving high temperature and pressure treatment in O_2 and H_2 and subsequent low pressure treatment in O_2 and CO [315]. Composition, adsorption properties and morphology of the model catalysts were characterized by XPS, CO titration, scanning electron microscopy (SEM) and AFM. Moreover, the structural integrity of the particles was checked prior and after cleaning and reaction by SEM (see Fig. 14) [239,240,314,315].

3.2.3. Other preparation methods

Few molecular beam experiments have been performed on model catalysts, prepared by other methods. For completeness, they are listed in the following.

3.2.3.1. Inverse model catalyst. Hayek et al. performed experiments using a molecular beam doser on so-called “inverse model catalysts” [93,156]. The specific reaction systems investigated were the CO adsorption, the CO dissociation and the CO hydrogenation on VO_x layers on Rh(1 1 1) and Pd(1 1 1). In studies by Netzer and coworkers, these layers were characterized in detail by means of STM, PES, HREELS and other experimental methods combined with DFT calculations (see, e.g. [316–324] and references therein). It was found that depending on the preparation conditions V can form structurally well-defined oxide islands and layers of different stoichiometry or surface alloys.

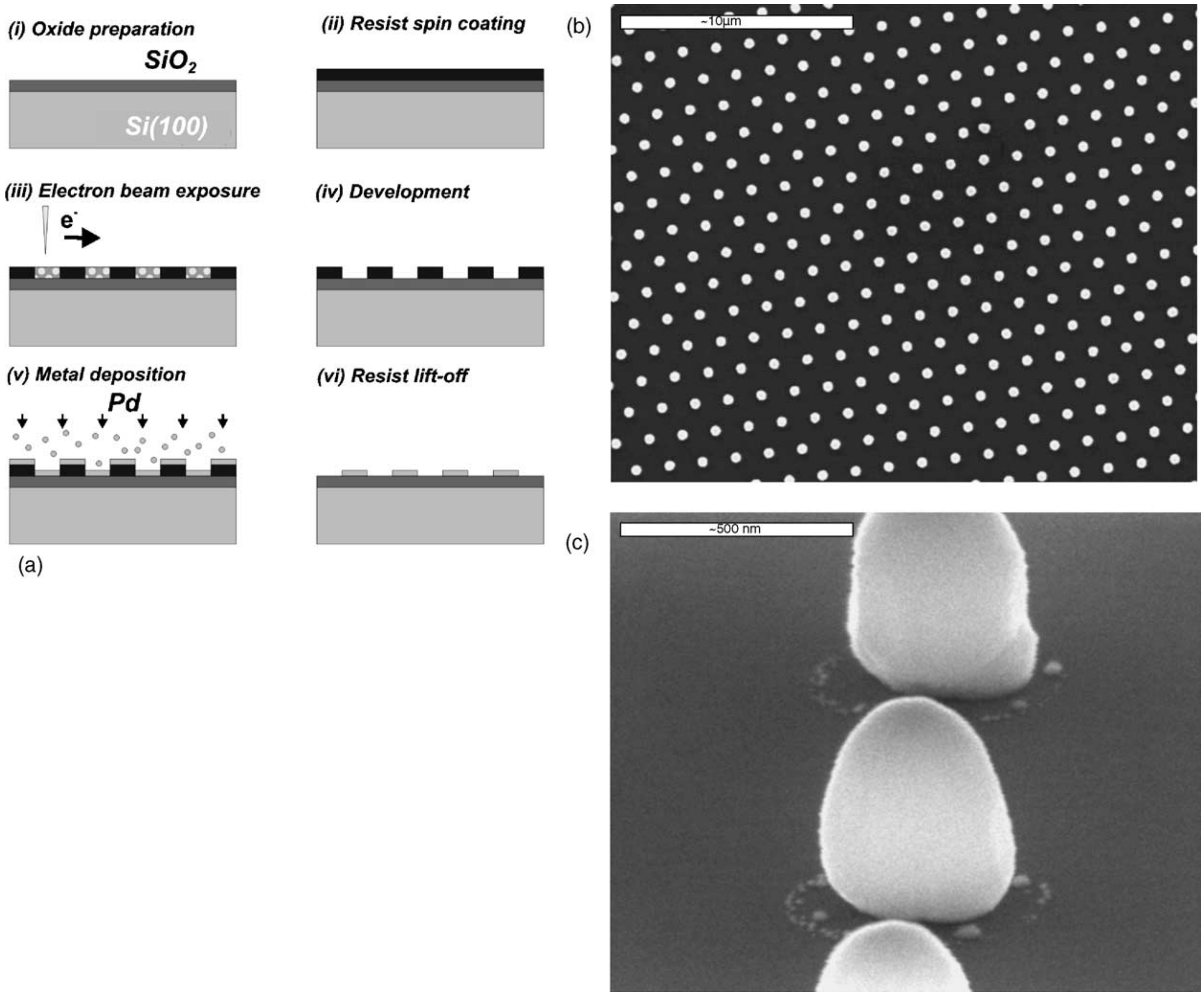

Fig. 14. Preparation of a supported model catalyst by electron beam lithography: (a) schematic representation of the preparation method, from [315], see also [185]; scanning electron microscopy (SEM) image of a Pd/SiO_2 model catalyst, particle size: 500 nm, from [315].

In contrast to ‘‘regular’’ supported model catalysts, in which oxide single crystals or oxide thin films are used as a support, inverse model catalysts are based on single crystals of the active metal, which are partially covered by the support material. By reversing the metal support relationship, investigations of the adsorption properties and catalytic activity of such systems provide valuable information, in particular on the role of electronic effects and on interactions between the metal and the support as well as on the role of interface sites at metal particle boundary.

3.2.3.2. Deposition of mass-selected clusters. The first MB experiments on supported model catalysts which were prepared by deposition of mass-selected metal clusters were recently reported by Heiz and coworkers [42,178,325]. The setup involving a MB doser based on a piezo-electric driven valve were initially tested on mass-distributed Pd clusters on MgO(1 0 0)/Mo(1 0 0) [325] and subsequently applied to mass-selected Pd clusters in the range between Pd_4 and Pd_{30} on the same support [178]. In contrast to various TPD studies using mass-selected clusters (see, e.g. [326–329] and references therein), the only reaction system studied by MB methods is the NO–CO reaction so far. The corresponding results will be discussed in Section 8. An overview of this approach has been published recently [42].

Briefly, the clusters are created by laser ablation from a metal target and thermalization of the generated plasma in He. Cold metal clusters are produced by supersonic expansion of the mixture and subsequent mass selection by means of a quadrupole filter. Finally, the clusters are deposited at low kinetic energy on the support (see [330] details). The accessible cluster size range depends on the experimental setup and is often in the range between 10^0 and 10^2 atoms. The unique feature of the mass-selected deposition is that the cluster size can in principle be controlled atom by atom. As a result, problems which arise as a result of the more or less broad size distribution obtained by nucleation and growth methods are avoided. With respect to studies in catalysis, however, two critical points have to be addressed. Firstly, coalescence of deposited clusters has to be avoided. Generally, this can be established by restricting the experiments to very low metal exposures. In the experiments by Heiz and coworkers, cluster densities below $10^{13}\,\mathrm{cm}^{-2}$ were used [178]. The second, and probably even more critical constraint is that the model system must be stable under reaction conditions for a sufficient number of catalytic cycles. Instability of the model system may, for example, be caused by dissociation of metal atoms from clusters or cluster mobility at elevated temperature and under the influence of reactants. Both effects may result in changes of the particle size, e.g. due to ripening or coalescence processes. As for the model systems prepared by PVD, an important point, which governs the anchoring and therefore the stability of the supported cluster systems is the defect structure of the oxide support. For a more detailed discussion of the role of oxide defects on the behavior of these systems, we refer to the literature (see [42] and references therein). Finally, it should be pointed out that one important result of the above mentioned MB study is that the authors were able to show that the size-selected Pd_n/MgO(1 0 0)/Mo(1 0 0) systems was indeed stable for several reaction cycles under the conditions of the CO–NO reaction [178]. Thus, it should indeed be possible to derive meaningful kinetic data on catalytic processes from this kind of model systems.

4. Molecular beam studies in catalysis

4.1. Experiments on single crystal surfaces

Employing MB methods, an enormous amount of experimental work has been performed on single crystal surfaces, addressing the kinetics and dynamics of elementary steps of heterogeneously catalyzed reactions. It is beyond the scope of this review to provide a complete survey over these studies. For completeness, however, we briefly list some examples of single crystal work, which is related to the model catalysts and reactions discussed in the following, i.e. the adsorption of CO (see, e.g. [123,156,331–351]) and O_2 (see, e.g. [283,332,337,344,352–380]), the CO oxidation (see, e.g. [90,121,161,381–403]), methanol adsorption, decomposition and oxidation (see, e.g. [404–415]), NO adsorption and dissociation (see, e.g. [118,122,334,337,416–444]) and the NO–CO reaction (see, e.g. [403,445–450]). For a more general discussion on MB studies on reaction kinetics on single crystals, we refer to the review articles and textbooks on this topic [63,64,66–68,76,77].

4.2. Experiments on supported model catalysts

The MB studies on supported model catalysts published up to date are listed in Table 1 [49,52,61,62,79,94,97,156,178,194–202,204,205,211–215,217,218,220,221,224–242,314,315,325,451–453]. In spite of the large amount of single crystal data the number of comparable studies on supported model catalysts or more complex surfaces in general is limited. In the following sections, we will review these studies in detail.

Pioneering work in this field has been perform by Henry and coworkers [79,194–205], who were the first to perform molecular beam studies on well-defined model catalysts. Focusing on CO oxidation as well as on the NO adsorption, dissociation and the NO–CO reaction on well-shaped Pd particles on MgO(1 0 0), several aspects of the reaction kinetics were studied, e.g. the particle size dependence of desorption energies, the influence of trapping of adsorbates on the support and the particle size

Table 1
Molecular beam studies on supported model catalysts

Reaction	Supported model catalyst	Reference
CO adsorption/desorption	Pd/MgO(1 0 0)	[79,194–196]
	Pd/γ-Al_2O_3	[215,94]
	Pd/γ-Al_2O_3, Pd/α-Al_2O_3(0 0 0 1)	[213]
	Pd/α-Al_2O_3(0 0 0 1), (1 −1 0 2)	[214]
	Rh/α-Al_2O_3(0 0 0 1), (1 −1 0 2), (1 1 −2 0)	[52]
	Pd/Al_2O_3/NiAl(1 1 0)	[224,237,451]
	Pd/TiO_2(1 1 0)	[220]
	VO_x/Pd(1 1 1) (inverse catalyst)	[156]
	Au/Al_2O_3/NiAl(1 1 0)	[241]
CO/O_2 adsorption	Rh/Al_2O_3	[218]
O_2 adsorption	Pd/Al_2O_3/NiAl(1 1 0)	[61,62]
CO oxidation	Pd/MgO(1 0 0)	[197–200]
	Pd/γ-Al_2O_3	[452]
	Pd/γ-Al_2O_3, Pd/α-Al_2O_3(0 0 0 1)	[212,453]
	Pd/α-Al_2O_3(0 0 0 1), (1 −1 0 2)	[211]
	Rh/γ-Al_2O_3	[217]
	Rh/α-Al_2O_3(0 0 0 1), (1 −1 0 2), (1 1 −2 0)	[49]
	Pd/MgO(1 0 0)/Mo(1 0 0)	[325]
	Pd/Al_2O_3/NiAl(1 1 0)	[97,224–229]
	Pd/Al_2O_3/NiAl(1 1 0), Pd/SiO_2/Si(1 0 0)	[239,240,314,315]
CH_3OH adsorption/decomposition	Pd/Al_2O_3/NiAl(1 1 0)	[230,451]
CH_3OH decomposition/oxidation	Pd/Al_2O_3/NiAl(1 1 0)	[231–233]
HCOOH adsorption/decomposition	Pd/TiO_2(1 1 0)	[221]
NO adsorption/dissociation	Pd/MgO(1 0 0)	[201]
	Cu/Al_2O_3/NiAl(1 1 0)	[242]
	Pd/Al_2O_3/NiAl(1 1 0)	[234–236,238]
NO + CO	Pd/MgO(1 0 0)	[202,204,205]
	Pd/MgO(1 0 0)/Mo(1 0 0)	[178]

dependencies of reaction rates under steady-state and transient conditions. Earlier studies were reviewed previously [19], and we mainly focus on the more recent work here.

Parallel to the work by Henry et al., the group of Matolin addressed particle size and structure-dependent effects, as well as the influence of supports on the adsorption of CO and oxygen, and on CO oxidation [49,52,94,210–218]. In their studies, the range of model systems investigated was extended to both Pd and Rh nanoparticles on various types of alumina supports.

Over the last year a large number of studies were published by our group, addressing various adsorption and reaction systems [61,62,97,224–240,314,315,451,454]. The systems studied include adsorption processes and reactions involving CO, O_2, NO and CH_3OH on supported Pd model catalysts on Al_2O_3/NiAl(1 1 0) (PVD) and on SiO_2 supports (EBL). A large part of the results discussed in the following originates from this work and will be discussed in comparison to the work by the other groups. Some specific aspects have been subject to brief reviews previously [71–74, 159,455,456].

Recently, several other groups have started to apply MB techniques to model catalysts as well. Bowker and coworkers have investigated substrate trapping effects in the adsorption of CO and the adsorption and decomposition of formic acid on Pd/TiO_2(1 1 0) [220,221]. Raval and coworkers have studied NO and CO on Cu and Au nanoparticles on Al_2O_3/NiAl(1 1 0) [241,242]. Recently, Heiz and coworkers have applied MB techniques in order to perform kinetic measurements on mass-distributed [325] (CO oxidation) and subsequently on mass-selected (CO–NO reaction) [178] Pd clusters on MgO(1 0 0)/Mo(1 0 0). An interesting complementary approach from a catalytic point of view are so-called inverse model catalysts, which have recently been used in experiments by Hayek et al. employing molecular beam doser techniques [156].

The interest in the application of molecular beam techniques on complex supported model catalysts is the consequence of a number of promising results, which show that these experiments indeed have the potential to reveal rather detailed insights into the corresponding reaction kinetics. One of the principal advantages is the quantitative nature of MB experiments as well as the extremely well-controlled conditions under which they are performed. This makes it relatively easy to obtain reliable and quantitative information on the subtle kinetic phenomena on complex catalyst surfaces. In the following, we will review the various types of experiments performed and model reactions investigated up to date, with a special focus on the microscopic interpretation and on the modeling of the kinetic phenomena on surfaces of supported catalysts.

5. Adsorption and desorption kinetics

5.1. Sticking coefficient measurements and capture zone effects

Most MB studies on supported model catalysts have focused on the quantification of so-called “capture zone” effects [52,156,195,201,205,210–214,218,220,224,230,241,242]. Briefly, the capture zone describes the adsorption of reactants on the support, typically in a weakly chemisorbed or physisorbed molecular state, which subsequently can migrate to the active particles. Under specific conditions, the capture zone might have an effect on the kinetics of the catalytic reaction. The phenomenon should be clearly distinguished from so-called “spillover” effects in heterogeneous catalysis (see, e.g. [24]). The latter term describes the migration of an activated species from the active particle to the support, which cannot be formed on the support itself. Transport of an activated species from the support to the active particle is denoted as reverse-spillover. Some important implications arise from this difference, which will be discussed in the following.

5.1.1. Capture zones—general remark

The capture zone effect on supported metal catalysts was first formulated by Gillet and Matolin for the CO oxidation on a Pd/mica system [26,457]. In their studies, they found exceptionally high adsorption and reaction rates, as well as turnover frequency (TOF) values depending on the particle density. These results could not be explained on the basis of the previous kinetic models. Similar phenomena were observed in earlier work by Ladas et al. [458] and later interpreted in terms of capture zone effects as well [459]. More recently, the effect was taken into account in several adsorption and reaction studies on similar systems, for example, by Henry and coworkers (see, e.g. [197,198], see Section 5.1.6). Models have been derived which allow support diffusion to be taken into account quantitatively in kinetic studies ([27,34,460], see also Section 5.1.6).

It should be noted that the capture zone effect is related to the so-called ‘‘porthole effect’’, suggested already in the 1960s [461]. The effect combines surface diffusion and reaction at specific active sites. In early work, Tsu and Boudart described an experimental example of the effect, investigating recombination of hydrogen at specific active sites of a pyrex surface [462].

The capture zone effect on a supported metal particle system is schematically depicted in Fig. 15. An impinging gas molecule may directly collide with the metal particle with a probability equal to the fraction of the surface covered by the metal. For many adsorbates impinging at low kinetic energy, adsorption on the metal proceeds via a precursor mechanism, i.e. the adsorbate is initially trapped in a physisorbed precursor state, from which it may either desorb or chemisorb on the surface. In case of a sufficiently mobile precursor, this leads to a sticking coefficient weakly dependent on coverage [463].

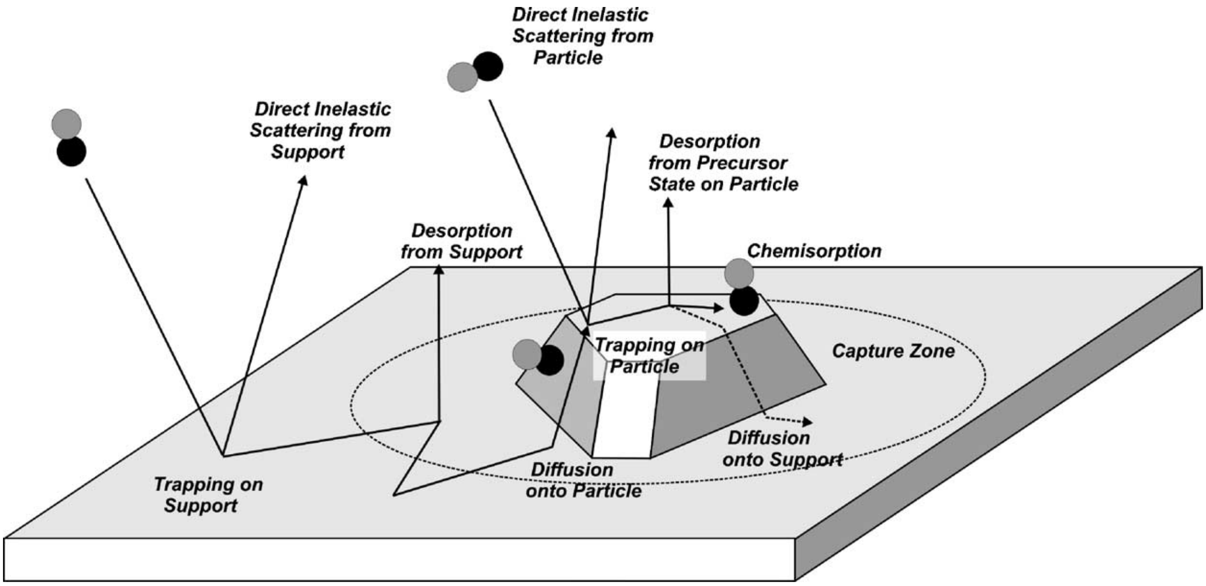

Fig. 15. Schematic representation of the capture zone effect during adsorption on a supported catalyst.

More likely, however, is a collision with the oxide support. Depending on the details of the interaction potential, the molecule may lose a sufficient amount of translation energy to be trapped in the physisorption well on the support (see, e.g. [63,64,67,68,464] and references therein). If the energy transfer is insufficient, on the other hand, it will be directly backscattered into the gas phase (direct inelastic scattering). Despite their short residence time (due to the weak interaction with the oxide support), the trapped molecules probe a substantial area via surface diffusion before desorption takes place (trapping desorption). These diffusing reactant molecules can be collected by metal particles, which considerably enhanced the flux of adsorbates to the particles. As suggested by Rumpf et al., the effect can be described in a simplified fashion by defining a capture or collection zone around the particle, from which adsorbates can reach the particles [459].

In contrast to the spillover or reverse-spillover phenomenon, where by definition coupling of the surface reservoir to the gas phase takes place only via one part of the surface (either active particles or support), adsorption and desorption occurs on both support and active particles in the case of the capture zone effect. As a result, it is important to note that the capture zone will only have an influence on the global reaction rate if the corresponding adsorption process has some degree of rate control. As an example, we consider the simple case of CO adsorption during the CO oxidation reaction: in the low temperature limit with the reaction being extremely slow or in the limit of high CO flux (high CO coverage and low O coverage on the particle surface, CO-rich regime), adsorbed CO and gas phase will be in fast equilibrium, both on the Pd particles and on the support. Thus, CO adsorption is not the rate determining step (for a definition and discussion of the terms ‘rate determining step’ (RDS) and ‘degree of rate control’ (DRC) see, e.g. and references therein [465–469]). The equilibrium implies that the steady-state CO coverage depends on the thermodynamics of adsorption only and from detailed balance it follows that the fluxes from the support to the particles and vice versa must be identical. Consequently, there is no net effect of the capture zone. Only under conditions of high oxygen and low CO coverage on the particle surface (O-rich regime), the CO adsorption rate can be the RDS. Then, the CO capture zone indeed plays a role for the total reaction kinetics and the effect, e.g. may be described as an effective increase of the CO pressure at the particle surface. Similar arguments hold for oxygen adsorption and dissociation. As a result the effect of the capture zones for both CO and oxygen change as a function of the CO/O_2 ratio upon transition between the kinetic regimes. At the same time, the steady-state O and CO surface coverages change drastically and thus do the rate constants of all processes involved. This complicates a consistent implementation of the capture zone and coverage dependent effects in microkinetic models.

5.1.2. CO adsorption

Most experimental studies on capture zone effects have been performed for CO adsorption on supported Pd particles. Henry and coworkers investigated the CO adsorption kinetics on a Pd/MgO(1 0 0) model catalyst [194,195]. Using modulated molecular beam scattering, it was possible to distinguish between the fast TD and the significantly slower chemisorption–desorption channel under conditions of rapid CO desorption. The chemisorption probability could be measured as a function of particle size and distance and as a function of the surface temperature. Large initial sticking coefficients were observed, which strongly exceeded the fraction of the support covered by the metal, immediately pointing to a significant enhancement of the adsorption rate due to the capture zone. The effect was quantitatively modeled using a simplified adsorption–diffusion model (see Section 5.1.6). From the fit to the model, the authors were able to derive an estimate of the trapping probability on the MgO(1 0 0) support

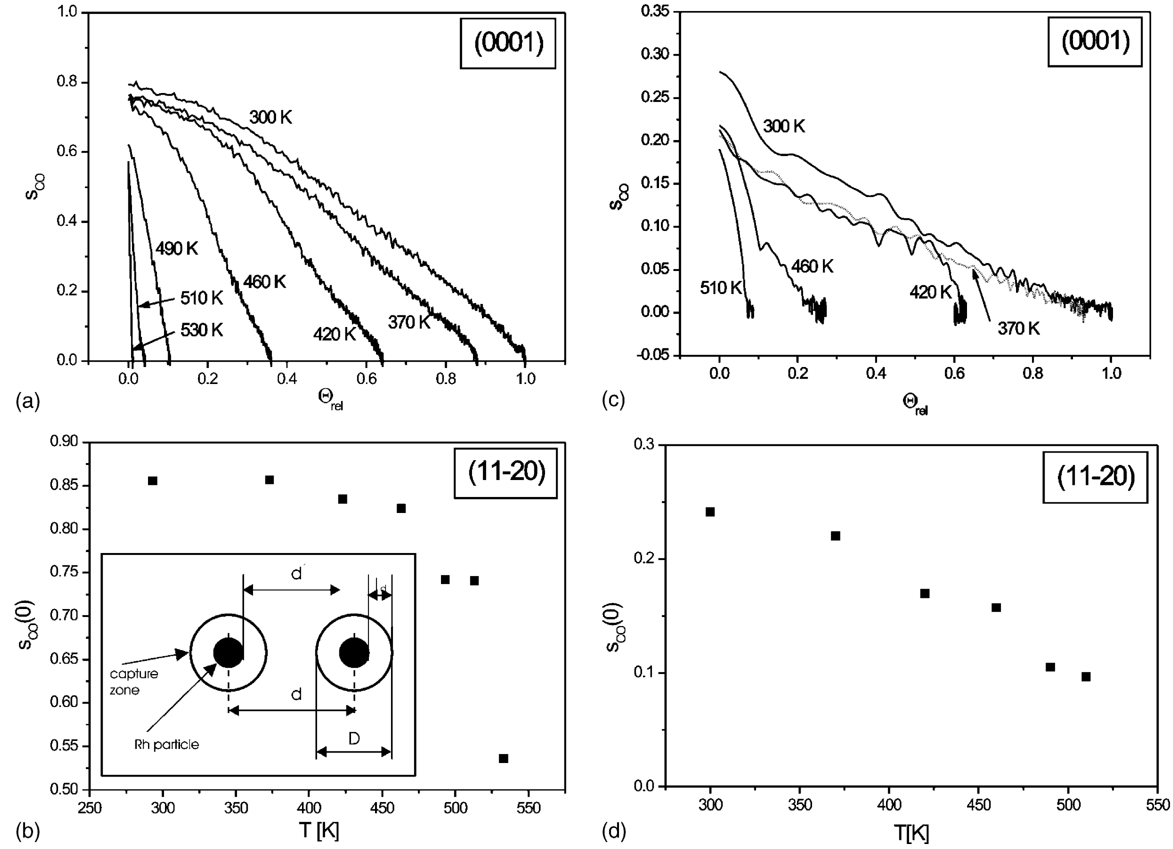

Fig. 16. Sticking coefficient measurements for CO on Rh/alumina model catalysts: (a) sticking coefficient as a function of CO coverage and surface temperature for Rh particles (high Rh coverage) on α-Al_2O_3(0 0 0 1); (b) initial sticking coefficient as a function of surface temperature for Rh particles (high Rh coverage) on α-Al_2O_3(1 1 −2 0); (c and d) as (a) and (b) at low Rh coverage, from [52].

(0.50 ± 0.05, compare other measurements or estimates of initial sticking or trapping probabilities on ordered oxides, e.g. [224,347–349,470]) and of the difference between the surface adsorption and surface diffusion barrier (0.25 ± 0.05 eV) [195].

In a series of investigations, Matolin and coworkers have studied the adsorption kinetics on Pd [210–214] and Rh particles [52,218] on various alumina supports employing sticking coefficient measurements as a function of sample temperature. An example of the type of experiment is reproduced in Fig. 16 (from [52]). The sticking coefficient as a function of the coverage at low temperature shows the typical shape for precursor mediated adsorption. The high absolute values indicate that a large fraction of the CO is adsorbed via the capture zone. With increasing temperature, two effects are observed. Firstly, the amount of CO adsorbed decreases as a result of the increasing desorption rate. Secondly, the initial sticking coefficient S_0 decreases with increasing temperature as well. There are three effects, which can contribute to the temperature dependence of S_0: (i) the temperature dependence of the trapping probability on the support, (ii) the temperature dependence of the size of the capture zone and (iii) the temperature dependence of the chemisorption probability on the metal particles themselves. Information on the latter effect can be obtained from single crystal data. Considering the trapping on the support, its temperature dependence is typically found to be rather weak. The diameter of the capture zone, on the other hand, exponentially decreases with $E_a - E_d$, i.e. the difference between the adsorption and diffusion energy on the support [459,460].

As a result, two regimes are expected to exist as a function of temperature: in the low temperature limit, the capture zones overlap and a weak temperature dependence of S_0 may arise as a result of the temperature dependent trapping on the support. With increasing temperature, a transition to a situation with non-overlapping capture zones is expected, leading to an exponential decay of S_0. Matolin and coworkers found a corresponding behavior with a nearly constant S_0 at low temperature and a decrease at higher temperature was observed experimentally in several cases ([52,210,213]). Bowker et al. recently observed the same effect on Pd/TiO_2(1 1 0) [220]. Whereas for temperatures below 320 K, an S_0 independent of temperature indicated overlapping capture zones, S_0 was observed to decrease rapidly at higher temperature. The corresponding decrease on the single crystal due to CO desorption was shown to occur at significantly higher temperatures. Similar temperature dependent investigations of the sticking coefficient of CO on Au/Al_2O_3/NiAl(1 1 0) identified a precursor mediated adsorption channel, but without further specification of the type of precursor state [241].

A quantitative analysis of the adsorption kinetics on the Pd/alumina and Rh/alumina catalysts by Matolin and coworkers showed that in a temperature region between 300 and 500 K the capture zones typically have sizes in the order of one to few nanometers [52,210–212,214]. It follows that for weakly interacting supports such as alumina or silica strong enhancements of the reactant flux are expected only for particle sizes in the lower nanometer regime. For supports which interact more strongly with the reactants, however, the capture zones could be significantly larger. In addition, it is noteworthy that both the trapping probability and the difference between adsorption and diffusion energy are expected to depend on the surface properties of the support. Thus, it is anticipated that the size of the capture zone will depend not only on the support material itself, but also on the details of its structure and the nature of defects. Experimentally, such variations were observed in comparative experiments for Pd/alumina and Rh/alumina catalysts employing different types and crystallographic orientations of Al_2O_3 supports as well as different preparation methods [52,210–212,214].

As a final point it is noteworthy that it is in principle possible to directly determine not only the sticking coefficient but also the trapping probability on the support by MB methods. By combination with morphological data, it is thus feasible to extract all kinetic parameters for adsorption directly without further fitting to a model. This is illustrated in the example depicted in Fig. 17 (from [224]). As a first step, scattering from the clean Al_2O_3/NiAl support is considered. As mentioned previously, we have to distinguish between trapping on the support and direct scattering. This is possible via measurements of the angular distribution and the KE distribution of molecules leaving the surface. Those molecules directly scattered from a flat surface (DI) show a lobular angular distribution which peaks close to the specular direction and are characterized by a KE which is related to the energy of the incident beam. The trapped molecules (TD), on the other hand, desorb from a physisorbed state, in which they have been accommodated to the surface temperature. Consequently, their kinetic energy will depend on the surface temperature and their angular distribution will reflect the surface symmetry (in many cases the azimuthal anisotropy is relatively weak). In Fig. 17b, a characteristic angular distribution is shown for CO scattered from the clean alumina model substrate, which can be separated into the two contributions, a lobular DI part and the broad symmetric TD part. Similarly, the two channels can be identified in time-of-flight measurements (it should be pointed out that the simple analysis in terms of a TD and a DI part to some

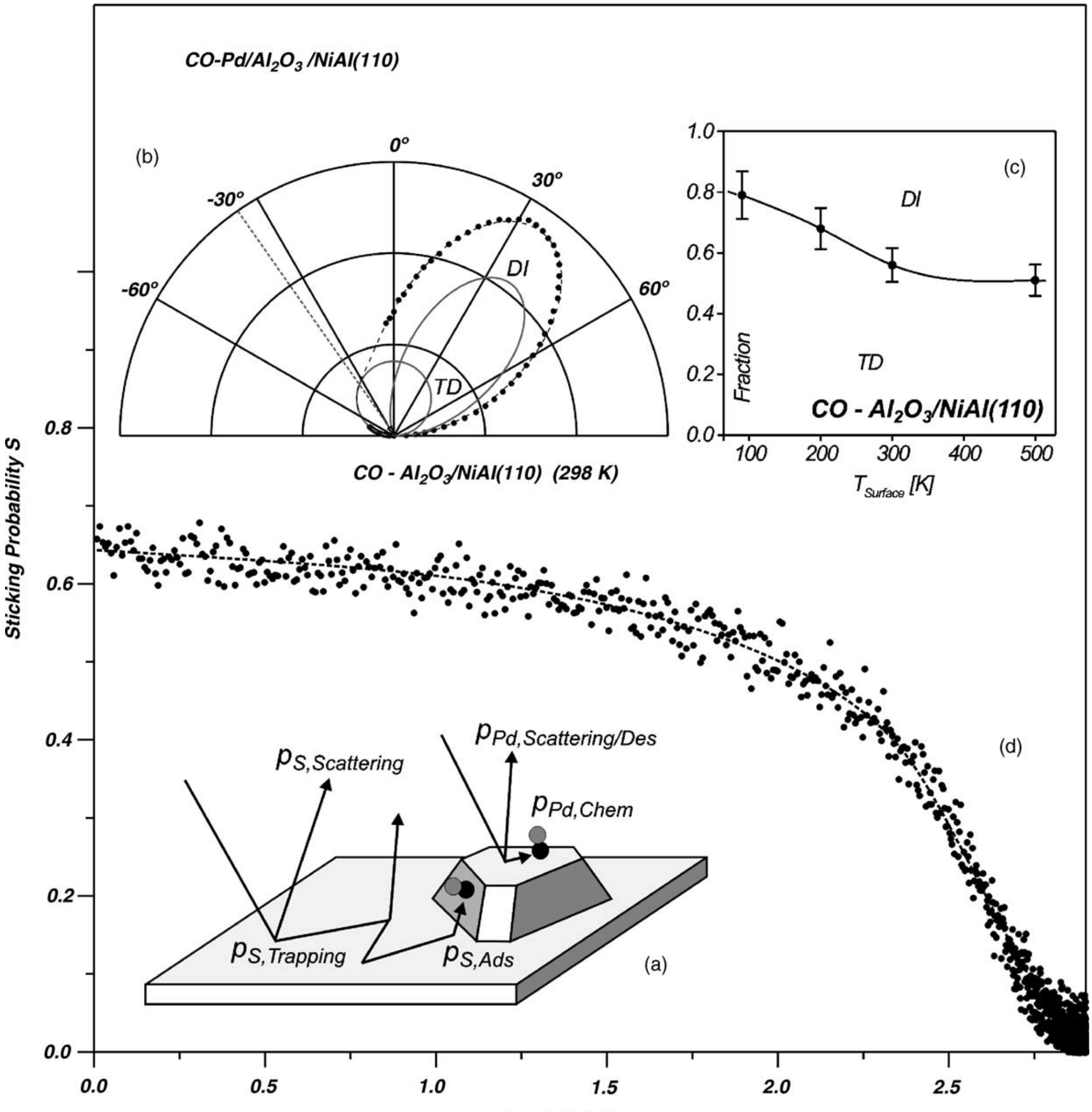

Fig. 17. Determination of the probability for different adsorption and scattering channels on a Pd/Al_2O_3/NiAl(1 1 0) model catalyst: (a) schematic representation; (b) angular distribution of CO (KE 86 meV) scattered from Al_2O_3/NiAl(1 1 0) (298 K); (c) trapping desorption (TD) and direct inelastic scattering (DI) component for CO scattering from Al_2O_3/NiAl(1 1 0) as a function of temperature; (d) sticking probability for Pd/Al_2O_3/NiAl(1 1 0) (particle size 6 nm, 298 K), from [224].

degree represents a simplification, as trapping and scattering processes can be significantly more complicated, e.g. due to partial accommodation and inefficient coupling of different degrees of freedom [64,67] or due to diffuse scattering from defects [19,195,471]). As displayed in Fig. 17c, the relative fractions of the trapping and the scattering component can be quantified as a function of substrate temperature. The trapping probabilities found are very similar to those found reported by Henry et al. for CO scattering from MgO(1 0 0) and α-alumina [194,460]. Finally, the nominal sticking coefficient on the Pd/Al_2O_3/NiAl(1 1 0) is determined. From the total initial chemisorption probability ($S_0 = 0.65$ [224]), the initial sticking coefficient on the Pd particles (estimated from single crystal data, $S_{0,\mathrm{Pd}(1\ 1\ 1)} = 0.96$ [332]), the projected Pd coverage ($\theta_{\mathrm{Pd}} = 0.20$ [61]), and the above mentioned trapping probability, it is possible to determine the probabilities for all processes shown in Fig. 17a. For the specific case displayed in Fig. 17, it is follows that nearly all adsorbate molecules trapped on the support are collected by the metal particles and desorption from the trapped state on the support is negligible (case of overlapping capture zones).

5.1.3. O_2 adsorption

Some experiments on capture zone effects for oxygen adsorption were performed by Matolin and coworkers on Pd and Rh particles on different alumina supports [210,211,214,218]. In general, it was found that the effect was similar to the one observed for the adsorption of CO. A quantitative analysis yielded somewhat smaller values for the diameter of the capture zone, however. As a function of the surface properties, type and pretreatment of the support the same systematic variations were observed as for CO adsorption.

It should be pointed out that as yet systematic sticking coefficient measurements have primarily been performed on weakly interacting and non-reducible supports. In addition to the capture zone, on reducible systems there should be the additional possibility of transport of atomic oxygen species via the particle-support boundary. Such processes, which according to the above definition, would be classified as spillover phenomena have not been subject to MB experiments yet.

5.1.4. NO adsorption

Detailed investigations on the adsorption kinetics of NO on Pd/MgO(1 0 0) model catalysts were performed by Piccolo and Henry ([201,204], see also [205], Fig. 18) and more recently also by Raval and coworkers on Cu/Al_2O_3/NiAl(1 1 0) [242].

In the work by Piccolo and Henry, MB experiments were performed over a large temperature region and on model catalysts with various particle sizes and densities. A typical gas phase response to a rectangular beam signal is displayed in Fig. 18a. As in a typical King and Wells type sticking coefficient measurement, it is possible to distinguish between an immediate increase in the NO partial pressure and a slower response in these experiments. The fast part of the response can include two contributions: (i) firstly, there is a DI scattering component from the MgO support and from the Pd particles, with the latter contribution typically being negligible due to the high S_0 on clean Pd and the low fraction of the support covered by the metal particles. (ii) The second contribution arises from TD on the support. This is because the steady coverage of NO on the MgO support is low and the adsorption–desorption equilibrium on the support is established on a time-scale which is short on the time-scale of the present experiment. The slow increase is entirely due to chemisorption on the Pd particles, with the area A_{on} yielding the adsorbing and the area A_{off} yielding the desorbing density of NO. It is noteworthy that in these experiments $A_{\mathrm{on}} > A_{\mathrm{off}}$ due to partial dissociation (see Section 8 for further discussion). For the present

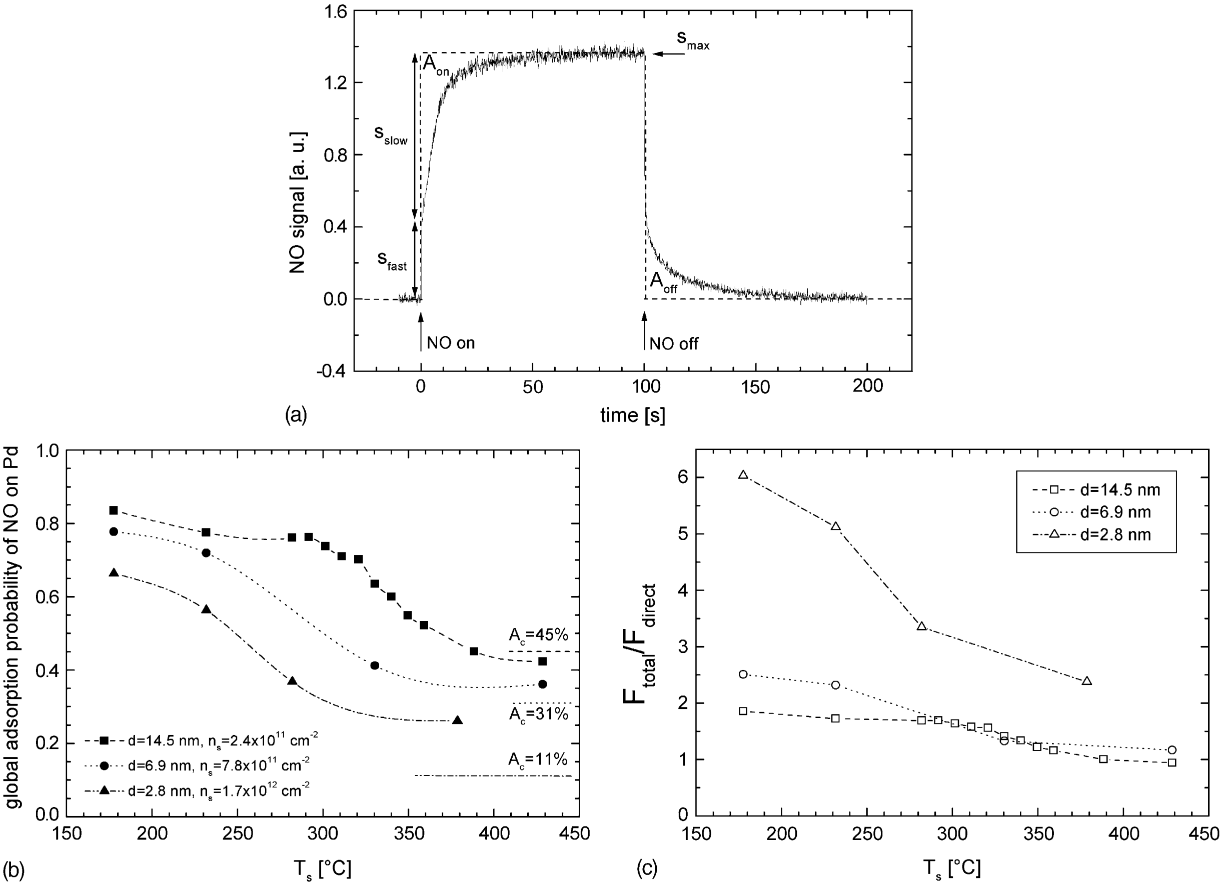

Fig. 18. NO capture zone effect on a Pd/MgO(1 0 0) model catalyst as determined from modulated molecular beam experiments: (a) example of a NO adsorption–desorption experiment, from [201]; (b) global sticking coefficient for NO as a function of particle size, density and sample temperature, from [201]; (c) ratios of the direct flux and the flux via the capture zone reaching the active particles, from [204].

discussion on the capture zone effect, the relevant quantity is S_0 of the entire model system, which is displayed in Fig. 18b as a function of particle size, density and temperature. Qualitatively, the behavior found is analogous to the case of CO adsorption discussed in Section 5.1.2. In the low temperature limit, the capture zones overlap and all adsorbates trapped on the support are transferred to the particles. Accordingly, the deviations from unity sticking are due to the finite trapping probability, primarily on the support. With increasing surface temperature, the size of the capture zone decreases and, finally, in the high temperature limit S_0 approaches a value determined entirely by direct impingement on the particles. The relative effect of the capture zone assisted adsorption kinetics becomes most relevant in the case of small particles and low temperature. This is more clearly illustrated in Fig. 18c, which shows the ratio of the total adsorbate flux reaching the active particles and the direct flux from the gas phase. For the smallest particles and sufficiently low sample temperatures, is clearly shown that the flux via the support strongly dominates over the direct impingement rate.

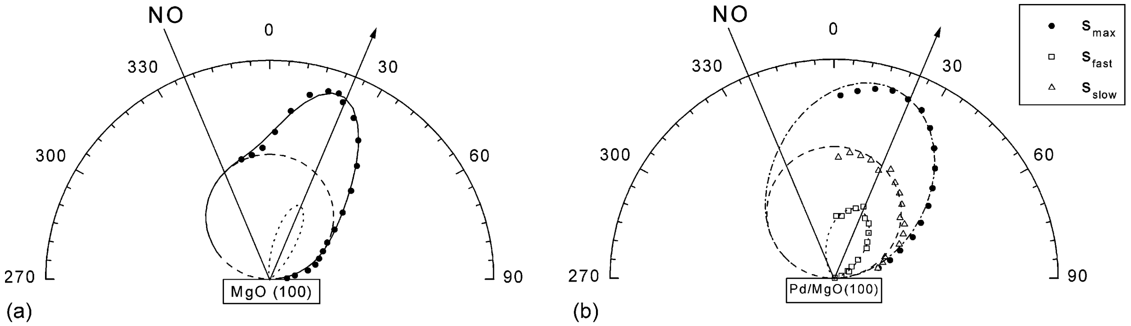

Fig. 19. NO capture zone effect on a Pd/MgO(1 0 0) model catalyst illustrated via angular and time-resolved scattering experiments: (a) angular distribution of NO scattered from the pure MgO(1 0 0) support cleaved in UHV and (b) angular distribution of NO scattered from Pd/MgO(1 0 0), from [201].

Similar to the case of CO adsorption (Section 5.1.2), not only the temporal but also the angular distribution of reactants can be used to discriminate between the adsorption and scattering channels. In Fig. 19a, corresponding experiment is shown from work by Piccolo and Henry on the same model system, who observed for NO scattering from MgO(1 0 0) a lobular component which was attributed to DI scattering channel and a symmetric component which could be attributed to TD on the support [201]. The trapping probability for NO on MgO(1 0 0) estimated from this data were similar to the values for CO on similar supports (see Section 5.1.2). It should be noted, however, that a determination of the trapping probability entirely on the basis of the angular distribution of scattered reactants, may be misleading due to the large scattering cross-sections of defects. The latter can also lead to diffuse backscattering as, e.g. demonstrated in a comparison for backscattering from air-cleaved and UHV-cleaved MgO [201]. As a result, a detailed analysis of the velocity distributions would be necessary in the case of a substantial contribution due to diffuse scattering from defects.

If diffuse scattering from defects is negligible, the probability for reactants to be trapped on the support and the probability to be captured by an active particle can directly be determined in a pulsed and angle-resolved experiment, as illustrated in Fig. 19b (from [201]). The angular distribution of the fast component (see Fig. 18a) provides information on the DI (lobular) and TD (symmetric) channel from the support and the slow channel (symmetric) stems from desorption from the particles only. In case of completely overlapping capture zones the fast symmetric component vanishes completely (see Fig. 19b).

5.1.5. CH_3OH adsorption

Certainly, the capturing of reactants via the support cannot only be monitored via the gas phase response, but also via surface spectroscopy. As an example, IRAS data acquired during adsorption of methanol on a $Pd/Al_2O_3/NiAl(1\ 1\ 0)$ model catalyst at 100 K are displayed in Fig. 20 [230]. It should be noted that for the low KE used in this study, the sticking coefficient for methanol on the support is near unity [230]. At low exposures, a single absorption band at 1002 cm^{-1} appears in the CO stretching frequency region shifting to higher frequency with increasing coverage. The feature can be assigned to molecular methanol adsorption or methoxy on the Pd particles (compare [472–475]; a more detailed analysis shows that methanol undergoes partial dissociation to form methoxy species at low temperature, see Section 7). This observation implies that there is rapid diffusion of methanol on the support and complete capturing of the methanol species on the support by the Pd particles. Only after saturation of the

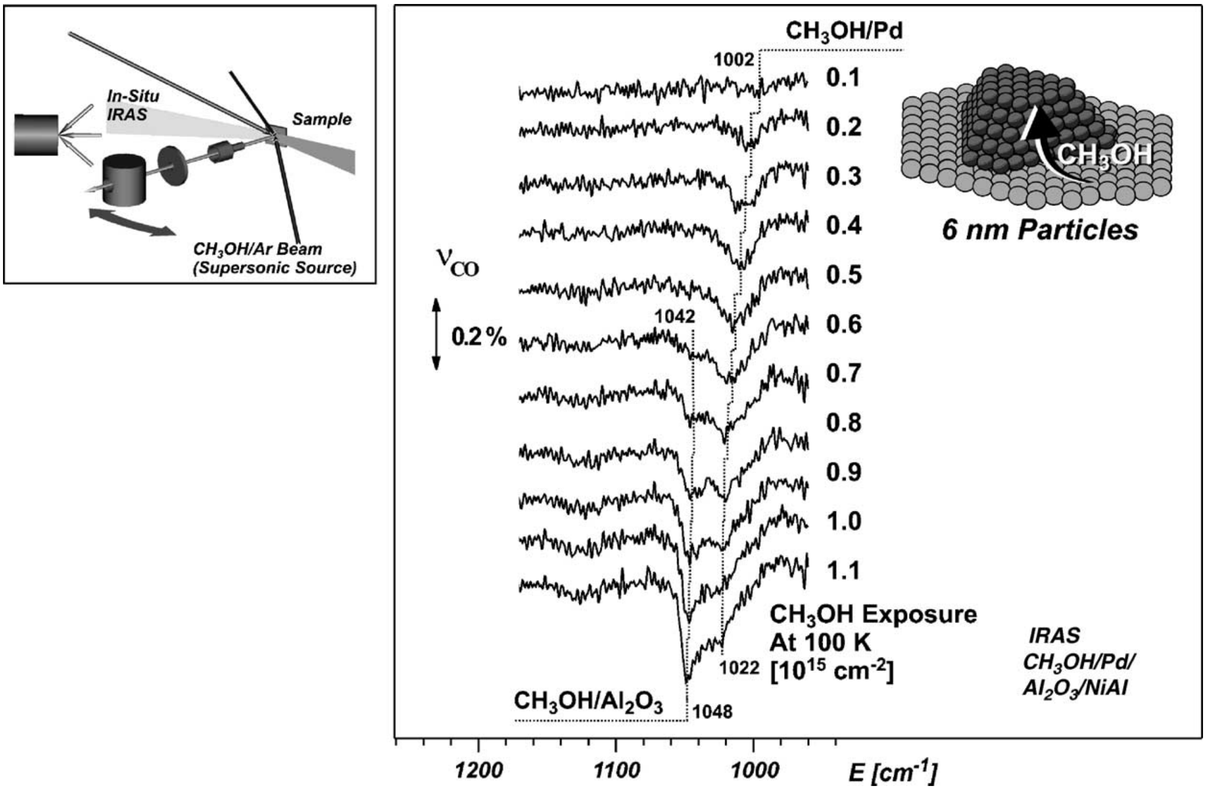

Fig. 20. Capture zone effect for methanol adsorption on a Pd/Al_2O_3/NiAl(1 1 0) model catalyst, as studied via IRAS of the CO stretching frequency region, from [230].

particle surface, further dosage leads to methanol adsorption on the alumina support, as indicated by a second absorption feature which appears at higher frequency. The latter can be identified as molecular methanol on Al_2O_3/NiAl by comparison with IR spectra for adsorption on the pristine Al_2O_3 film.

5.1.6. Microkinetic models

Several kinetic models have been used in the literature in order to account for capture zone effects and spillover phenomena in catalytic reactions (see, e.g. [27,34,195,197,202,204,459,460,476–478] and references therein). General models treating the adsorption and diffusion on the support were proposed early (see, e.g. [476,477]). The simplest models applied to CO adsorption and oxidation, such as, e.g. the one put forward by Rumpf et al. [459] used simple estimates of the sizes of the diffusion zones. The ‘‘collection’’ zone is represented as a ring around the particle with a width, which is given by the mean diffusion length of the adsorbates. The critical parameter, which determines the diffusion length is the difference between the activation energies for desorption and diffusion. Accordingly, the reactant flux toward the particle is the sum of the direct flux and the flux impinging on the collection zone (the trapping probability on the support was disregarded in the original model). Once again, it should be pointed out that the increased flux toward the particles is not equivalent to an increased pressure of the reactant. Only in cases in which the adsorption step is rate-controlling, i.e. the adsorption–desorption step is far from equilibrium on the active particles, the capture zone has a direct influence on the rate. If the adsorption–desorption step is near equilibrium, the adsorbate fluxes via the particle boundary in both directions cancel each other (see Section 5.1.1).

Henry and Chapon [478] suggested a model which uses a solution of the diffusion equation, describing the supported catalyst as a system of isolated particles. Later, Henry [460] applied a model, which is capable of describing the case of competition between particles, to the experimental data published by Rumpf et al. [459]. The diffusion model again treated the particles as perfect sinks for the adsorbate and took into account the interaction between the diffusion field around each particle under steady-state conditions. From this model, it was possible to derive information on the activation energy difference for diffusion and desorption. Also, it was concluded that the trapping probability on the support should be significantly smaller than unity. More recently, similar models were used in the analysis of kinetic MB experiments on different reaction and adsorption systems [195,197,202,204].

Zhdanov and Kasemo analyzed the kinetics of a general surface reaction representing the key features of the CO oxidation, using a model which treats the reaction on the particles and the adsorption, desorption and diffusion on the support in a self-consistent fashion [27,34]. Again, two cases were treated, the case of widely separated particles and the case of overlapping diffusion zones [34]. An analysis of the reaction rate as a function of the reactant pressures showed that both the reaction rate (only in the O-rich regime for the case of CO capturing via the support) and the point of transition between the two regimes are expected to be strongly modified by the capture zone effect [27].

5.2. Other adsorption–desorption experiments

Among the standard applications of MBRS are quantitative measurements of the residence times of adsorbates and the determination of Arrhenius parameters for desorption processes (see, e.g. [63]). On supported model catalysts, such measurements have been performed for few adsorption–desorption systems only [62,79,194,196,201,205]. First experiments of this type were conducted by Henry et al. for CO adsorption and desorption on Pd/MgO(1 0 0) [79,194,196]. For the case of large particles (7 nm), they found desorption parameters, which are in good agreement with Pd films and single crystals. For smaller particles, however, a noticeable increase of the desorption activation energy was reported. Later experiments on Pd/Al_2O_3/NiAl model catalysts confirmed the presence of specific sites on small Pd particles with an enhanced CO binding energy, but the effect observed was much smaller than reported in the previous work [62]. The enhanced adsorption energy in the low coverage limit could, for example, be related to the presence of minority facets on the particles, step sites or other defects sites as well as electronic modifications, which could result in a slight increase of the CO adsorption strength. The situation is further complicated in those cases in which surface reactions and adsorption–desorption processes compete. For example, this is the case for NO adsorption on supported Pd particles (see Section 9). An example is provided by a recent study of NO adsorption–desorption from large Pd particles on MgO(1 0 0) under conditions of partial dissociation [201,205]. Here, desorption activations energies were observed fully consistent with the single crystal data for the (1 1 1) and (1 0 0) facets, which constitute the surface of the supported nanocrystallites, but it has to be taken into account that a fraction of the adsorbing NO dissociated and irreversibly blocks specific sites on the particles (see discussion in Section 8).

It should be pointed out that the analysis of this type of modulated MB experiment is somewhat problematic in those cases in which the desorption rate constant is strongly coverage dependent. For CO desorption from metal single crystals the coverage dependence of the Arrhenius parameters is typically strong [479]. On supported particles the situation is further complicated by the presence of non-equivalent sites. As a result, a straightforward analysis of the desorption rate in terms of a first order kinetics is valid in the limit of low coverage with adsorption at equivalent sites only. At higher coverage or with different types of sites playing a role in the adsorption–desorption process, it is, of course, still possible to determine desorption rates via MBRS, but the calculation of rate constants requires the determination of the desorption rate as a precise function of coverage.

The problem is illustrated in Fig. 21 (from [62]) for the case of a CO adsorption–desorption experiment on Pd/Al_2O_3/NiAl. The surface is exposed to a modulated CO beam and the integral gas phase response is detected (see Section 2). As discussed earlier, the instantaneous rise and fall of the CO partial pressure is due to DI scattering and TD from the support and the slower response is due to adsorption–desorption from the Pd particles. From the desorption rate, the corresponding time constants are determined, as indicated in Fig. 21b. Eventually, the activation parameters for CO desorption are obtained from their temperature. As expected, the analysis for the well-shaped 6 nm Pd particles, which are mainly terminated by (1 1 1) facets, yields values for the desorption energy and pre-exponential factor which in good agreement with Pd(1 1 1) single crystal data [332]. The comparison is limited to the low coverage regime, however. At higher coverage or lower temperature there are deviations from the simple first order desorption kinetics and finally incomplete desorption occurs on the time-scale of the experiment ('increasing coverage' regime in Fig. 21, see [62] for more details). Of particular interest with respect to the possible origin of size effects in reaction kinetics is a comparison of the desorption behavior as a function of size. A comparison of the residence times for the two types of Pd particles in the low coverage limit is displayed in Fig. 21b. Significantly enhanced residence times are found for the smaller and more defect-rich 1.8 nm particles, indicating the presence of sites with slightly enhanced CO adsorption energy (an estimate yields approximately 5 kJ mol^{-1}). As discussed in Section 3.2.1, this observation is consistent with TPD data, which show an increase of the maximum desorption temperature with decreasing particle size [62].

6. CO oxidation

6.1. General remarks

As a first reaction system we focus on CO oxidation, primarily on Pd catalysts. CO oxidation on noble metal surfaces has attracted considerable attention over several decades and, today, is certainly one of the best studied reactions in surface science. Using molecular beam methods, numerous studies have been performed on single crystal surfaces (see, e.g. [10,90,161,383,385,389–392,395,396,399,400,402,480], see also Section 4.1). Different aspects of the reaction dynamics and kinetics on transition metals (for example, Pd, Pt, Rh, Ir, Ru or Ag) have been considered, such as, e.g. the basic reaction mechanism, the differentiation between different active species, the determination of activation parameters and the details of the reaction and desorption potential energy surfaces via measurements of the angular and velocity distribution of the product. The reasons why CO oxidation has attracted attention may be found in the apparently simple mechanism, the high reaction probability and the moderate reaction conditions. As a result of the numerous experiments, we have a relatively detailed understanding of CO oxidation kinetics on single crystal surfaces today.

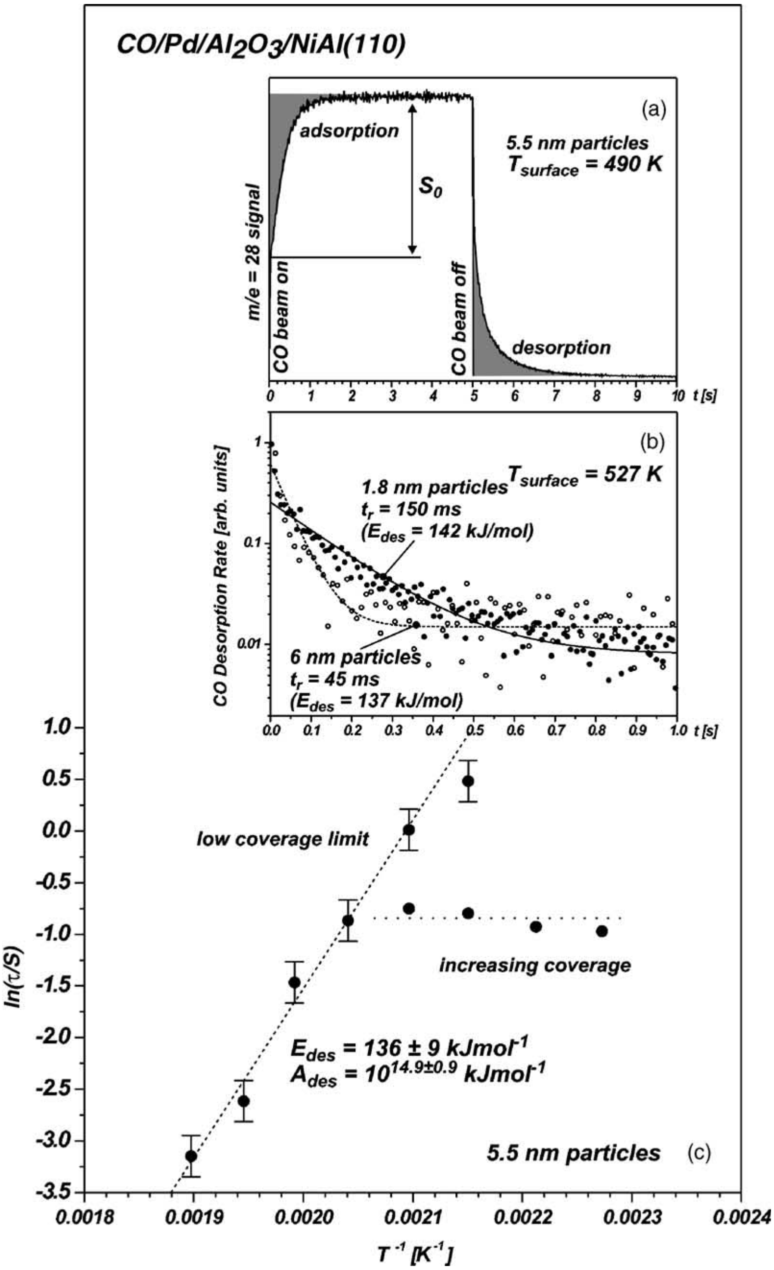

Fig. 21. CO residence time on Pd/Al_2O_3/NiAl(1 1 0) model catalysts: (a) schematic representation of the experiment; (b) comparison of residence times for 1.8 and 6 nm Pd particles; (c) activation parameters for CO desorption for 6 nm particles, from [62].

The situation is different on supported particles catalysts, however. Relatively little quantitative work on the reaction kinetics has been done on well-defined model systems, and in even fewer studies MB techniques have been employed. Although some dependencies on the particle size, the structure and the support have been observed, the origin of these effects is, nevertheless, unclear in many cases.

The mechanism of the reaction has been established in the pioneering molecular beam work by Engel and Ertl on Pd(1 1 1) [161,481], see also [10,482]. Briefly, CO adsorbs molecularly on Pd, whereas O_2 adsorbs dissociatively. The reaction itself follows a *Langmuir–Hinshelwood* (*LH*) mechanism, leading to the formation of CO_2, which in general only weakly adsorbs on noble metal surfaces. The LH activation energy is on the order of 100 kJ mol^{-1} at low coverages, but may decrease on adsorbate-covered surfaces [10,161]. This effect was related to repulsive adsorbate interactions at high coverage, which may lead to a decrease in the activation barrier as well. With respect to the kinetics, it is worth noting that pre-adsorbed CO has a strongly inhibiting effect on the chemisorption of oxygen, whereas the effect of pre-adsorbed O on the CO sticking is moderate. As a consequence, the reaction rate is found to be approximately inversely proportional to the CO partial pressure under conditions of high CO coverage (see, e.g. discussions in [10,161]). Also, regions of kinetic bistability arise as a result of the differences in the CO and O_2 adsorption kinetics (see, e.g. [483] for an introduction). It is noteworthy that most recent studies showed no indications for CO dissociation on Pd surfaces, even at high pressures (see, e.g. [484] and references therein), although dissociation was reported in some earlier studies [485,486] and in a recent study at high temperature and pressure as well [487].

Apart from the work on Pd single crystals, several molecular beam studies on CO oxidation on other noble metals have been published (see, e.g. [90,383,385]), which were able to provide insight into not only the kinetics but also the dynamics of the reaction. With respect to following discussion, it is of particular importance, however, that for the specific system of CO + O/Pd(1 1 1), quantitative data are available on sticking coefficients, activation energies and pre-exponential factors (see, e.g. [161,332]) which can be used as a starting point in microkinetic modeling.

The work on the kinetics of CO oxidation on supported model catalysts until 1997 has been reviewed by Henry [19] and we restrict ourselves to brief summaries with respect to those studies, which have already been discussed there. It should be pointed out that CO oxidation on Pd (as well as on other Pt group metals) is in general considered to represent a structure insensitive reaction. Structure insensitivity implies that the reaction kinetics should be very similar on single crystal surfaces of different orientation. Indeed, this was found to be the case experimentally (see, e.g. [482] and references therein [488–491]). Considering the specific situation of a supported catalyst, structure insensitivity also implies the absence of size effects. Indeed, size and structure dependencies for the CO oxidation on Pd surfaces are moderate, but is has also been shown in several studies that to some extent structure, size and support dependent effects do exist and can be quantified and can be clearly identified experimentally.

There are several possible origins of such effects, some of which are mentioned in the following and addressed in the next sections: (i) firstly, *capture zone effects* may play a role, which were discussed in detail in Section 5. This phenomenon was first taken into account after early experiments of Ladas et al., who attempted to verify the absence of particle size effects for the case of Pd/α-alumina catalyst, but found substantial dependencies of the turnover frequency for samples with different particle size [458]. An explanation based on the capture zone was first proposed by Gillet et al. [26,457] and later used, e.g. by Rumpf et al. [459], Henry and coworkers [195,197,460] and others to account for experimental results. (ii) Of course, there are other possible reasons for size effects. For example, it has been experimentally established that the *CO adsorption properties* vary drastically as a function of particle size and structure (see, e.g. [62,79,194,196], also [46] and references therein). For larger particles on weakly interacting supports such as Al_2O_3, SiO_2 or MgO, these variations may be the result of *specific geometric sites* such as different crystallographic facets, edges, corners or steps which are present on the particle surface. For smaller particles or aggregates on more strongly interacting supports, such modification may also arise as a result of *modifications of the electronic properties* of the particles (see, e.g. [30,220,492]). In addition, *communication effects* (iii) arising from coupling of different surface sites via surface diffusion [20,27,34,35] or (iv) *coverage fluctuation* can have an impact on the kinetics [37–39] (see Section 1). Another effect which for Pd surfaces has been discussed for a long time and recently attracted renewed attention is the *formation of subsurface oxygen and surface oxidation* (v) [274–297]. Although no kinetic studies on supported Pd model catalysts addressing such phenomena have been reported yet, the relation of bulk and surface oxide phases and subsurface species to the reaction kinetics as well as the role of *poisons and promoters* (vi) will probably be one of the major challenges in future studies in this field.

In this section, we will review MB experiments on the CO oxidation on model catalysts, addressing some of the effects discussed above. In particular, we will focus on the microscopic understanding of these phenomena by comparison of the experimental results with microkinetic simulations.

6.2. Steady-state and transient kinetics

Most of the experimental MB studies on the steady-state and transient CO oxidation kinetics have been performed on Pd model catalysts and we will focus on the corresponding results. For completeness, it should be mentioned that some work has been done on other model systems as well [49,217,241], but the amount of data is limited and the interpretation of the results in terms of microscopic concepts or models remains largely lacking.

6.2.1. Experiments on supported Pd model catalysts

Steady-state and transient MB experiments on the kinetics of CO oxidation on supported Pd model catalysts were performed by Matolin and coworkers [210–212,216], by Henry and coworkers [197–200,203], very recently by Heiz and coworkers [42], and by our group [61,225–229,239,240,314,315].

Matolin and coworkers performed transient experiment on Pd particles of different size on various Al_2O_3 supports [210–212,216]. In these experiments, the model catalysts were pre-dosed with O_2 and, subsequently, the transient CO_2 production rate upon exposure to a MB of CO was detected as a function of sample temperature. As a most important result from this work, it was found that there were strong dependencies of the transient reaction rate and oxygen absorption capacity for different particle sizes, densities and supports. The exact origin of these effects could, unfortunately, not be identified in detail. As a possible explanation, the influence of the capture zone was discussed, which enhances the flux of CO onto the particles and thus can lead to a higher initial reaction rate after impingement of the beam. Other effects that were invoked include the formation of more dense oxygen phases or subsurface oxygen species or a possible restructuring of the particle in adsorbate atmosphere.

Recently, Heiz and coworkers measured the TOF as a function of surface temperature for small mass-distributed Pd clusters ($Pd_{55\pm25}$) on MgO(1 0 0)/Mo(1 0 0) using a pulsed CO MB source and O_2 dosing from the background pressure [42,325]. As the most remarkable result from this work, it was pointed out that the TOF value was comparably high with a maximum appearing at significantly lower surface temperatures as compared to larger Pd particles. These effects indicate the presence of particle size dependent kinetic effects. Such comparisons have to be treated with care, however, due to the substantial differences in the experimental procedures applied. In particular, it has to be taken into account that the experiments were performed under transient conditions, starting from oxygen pre-covered particles. As discussed before, the RDS under such conditions is the adsorption of CO. The larger TOF values are therefore expected to be related to the higher CO pressures used [42,325], in comparison with previous studies on model catalysts [197]. As already pointed out by the authors [42,325], a more correct comparison would involve the CO reaction probability either taking into account the impingement rate on the catalyst or – correcting for metal coverage and the capture zone effects – the CO arrival rate on the catalyst particles [197].

Becker and Henry performed steady-state and transient measurements for the CO oxidation on Pd/MgO(1 0 0) model catalysts [197,198]. In these experiments, O_2 was continuously dosed from the background pressure and a MB of CO was employed to supply the second reactant. There are two important results obtained from this work:

(i) With respect to the steady-state reaction rates it was shown that these exhibited indeed some particle size dependence for the TOF measured under a given set of conditions. In order to identify the origin of this effect, Becker and Henry modeled the contribution of the capture zone effect to the particle size dependence. From their results, they concluded that there is indeed an effect of the particle size and structure on the TOF, which is beyond a pure capture zone contribution. It is to be stated, however, that this effect is moderate.

(ii) Upon termination of the CO beam a specific transient CO_2 response was observed, which includes a minimum immediately after termination of the beams followed by a maximum at later time. This effect was more pronounced for smaller particle sizes. Following earlier work, in which experimental indications for specific adsorption sites on the Pd particles with higher CO binding energy were observed, this feature was attributed to the presence of specific defect sites on the particles [79,194,196]. This result is noteworthy as it represents the first experimental evidence for the specific role of different reactive sites in the kinetics of CO oxidation on Pd particles.

In recent work of our group, this interpretation of Becker and Henry was confirmed in as far as the feature was indeed found to be related to the simultaneous presence of different active sites on the particles. Details of the model had to modified, however, with respect to the type of defect sites involved [225–228]. In the following, we will discuss this issue in more detail.

The experimental setup used is schematically illustrated in the insets of Fig. 22. Two effusive beams of variable intensity are superimposed on the sample, i.e. a modulated beam of CO and a continuous beam of O_2, and the global CO_2 production rate is recorded. Systematically, the experiment is repeated as a function of the CO to O_2 ratio, quantified via the CO flux fraction x_{CO}:

$$x_{CO} = \frac{F_{CO}}{F_{CO} + F_{O_2}}$$

Here, F_i is the partial flux of component i at the sample position. For every set of conditions, the fluxes are chosen such that the total effective total pressure p_{total}

$$p_{total} = p_{CO} + p_{O_2} \quad \text{with} \quad p_i = F_i(2\pi m_i kT)^{0.5}$$

at the sample position is kept constant with both beams operating (with m_i representing the molecular mass and T_i describing the temperature of the velocity distribution of species i; $T_i \approx 300\,\mathrm{K}$ for the effusive sources as there is no cooling of any degree of freedom; see Section 2).

Upon admission of the CO beam, a transient response in the reaction rate is observed before the steady-state is finally established. After termination of the beam, another transient interval follows, before the CO_2 production ceases. Thus, two pieces of kinetic information are obtained from this type of experiment: (i) the *steady-state reaction rate* as a function of the reaction conditions (i.e. x_{CO}, p_{total}, T_{Surface}) (Fig. 22a) and (ii) the corresponding *transient reaction rates* (Fig. 22b). Simultaneously with the reaction rate measurements, information on the adsorbed species is obtained by in situ IRAS, either under static conditions after the steady-state has been established or in a time-resolved mode in the transient region. We return to the latter point below.

In the experimental steady-state reaction rates in Fig. 22a, we can clearly distinguish between two reaction regimes: under conditions of high oxygen flux, the surface is to a large extent covered by oxygen and the CO coverage is low. In this range, which in the following will be denoted as the *O-rich regime*, the reaction rate is proportional to the CO flux. Once a critical CO flux is reached, a rapid kinetic transition occurs to a steady-state, which is characterized by high CO coverage and low oxygen coverage. These conditions are denoted as the *CO-rich regime*. Here, the CO, which accumulates on the surface, inhibits the dissociative adsorption of oxygen. As a result, the reaction rate drops rapidly upon crossing the point of transition. Moreover, the reaction rate shows negative orders with respect to the CO flux. This type of behavior as a function of the CO and oxygen flux is well-known from single crystals (see, e.g. [10,112,113,161]). It is noteworthy, however, that on the supported particle system the kinetic transition was found to occur in a more gradual fashion as compared to the behavior on single crystals surfaces. This effect is presumably related to heterogeneity effects as discussed in the following.

The dependence of the reaction rate on the sample temperature is qualitatively explained as follows: in the limit of low CO flux, CO adsorption is the RDS. The fact that the reaction rate is independent of the surface temperature is a result of the similarity of the steady-states (high oxygen coverage and very low CO coverage). In addition, the CO sticking coefficient (and therefore the reaction rate) is only weakly dependent on the oxygen coverage. In principal, S_{CO} is expected to decrease slightly with increasing temperature due to the decreasing lifetime of the precursor states on the support and on the particles. The effect, however, is weak and cannot be identified from the present data. With increasing surface temperature, the removal of CO from the surface by reaction and desorption becomes faster, leading to a shift of the kinetic transition to the O-rich regime toward higher x_{CO}. In the limit of high CO flux, the RDS is oxygen dissociative adsorption (or more precisely *oxygen dissociation* at low temperature, i.e. at high CO coverage, and *oxygen adsorption* at high temperature, where the CO coverage is low due to fast CO desorption and O_2 dissociation is not inhibited). The reaction rates are temperature dependent in this region due to the temperature-dependent CO steady-state coverage and the pronounced influence of CO on the S_{O_2}.

Some data on the transient behavior is displayed in Fig. 22b. It is apparent that the two reaction regimes, O-rich and CO-rich, exhibit different characteristic types of transient response (see also Fig. 23) [200,226]:

(i) Transient type I, O-rich regime (Fig. 23, lower trace): a simple type of transient behavior is observed, in which, starting from oxygen saturation coverage, an instantaneous increase in the CO_2 production is found immediately after admission of the CO beam. As pointed out by Piccolo et al. [200], this behavior is due to the rapid formation of a low steady-state coverage of a weakly adsorbed precursor

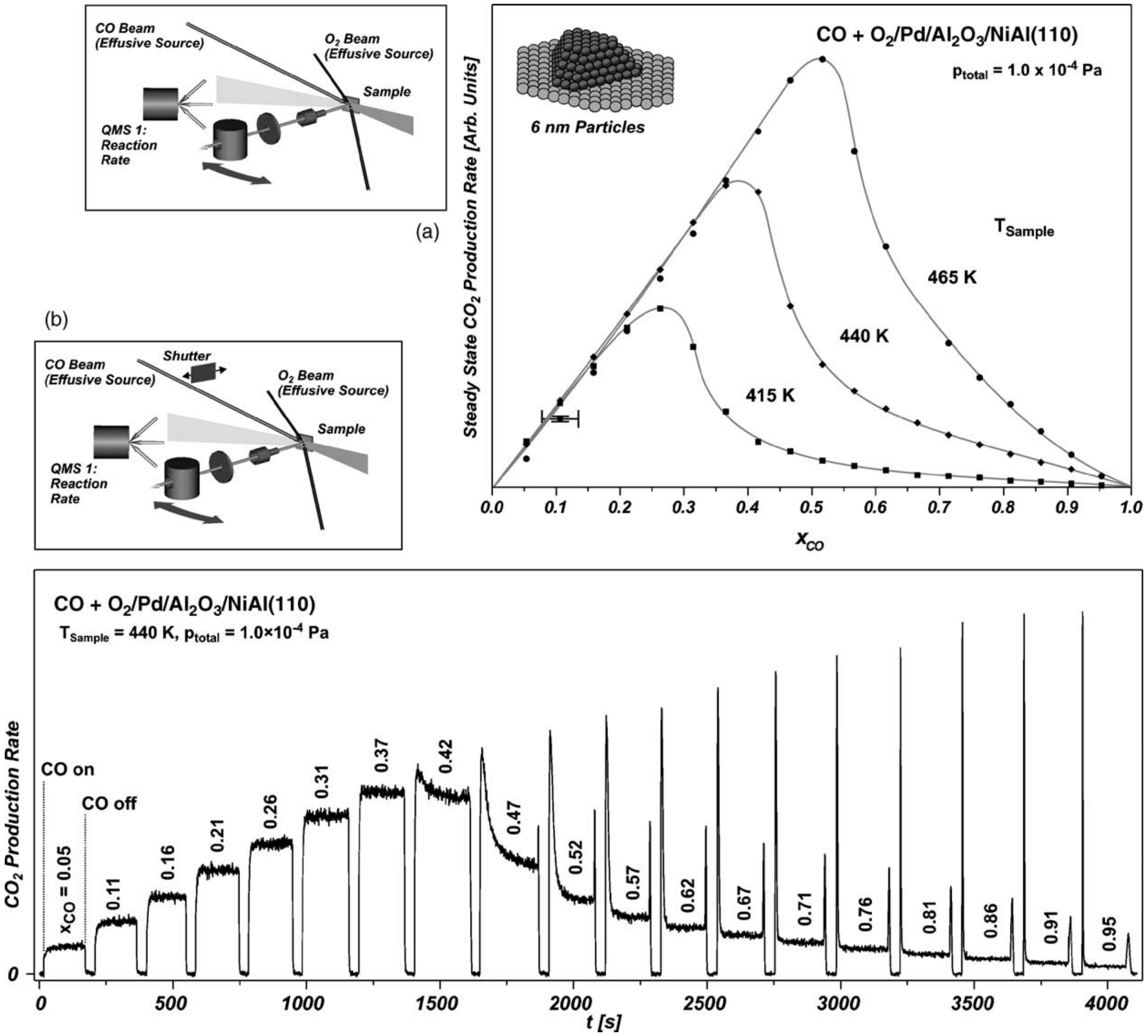

Fig. 22. (a) Steady-state CO oxidation kinetics on a Pd/Al_2O_3/NiAl(1 1 0) model catalyst. The transient experiment is performed as a function of the fraction of CO in the total gas flux x_{CO} at constant total effective pressure; (b) transient CO oxidation kinetics on a Pd/Al_2O_3/NiAl(1 1 0) model catalyst. The reaction rate is recorded employing a continuous oxygen beam and a modulated CO beam. The transient experiment is performed as a function of the fraction of CO in the total gas flux x_{CO} at constant total effective pressure, from [226].

state. From the precursor state, the CO molecule either desorbs or chemisorbs, in the latter case followed by fast oxidation to CO_2. As the reaction progresses, oxygen vacancies are generated, leading to an increased chemisorption probability of the CO precursor, reflected by the slow increase in the reaction rate, before steady-state conditions are finally reached. It should also be noted that the steady-state is characterized by high oxygen and low CO coverage conditions. After switching off

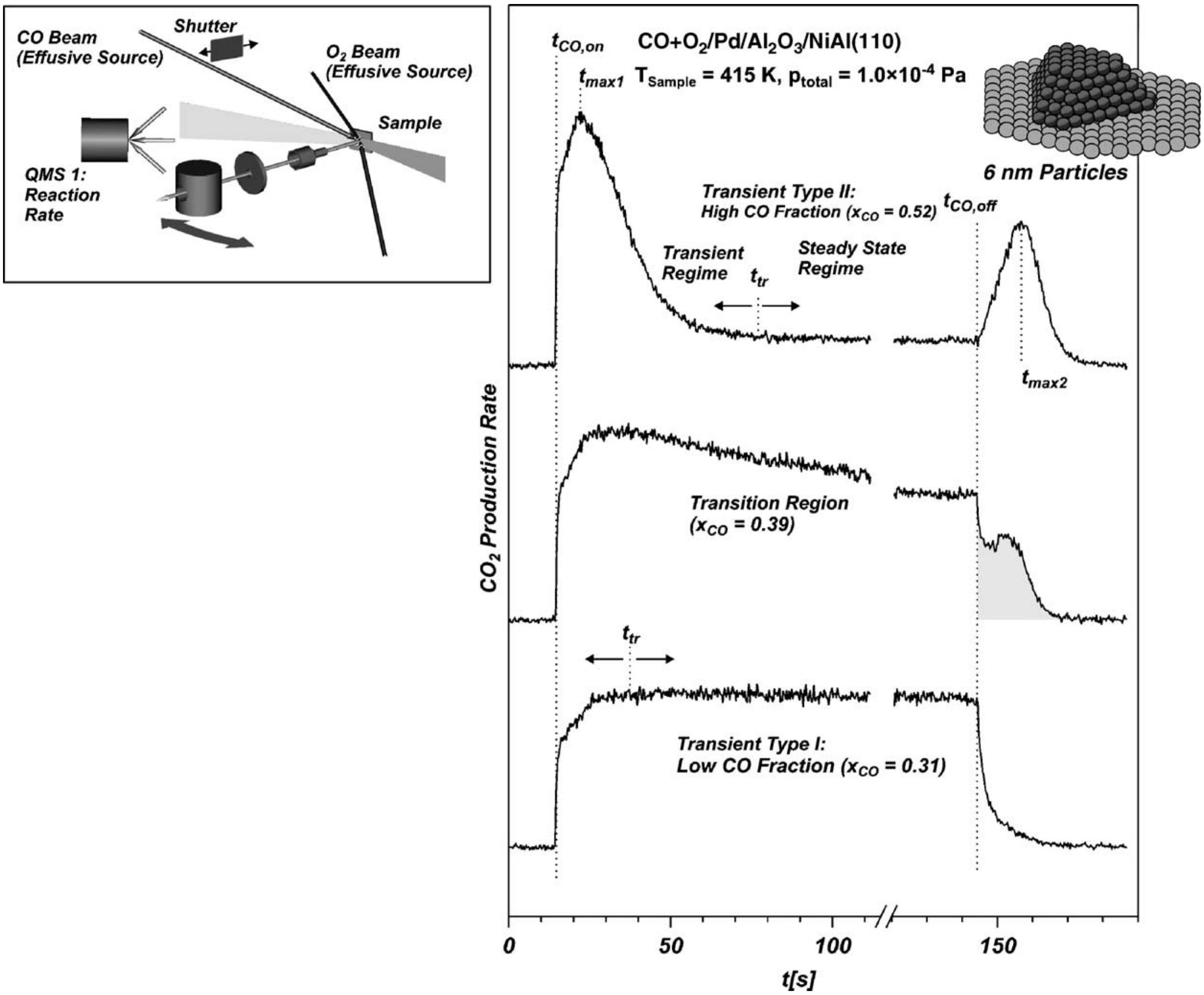

Fig. 23. Transient behavior of the CO_2 production rate on a $Pd/Al_2O_3/NiAl(1\,1\,0)$ model catalyst (continuous O_2 beam and a modulated CO beam) under CO-rich conditions (upper trace, transient type II), under O_2-rich conditions (lower trace, transient type I) and in the transition region (middle trace), from [228].

the CO beam, the low amount of CO present on the surface is consumed rapidly and the CO_2 production rate decreases.

(ii) Transient type II, CO-rich conditions (Fig. 23, upper trace): similar to the O-rich case, the transient starts from oxygen saturation and shows an instantaneous increase of the CO_2 production upon admission of the CO beam (build-up of a CO precursor coverage), followed by a slower increase in the reaction rate (increasing chemisorption probability of the CO precursor). Then, an entirely different behavior is observed with the reaction rate reaching a maximum and subsequently decreasing. This effect is a consequence of the inhibiting effect of CO on the O_2 adsorption. Accordingly, the steady-state is characterized by high CO and low O coverage. Upon termination of the CO beam, the process is reversed: adsorbed CO is consumed, opening free sites for O_2

dissociation. Thus, O_2 dissociative adsorption is accelerated and the reaction rate reaches a maximum, before it finally decreases due to CO depletion.

The above transients are fully explained on the basis of a simple homogeneous surface model. The situation changes, however, if the transient behavior in between the two reaction regimes is taken into consideration. In a certain range of flux conditions, in the following denoted as the *transition regime* between O-rich and CO-rich conditions, a rather peculiar transient behavior can be observed (Fig. 23, middle trace). It is characterized by a sudden drop in the reaction rate upon termination of the CO flux, followed by a CO_2 production peak at later time. As mentioned earlier, the effect has previously been observed by Becker and Henry [197,198], and was tentatively related to the presence of particle defect sites. The exact origin of the modified transient kinetics can be probed by correlated TR-IRAS experiments, as discussed in the following.

We start by considering static IRAS measurements under steady-state conditions as a function of x_{CO}. Corresponding spectra of the CO stretching frequency region for different types of Pd model catalysts are displayed in Fig. 24 (from [228]). Focusing on the larger and well-ordered particles (6 nm) first, three types of CO absorption features can be distinguished on the Pd particles and can be assigned on the basis of single crystal data (see [493–502] and references therein): (i) a weak feature at ~2060 cm^{-1} can be attributed to CO bonded to Pd at on-top sites, which is presumably at least partly of a defect nature [46,226]; (ii) a feature between 1900 and 1930 cm^{-1}, which is assumed to be dominated by CO on three-fold hollow and bridge sites on (1 1 1) facets (compare [499–502] and references therein) but may also contain contributions from defect sites and from Pd(1 0 0) facets [57,60] and (iii) features between 1815 and 1870 cm^{-1} originating from CO adsorbed on hollow sites, mainly on (1 1 1) facets [46,57,60,226,237] and references on single crystal work).

The dependence of the absorption features as a function of x_{CO} is summarized in Fig. 24c–e (from [228]). Three specific quantities are displayed: the total integral absorption in the CO stretching frequency region, the relative intensities of the CO features, and the corresponding stretching frequencies. The signature of the kinetic transition between the O-rich and the CO-rich state can be identified in each of the plots. The total absorption signal (Fig. 24c) directly reflects the sudden increase of the steady-state CO coverage at the transition between the two regimes (keeping in mind, however, that in IRAS there is no simple relationship between integral absorption and surface coverage, see, e.g. [125]). Information on the site occupation and the development of adsorbate structures under reaction conditions can be derived from the relative intensities of the absorption features (Fig. 24d) and their vibrational frequencies (Fig. 24e). For the larger well-ordered particles, strong rearrangements of the CO adsorbate layer are observed as a function of x_{CO}. In contrast, no similar effects are found for the defect-rich particles. This indicates that similar structural transitions in the adsorbate layer are suppressed in the latter case, possibly as a result of larger differences in adsorption energy between the adsorption sites on the more defect-rich particle surface.

To some extent, the rearrangements as a function of x_{CO} can be understood in terms of the CO adsorption behavior on Pd(1 1 1), where several sites have similar CO adsorption energies. As a consequence, a large number of adsorbate structures are formed as a function of coverage [497]. At low coverage, CO adsorbs in fcc hollow sites, changing to a mixture of fcc and hcp hollow sites at coverages of up to 0.5 [499,500]. Alternatively, adsorbate structures in which CO adsorbs on bridge sites as well as mixed structures have been reported [501,502]. Various ordered structures are observed in this region related to absorption features in the range between 1800 and 1930 cm^{-1} [125,497,503,504]. The

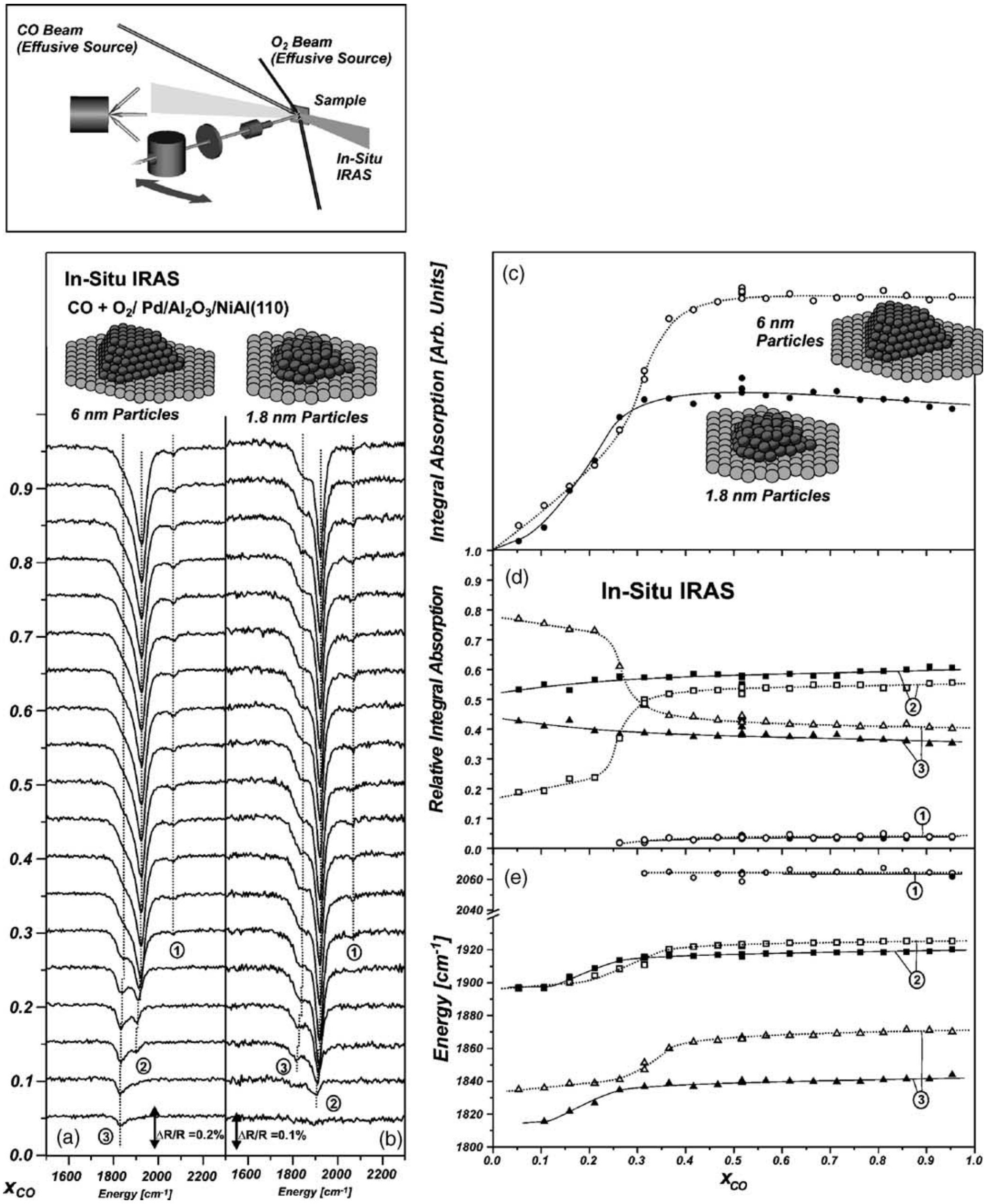

Fig. 24. In situ IR reflection absorption spectra recorded under steady-state conditions: (a) CO stretching frequency region for 6 nm Pd particles (415 K, 10^{-4} Pa); (b) CO stretching frequency region for 1.8 nm Pd particles; (c) integral absorption for both types of particles; (d) relative intensities of the CO features indicated in (a) and (b); (e) stretching frequencies of the CO features indicated in (a) and (b) (open symbols: 6 nm particles; solid symbols: 1.8 nm particles), from [228].

coverage-dependent frequency shifts are induced by both static and or dynamic coupling effects between adsorbate molecules and have recently been the subject of theoretical investigations [500]. It is the coverage range below 0.5, which is of relevance for all adsorption and reaction experiments at elevated temperature. In UHV experiments, higher CO coverage structures on Pd(1 1 1) are accessible below room temperature only. Here, bridge-bonded species are found at a coverage of around 0.6, giving rise to absorption in the range between 1960 and 1970 cm^{-1} [497,504]. A further increase in coverage results in the occupation of three-fold hollow and on-top sites, characterized by signals in the range of 2097–2110 and 1893–1895 cm^{-1} [497,498,501–505].

In a second type of IRAS experiments, the temporal evolution of the CO species were investigated under transient conditions. Here, it is particularly interesting to focus on the behavior in the transition region between CO-rich and O-rich conditions, under which the minimum in the reaction rate occurs (see above). In the experiment displayed in Fig. 25 (from [226,227]), IR spectra were recorded simultaneously with the reaction rate measurement. From this type of experiment, information on the type of defect sites can be derived, which is responsible for the transient minimum in the reaction rate. Here, the most important observation is the fact that there is no sudden decrease in intensity or frequency change is correlated with the dip in the reaction rate. As will be discussed in detail in Section 6.2.2, it follows from this result that the transient reaction rate minimum is related to a minority species of defect sites on the particle surface, which are characterized by relatively weak adsorption of CO.

As has been shown in previous work, the density of defect sites with both stronger and weaker adsorption strength increases with decreasing particle size (see [46,62] and references therein). As a result, a direct effect of the particle size and structure on the transient behavior is expected. A corresponding comparison of the transient experiments for two particle sizes is shown in Fig. 26 (from [228]). Indeed, it is found that the transition region characterized by the reaction rate minimum appears significantly more pronounced for the small and defect-rich Pd aggregates than for the larger and well-ordered particles. Whereas for the large and ordered particles the minimum in the reaction rate is detectable within a very narrow range of flux ratios only, for the small particles the effect is observed over a broad range of fluxes.

A quantitative analysis as a function of particle size shows characteristic differences not only for the transient response, but with respect to the steady-state reaction rates as well. These differences can be more clearly identified in a direct comparison of the turnover frequencies, obtained by normalization of the reaction rate with respect to the density of Pd surface atoms (derived from STM data). A corresponding plot is reproduced in Fig. 26a (from [228]). It is apparent that the TOF shows a particle size dependence. The effect, however, depends on the reaction regime: under oxygen-rich conditions, larger TOFs are found with increasing particle size, whereas the reverse dependence is observed under CO-rich conditions. It should be pointed out that the model catalysts were chosen such that the island density was higher for the smaller particles, and as a result, the total Pd surface area was similar in both cases ([228], see also Section 3). It follows that the differences in activity cannot be related to capture zone effects alone, which should be more pronounced for the smaller particle case and, correspondingly, should rather lead to an enhancement of the rate at low x_{CO}.

Concerning the possible microscopic origin of the particle size dependence under O-rich conditions, one possible effect is related to the interaction of the Pd particles with oxygen, e.g. including the possible formation of dense O adlayers, subsurface oxygen and surface oxides [274–293,297]. On single crystal surfaces it has been shown that the activity of the Pd surface strongly depends on the nature of the oxygen phase or species present (see, e.g. [294,506]). It is expected that the formation of subsurface oxygen and

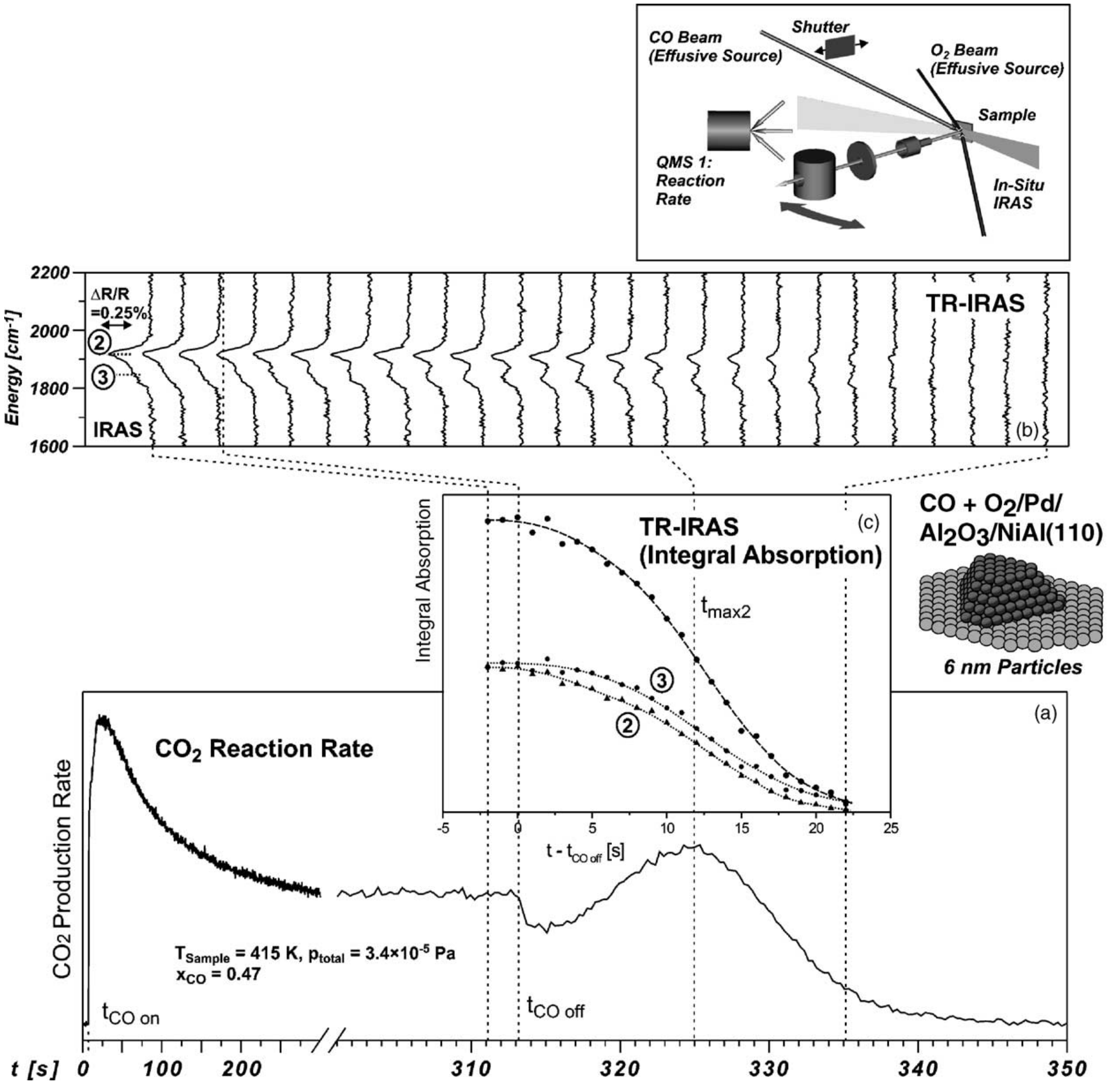

Fig. 25. Correlated time-resolved IRAS and transient reactivity experiment for the CO oxidation on a Pd/Al_2O_3/NiAl model catalyst of type I: (a) transient reaction rate; (b) TR-TRAS experiment in the transient region; (c) integral and partial intensities of the CO stretching vibration features, from [226].

surface oxides phases depends on the particle size and structure, but there is no experimental proof yet that the particle size dependencies observed during CO oxidation are directly related to such effects.

In the following, we focus on the behavior under CO-rich conditions. Here, it is found that the larger particles reveal a more pronounced inhibition effect with increasing CO flux, reflected by the steeper drop in the reaction rates with increasing x_{CO}. For the smaller particles, the weaker inhibition results in a

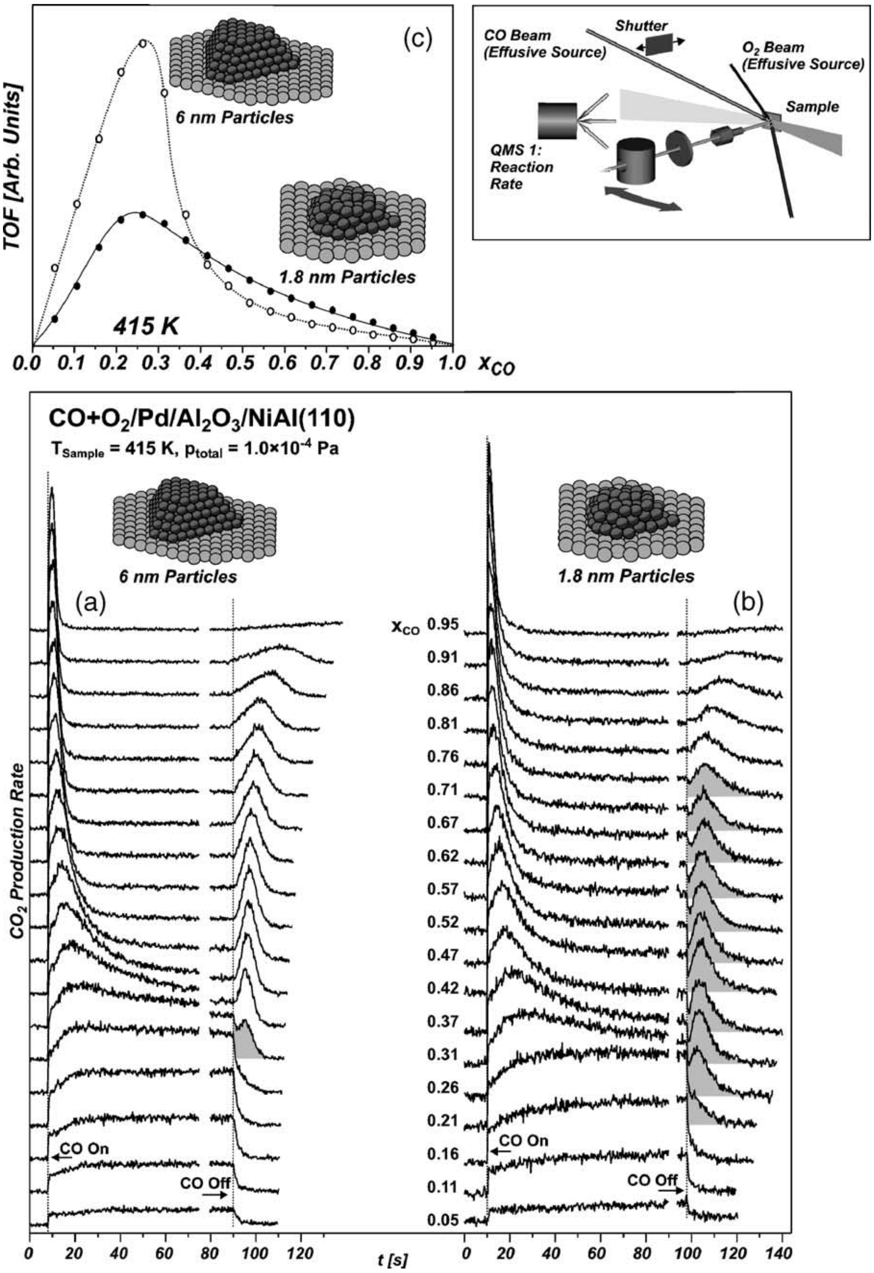

Fig. 26. Particle size dependence of the steady-state and transient reaction rates on the Pd/Al_2O_3/NiAl(1 1 0) model catalyst of different particle size: (a) transient behavior of the CO oxidation rate for 6 nm Pd particles and (b) for 1.8 nm Pd particles; (c) comparison of the TOF for both types of model systems, from [228].

higher TOF in the limit of high x_{CO}. These results can be interpreted in terms of the heterogeneity of the model catalysts, i.e. the presence and interplay of various types of adsorption and reaction sites, as will be discussed in Section 6.2.2.

6.2.2. Microkinetic simulations

Microkinetic simulation of transient and steady-state MB experiments were performed by Piccolo et al. [199,200] and by our group [225,226]. For a general overview over some methods of kinetic modeling, we refer to several reviews articles (see, e.g. [6,20,483,507]).

The general features of the MB experiment discussed in the previous sections are reproduced by a simple mean field (MF) model assuming a homogeneous surface, whereas the interpretation of the particle size or structure dependent phenomena requires the application of models which explicitly take into account the heterogeneity of the surface, i.e. the presence of different types of adsorption and reaction sites. In the following, we briefly review the results from both types of models.

6.2.2.1. Homogeneous surface models. Qualitatively, the steady-state and transient experiments discussed in Section 6.2.1 can be simulated on the basis of a MF model assuming a homogeneous surface ([226], see also [233]). Briefly, the kinetic parameters used in the model were derived from single crystal data available in the literature as well as from separate kinetic experiments on supported Pd particles. For the transient experiments in Fig. 22, the initial conditions before switching on the CO beam are $\theta_{CO} = 0$ and $\theta_O = 0.25$, assuming that CO and oxygen adsorption is similar as on Pd(1 1 1) and no formation of dense oxygen layers or surface oxides occurs. For the MB experiments, the latter is expected at least in the range of moderate temperature and pressure conditions (compare, e.g. [289,291,293]). Typical results of the simulation are reproduced in Figs. 27 and 28. As an example, the two principle types of CO_2 transients, i.e. the transients under O-rich conditions and under CO-rich conditions, are shown in Fig. 28. The shape of these transients has already been discussed in Section 6.2.1 (see also [199,200,226]). A comparison with the experimental data in Fig. 23 shows that the main features of the experimental reaction rates are well-reproduced. Thus a qualitative interpretation of the experiments can be given on the basis of this simple model. Also, a near quantitative agreement of the steady-state rates as a function of x_{CO} and the surface temperature can be obtained by optimization of the kinetic parameters for the range of larger and well-ordered particles [233].

It should be pointed out, however, that – as usually the case in microkinetic modeling – the quantitative agreement does not imply accuracy of the model at the microscopic level. In the present case, e.g. (i) the exact coverage dependence of both the CO and O_2 sticking coefficients is not taken into account; (ii) the coverage-dependency of energy barriers and pre-factors is only roughly considered; (iii) the influence of any effects beyond the MF model (islanding, etc.) is completely neglected.

With respect to the particle size dependence considered in Section 6.2.1, it is useful to compare the transient behavior predicted by the microkinetic model with the experimentally observed data in the transition regime between the O-rich and the CO-rich regions (see inset in Fig. 27). It is found that the dip in the reaction rate, typically found in experiments upon termination of the CO beam is not reproduced by the homogenous MF model. Also, the model cannot account for the differences in the steady-state TOFs.

6.2.2.2. Heterogeneous surface models. In general, many typical features of the steady-state and transient kinetics are well-described by the homogeneous surface model, at least at a qualitative level. However, deviations remain, in particular for small and defect-rich particles. Here, the assumption that the

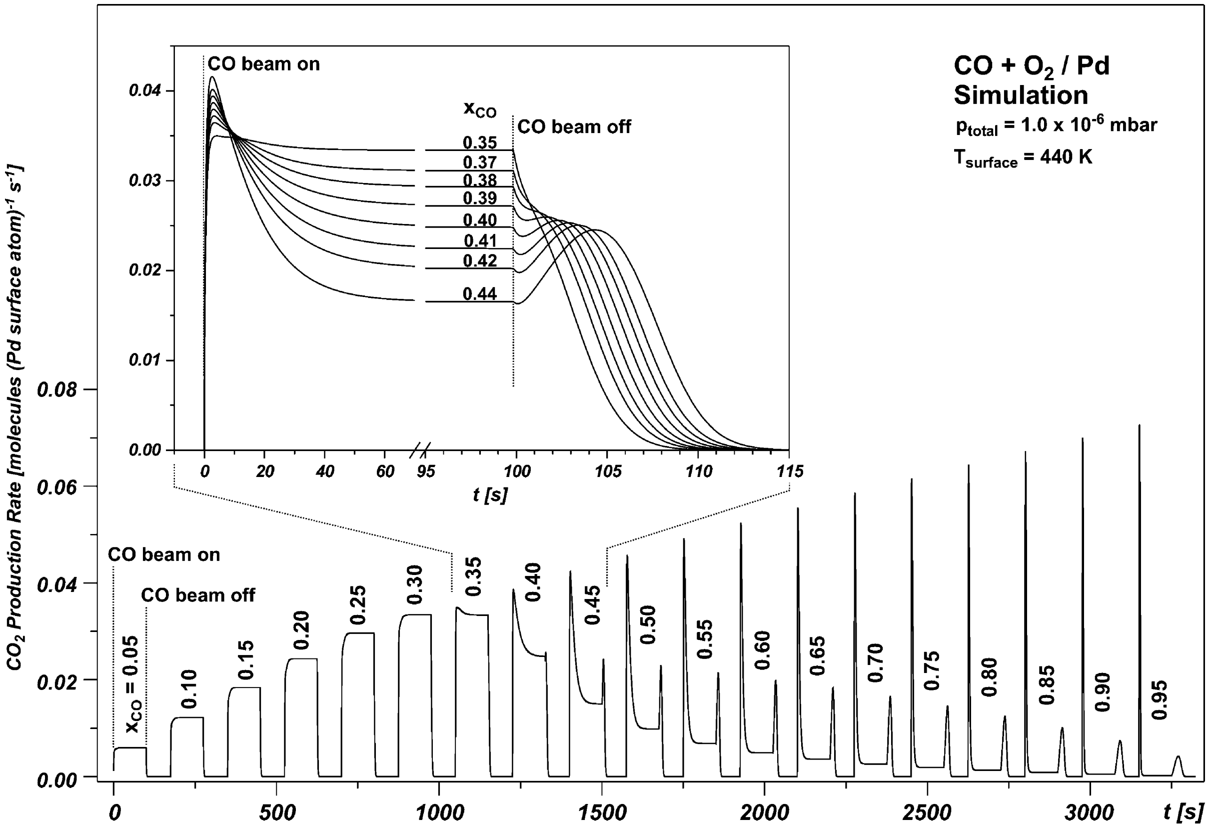

Fig. 27. Simulation of the transient CO oxidation kinetics on a homogeneous Pd surface under the conditions of the experiment displayed in Fig. 22. The inset shows the transient behavior in the transition region between the CO-rich and the O-rich regime, from [226].

kinetics can be described by a homogeneous surface does not provide a satisfactory description, even if, e.g. coverage dependencies of desorption and reaction parameters are included in the description [225].

Naturally, it can be anticipated that these particle size and structure dependent deviations are related to the heterogeneity of the catalyst. The different types of heterogeneity effects, which are expected on a supported model catalyst are schematically illustrated in Fig. 29a. First of all, it has to be taken into account that the model catalyst consists of a large number of active particles. These particles can behave as individual microscopic reactors or – depending on the reaction conditions – may be coupled by adsorbate exchange via surface diffusion or via the gas phase (in case of at higher pressure conditions). Every particle exposes a specific ensemble of different reactive sites, e.g. including majority and minority facets, edges, steps, corners and interface sites. Moreover, the individual adsorption and reaction properties of specific sites can be influenced, e.g. by electronic size and support effects and by a particle's surroundings ('capture zone', see Section 5.1).

With respect to the relation of heterogeneity effects to the overall kinetics, two cases can be distinguished: first, we may assume that different reactive sites are located on a single particle, in the following denoted as *intraparticle heterogeneity*. As a second type of heterogeneity, individual

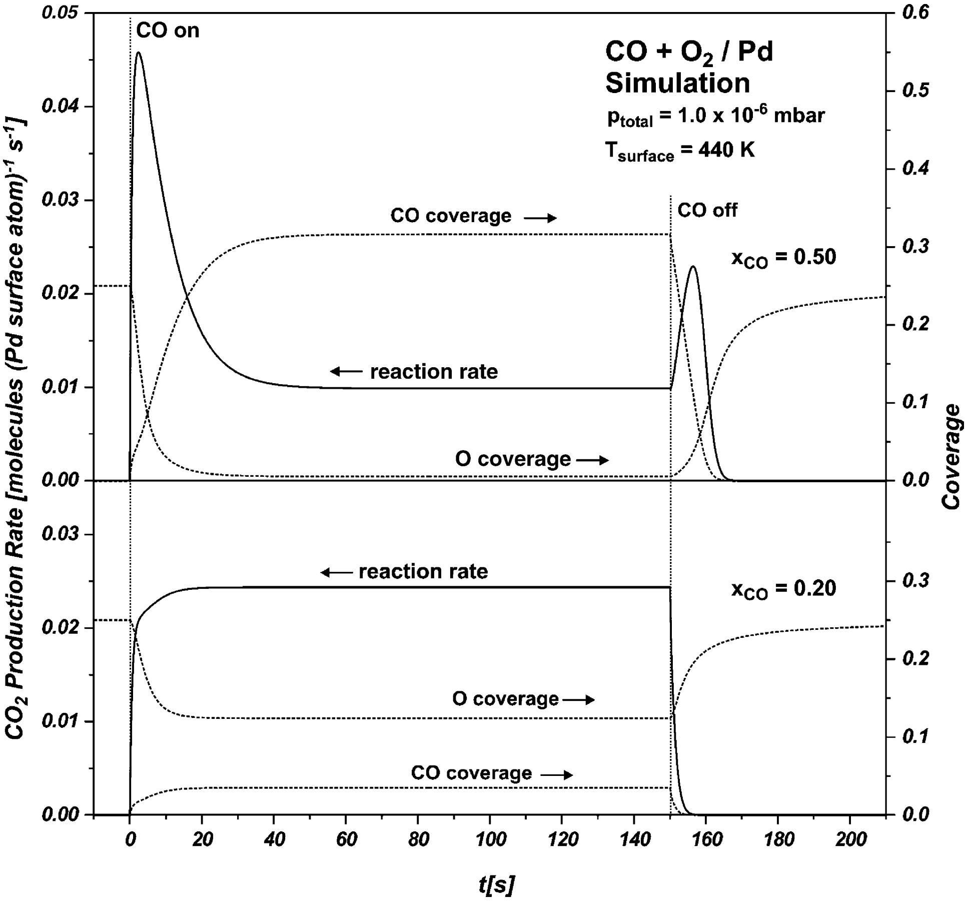

Fig. 28. Simulation of the typical transient CO oxidation rate and the adsorbate coverages on a homogeneous Pd surface under CO-rich (top) and O-rich (bottom) conditions, from [226].

particles are considered which expose different combinations of active sites or have different surroundings, giving rise to differences with respect to their overall adsorption, reaction or desorption properties. This type of situation is denoted as *interparticle heterogeneity*.

A key difference between the two cases is related to the surface diffusion of reactants. For many adsorbates, surface diffusion on a single active particle is rapid under reaction conditions, resulting in equilibration of the coverages on the different types of sites. For the specific case of the CO oxidation, CO diffusion is, for example, in general anticipated to be fast on the time-scale of the reaction (for a discussion on the surface mobility of oxygen see Section 6.3). In the case of interparticle heterogeneity, on the other hand, the efficiency of reactant exchange between particles strongly depends on several factors including the adsorption properties of the support, the particle distance and the specific reaction conditions. Often large distances and large diffusion barriers are present between the different particles (the latter as a consequence of the weak interaction of many reactants with the oxide support). In these cases, the exchange of adsorbates between different particles via surface diffusion can be strongly suppressed and the particles can behave like isolated nanometer scale reactors.

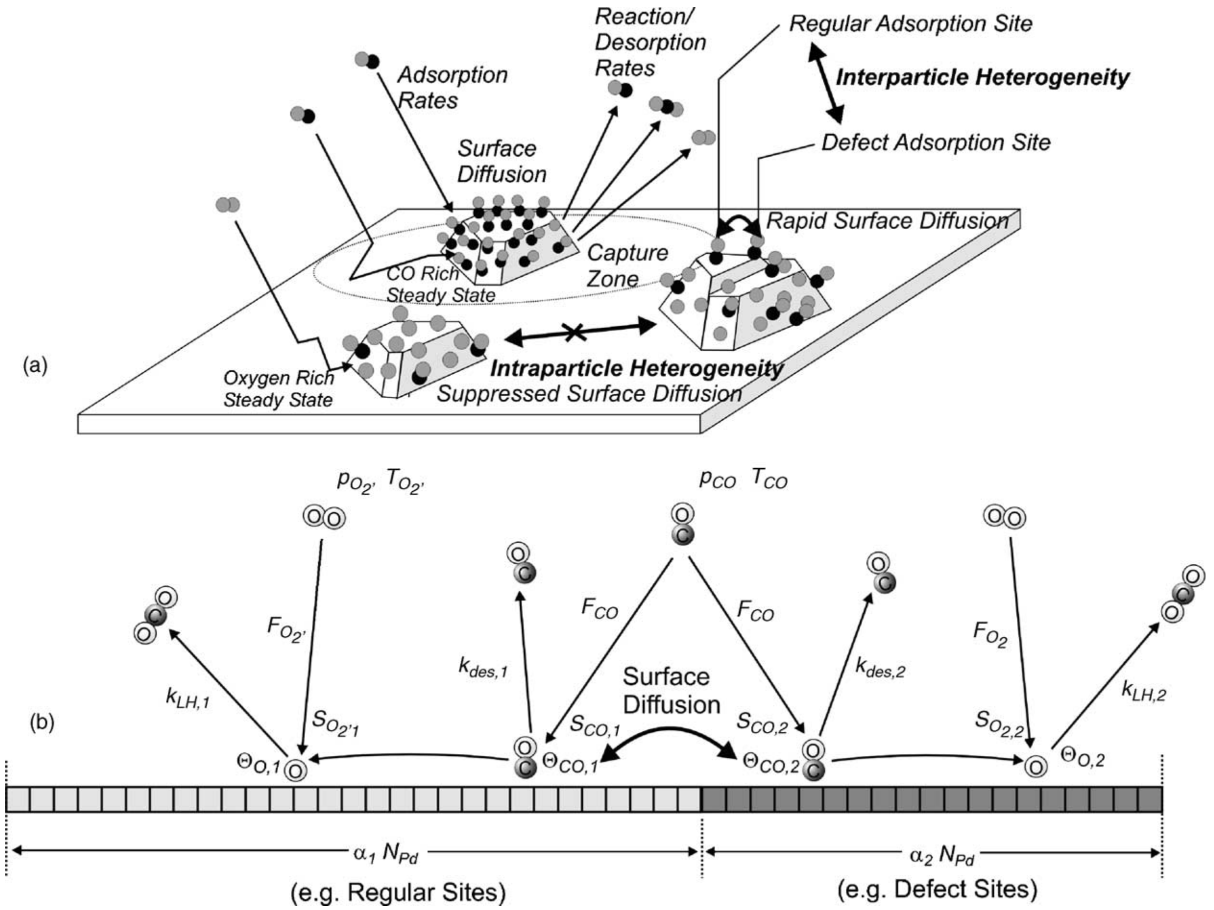

Fig. 29. (a) Schematic representation of the different types of heterogeneity on a supported model catalyst and their relation to the reaction kinetics and (b) simple kinetic model for the CO oxidation on a heterogeneous surface, from [225].

In the case of inhibited diffusion, the transient behavior in the transition region between O-rich and CO-rich conditions can be qualitatively rationalized as follows: local variations of the adsorption and reaction kinetics can be anticipated to result in a coexistence of O-rich and CO-rich regions on the surface under flux conditions which are close to the kinetic transition. As a consequence, a continuous transition occurs between the regimes instead of the sudden switching observed on single crystal surfaces (see, e.g. [483] for a detailed discussion). In the transition region, the total reaction rate is given by a superposition of both types of transients, with relative contributions depending on the exact reaction conditions. This type of scenario is qualitatively compatible with the experimentally observed transient and flux dependent behavior [226].

In order to put these arguments onto a more quantitative basis, microkinetic descriptions of heterogeneity effects have be developed using heterogeneous MF models (see schematic representation in Fig. 29b, from [225]). Here, the key feature is the incorporation of different types of active sites. Although there is no restriction with respect to the number and the properties of the types of sites that can be included, the essential points can be easily demonstrated using a very simple two-site model [225].

Following the experimental results on the structure and adsorption properties (see Section 6.2.1), it is assumed that the majority of sites are characterized by the adsorption properties of regular (1 1 1) single crystal facets. Additionally, a minority of defect sites with different adsorption properties is introduced. According to previous work (see, e.g. [46,62] and references therein), both more strongly and more weakly adsorbed CO species were observed on the smaller Pd particles. Piccolo et al. performed simulation using a heterogeneous MF model and showed that some aspects of the transient behavior can be reproduced assuming defect sites, which bind CO more strongly than the regular sites of the particle facets [199]. Later, the TR-IRAS experiments described in Section 6.2.1 led to the conclusion that the more strongly adsorbed CO most likely does not represent the key species responsible for the modified transient kinetics [226,228]. In the following, this was corroborated by simulations, which show that part of the experimentally observed transient behavior cannot be reproduced by taking into account a strongly bonded defect species only (see [225] for details).

Instead, the influence of a weakly adsorbed defect species was investigated. Typical simulated transients and steady-state rates are reproduced in Fig. 30, from [225]. Again, two limiting cases are being considered: either it is assumed that there is no exchange of CO between the two types of sites on the time-scale of the reaction (Fig. 30, dashed lines) or it is anticipated that diffusion is rapid (Fig. 30, solid lines). In the latter case, the CO coverages were equilibrated at any time during the reaction. It was found that the differences observed in both transient and steady-state kinetics as a function of particle size and structure are well-reproduced by the model. Specifically, (i) the steady-state reaction rates show a strongly reduced inhibition upon transition to the CO-rich regime and (ii) a pronounced minimum in the transient reaction rate is found over a broad range of flux conditions. The trends can be rationalized as follows: (i) with respect to the effect of the defects on the steady-state reaction rate it has to be taken into account that the weakly CO-binding sites are less prone to CO poisoning. Thus, they open a channel for oxygen adsorption, even under conditions under which the perfect single crystal surface would be nearly fully poisoned by CO. As a result the reaction rate remains relatively high in the CO-rich regime. (ii) With respect to the transient response, we have to consider conditions close to the transition between the kinetic regimes. Here, the CO coverage on more weak CO adsorbing minority sites would be significantly lower than on more strongly adsorbing sites. As a result, a large fraction of CO_2 is produced on the minority sites under steady-state conditions (or by oxygen adsorption via the minority sites). Upon termination of the CO beam, the CO coverage on the minority sites decreases rapidly, giving rise to the fast decrease in reaction. At a later time, the CO coverage decreases on the majority sites leading to the maximum in the reaction rate.

Details of the effect depend on the exchange of adsorbates between the reactive sites via surface diffusion (see [225] for a detailed discussion). It can be concluded, however, that the kinetic effects observed as a function of particle size and structure are qualitatively reproduced by a microkinetic model, which explicitly accounts for the heterogeneity of the surface.

The example illustrates how physically and chemically meaningful microkinetic descriptions of kinetic size and structure effects can be obtained by combination of quantitative kinetic experiments and microkinetic modeling. On the other hand, it has to be pointed out that the present models still represent drastic simplifications of the surface properties of the catalyst particles. Also, the quantitative information abundance and properties of different sites have not been derived from independent investigations but are the result of a fit to the kinetic model. A challenge for future studies would be the development of kinetic models based on a microscopic analysis of the type and density of different types of reactive sites as well as their individual adsorption and reaction properties as determined by experimental and theoretical methods.

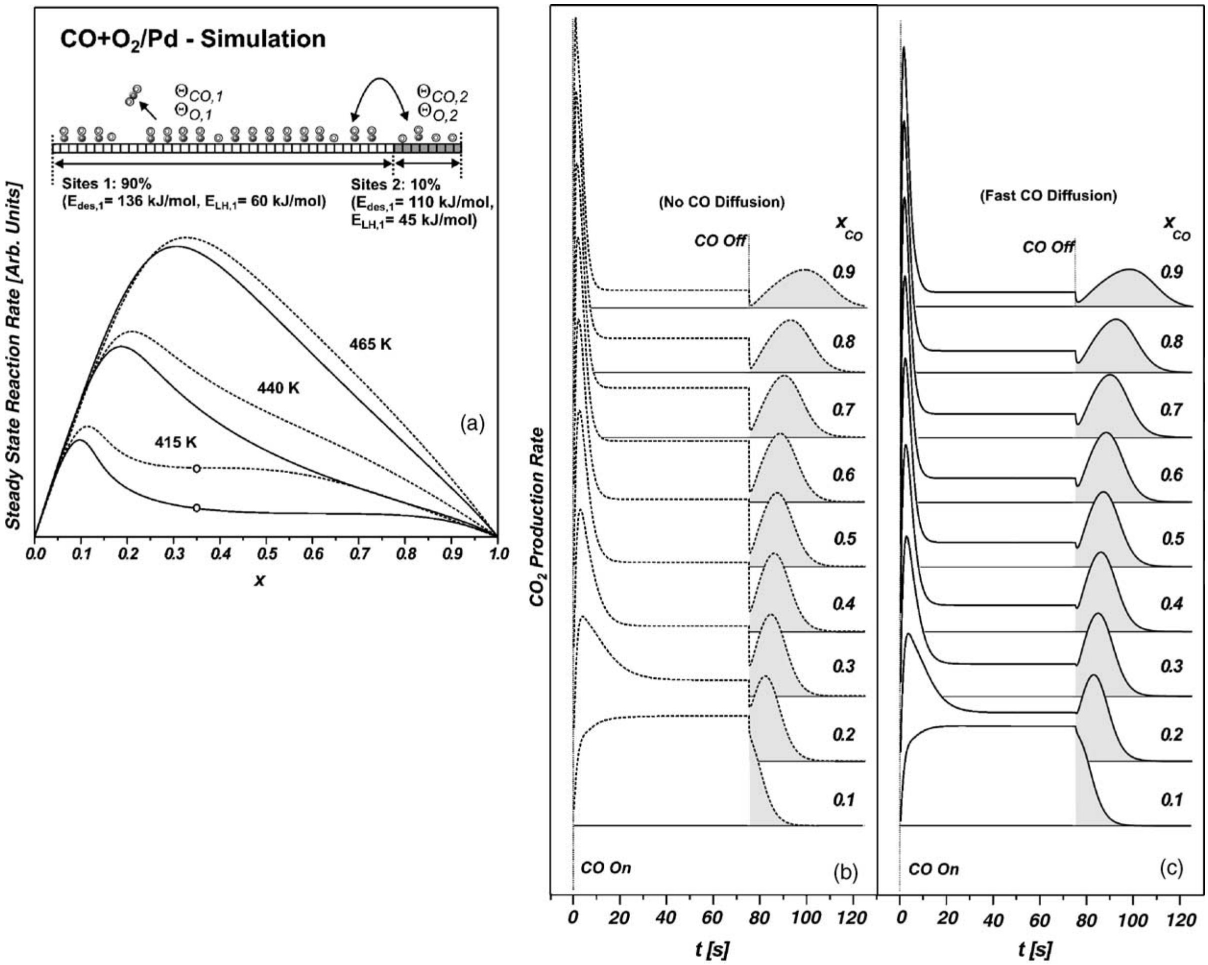

Fig. 30. Simulation of the transient and steady-state reaction rates on the basis of a heterogeneous surface model: (a) steady-state reaction rates (10^{-4} Pa; dashed lines: no CO diffusion between the two types of adsorption sites; solid lines: fast diffusion between the two types of sites); (b) transient reaction rates neglecting; (c) including surface diffusion (10^{-4} Pa, 415 K), from [225].

6.3. Angle-resolved experiments and surface diffusion

In most kinetic experiments on model catalysts, reaction rates were measured via the response in the background gas phase. Such experiments provide global kinetic information only. As a possible experimental approach to the determination of local reaction rates on supported nanoparticles, we have recently suggested the use of angular or velocity distribution of products desorbing from the active surface (see Fig. 31a) [229,314,315].

Briefly, the idea of the experiment is as follows: let us assume that a product molecule is formed at an active site on a supported particle. If the desorption of the product occurs immediately after formation, the velocity, internal energy and direction of the desorbing product molecule will contain information on the desorption or reaction potential energy surface characterizing the active site. Matsushima and

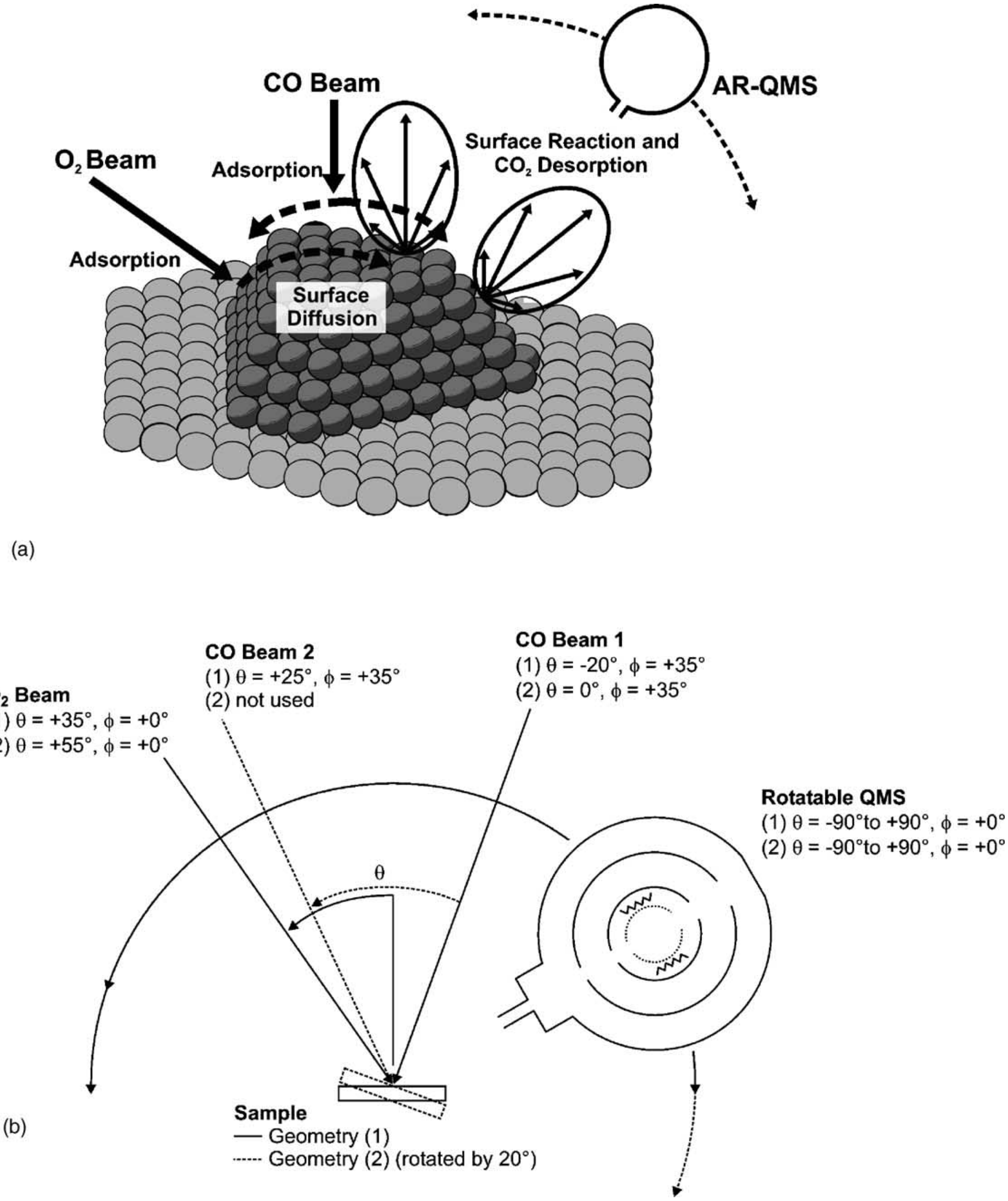

Fig. 31. (a) Schematic representation of an angle-resolved CO oxidation experiment on a planar model catalyst and (b) geometry of the setup used in the experiments, from [314].

coworkers have shown for different reactions on single crystal surfaces that such measurements can indeed provide valuable information on the active reaction or desorption sites (see [116] and references therein). If desorption is not immediate, accommodation of the product molecule occurs and the information on the reaction potential energy surface is lost. Still, the adsorption site of the physisorbed or chemisorbed product contains information on the location of the active center. Depending on the diffusion length, this information may also be lost or preserved until desorption. As discussed previously, the diffusion length depends on the ratio between surface diffusion and desorption rates under reaction conditions. In the case of a very weakly bound product molecule, the product diffusion length is short and, as a result, the desorption site will be in close proximity to the site of formation. For the case of surfaces structured on the nanometer scale this means that desorption is likely to occur from the same surface region or from the same facet on which the molecule was initially formed. As a result the angular distribution may still provide valuable data on the activity of specific surface regions. For the specific case of metal catalysts on planar supports, two types of information become available experimentally:

(i) *Local reaction rates* on nanoparticles: in principle, the quantitative analysis of the angular distribution of desorbing products allows the determination of local reaction rates on different parts, facets or sites on supported nanoparticles. However, the pre-requisite for a quantitative deconvolution would be an exact knowledge of the local angular distributions of products from all relevant sites and an exact structural characterization. Whereas latter information is available for some supported model catalysts, the knowledge on the angular distribution is still limited (see [116] for an overview).

(ii) *Surface mobility* under reaction conditions: in combination with MB techniques, local reactant fluxes impinging on different parts of a nanostructured surface can be controlled. For the case of three-dimensional supported catalysts particles, for example, the flux of various reactants onto the differently aligned nanofacets can be controlled via the incidence angles. This type of experiment can provide information on the surface mobility of reactants and on so-called communication effects, arising as a result of coupling of different surface regions via surface diffusion (see Section 1 and [20,27,34,35]).

6.3.1. Experimental results

Angle-resolved measurements of desorbing products from supported model catalysts have been performed in our group only recently [229,314,315]. For this type of study, CO oxidation is a favorable case, as CO_2 adsorbs only weakly on most transition metal surfaces and, consequently, desorption occurs on a very short time-scale after formation (see, e.g. [10]). Recently, Matsushima and coworkers have investigated the angular and velocity distribution of CO_2 desorbing from Pd and Pt single crystal surfaces under steady-state oxidation conditions [112–115]. In their studies, they were able to show that both the angular and the velocity distribution sensitively depend on the reaction conditions and that these effects relate to a change of the active site or the surface structure. For the specific case of CO oxidation on Pd(1 1 1) at low coverage, the angular distribution of CO_2 has been found to be close to a cosine distribution [161]. At higher coverage, lateral interactions lead to modifications of the potential energy surface, giving rise to angular distributions, which are highly directed along the surface normal [508]. Thus, we expect that on a nanocrystalline system such as the supported Pd model catalysts on various supports, desorption will preferentially occur along the surface normal of the nanofacet on which the molecule is formed. As a result, the angular distribution of CO_2 is expected to contain information about reaction rates on specific facets.

Following this discussion, a simple experiment was performed, schematically shown in Fig. 31. The model catalyst was exposed to a symmetric flux of CO, created by one or by the superposition of two MB sources. In addition, a third beam supplied the O_2. The key point in the experiment is the O_2 incidence angle, which was chosen to be tilted with respect to the surface normal. As a result, different parts of the surface of each individual particle were exposed to different local fluxes of O_2; some parts were exposed directly to incident O_2, while other parts were shadowed and not exposed at all. It thus depends on the rate of surface diffusion of adsorbed oxygen, whether these differences in reactant flux lead to local variations of the steady-state coverages and reaction rates (note that CO diffusion is always fast compared to oxygen diffusion, see [509]). If the surface diffusion length (determined by the diffusion rate and the residence time) exceeds the particle size, full equilibration of the coverages is expected. Otherwise, gradients in coverage and reaction rate are expected to develop (it should be mentioned that a quantitative description may also require other effects to be taken into account such as diffuse scattering of reactants or diffusion of physisorbed and chemisorbed precursors, see also Section 6.3.2).

In the initial set of experiments were performed on $Pd/Al_2O_3/NiAl(1\,1\,0)$ model catalysts (6 nm particle size), prepared by PVD (see [229], Fig. 32a), it was found that under both CO-rich and O-rich conditions the angular distributions of desorbing CO_2 were very similar. It is noteworthy that the experimental distributions from the model catalyst were broader than a cosine distribution, indicating that CO_2 production at the side facets of the particles could indeed be identified. As a second important observation, no significant asymmetry of the angular distribution could be detected, indicating a homogeneous distribution of oxygen over the Pd crystallites and, therefore, a diffusion length of adsorbed oxygen, which was larger than the particle size. The limited range of the particle sizes available via PVD precluded, however, equivalent experiments on substantially larger Pd particles.

More recently, these limitations were overcome by the use of supported model catalysts prepared by EBL (see Section 3.2.2) [314]. The method does not only expand the accessible range of particle sizes to significantly larger aggregates, but also provides a narrow size distribution, a well-controlled particle distance and a variable aspect ratio. In the experiments, large Pd particles (diameter: 500 nm; height: 450 nm) were used, which were arranged in a perfect hexagonal array. A summary of the corresponding experimental results is displayed in Fig. 32. In the first step, the influence of the CO to oxygen ratio (i.e. the fraction of CO in the total flux, x_{CO}) on the angular CO_2 distribution was investigated. It was possible to identify clear differences between the CO-rich and the O-rich regime. Specifically, it was found that under O-rich conditions the angular distributions were symmetric whereas under CO-rich conditions the distributions were asymmetric, with a considerably enhanced CO_2 production on the side facing the O_2 beam. It was found that the CO_2 distribution switches within a narrow x_{CO} range from a symmetric to an asymmetric shape (Fig. 32c). The switching occurs at the transition point from the O-rich to the CO-rich region. These results demonstrate that under O-rich conditions, oxygen diffusion over the particle is sufficiently fast to result in complete equilibration of the local O coverage, whereas there is no complete equilibration under CO-rich conditions. As will be discussed in detail in Section 6.3.2, it is possible to extract quantitative information on the mobility of adsorbed oxygen under reaction conditions from these data.

In addition to the dependence on x_{CO}, the influence of the surface temperature was investigated (Fig. 32c). In contrast to the pronounced influence of x_{CO}, the temperature dependence, both under O-rich and under CO-rich conditions, is weak. The origin of this weak dependence is the result of a partial cancellation of the temperature dependencies of several parameters including the diffusion coefficient, the steady-state coverages, and the reaction rates, as was analyzed in detail recently [315].

6.3.2. Microkinetic simulations

A rough estimate of the diffusion coefficients from the angle-resolved experiments described in the previous section is possible on the basis of the Einstein relation and the MF models described in Section

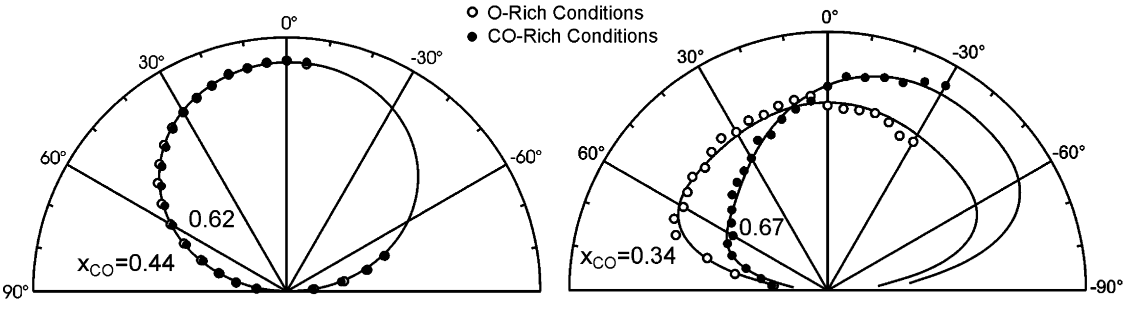

(a) $Pd/Al_2O_3/NiAl(110)$, Particle Size 6 nm (Experimental Geometry 1)

(b) $Pd/SiO_2/Si(100)$, Particle Size 500 nm (Experimental Geometry 2)

(c) $Pd/SiO_2/Si(100)$, Particle Size 500 nm (Experimental Geometry 2)

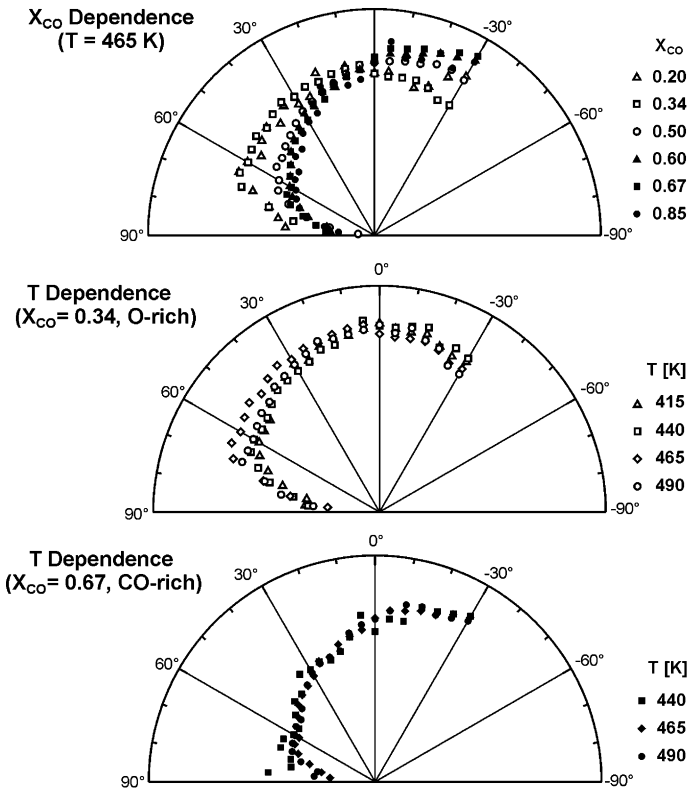

Fig. 32. Angular distribution of CO_2 desorbing under steady-state conditions under CO-rich (solid symbols) and O-rich (open symbols) conditions: (a) $Pd/Al_2O_3/NiAl(1\ 1\ 0)$, particle size 6 nm; (b) $Pd/SiO_2/Si(1\ 0\ 0)$, particle size 500 nm (note that for both experimental geometries used, the O_2 beam is blocked by the detector for a range of desorption angles); (c) angular distribution of CO_2 desorbing from $Pd/SiO_2/Si(1\ 0\ 0)$ (particle size 500 nm) as a function of x_{CO} and surface temperature, from [314].

6.2.2 [314]. A more quantitative analysis requires the application of coupled diffusion reaction models, which explicitly take into account the morphology of the catalyst surface [229,315]. We will review the key results of both approaches briefly.

Starting with the rough estimate, the key quantity, which determines the equilibration of the reactant coverages on a particle, is the oxygen diffusion length on the time-scale of surface residence. For adsorbed oxygen, the surface residence time $\tau_O = \theta_O \cdot \mathrm{TOF}^{-1}$ is determined by the steady-state coverage θ_O and the TOF. Both values sensitively depend on the reaction conditions and are experimentally accessible. An estimate of τ_O derived from the MF model discussed in Section 6.2 is shown in Fig. 33. As already suggested by the experiments, a strong dependence of the residence time on x_{CO} is found, together with a sudden decrease at the transition point between the O-rich and CO-rich regimes. The latter effect is due to the rapidly decreasing θ_O upon crossing the kinetic phase transition between the two regimes. In contrast to the strong influence of x_{CO}, the dependence of the residence time on T_S is moderate. In order to obtain some information on the oxygen diffusion barrier E_{diff}, the surface residence times required for diffusion across the particles were estimated based on the Einstein relation as a function of particle size, surface temperature and diffusion activation energy E_{diff}. In combination with the experimental results on the angular CO_2 distributions, upper und lower limits for the activation barriers for oxygen diffusion under reaction conditions were obtained [314].

A more accurate description requires the use of coupled diffusion reaction models. In order to account for the experimental results, both Monte-Carlo (MC) [229] and MF models [315] have been used.

The advantage of the MC method is the microscopic approach to the kinetics (see, e.g. [20] and references therein). In order to supplement the experiments on smaller Pd particles, simulations of the CO oxidation on realistic supported particle models were performed [229]. As a first step, a model of the catalyst particles was constructed, based on an analysis of the morphology as investigated by STM (see Fig. 34) [46,61,62]. In a second step, a MC model was setup and adjusted so that the experimentally observed steady-state reaction rates and surface coverages were well-reproduced as a function of the reactant fluxes and reaction temperatures. Once the overall reaction rates are reproduced, the individual rates on the nanofacets can be investigated (Fig. 34f). The influence of oxygen diffusion was studied in a model in which there was no oxygen adsorption on one of the particle facets. Typical snapshots of the MC simulation as a function of the oxygen diffusion rate are shown in Fig. 34b–e. Similar as discussed above, the comparison of the experimental results and the simulations provides an estimate of the oxygen diffusion barrier under reaction conditions.

With respect to the application to model catalysts, MC simulations represent a simple and straightforward way of developing realistic microscopic models, which take into account the exact morphology of the system. On the other hand, MC methods are computationally demanding, in particular for larger systems, and the systematic variation or adjustment of the large number of parameters involved is non-trivial problem. It should be mentioned, however, that in future work theoretical calculations may help to overcome this problem by providing reliable information on the rate a large number of elementary processes on which experimental information is not available (see, e.g. [510]).

In order to obtain a quantitative description of the angular distribution of desorbing CO_2 for the large particles (500 nm) prepared by EBL, a MF reaction–diffusion model was developed [315]. Schematically, the model is illustrated in Fig. 35. The catalyst particle is represented by a half prolate spheroid, placed on a large planar support disc. The surface reaction is described according to the MF model discussed in Section 6.2.2. The reactant fluxes are calculated at each point of the model surface, assuming O_2 and CO beam geometries corresponding to the setup used in the experiments and taking beam shadows and

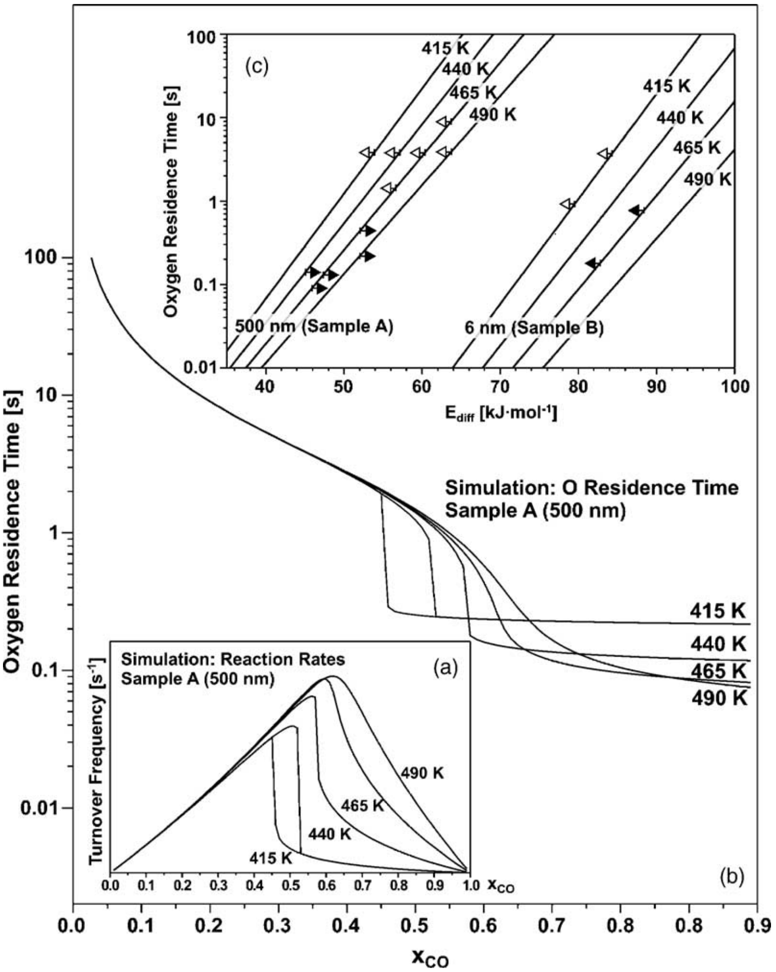

Fig. 33. (a) Simulation of the steady-state reaction rate on the Pd particles as obtained from a fit of the microkinetic model described in Section 6.2.2; (b) oxygen residence times as calculated from the simulation; (c) estimate of the activation barrier for oxygen diffusion on the Pd particles based on the oxygen residence times in (b). An Arrhenius type temperature dependence of the diffusion coefficient with a pre-exponential factor of $D_0 = 10^{-3}$ cm^2 s^{-1} was assumed. The arrows indicate upper and lower limits for the diffusion barrier under CO-rich (solid symbols) and O-rich conditions (open symbols) as derived from the angle-resolved data, from [314].

backscattering of reactants from the support due to TD and DI scattering into account. It should be noted that in the simulation of the experimental data on large Pd particles, capture zone effects were neglected due to the fact that the area of the capture zone is negligible in comparison to the particle surface (compare discussion in Section 5.1). Such effects can, however, be of relevance for smaller particles. Due to the small diffusion barrier for CO on close packed noble metal surfaces, CO diffusion was assumed to be fast on the time-scale of reaction (for Pd(1 1 1) see [511], for a general overview see [509]). After establishing the local reactant fluxes, the reaction diffusion equations were numerically integrated using the finite element method. The angular distribution of the desorbing CO_2 from an area element is modeled by a $\cos^n \phi$

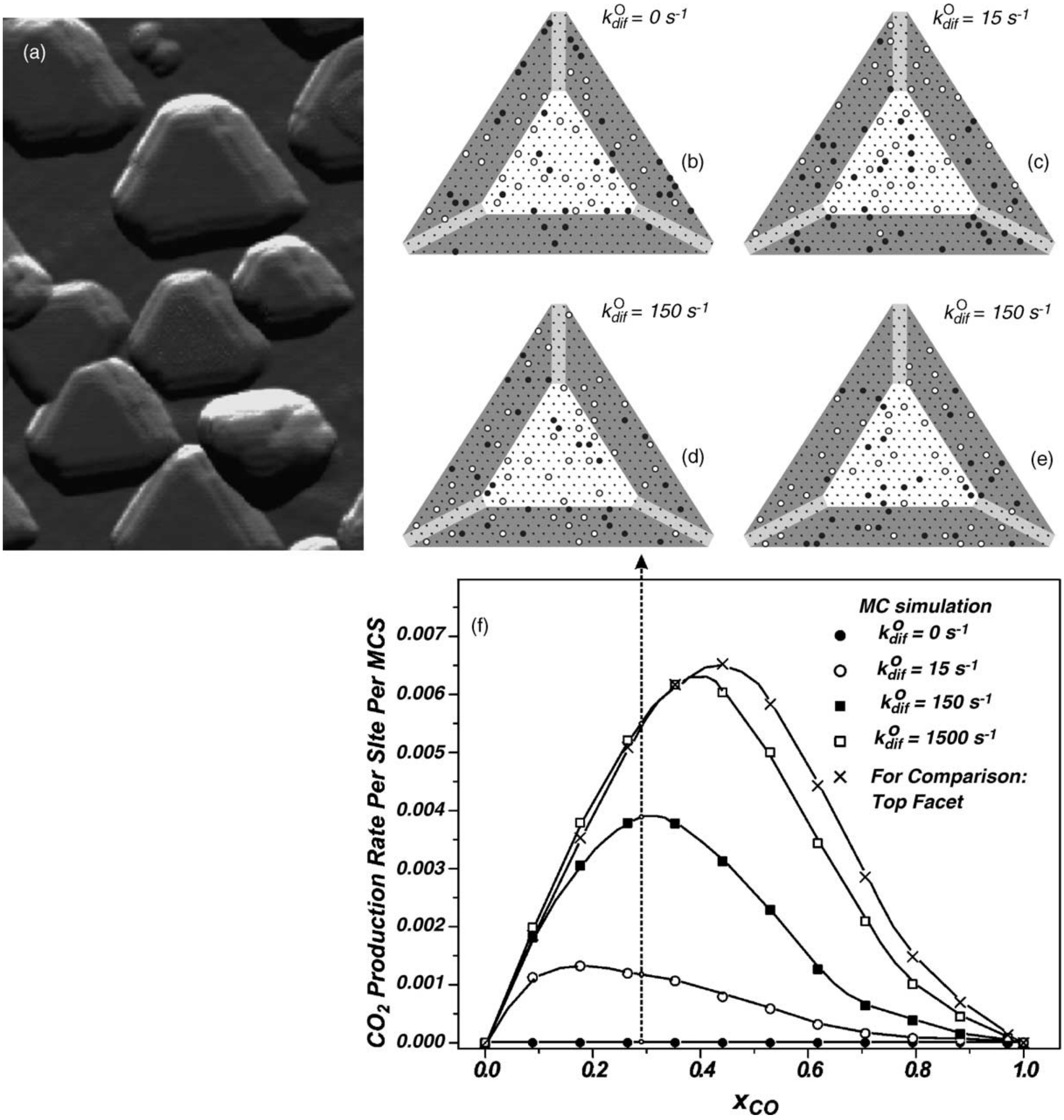

Fig. 34. (a) STM image (35 nm × 25 nm) of the alumina supported Pd particles; (b–e) snapshots of a catalyst particle in a Monte-Carlo model under steady-state reaction conditions with no oxygen adsorption on the shaded side (bottom) facet for different rates of oxygen surface diffusion ($x_{CO} = 0.29$). Oxygen atoms and CO molecules are indicated by open and filled circles, respectively; (f) steady-state reaction rate on the shaded facet at different rates of oxygen diffusion ($T_{Sample} = 465$ K). For comparison, the reaction rate on the top (central) facet at high O and CO mobility is added, from [229].

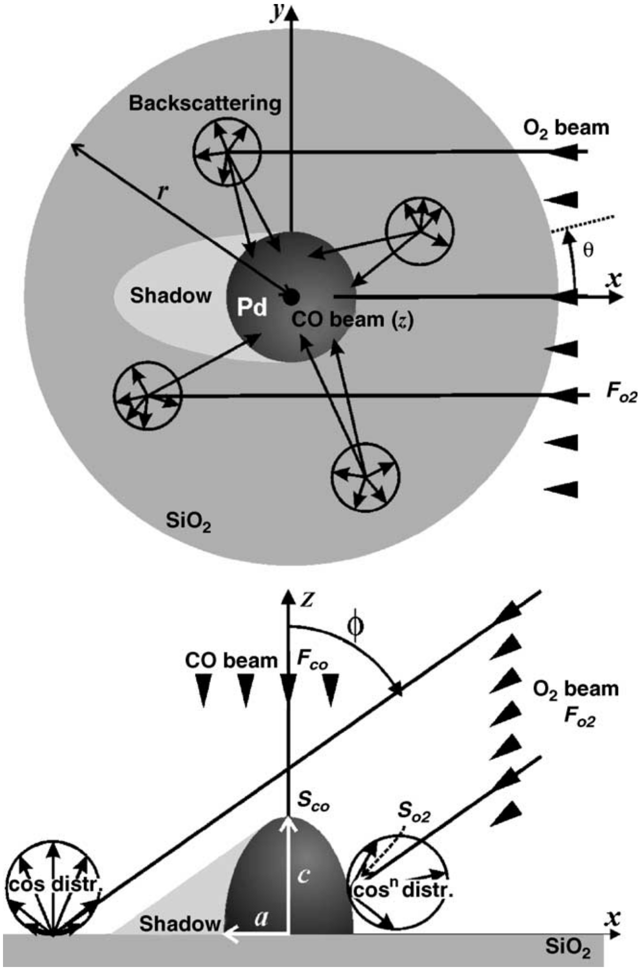

Fig. 35. Diffusion reaction model used in the microkinetic simulations: the Pd particle is represented by a half prolate spheroid, sitting on a large planar support disc. The CO flux is incident along the surface normal and the O_2 beam is tilted with respect to the surface normal, thus creating an area where the particle and the support receive no direct flux from the O_2 beam. Backscattering of the reactants and products from the support is also included in the model, from [315].

distribution. With respect to the desorbing CO_2, backscattering effects from the support have to be taken into account in analogy to the support backscattering effects for the reactants.

Typical results obtained from the model are shown in Fig. 36 (from [315]). The oxygen coverage profiles and the angular distribution of desorbing CO_2 is displayed as a function of the activation energy for surface diffusion of oxygen under both CO-rich and O-rich reaction conditions. Focusing on the θ_O profiles first, it is seen that for low diffusion activation barriers $E_{diff,O}$, the oxygen distribution is symmetric, both under CO-rich and O-rich conditions. This indicates an equilibration of θ_O over the particle surface, independent of the reaction conditions. As a consequence, the CO_2 distributions are symmetric and independent of x_{CO}. With increasing $E_{diff,O}$, first the θ_O profile under CO-rich conditions becomes asymmetric, before the asymmetry appears in θ_O under O-rich conditions as well. In the limit of slow oxygen diffusion, both θ_O profiles finally become strongly asymmetric. The difference between the behavior under CO-rich and

O-rich conditions is the result of the differences in the oxygen residence time typically increasing by one to three orders of magnitude upon transition between the regimes. A comparison with the experimental results yields an estimate for the activation energy for the oxygen diffusion under reaction conditions of $55 \pm 10\,\mathrm{kJ\,mol^{-1}}$, consistent with recent density functional theory (DFT) calculations by Honkala and Laasonen, who derived an activation barrier of $54\,\mathrm{kJ\,mol^{-1}}$ on Pd(1 1 1) [512].

Nonetheless, such comparisons should be treated with care as the present measurements correspond to a surface under reaction conditions, i.e. at high oxygen or CO coverage, and consequently, diffusion activation energies are expected to be substantially modified by adsorbate interactions. In addition, it has to be taken into account that on the metal nanoparticle there might be significant contributions to the effective diffusion rates from particle specific and irregular sites such as, e.g. step, edges and defects.

6.4. Kinetic bistabilities and coverage fluctuations

In addition to the surface diffusion and communication effects addressed in the previous section there are other phenomena, which can lead to modification of the chemical kinetics on small supported particles, without a direct modification of the adsorption properties. One of these effects are coverage fluctuations occurring in small confined reaction systems. As the relative amplitude of the internal noise in a confined system scales with $N^{-1/2}$ (N being the number of molecules involved, i.e. the system size), a strong influence is expected on the length scale of a typical catalyst particle. Due to their fundamental importance, fluctuations have received extensive theoretical attention (see, e.g. [513]). In several theoretical papers, an influence of noise effects on the catalytic activity were predicted, including early work by Fichthorn et al. [37] and later by other groups [39,514,515]. To date, however, there is little experimental evidence for a fluctuation induced contributions to the reaction rates, except from field electron microscopy/field ion microscopy (FEM/FIM) studies [38,516–519] on catalytically active field-emitter tips. This shows that the experimental identification of noise induced effects in the global reaction kinetics of a macroscopic system is a rather difficult problem.

6.4.1. Experimental results

Recently, the influence of coverage fluctuations on the global CO oxidation kinetics was studied by performing transient and steady-state reaction rate measurements using MB methods on different types of supported Pd model catalysts [239]. For this purpose, the appearance of kinetic bistabilities for the CO oxidation on transition metal surfaces was utilized. The term bistability describes the existence of two kinetic states for a given set of reaction conditions, which are stable with respect to small perturbations. Such bistable behavior is observed for several reaction systems on various single crystal surfaces (see, e.g. [520] and references therein). For the case of CO oxidation, the effect arises as a result of the different influence of oxygen on the adsorption of CO and vice versa and is limited to a well-defined x_{CO} window (the so-called bistability window) near the so-called ‘kinetic phase transition’ between the CO-rich and the O-rich regime (see, e.g. [483] for an introduction). It is noteworthy that coupling of this type of kinetics to surface diffusion opens up the possibility for the formation of chemical waves (see, e.g. [521]). Transitions from one kinetic regime to the other are actually initiated by the nucleation and propagation of such waves [483,521] and the corresponding phenomena are well-understood both theoretically and experimentally (see, e.g. [483,520]).

For the investigation of the bistability behavior, experiments were performed both on $Pd/Al_2O_3/NiAl(1\,1\,0)$ model catalysts prepared by PVD and on $Pd/SiO_2/Si(1\,0\,0)$ model catalysts prepared by

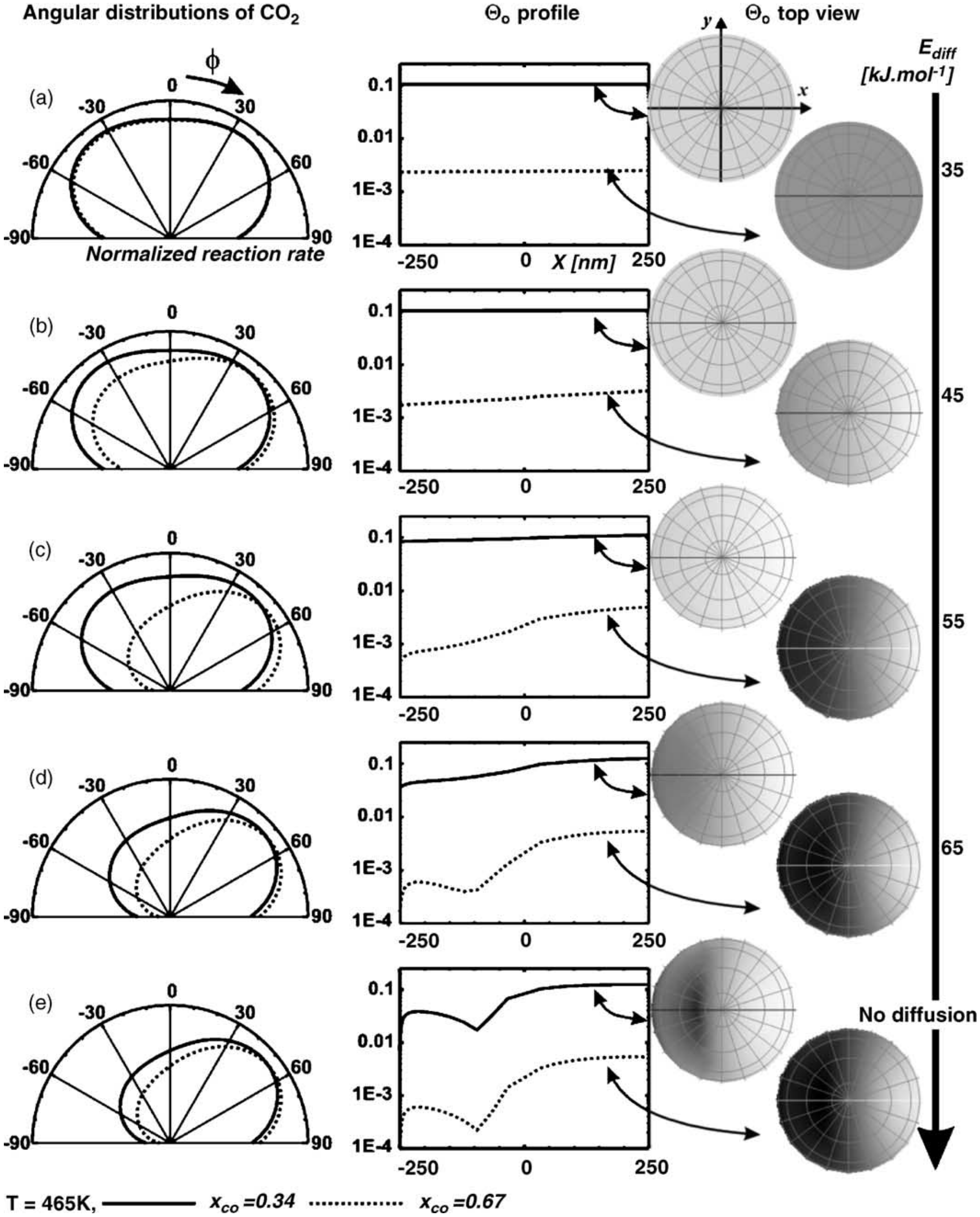

Fig. 36. Simulation of the influence of the oxygen diffusion barrier on the oxygen distribution on the catalyst particles during CO oxidation under steady-state conditions and on the angular distribution of desorbing CO$_2$ (solid lines: O-rich conditions, dashed lines: CO-rich conditions), from [315].

EBL, in order to cover a large range of particle sizes. Typical transient and steady-state kinetic measurements are displayed in Fig. 37. As in previous experiments, a combination of two molecular beams (CO and O_2) superimposed on the catalyst surface were employed.

Focusing on the reaction kinetics on large Pd particles first, the typical features of the CO oxidation system were observed, including an O-rich and a CO-rich reaction regime (see Section 6.2). The existence of a kinetic bistability was shown by superimposing two transient experiments starting from an CO and from oxygen pre-covered surfaces, respectively, for every set of reaction conditions. A well-defined bistability window could be identified as a function of x_{CO} and the surface temperature, similar to the experimentally observed and theoretically expected behavior for typical single crystal surfaces (see, e.g. [483,522]).

Proceeding to smaller particle sizes, it was found, however, that in the expected bistability window both kinetic states, oxygen-rich and CO-rich, become increasingly unstable and a single global reaction rate is established, independent of staring conditions. The time-scale on which the common state is reached decreases with decreasing particle size. On the basis of microkinetic simulations it was concluded that the effect is due to fluctuation induced transitions between the kinetic states, leading to a dynamic equilibrium between particles in both states (see Section 6.4.2). On account of these experiments, it was suggested that the experimentally observable bistability effects on macroscopic surfaces should in general vanish for sufficiently small particles. The transition to a globally monostable kinetics should occur in a continuous fashion via a decreasing lifetime of the global kinetic states with decreasing particle size.

6.4.2. Microkinetic simulations

Typically, there are two effects which may have an influence on the bistability behavior: (i) the influence of defect sites and (ii) coverage fluctuation as a result of the small system size. The appearance of kinetic bistabilities can in general be described on the basis of a kinetic rate equation approach with in a MF model [483]. Within the heterogeneous MF models of the type discussed in Section 6.2.2.2, the influence of defects can in principle also be described. In order to account for fluctuation induced effects, stochastic noise induced by the limited particle size has to be taken into account as well (see, e.g. [513]). For the case of catalytic reactions, such effects have been modeled applying MC and other methods (see, e.g. [20,37–39,515,519,523,524,239,525,526] and references therein).

Considering the role of defect sites, it is expected that the density of such defects, e.g. edges, steps, corners, interface sites or other irregularities, increases with decreasing particle size. The differences in chemisorption energy at such sites in comparison with the regular sites on particle facets is expected to result in an increased coverage dependence of the adsorption energies. Indeed, such effects have been experimentally verified for CO adsorption and oxidation on the model catalyst utilized in this work [46,71]. With respect to the bistability behavior, Zhdanov and Kasemo have shown that an increasing coverage dependence of the CO desorption energy leads to a decreasing size of the bistability region [483]. As a result, the high defect density on small particles could generate a coverage dependence of the CO adsorption energy, which in turn may potentially lead to a quenching of the kinetic bistability.

In order to pinpoint the origin of the experimentally observed size dependent bistability behavior, microkinetic simulations were performed on the basis of a heterogeneous MF model based on KREs described in Section 6.2.2.2 [239]. Toward this aim, the model was fitted to reproduce the reactivity data for the largest Pd particles as a function of x_{CO} and surface temperature. In previous work, it was shown

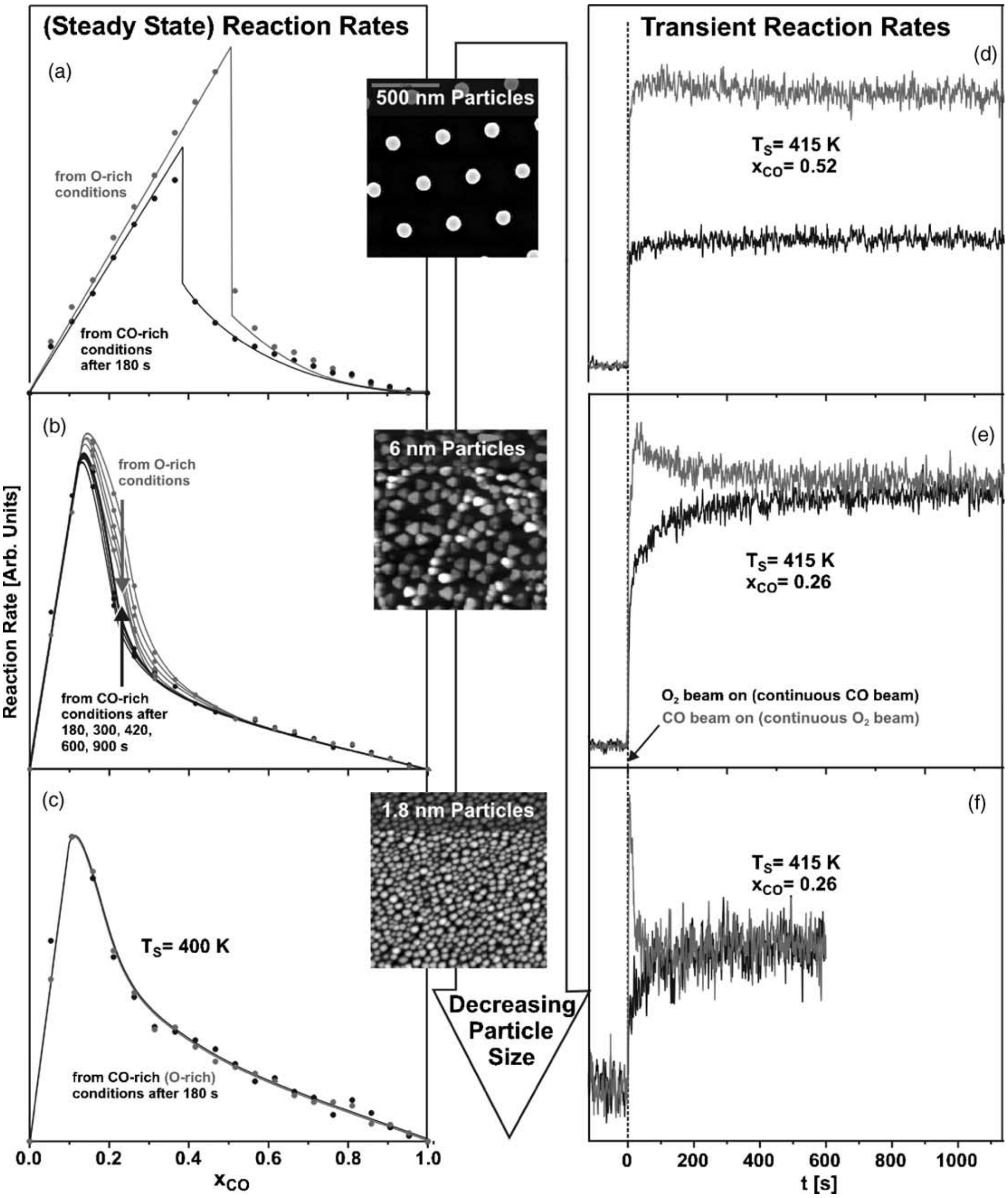

Fig. 37. Particle size dependent bistability and hysteresis: (a and d) on large Pd particles (500 nm particle size, Pd/SiO_2/ Si(1 0 0), EBL) the CO oxidation shows a perfectly stable bistability behavior; (b and e) on smaller particles (6 nm particle size, Pd/Al_2O_3/NiAl(1 1 0)) a slow transition toward a single global state is observed in the transition region between the CO-rich and the oxygen-rich reaction regimes; (c and f) for very small particles (1.8 nm particle size, Pd/Al_2O_3/NiAl(1 1 0)), the globally monostable kinetics is rapidly established under all conditions (total local pressure: 10^{-4} Pa), from [239]).

that the reactivity changes observed in the transient and steady-state behavior on small Pd particles were mainly related to the presence of defect sites, which are characterized by a weaker chemisorption of CO ([71,225], see Section 6.2). In order to explore the influence of these sites on the bistability, the transient and steady-state kinetics was simulated as a function of the fraction of weakly adsorbing CO sites [239]. It was found that the bistability window shows the expected decrease in size with increasing defect density, but the changes in the transient behavior were not compatible with the experimental observations.

The second contribution to be considered is the influence of coverage fluctuations. In the limit of negligible surface diffusion via the oxide support, the particles act like isolated nanoreactors. As a result, the amplitude of coverage fluctuations increases with decreasing particle size leading to an increasing probability of fluctuation induced transitions between the two kinetic regimes. The effect can be simulated on the basis of a simple stochastic MF model, describing the CO oxidation by a Markovian process based on a master equation (ME) approach ([239], compare [519,524]). Note that according to the results discussed in Section 6.3, O and CO diffusion is fast on the time-scale of the reaction for the smaller particles, justifying the application of a MF model in contrast to previous work on other systems [519,524]. It is noteworthy that the parameters for the ME model can be derived from the fitted KRE description in the large particle limit. Similarly as for the KRE model, the ME approach provides a quantitative description of the experimental results, but in addition the latter takes into account the role of fluctuations in a confined system (see Fig. 38, from [239]). In contrast to the KRE model, in which the oxygen-rich and CO-rich steady-states are represented by a single point in coverage space, the stochastic ME model describes the same situation as a probability distribution of finite width. With increasing particle size, the widths of the probability maxima become more narrow and the reaction rates asymptotically approach the KRE limit. Under these conditions no transitions between the CO and the oxygen-rich states occur. With decreasing particle size the width of the probability distribution increases and, as a result the enhanced probability of finding the system in the transition region between both regimes, spontaneous transitions between both kinetic states become more frequent. In order to obtain a direct comparison to the experiment, the global transient response can be simulated by propagating the probability distributions starting from fully CO and oxygen saturated surfaces, respectively. The results indicate that on the basis of a defect-free surface model the fluctuation induced transitions are considerably slower than observed experimentally. A near quantitative agreement could be obtained, however, by taking into account the combined effect of defects and fluctuations via a modification of the adsorption, desorption and reaction probabilities according to the heterogeneous KRE model. The effect can be traced back to a defect induced modification of the steady-states in both regimes, leading to an enhanced transition probability.

It follows that the transition to the globally monostable kinetics with decreasing particle size is the result of coverage fluctuations which occur in confined systems in the nanometer size range and induce transitions between the two stable kinetic states. In addition, defect sites on the nanoparticle surface leading to small modifications of the adsorption properties, can play a crucial role for the time-scale on which these transitions occur.

A final remark concerns the experiments and simulations on the particles prepared by EBL: here, it should be noticed that the local ratio of the CO and O_2 flux, i.e. the local x_{CO} value, impinging on a surface element of the Pd particles varies drastically, depending on the exact position on the particle. As a consequence, it is not clear to what extent the global transient and steady-state reaction kinetics on the system (including the bistability behavior) can be described on the basis of a standard homogeneous

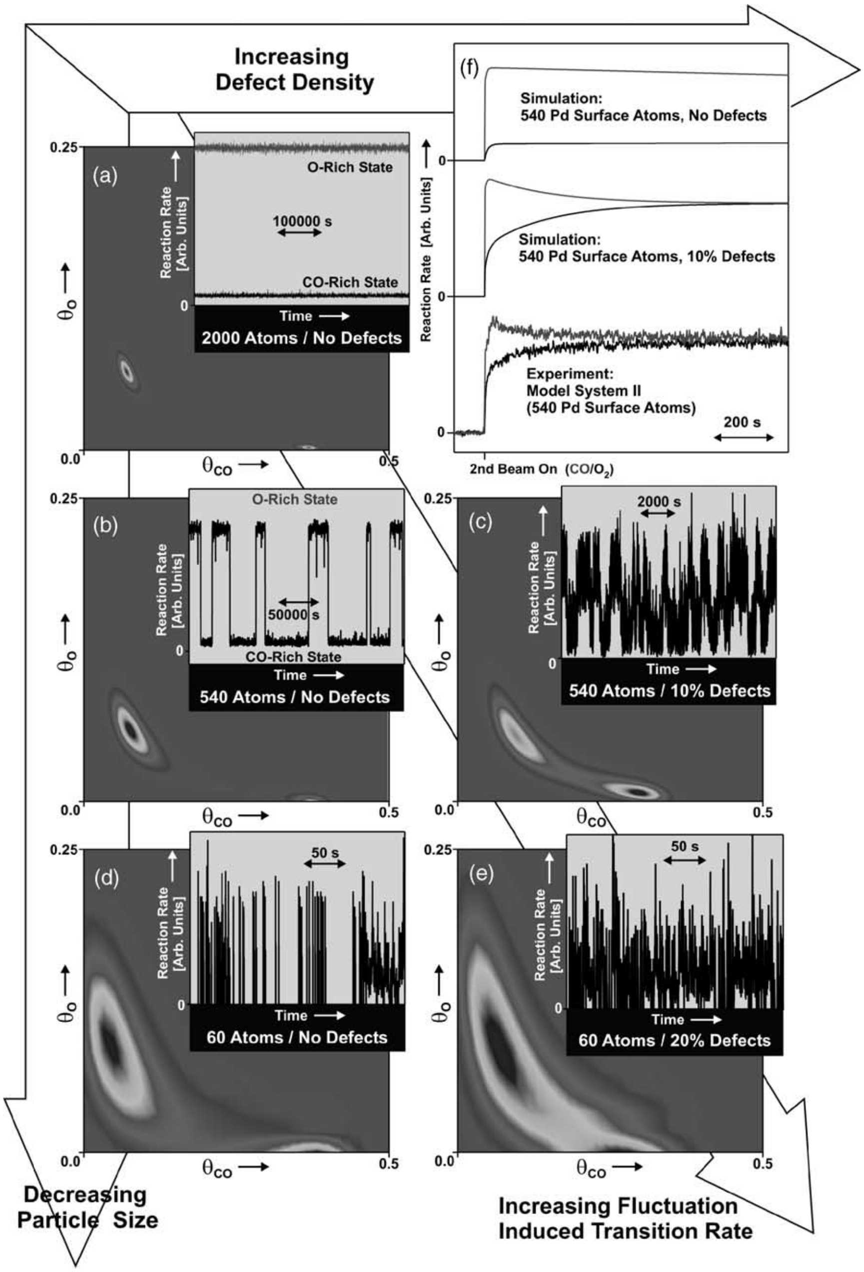

Fig. 38. Stochastic mean field simulations illustrating the combined effect of limited particle size and surface defects on the kinetic bistability: (a, b, d) due to the increasing amplitude of fluctuations the width of the probability distributions in coverage space increases with decreasing particle size and spontaneous transition between both reaction regimes become more frequent (insets show the reaction rate on an individual particle). For an ensemble of particles, this results in a dynamic equilibrium being established between both reactive states; (c and e) the transition rate further increases upon modification of the adsorption and reaction behavior due to defect sites (see insets); (f) by integrating over an ensemble of particles, the transient response predicted by the stochastic model can be compared with the experimental data, from [239].

surface model. Therefore, the MF diffusion–reaction model discussed in Section 6.3 was applied in order to investigate the global reaction behavior of the EBL model catalyst under monostable and bistable conditions [240]. In Fig. 39, corresponding data is shown for the transient behavior, both starting from oxygen and CO pre-covered surfaces. The transient CO_2 response in the O-rich (no reaction rate maximum) and CO-rich reaction regime (transient reaction rate maximum), starting from oxygen pre-coverage has already been discussed in Section 6.2. Starting from the CO pre-covered surface instead, the reverse behavior is observed with a transient reaction rate maximum under O-rich conditions and no maximum under CO-rich conditions. The slow response for the CO pre-covered case under all conditions is a result of the inhibition of O_2 dissociative adsorption at high CO coverage. Close to the bistability region, the second kinetic state becomes successively stable, leading to a slow switching behavior in which the reaction system prevails in the unstable state for a certain time before it suddenly crosses over to the stable state. In the bistability region both state finally are stable for infinite time, at least on an ideal and infinite surface, i.e. without pertubations or defects. These different types of transients have also been observed experimentally in a recent study [240].

It is noteworthy that in spite of the strong variations in the local x_{CO} value on the particle surface and in spite of the restricted oxygen mobility, a well-defined transient switching behavior is expected. Also, the particles show a steady-state and bistability behavior, which is only slightly modified in comparison to the homogeneous MF case. A corresponding comparison is shown in Fig. 40, displaying the steady-state rates for the MF reaction–diffusion model and a hypothetical homogeneous MF model, using average CO and O_2 fluxes. Minor shifts are observed, which are the result of the non-homogeneous O coverage in the case of the MF diffusion–reaction model. The similarity of both models with respect to their steady-state and transient behavior was attributed to the fast CO diffusion over the particle surface. Even if the oxygen diffusion is slow on the time-scale of the surface reaction (i.e. on large particles and under O-rich reaction conditions, see Section 6.3), CO equilibration over the particle surface leads to a synchronization of the transition between the two kinetic regimes, in agreement with the experimentally observed steady-state and transient behavior [240].

7. Methanol decomposition and oxidation

7.1. Methanol decomposition on Pd surfaces—general remarks

In comparison to the CO oxidation, which represents one of the most simple and best studied model reactions in surface science, the experimental work performed on the kinetics of methanol decomposition and oxidation is rather limited. In addition, the latter reaction system is substantially more complex. On the microscopic level, the system contains a large number of elementary steps, several possible intermediates and different competing reaction pathways. Many open questions remain with respect to both the mechanism and the kinetics of the reaction. From an experimental point of view, it is important to note that the methanol oxidation system is closely related to CO oxidation. As a result, kinetic information on several elementary steps can be derived from studies of the CO oxidation reaction, which subsequently can be used in descriptions of the methanol oxidation system.

The adsorption and reaction of methanol on Pd surfaces has attracted considerable attention due to the activity of Pd catalysts with respect to processes such as synthesis, e.g. [14,15], or the partial and total oxidation of alcohols, e.g. [527–529]. Indications for pronounced support [530–532], particle size

(a) **O precovered**

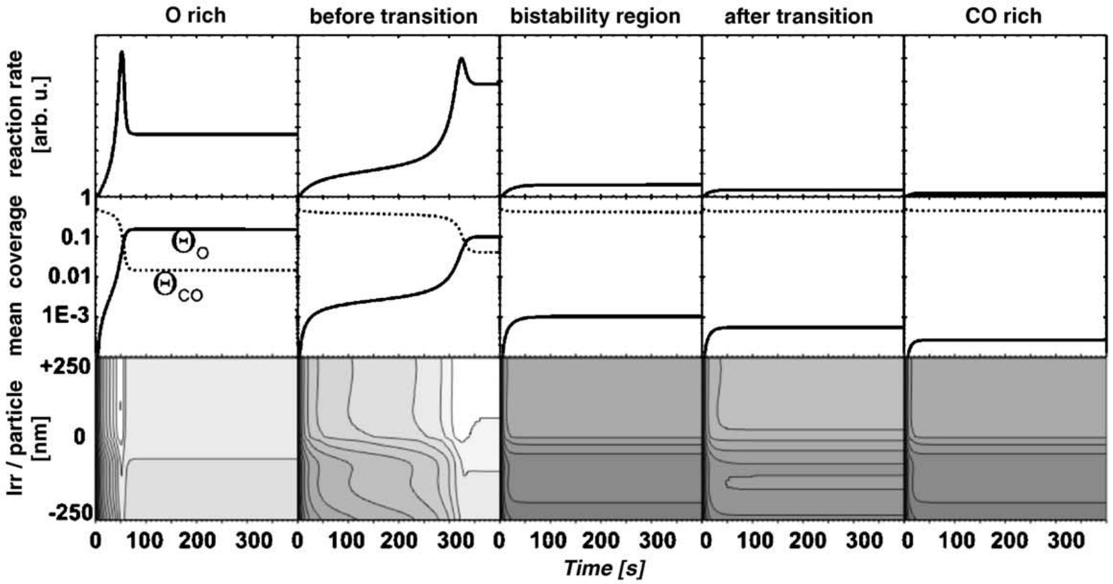

(b) **CO precovered**

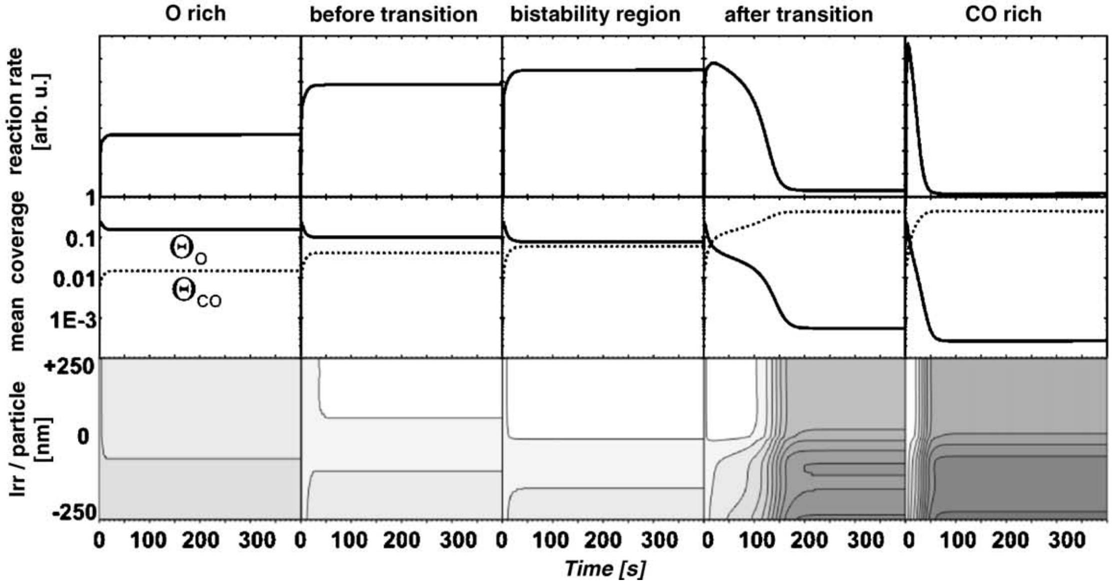

Fig. 39. Transient CO oxidation rates on a supported 500 nm Pd particle, simulated by the reaction diffusion model according to Fig. 35, starting either from: (a) a CO pre-covered or (b) an O pre-covered surface. The temporal evolution of the global reaction rate (top rows) and the global CO and O coverage are shown (middle rows). The bottom rows show a profile of the local reaction rate over the particle as a function of time. Typical transients in the O-rich regime, in the CO-rich regime, inside the bistability window and very close to the bistability region are shown ($T = 400$ K, total local pressure: 10^{-4} Pa, $E_{\text{diff,O}} = 55$ kJ mol^{-1}), from [240].

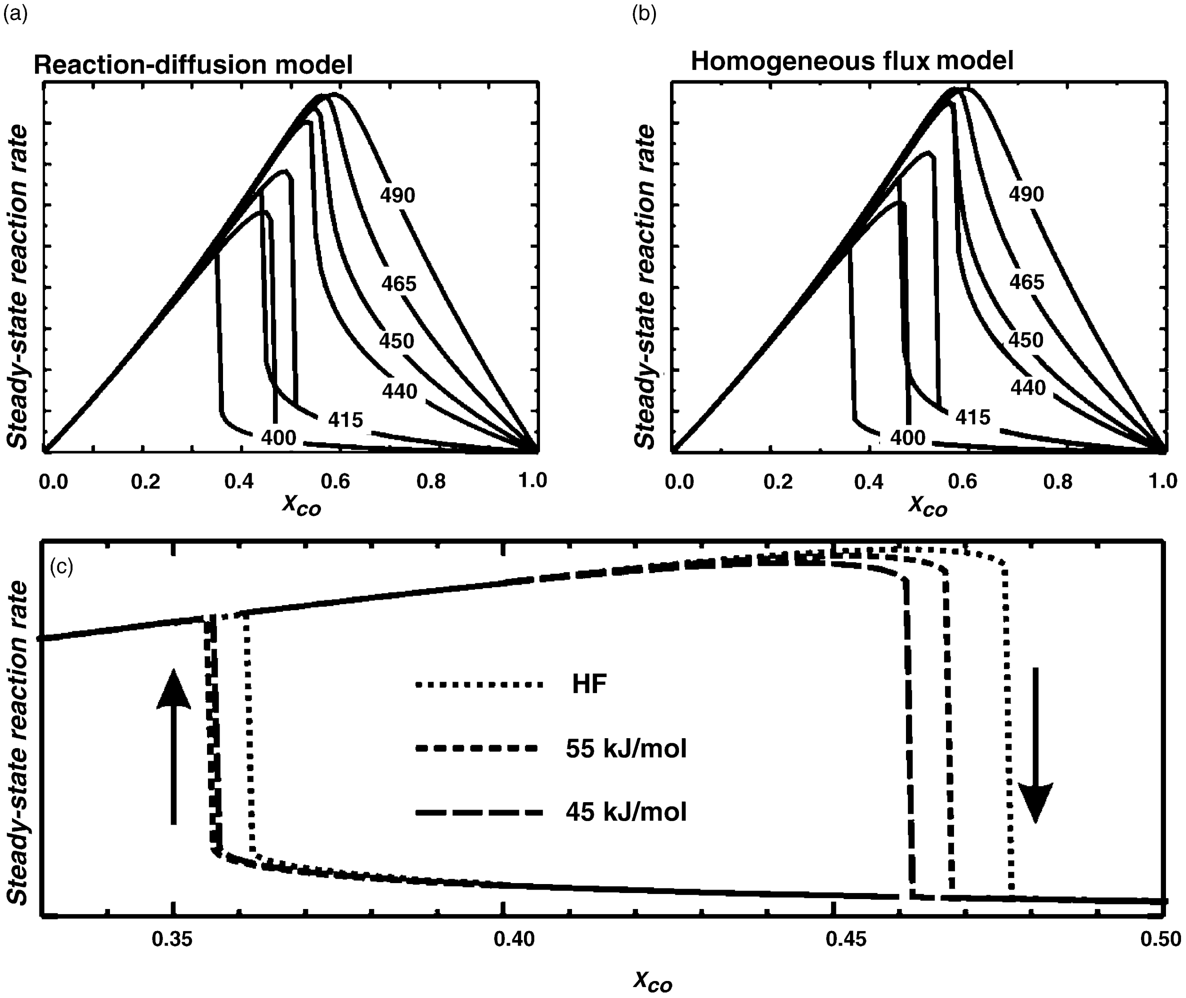

Fig. 40. Comparison of the global steady-state CO oxidation rates under conditions of bistability: (a) derived via a reaction diffusion (RD) model according to Fig. 35 ($E_{\mathrm{diff,O}} = 45$ and 55 kJ mol^{-1}); (b) derived via a mean field model assuming a homogeneous flux over the particle surface (HF); (c) close-up of the bistability window ($T = 400$ K, total local pressure: 10^{-4} Pa), from [240].

[532,533] and promoter effects [16,534,535] (see also [15]) have been reported. The microscopic origins of these effects are still unclear, however.

Motivated by these observations, some studies have been performed under UHV conditions on single crystal surfaces [409,413,472–475,536–546], Pd thin films [547] and Pd alloys [406,411]. Various methods were employed, including, e.g. TPD, secondary ion mass spectrometry (SIMS), molecular beam experiments, HR-EELS, IRAS and XPS. In addition, the synthesis and decomposition of methanol on Pd surfaces was studied theoretically [413,548–550]. Recently, the surface science work on the mechanism of methanol decomposition and oxidation on transition metal surfaces has been reviewed by Mavrikakis and Barteau [551]. A simplified reaction scheme is displayed in Fig. 41. In general, it is found that the dominant reaction pathway involves the dehydrogenation of methanol, yielding CO as the final product.

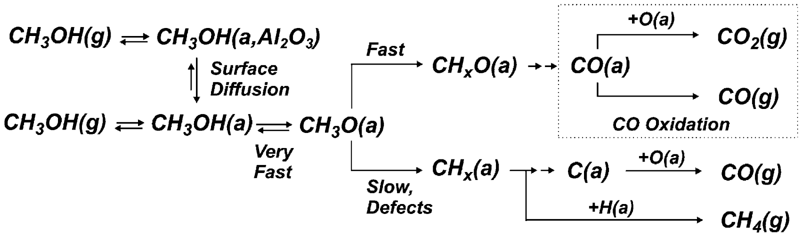

Fig. 41. Schematic reaction diagram for methanol decomposition and oxidation on a supported Pd catalyst, from [233].

The first intermediate is a methoxy (CH_3O) species, which has been experimentally observed by several groups [473,474,538–541]. As intermediates of dehydrogenation, formaldehyde (CH_2O) and formyl (CHO) have been proposed [472,473,542].

Until now, some controversy remains with respect to the role of C–O bond scission as a pathway competing with dehydrogenation. C–O bond activation on a Pd single crystal surface was first reported by Levis et al. [544,545] and later observed by several other groups as well [538,540–542]. The process leads to the formation of surface carbon and CH_x species, which may be stable up to elevated temperatures [541]. In order to analyze the role of C–O bond scission more closely, Guo et al. [543] performed isotopic scrambling experiments. No isotope mixing was found in the desorption of CO produced from dehydrogenation, clearly showing that dehydrogenation proceeds without C–O bond scission. In all cases, the reaction probability for C–O bond scission was observed to be small and it has been speculated that the process may be related to the presence of specific defect sites [409,541,551]. A recent study emphasized the role of intermolecular interactions via H bonds for the C–O bond activation [413].

The influence of oxygen on the adsorption and decomposition of methanol [409,540,547,552], as well as on formaldehyde as a possible intermediate [553] has been studied on Pd single crystals and films. Pronounced differences in the product spectrum have been observed upon oxygen pre-coverage [409,547,552]. The effects have been related to the formation of new intermediates such as formate (HCO_2) [551,552] or the modified stability of intermediates (specifically in the case of CH_2O species [551,553,554]).

In spite of the large amount of single crystals data, few MB studies have been conducted on supported Pd particles so far [230–233]. In the following, a summary of this work is given, mainly focusing on the mechanism of the reaction (Section 7.2), the kinetics of dehydrogenation and total oxidation (Section 7.3), the identification of specific reaction sites (Section 7.4), and the microkinetic modeling of the kinetics (Section 7.4).

7.2. Mechanism

Mechanistic and qualitative kinetic aspects of methanol adsorption, desorption and decomposition on $Pd/Al_2O_3/NiAl(1\,1\,0)$ model catalysts were recently addressed in a combined TPD, IRAS and MB study by Schauermann et al. [230].

In a first step, adsorption and desorption of methanol on the clean Al_2O_3 model support was investigated by TPD and IRAS (Fig. 42). The TPD (Fig. 42a) spectra showed two different desorption features of CH_3OH in the submonolayer regime (170–230 K) and a multilayer desorption peak appears at higher coverage (140–150 K). From the corresponding IR spectra (see Fig. 42b), the submonolayer species could be identified as molecular methanol, in accordance with previous studies of methanol adsorption on alumina surfaces [555,556]. From the TPD data, the desorption energy was estimated as 45–50 kJ mol^{-1} [230]. In IRAS, the existence of two adsorption states is reflected by coverage dependent intensity changes of CH stretching frequency modes, which differ in orientation of the dynamic dipole with respect to the molecular CO axis (Fig. 42c, assignment of the absorption bands: compare [557] and references therein). The behavior is considered as an indication of a pronounced change in molecular orientation as a function of coverage. Similar coverage dependent orientation effects have been observed for methanol adsorption on other oxide surfaces [558]. The low coverage adsorption species was tentatively assigned to adsorption at oxide defect sites.

In the second step, adsorption on Pd/Al_2O_3/NiAl(1 1 0) was studied using in situ IRAS and TPD [230]. From vibrational spectroscopy, it was concluded that the high mobility of molecularly adsorbed methanol on the support and the differences in adsorption energy lead to diffusion of adsorbed methanol to the Pd particles and formation of a mixed overlayer of methoxy and molecular methanol at 100 K. At higher temperature, formation of methoxy is followed either by C–H bond scission (dehydrogenation) or by activation of the C–O bond. Dehydrogenation was observed to be the dominating reaction pathway in all cases.

As shown in a series of TPD experiments (Fig. 42e), the dehydrogenation probability of adsorbed methanol sensitively depends on coverage. At low coverage, molecular desorption of methanol from Pd/Al_2O_3/NiAl is strongly suppressed, i.e. the dehydrogenation probability is near unity, whereas at higher coverage desorption competes more efficiently with dehydrogenation.

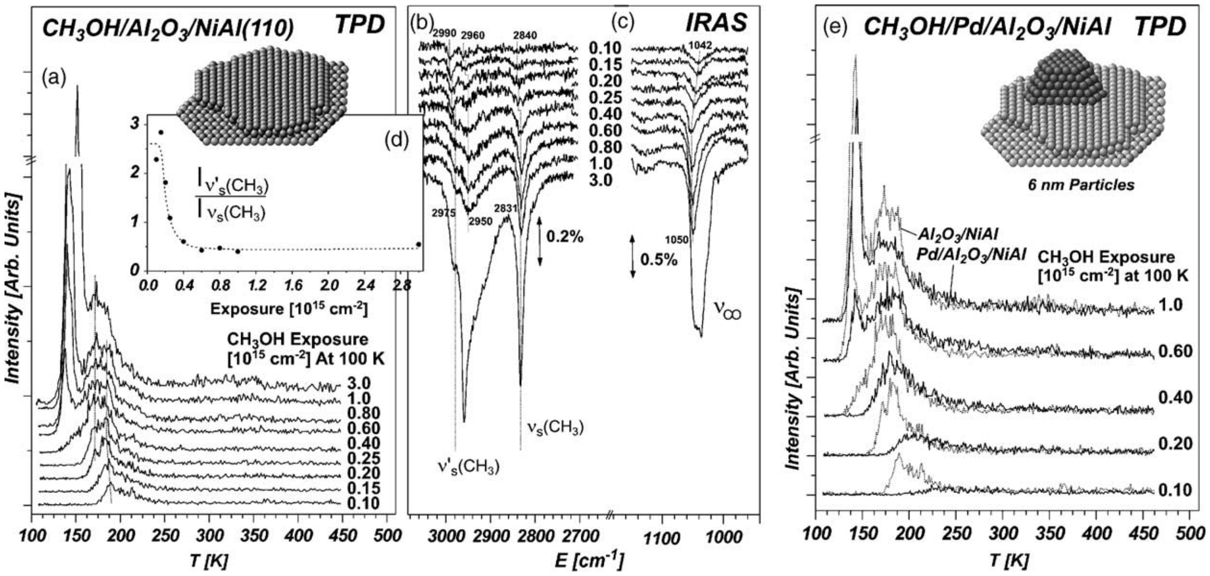

Fig. 42. Methanol adsorption on the Al_2O_3/NiAl(1 1 0) model support (100 K): (a) TPD spectra as a function of methanol exposure; (b) IR spectra of the CH stretching frequency region; (c) IR spectra of the CO stretching frequency region; (d) intensity ratio of the $\nu'(CH_3)$ and $\nu(CH_3)$ bands for adsorbed methanol as a function of coverage; (e) comparison of TPD spectra for methanol adsorbed on a Pd/Al_2O_3/NiAl model catalyst (solid lines) and on the pristine Al_2O_3/NiAl model support (dotted lines), from [230].

These results are corroborated by single crystal studies on Pd(1 1 1) [538] and Pd(1 0 0) [474,475], where a qualitatively similar desorption and reaction behavior was observed. In these studies, the low temperature part of the submonolayer desorption was assigned to a molecular species, whereas desorption at higher temperatures was attributed to a recombinative processes involving methoxy. However, some discrepancies with respect to the single crystal studies were reported regarding the dehydrogenation probability of the methoxy species [230].

In addition to the experiments involving clean Pd/alumina model catalysts, adsorption and desorption of methanol from oxygen and CO pre-covered surfaces was investigated. Briefly, CO was found to suppress methanol adsorption on the particles, whereas pre-adsorbed oxygen, did not suppress methanol adsorption, but reduced the dissociation probability [230].

In order to study dehydrogenation as a function of surface temperature, isotopic switching experiments using CH_3OH and a CD_3OD, respectively, were combined with in situ IRAS under steady-state conditions (see Fig. 43) [230]. In the limit of low surface temperature (160 K), the spectra show several intense features, which were attributed to different CH and CD stretching modes of molecular methanol (compare, e.g. [557]). In addition, two weak low frequency shoulders could be assigned to methoxy species on the basis of single crystal data [557,559–561] and in accordance with studies on Pd(1 1 1), in which molecularly adsorbed methanol and methoxy were observed to coexist at 170 K [472]. Upon isotope switching from CH_3OH to CD_3OD, all CH absorption bands were found to be replaced by the corresponding CD bands, indicating complete exchange between methanol and methoxy species. It is noteworthy that some differences between the spectra of CH_3OH and CD_3OD can arise from different effects of Fermi resonances between the two molecules. Time-resolved IR spectroscopy studies of the isotopic exchange process revealed a nearly constant intensity ratio between both species during exchange. From this observation, it was concluded that there is a fast equilibrium between the methanol and methoxy species. As possible mechanisms of this exchange process, direct hydrogen transfer between molecular methanol and methoxy or hydrogen transfer via the surface can be invoked.

With increasing surface temperatures, the steady-state coverage of molecular methanol decreases, whereas the methoxy species is hardly affected (see Fig. 43). At temperatures above 200 K, CO is formed through total dehydrogenation. It should be pointed out that no intermediates other than methoxy could be detected via IRAS, indicating that the lifetime of all other dehydrogenation intermediates is short.

7.3. Dehydrogenation and oxidation under transient and steady-state conditions

After the qualitative considerations on the mechanism, we proceed to a quantitative study of the methanol decomposition and oxidation kinetics on Pd model catalysts. According to the discussion in preceding sections, the main reaction pathway is dehydrogenation to CO without CO bond activation. In the presence of adsorbed oxygen and at sufficiently high surface temperatures, CO is further oxidized to CO_2.

The kinetics was recently studied by MB methods and TR-IRAS, following the same concept as previously applied in the case of CO oxidation (Section 6.2) [233]. An experimental setup involving two beams of variable intensity superimposed on the sample surface was used, one providing CH_3OH and one providing the O_2 (see Fig. 44). The experiments were performed at constant total effective pressure of CH_3OH and O_2, using a modulated CH_3OH and a continuous O_2 beam or vice versa. The rate of CO_2

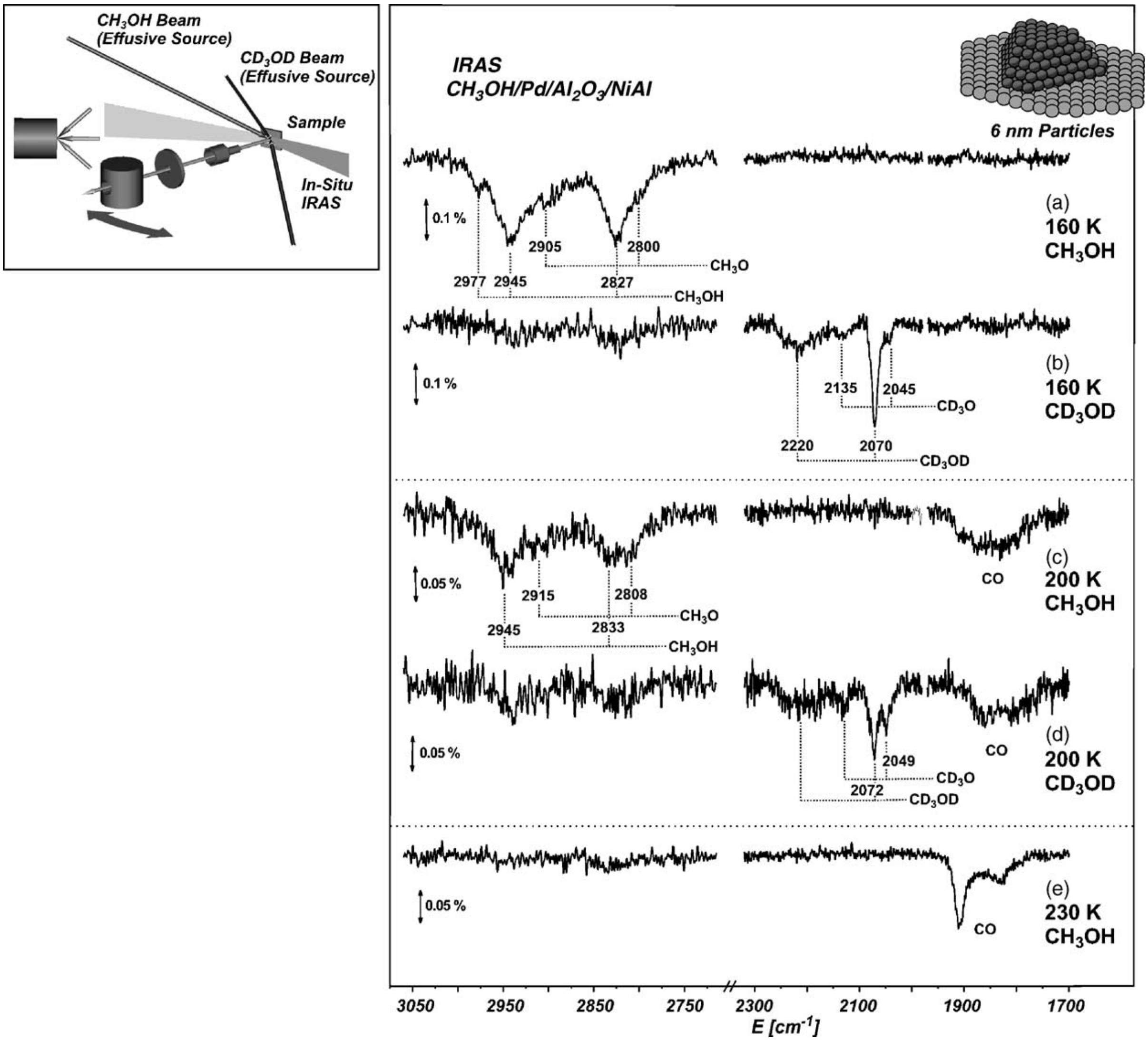

Fig. 43. IR spectra of the CH, CD and CO stretching frequency regions recorded at various temperatures during exposure of a $Pd/Al_2O_3/NiAl$ model catalyst to a beam of CH_3OH and CD_3OD, respectively, from [230].

formation was detected as a function of the fraction of methanol in the total flux impinging on the sample in analogy to the experiments on the CO oxidation (see Section 6.2):

$$x_{\mathrm{MeOH}} = \frac{F_{\mathrm{MeOH}}}{F_{\mathrm{MeOH}} + F_{\mathrm{O_2}}}$$

where F_i is the partial flux of reactant i at the sample position. Under the reaction conditions applied and at surface temperatures exceeding 200 K, adsorbed CO and oxygen are the only surface species present in large concentrations for both reaction systems, CO and methanol oxidation. Thus, variations in the

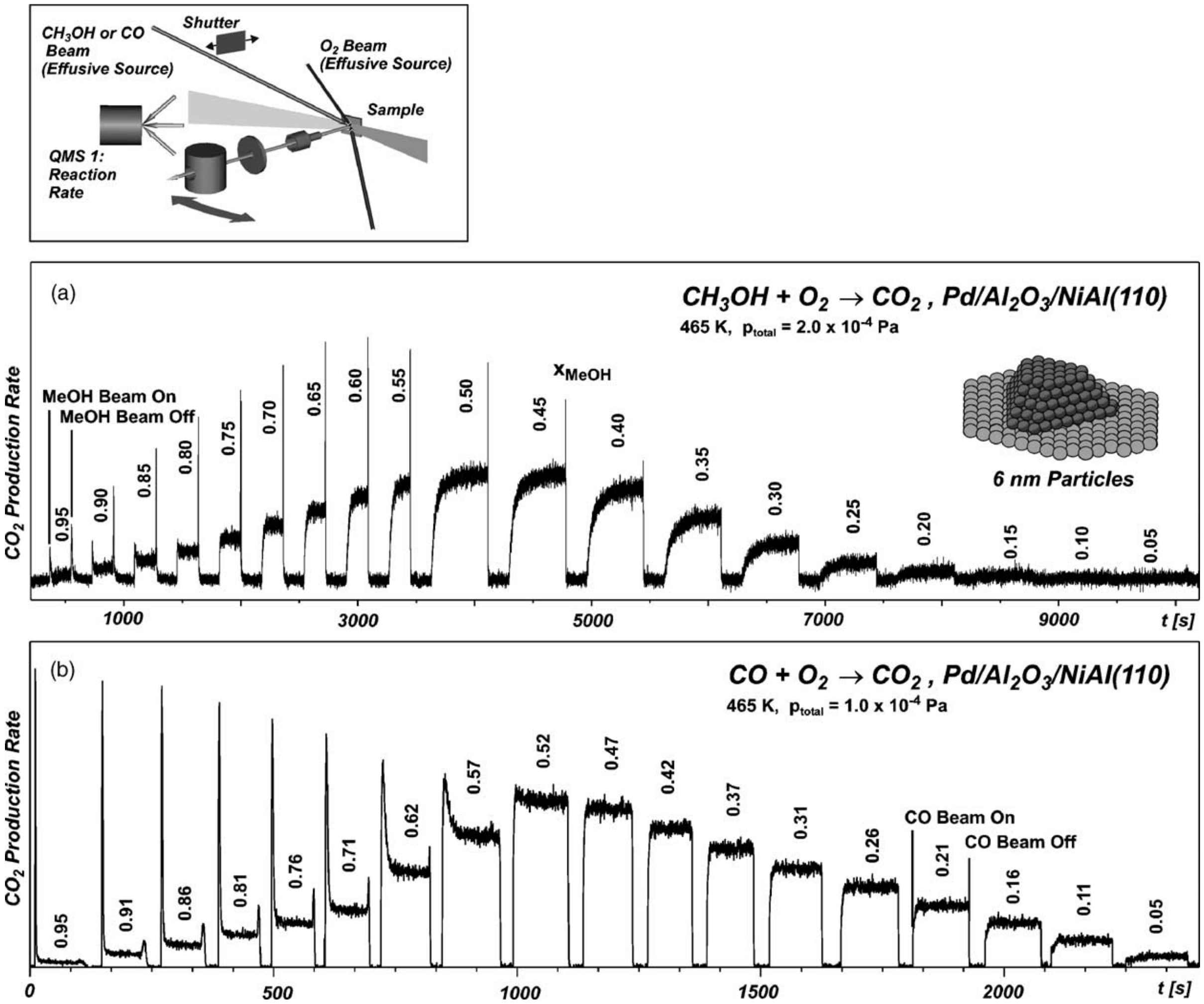

Fig. 44. (a) Transient formation rate of CO_2 during methanol oxidation on a $Pd/Al_2O_3/NiAl$ model catalyst as a function of the fraction of methanol x_{CH_3OH} in the total flux; (b) transient CO oxidation experiment for comparison, from [233].

kinetics of CO_2 formation can be directly attributed to differences in the decomposition kinetics of methanol as compared to the kinetics of CO adsorption.

In analogy to the CO oxidation case, information on both the steady-state rates and the transient kinetics were obtained from this type of experiment. In addition, the experiments were combined with static and time-resolved IRAS in order to obtain information on the CO coverage and sites occupied under reaction conditions (see Figs. 44–46).

A plot of the steady-state CO_2 formation rates as a function of the methanol fraction x_{MeOH} is displayed in Fig. 45a for a series of different reaction temperatures. For comparison, a similar set of experiments for CO oxidation is shown in Fig. 45b. The steady-state behavior for CO oxidation has been discussed in detail in Section 6.2. Briefly, two reaction regimes can be distinguished, denoted as the *O-rich* and the *CO-rich* regime, respectively. Under O-rich conditions ($\theta_O \gg \theta_{CO}$), a linear increase of the reaction rate with increasing CO flux is observed. This linearity reflects the fact that pre-adsorbed oxygen has a minor effect on S_{CO} only. Exceeding a given x_{CO} value, the kinetic transition to the CO-rich regime ($\theta_{CO} \gg \theta_O$) is related to a rapidly dropping reaction rate, indicative of the inhibiting effect of pre-adsorbed CO on the dissociative adsorption of oxygen. With increasing surface temperature, the kinetic transition shifts to larger x_{CO} values, caused by decreasing CO residence times.

The CO data can be directly compared with corresponding data for the case of methanol oxidation, taking into account that the differences in the reaction behaviors arise from the different kinetics of methanol dehydrogenation as compared to CO adsorption only. Similarly to the case of CO, two regimes can be identified for the methanol system: a flux region in which the surface is predominantly covered by oxygen (*O-rich* regime) and a region in which it is mainly covered by CO (*CO-rich* regime) as the product of dehydrogenation. The steady-state plots, however, reveal some characteristic differences between the two cases. The most apparent observation is that the CO_2 production from methanol is strongly suppressed at low x_{MeOH} and that the increase in rate is non-linear with increasing x_{MeOH}. Moreover, the CO poisoning effect is less pronounced when compared to the CO oxidation case and the flux conditions at which the kinetic transition occurs is nearly independent of the surface temperature.

These above-mentioned effects were further explored using static IRAS under reaction conditions (see Fig. 45c and d) [233]. Briefly, the same CO stretching frequency features were observed as for CO oxidation (Section 6.2). Focusing on the integral absorption only, clear differences were found between both reaction systems. In the case of CO oxidation, the CO absorption signal shows a linear increase with increasing x_{CO} under O-rich conditions, together with a sharp step upon transition to the CO-rich regime. For methanol oxidation, on the other hand, the absorption signal is very weak in the O-rich regime with a strongly non-linear dependence on x_{CO} in the transition region and, finally, increases continuously at larger methanol flux, without showing the pronounced step-like behavior of the CO oxidation system. Qualitatively, this behavior reflects the inhibiting effect of pre-adsorbed oxygen on the methanol dehydrogenation already observed in the reaction rate measurements. At the molecular level, several contributions were invoked as a possible origin of this inhibition effect, such as, e.g. (i) simple site blocking for the dissociation process, (ii) variations of the activation barrier for dissociation and desorption induced by co-adsorbed oxygen and (iii) the formation of islands of chemisorbed oxygen with specific reaction properties or, at higher temperatures, even the formation of subsurface oxygen species or surface oxides. With respect to the first point, previous adsorption measurements have shown that pre-adsorbed oxygen does not prevent methanol adsorption and methoxy formation on the Pd particles at low temperature, but reduces the dehydrogenation probability [230]. Similar inhibiting effects have been found for methanol decomposition on other surfaces, such as, e.g. Mo(1 1 0) [562] or Cu(1 1 0) [408]. In the latter case, it was shown that oxygen forms islands with only very few active centers with respect to methanol.

In contrast to total oxidation leading to CO_2, measurements of the total dehydrogenation rate leading to either CO or CO_2 are more demanding due to the fact that a direct detection of the rate of CO formation by quadrupole mass spectrometry in the gas phase is difficult due to the large abundance of CO ($m/e = 28$) in the methanol cracking pattern. The problem can be circumvented, however, by performing steady-state isotopic exchange experiments combined with TR-IRAS (Fig. 46) [233]. In this experiment, two beams of equal intensity are superimposed on the sample, either supplying $^{12}CH_3OH$ or isotopically labeled $^{13}CH_3OH$. Simultaneously, oxygen is dosed via a third beam source at variable intensity. Switching between both CH_3OH beams, the time constant of exchange between the adsorbed dehydrogenation

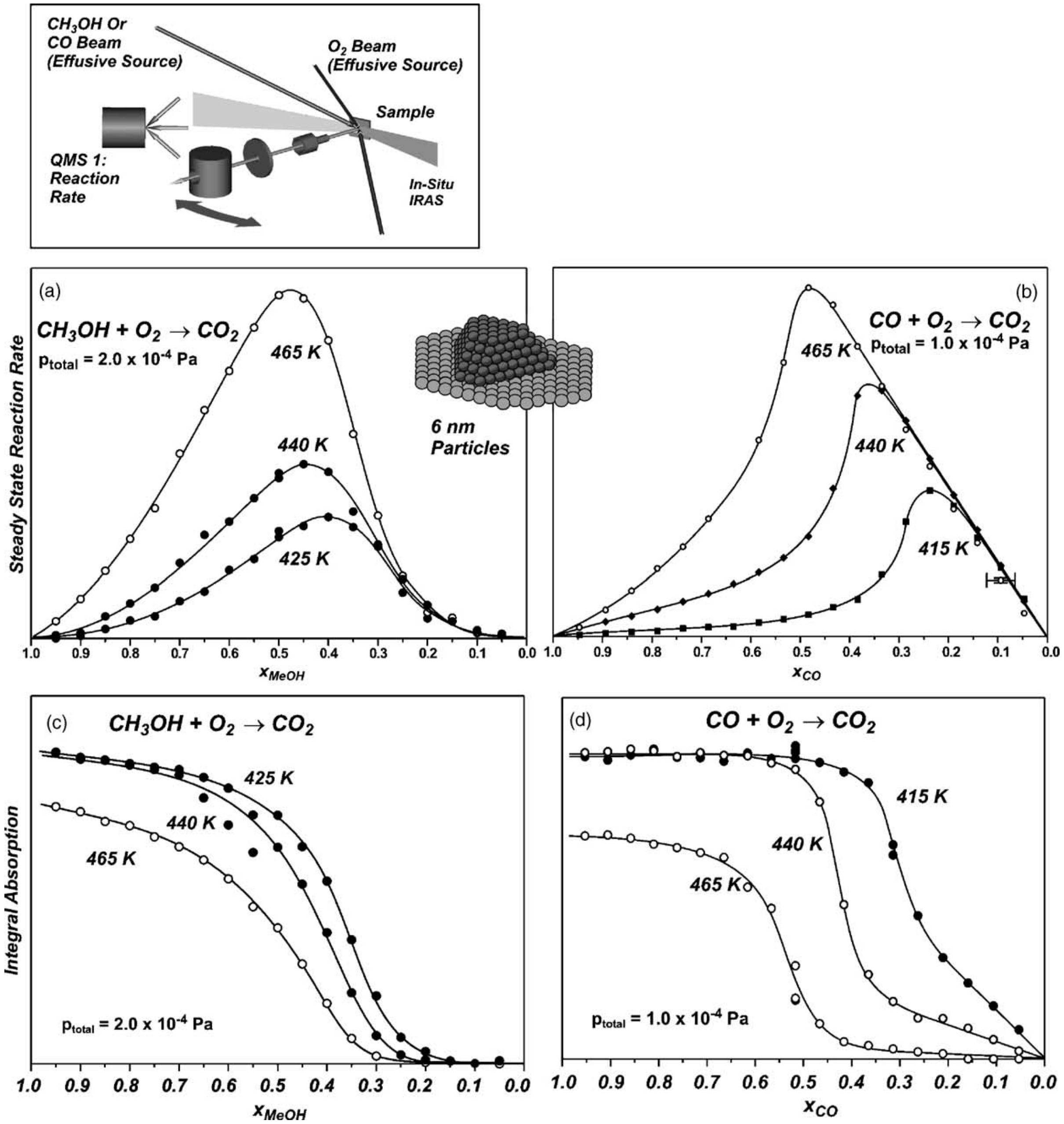

Fig. 45. Steady-state production rate of CO_2: (a) during methanol oxidation on a $Pd/Al_2O_3/NiAl$ model catalyst as a function of the fraction of methanol x_{CH_3OH} in the total flux; (b) during CO oxidation on the model catalyst as a function of x_{CO}. Integral absorption in the CO stretching frequency region as derived from static in situ IRAS under reaction conditions; (c) during methanol oxidation as a function of x_{MeOH}; (d) during CO oxidation a function of x_{CO}, from [233].

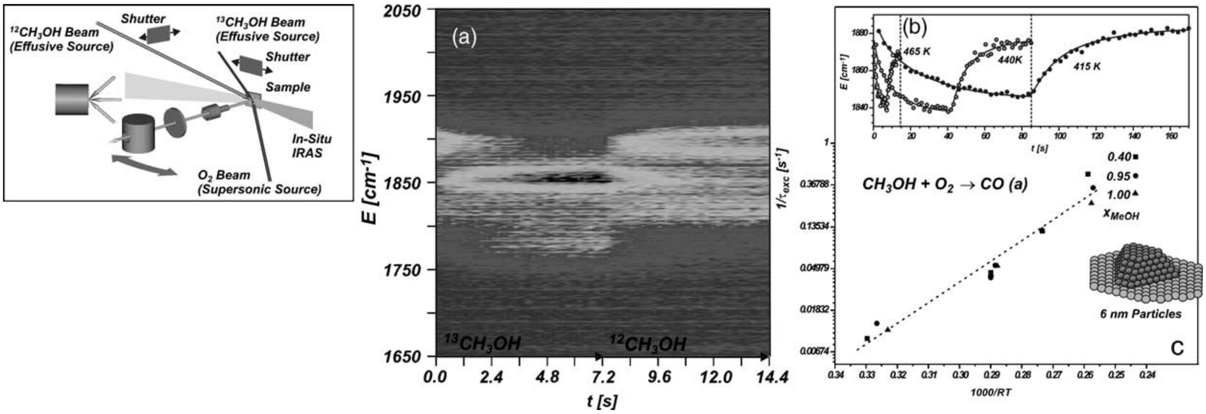

Fig. 46. Isotopic exchange experiment for determination of the steady-state methanol dehydrogenation rate on a Pd/Al$_2$O$_3$/NiAl(1 1 0) model catalyst: (a) CO stretching frequency region upon exchange between ^{12}CH$_3$OH and ^{13}CH$_3$OH (465 K, $p_{\mathrm{eff}} = 2 \times 10^{-6}$ mbar); (b) temporal response of the mean absorption energy in the CO stretching region at different surface temperatures ($x_{\mathrm{MeOH}} = 0$); (c) time constant of isotopic exchange for different surface temperatures and fractions of methanol x_{MeOH} in the impinging gas flux ($p_{\mathrm{total}} = 2 \times 10^{-6}$ mbar), from [233].

products ^{12}CO and ^{13}CO can be monitored via TR-IRAS. The exchange time measured for both species is directly related to the total rate of CO removal from the surface, i.e. the sum of both processes desorption and oxidation.

An example for the type of data obtained in this experiment is displayed in Fig. 46b. IRAS provides a sufficient temporal and spectral resolution to follow the exchange between ^{12}CO (absorption band at 1900 cm^{-1} with a shoulder at 1840 cm^{-1}) and ^{13}CO (absorption band at 1860 cm^{-1} and a shoulder at 1800 cm^{-1}). The time constant of exchange can be directly determined from the time dependence of the average absorption energy in the CO stretching region. Corresponding data as a function of x_{MeOH} and the surface temperatures is displayed in Fig. 46c. At $x_{\mathrm{MeOH}} = 1$, the time constant for isotopic exchange is determined by CO desorption exclusively. In the presence of oxygen, both processes, CO desorption and CO oxidation, contribute to the CO removal rate. It is found that the time constant for CO exchange shows only a weak dependence on the oxygen flux applied. Under oxygen-poor conditions, the reaction proceeds with CO being formed as the main product, whereas under oxygen-rich conditions the majority of CO is oxidized to CO$_2$.

After investigating the basic features of the steady-state behavior we now focus on the transient kinetics. A direct comparison between the transient CO$_2$ response for the cases of CO oxidation and methanol total oxidation is displayed in Fig. 44.

The CO oxidation was discussed in Section 6.2. Briefly, the two reaction regimes, CO-rich and O-rich, were found to be connected with two characteristic types of transient response: under O-rich conditions, a monotonous increase in the reaction rate is observed upon admission of the CO beam to the oxygen saturated surface, as well as a monotonous decrease upon termination of the beam. It is important to note that the increase in the reaction rate is characterized by two slopes due to the presence of a CO precursor state and the fact that the chemisorption probability of the precursor changes as a function of oxygen coverage. Under CO-rich conditions a maximum in the CO$_2$ production occurs both upon admission and upon termination of the beam, which is the consequence of the inhibition of oxygen chemisorption at high CO coverage (in addition, a third type of transient was observed in a transition region between the CO-rich and the O-rich regime, which is characterized by a minimum in the reaction rate, and which is related to the presence of defects sites and surface heterogeneities [197,198,225,226,228], see Section 6.2).

Comparing the transient response for methanol total oxidation (Fig. 44a) and CO oxidation (Fig. 44b) there are characteristic differences, which were primarily related to the inhibiting effect of pre-oxygen on methanol dissociation [233]. Specifically, it was found that under O-rich conditions, there is no instantaneous increase in the reaction rate upon exposure to the methanol beam. Instead, the reaction rate increases slowly toward the steady-state level on a time-scale, which is typically one order of magnitude slower as compared to the CO case. Under CO-rich conditions (high x_{MeOH}), the first transient CO_2 peak was found to be strongly attenuated as compared to the case of CO oxidation. At the same time, the absence or presence of the second CO_2 peak upon termination of the methanol beam demonstrates low and high CO coverage, respectively, in accordance with the steady-state IRAS data. Finally, it is noteworthy that under the reaction conditions investigated so far, a transient behavior similar to that for CO oxidation in the transition region between the CO-rich and the O-rich, i.e. a minimum in the reaction rate after termination of the CO beam (see Section 6.2), could not be observed for the methanol case yet.

Transient TR-IRAS experiments for methanol oxidation on the supported Pd model catalyst showed similar differences in comparison to the case of CO oxidation as the data obtained via gas phase detection (see Fig. 47) [233]. In contrast to the latter case in which the rate of CO_2 production was detected, the TR-IRAS experiment monitors the CO coverage on the surface. The experiments were performed under flux conditions in which the transient response to the methanol beam was slow (see above). Two complementary measurements are displayed, using a continuous methanol and a modulated O_2 beam (Fig. 47, open symbols) or, alternatively, a modulated methanol beam and a continuous O_2 beam (Fig. 47, solid symbols). The integral absorption in the CO stretching frequency region was detected. In accordance with the rate measurements in the gas phase, the transient response starting from the O pre-covered system is slow, whereas there is a fast response for the CO pre-covered system.

In order to quantify the TR-IRAS data, a calibration was performed on the basis of a combined sticking coefficient measurements and TR-IRAS experiment. From this, the absorption–coverage relationship was derived (Fig. 47b), which in turn could be used to convert absorption data into surface coverages. It should be noted that this type of calibration is primarily suitable for the region of low coverage. At high coverage the coverage dependence of the integral absorption becomes weak or may even change sign (compare, e.g. [125] and references therein). Calculated CO coverages θ_{CO} and the rate of CO accumulation on the surface $\mathrm{d}\theta_{\mathrm{CO}}/\mathrm{d}t$ calculated from this data are displayed in Fig. 46c and d, respectively.

Both the transient reaction rate measurements and the TR-IRAS indicate that, starting from a CO pre-covered surface, the rate of CO formation shows an immediate increase on the time-scale of the experiment and the steady-state is reached rapidly. At the microscopic level this implies that for the molecular oxygen precursor formed initially there is a high probability for finding an active dissociation site, i.e. that the CO coverage is not sufficient to result in a strong inhibition of the dissociation process. This effect can be understood from the fact that θ_{CO} in the steady-state is generally lower if produced from methanol dehydrogenation as compared to molecular CO adsorption (compare Fig. 45). In addition, the effect may be enhanced by the heterogeneity of the Pd particle surface, which tends to enhance oxygen dissociation under CO-rich conditions (compare Section 6.2). In contrast, the initial reaction rate

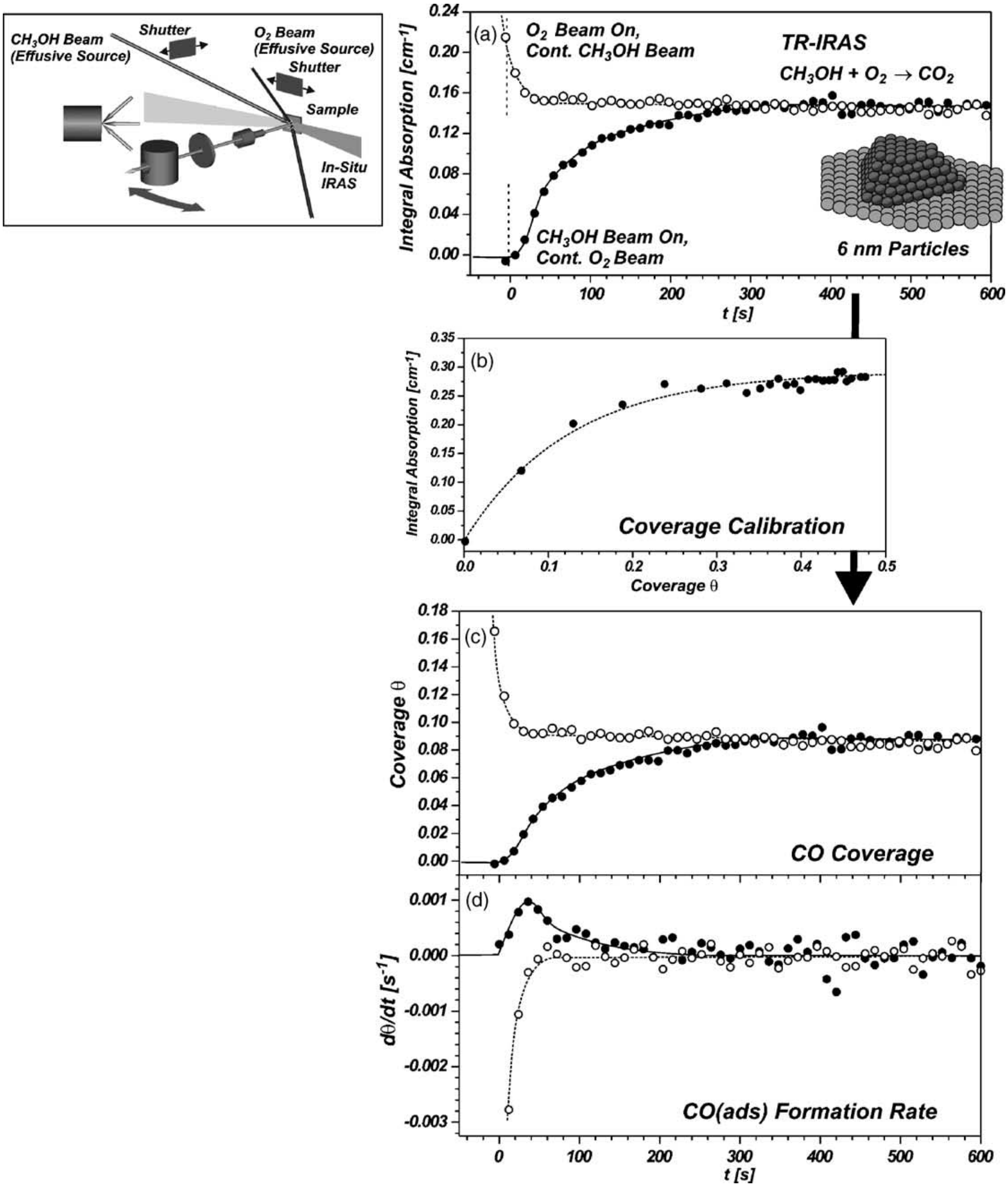

Fig. 47. (a) TR-IRAS experiment showing the integral absorption in the CO stretching frequency region during methanol oxidation on a Pd/Al_2O_3/NiAl(1 1 0) model catalyst; hollow symbols: transient experiment with continuous methanol beam and modulated oxygen beam; solid symbols: transient experiment with modulated methanol beam and continuous oxygen beam; (b) integral absorption as a function of CO coverage; (c) CO coverage in the transient region as calculated from (a) and (b); (d) derivative of the CO coverage in the transient region (465 K, $x_{\mathrm{MeOH}} = 0.50$, $p_{\mathrm{eff}} = 2 \times 10^{-6}$ mbar), from [233].

is very low when starting from an oxygen pre-covered surface. Thus, for the methanol precursor initially formed on the oxygen pre-covered particles, the probability of finding an active site for dehydrogenation is strongly reduced and desorption is predominant. Once oxygen is consumed in the course of the reaction, however, the reaction rate strongly increases, again indicating a inhibiting effect of the oxygen adlayer on the dehydrogenation step.

In spite of these insights, the details of the kinetics of methanol decomposition are far from being well-understood. In particular, this is the case for the role of oxygen in the microkinetics and the microscopic origins of the kinetics effects discussed above (see also Section 7.5). In addition, the effect of formation of surface oxides or subsurface and bulk oxygen species, which has already been mentioned in connection with the case of CO oxidation (Sections 3.2 and 6.2), has not been considered in detail, yet. The situation is further complicated by the formation of carbon as a result of CO bond activation. In the limit of high x_{MeOH}, i.e. low O_2 flux, accumulation of carbonaceous species, in particular in the vicinity of defect sites on the Pd particles, is expected. In the following section, the role of CO bond scission and carbon accumulation is discussed in more detail.

7.4. *Specific reaction sites*

One of the most delicate and at the same time most relevant aspects in catalysis is selectivity. On supported particle systems, it is often speculated that specific reactive sites may kinetically favor specific reaction pathways and thus control the selectivity of the catalyst. Specific cases are scarce, however, in which differences in activity and selectivity could be assigned to specific particle sites at the molecular level. Here, methanol decomposition on Pd catalysts is a well-suited example in the sense that methanol decomposition proceeds via two competing pathways: (i) dehydrogenation (C–H bond scission) leading to formation of CO or in the presence of adsorbed oxygen to CO_2 and (ii) C–O bond scission resulting in the formation of hydrocarbon and carbon species. It has previously been speculated that defect sites on Pd surfaces play a crucial role for the process of C–O bond scission [409,541,551].

A natural question to ask is, whether specific differences in activity can be identified for the typical sites exposed by the Pd particles of a supported model catalysts. Toward this aim, a two-step procedure was followed [231,232]. In the first step, the adsorption sites of atomic carbon species on the Pd particles were identified. In a second step, the effect of these carbon deposits on the kinetics of both competing reaction pathways was investigated.

In order to verify that C–O bond scission occurs on Pd model catalysts, a series of different experimental techniques was employed ranging from in situ IRAS via TPD to XPS experiments [231,232]. The first indication for C–O bond scission was obtained from in situ IRAS during methanol decomposition at elevated temperature. The corresponding IR spectra show an initial rapid build-up of a steady-state CO coverage followed by a slow decrease in the CO absorption signal. The latter effect was attributed to a loss of CO adsorption capacity due to accumulation of carbon and hydrocarbon species. The assumption was corroborated by the observation of weak bands in the CH stretching frequency region, indicating the presence of CH_x species ([232], compare, e.g. [541]). Additionally, TPD experiments reveal desorption of hydrocarbon species and recombinative desorption of CO ([232], compare, e.g. [563]). Recently, XPS studies provided direct evidence for the build-up of carbon upon extended methanol exposure [232,536,537]. It is important to note at this point that similar effects are not observed during extended exposure to CO (see Section 6.1). From this observation, it can be inferred that the carbon deposits do not originate from CO dissociation, but from breakage of the C–O bond in the course of the dehydrogenation process only.

In order to identify the specific adsorption sites occupied by the carbon species, IRAS is employed using CO as a probe molecule [231,237,454]. A comparison of corresponding spectra for the pristine Pd particles immediately after preparation and for the partially carbon poisoned sample after extended exposure to methanol is displayed in Fig. 48 (from [231]). If we focus on the CO spectra for the pristine sample first, it is found that the CO stretching region is dominated by a sharp absorption feature at ~1960 cm^{-1} (1) with a broad low frequency shoulder at approximately 1930 cm^{-1} (2). The shoulder extends to approximately 1840 cm^{-1}. Additionally, a weak feature at 2080 cm^{-1} (3) can be observed. On the basis of previous investigations on the same systems [57,58,60,564] and recent calculations [237] the broad features between 1930 and 1840 cm^{-1} (2) were assigned to CO mainly adsorbed on Pd(1 1 1) facets. The absorption peak (3) at 2080 cm^{-1} was related to CO adsorbed in on-top geometry, partially at defect sites. The prominent band (1) was assigned to a superposition of bridge-bonded CO on (1 0 0) facets and to CO adsorbed at defect sites such as particle edges or steps [57,58,60]. For the specific model catalysts used, the contribution of (1 0 0) facets is expected to be minor, because the fraction of these facets was small and their geometry was tilted with respect to the surface normal. Recently, this spectroscopic assignment was corroborated by a DFT study on CO adsorption on Pd nanoparticles [237]. In this work, CO was found to adsorb strongly at bridge sites on particle edges and the corresponding species was assigned to the absorption feature under discussion. It should be noted, however, that the due to dipole coupling effects the relative intensities of the features are not expected to reflect the relative fraction of CO adsorbed on the corresponding sites (compare, e.g. [58,565]).

IR spectra recorded under identical conditions on a partially C-covered sample prepared by extended exposure to methanol showed an almost complete attenuation of the defect, edge and (1 0 0) related peak (2) and a strong increase of absorption signal in the on-top region (3). Based on these observations it was concluded that surface carbon is preferentially adsorbed at particle defect, edge and (1 0 0) sites of the Pd particles and that CO adsorption is blocked or modified in the vicinity of these sites. In a more recent DFT calculation, it was suggested that these carbon deposits may, at least partially, not only be located at surface but may occupy subsurface sites as well [566].

The kinetics of the two reaction pathways on the clean and partially carbon-covered particles was studied using TR-IRAS [231,232]. Focusing on C–O bond activation first, the fraction of the Pd surface covered by carbon was estimated from the absorption in the CO stretching region under steady-state conditions. In analogy to the procedure discussed in Section 7.3, the coverage was calibrated on the basis of a combined sticking coefficient/TR-IRAS experiment. The data shown in Fig. 49 indicate that on the pristine Pd particles carbon formation is fast, but the rate drops rapidly with increasing carbon coverage. This result was interpreted in terms of an enhanced activity of edge, defect and (1 0 0) sites for CO bond scission. With these highly active sites becoming preferentially poisoned in the course of the reaction, the total rate of CO bond scission on the particles decreases rapidly.

It remains the question to what extent the second reaction pathway, i.e. methanol dehydrogenation, is affected by carbon accumulation. As discussed in Section 7.3, direct measurements of the steady-state CO formation rate via QMS are difficult, but the dehydrogenation rate can be determined by isotopic exchange TR-IRAS experiment instead (see Section 7.3 for details). It was found that only minor variations of the kinetics of CO exchange occur as a function of carbon coverage. The moderate decrease of the CO dehydrogenation rate going from the pristine to the partially C-covered sample

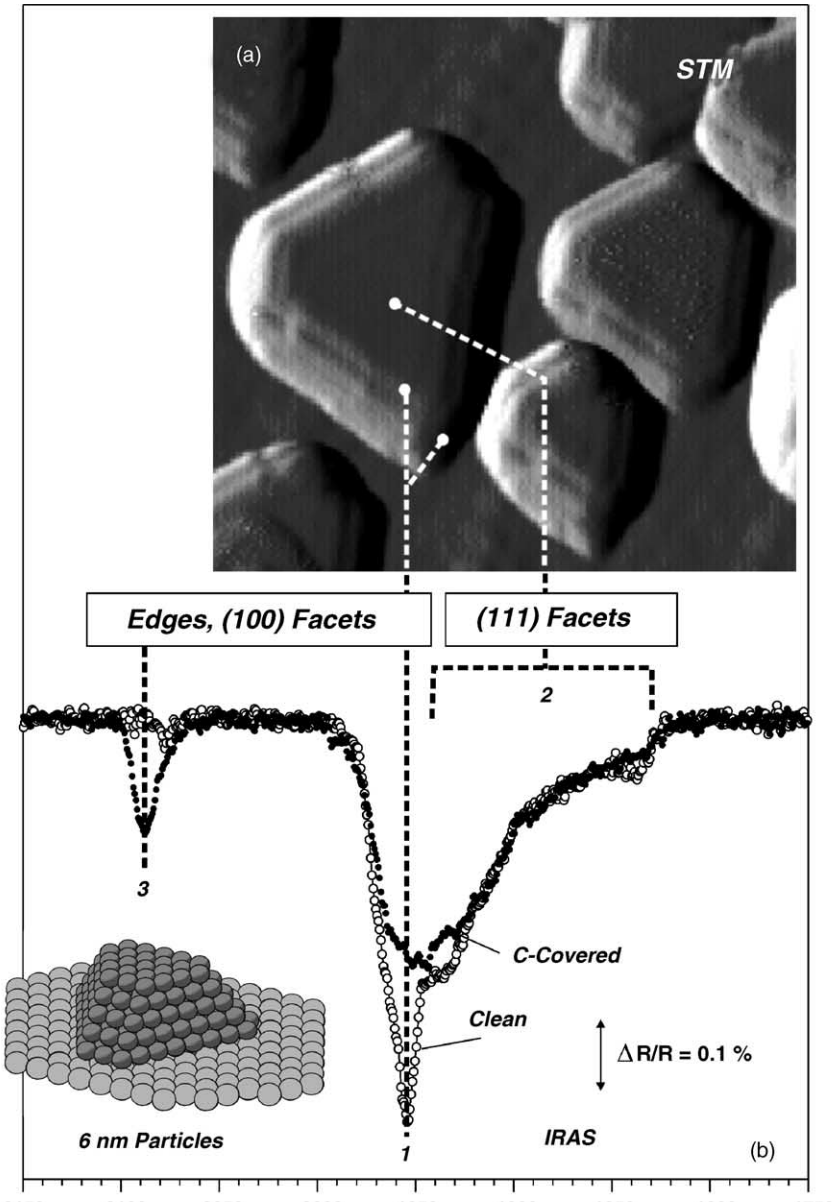

Fig. 48. (a) STM image of Pd particles grown at 300 K on Al_2O_3/NiAl(1 1 0) (20 nm × 20 nm), from [61]; (b) IR spectra for CO adsorbed on Pd/Al_2O_3/NiAl(1 1 0) (sample temperature 100 K, after CO exposure at 300 K). Open symbols: clean Pd particles immediately after preparation; solid symbols: partially C-covered particles after prolonged exposure to methanol at 440 K, from [231].

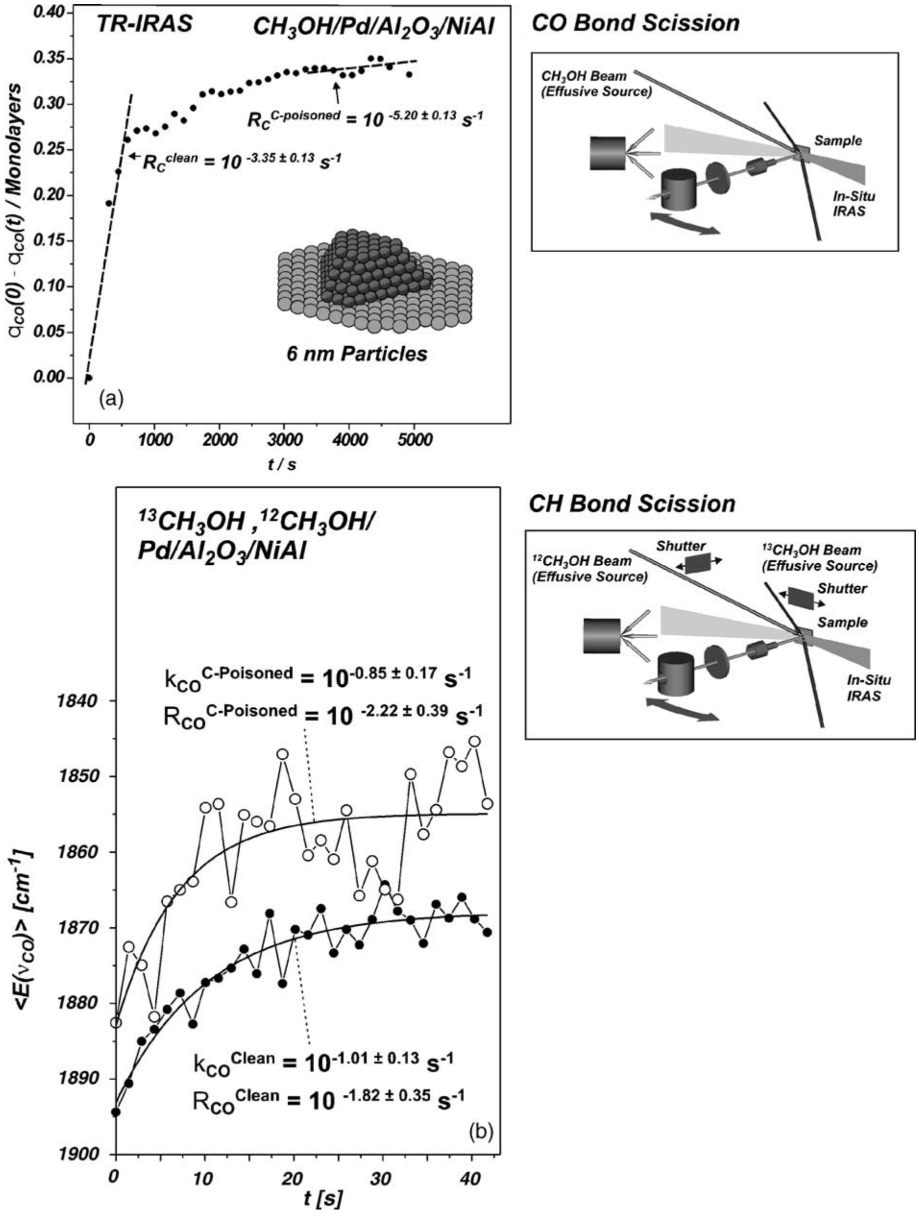

Fig. 49. (a) TR-IRAS experiment for the determination of the rate of CO bond scission for CH_3OH on a $Pd/Al_2O_3/NiAl(1\ 1\ 0)$ model catalyst: change in the CO coverage as a function of exposure time to the methanol beam, as derived from IR spectra after calibration of the band intensity via combined sticking coefficient/TR-IRAS measurements and (b) isotopic exchange experiment for determining the rate of CH bond scission for CH_3OH on the $Pd/Al_2O_3/NiAl(1\ 1\ 0)$ model catalyst: TR-IR spectra are recorded for the $^{13}CH_3OH/^{12}CH_3OH$ isotopic switching experiment and the exchange rate is determined from the mean absorption energy in the CO stretching frequency region. Similar kinetics are found for a pristine sample (solid symbols) and a partially C-covered sample after extended exposure to methanol (hollow symbols), from [231,232].

mainly reflects the decease in the available clean Pd surface rather than a change of activity of reaction sites. From these results, it was concluded that methanol dehydrogenation proceeds with similar kinetics on all particle sites with no indications for an enhanced dehydrogenation activity of particle defect or edge sites.

Summarizing the results described above, there are important implications with respect to the selectivity of methanol decomposition on a supported Pd model catalyst. Briefly, it follows that different sites coexisting on a supported particle sites have different activity for the competing reaction pathways, i.e. dehydrogenation (CH bond scission) shows no pronounced preference for specific sites whereas CO bond scission preferentially occurs at particle edges, steps, defects or (1 0 0) sites. Thus, the microscopic structure of the particles is expected to control the selectivity of the reaction system.

7.5. Microkinetic simulations

As described in the previous sections, a large amount of information was collected on the mechanism and kinetics of methanol decomposition. Similar to the case of CO oxidation, the ultimate goal of such work is a quantitative understanding of the reaction kinetics, taking into account structural or morphological properties at the microscopic level, including, e.g. the role of the particle size, the particle structure, the support or promotors and poisons.

In contrast to the case of CO oxidation considered in Section 6, for methanol decomposition and oxidation the situation is by far more complex. Nevertheless, some attempts have been made in order to describe the experimentally observed kinetics on the basis of microkinetic models [233]. To start with, a simplified reaction scheme was applied, which was setup according to the experimental findings discussed in Section 7.2 (see Fig. 50, from [233]). The first step is the adsorption of molecular methanol, which may be modified by trapping on the support and surface diffusion. As the interaction with the support is weak, however, the process is fast on the time-scale of the reaction and all trapping effects can in principle be accounted for by introducing an effective sticking coefficient for every species (see Section 5.1). Subsequently, the adsorbed methanol undergoes partial dissociation to methoxy and a fast equilibrium between both species is established. Consequently, both species can be treated as a single intermediate, the reaction rate of which depends on the actual surface coverage. It should be noted that at elevated temperatures, dehydrogenation is fast and, accordingly, the steady-state coverages of methoxy and methanol are low. The lifetimes of all further dehydrogenation intermediates are even shorter, so that the corresponding dehydrogenation steps can be represented by a single step in the kinetic scheme. CO produced in the reaction may either desorb or react with adsorbed oxygen to form CO_2, which itself

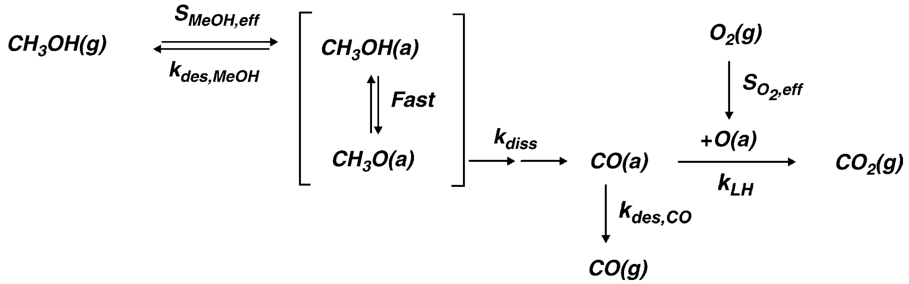

Fig. 50. Simplified reaction diagram used in the microkinetic simulation of methanol oxidation, from [233].

desorbs rapidly. CO bond scission was omitted at this point. The reasons are that, firstly, the process is slow as compared to dehydrogenation and, secondly, that the carbon species formed by CO bond scission are rapidly oxidized to CO in the presence of oxygen [230]. It should be noted, however, that carbon accumulation may occur at sufficiently low oxygen flux and the blocking or modification of specific particle sites by carbon species may then play an important role in the kinetics.

Under the reaction conditions employed, CO and O are the only surface species present in large concentrations. Taking this point into account, simulations were performed in a two-step strategy: in the first step, the kinetics of CO oxidation were modeled quantitatively. From this model, several kinetic parameters were extracted, which, in a second step, were used in the model for the methanol oxidation system. All remaining parameters were adjusted during a second fitting procedure.

The results of the microkinetic model were discussed in detail by Hoffmann et al. [225,233], concluding that for the case of CO oxidation a near quantitative description could be obtained on the basis of a homogenous surface model. With respect to the steady-state and transient CO oxidation kinetics, the flux and temperature dependent behavior, the time-scale of the transient response and relative intensity of the transient peaks was found to be well-reproduced. In the second step, adsorption, desorption and dehydrogenation steps for methanol and methoxy were added to the CO oxidation system, according to the reaction diagram indicated in Fig. 50. This implies that a multitude of additional parameters had to be added, e.g. accounting for the coverage and co-adsorbate dependencies of sticking coefficients or the effect of co-adsorbates on the activation parameters for methanol desorption and dissociation. The model was applied to methanol total oxidation discussed in Section 7.3, both under steady-state and under transient conditions. In general, it was found that the steady-state rates could be reproduced, with respect to their temperature and flux dependence and with respect to the magnitude of the TOFs, both under O-rich and CO-rich conditions. Substantial deviations remained, however, with respect to the transient behavior.

Also, the kinetic model was analyzed in terms of the DRC of the different reaction steps. Briefly, a fast chemisorption/desorption equilibrium of methanol (which in turn is in equilibrium with the methoxy species) is established under conditions of high oxygen flux, with the reaction rate being low due to inhibition of dehydrogenation in the presence of pre-adsorbed oxygen. The RDS is dehydrogenation, i.e. breakage of the first C–H bond, and dissociative oxygen adsorption has a negative DRC control, i.e. more facile dissociation inhibits the reaction. At larger methanol fluxes, the transition point between O-rich and CO-rich condition roughly coincides with the maximum of the CO_2 production rate. At higher methanol ratios, CO desorption starts to compete with CO oxidation, leading to the evolution of CO as a second product. The kinetic situation is more complex in this parameter range with several processes having a substantial DRC. At highest x_{MeOH}, dehydrogenation to CO becomes the dominant pathway, and dissociative adsorption of oxygen is rate-controlling.

In spite of the good agreement obtained between steady-state kinetics and microkinetic modeling, the results have to be treated with care, because of deviations between experimental data and the model with respect to the transient behavior [233]. Several possible explanations have been invoked, which may be responsible for these disagreements: firstly, the parameterization used in the kinetic model may not provide the necessary flexibility to reproduce the experimental kinetics. Secondly, essential features of the mechanism might be missing in the model. Among the parts of the microscopic reaction kinetics, which have not yet been described properly are, e.g. variations of the dehydrogenation rate as a result of carbon formation under conditions of high methanol flux or a realistic modeling of the behavior of oxygen (including, e.g. the formation of subsurface and bulk oxygen and surface oxides, see comments in

Sections 3.2.1 and 6.2.1). In addition, kinetic effects beyond the MF approximation have to be invoked, such as, e.g. differences in the spatial adsorbate distribution under transient and steady-state conditions. Such effects can lead to drastic variations of the reaction rates as has been observed for other systems, e.g. due to the formation of islands (see, e.g. [408]). A refinement of kinetic models would be possible, e.g. on the basis of a Monte-Carlo approach, as has been shown, e.g. for the case of CO oxidation on Pt(1 1 1) [567], but would in general require more detailed microscopic data on the distribution of reactants over the model catalyst surface under reaction conditions.

8. NO decomposition and reduction

8.1. NO decomposition on Pd surfaces—general remarks

In the last section, we focus on the adsorption, dissociation and reduction of NO on supported model catalysts. Recently, the catalytic reduction of NO_x has attracted considerable attention in environmental catalysis due to the fact that modern lean-burn engines produce oxygen-rich exhaust gas conditions, under which conventional three-way catalysts may not operate efficiently [11]. As a result, alternative reduction pathways involving, e.g. hydrocarbons and nitrogen storage mechanisms have been considered (see, e.g. [21,22,568]). Scientifically, these attempts introduce several new aspects to the fundamental work in this field. On one hand, the origin of size and structure dependent effects and their relation to the kinetics is of pivotal importance. On the other hand, processes involving the support play an increasing role.

More recently, the use of supported Pd catalysts has been suggested and used in addition to the Rh and Pt based catalyst systems and it has been subject to intense investigations (see, e.g. [569–573] and references therein). Most MB work has been performed on Pd model catalysts so far. Therefore, we focus on the interaction of NO with Pd surfaces instead of the more traditional Rh based catalysts (see, e.g. [574] and references therein). Surface science experiments on the adsorption and dissociation of NO have been performed on Pd single crystals with different crystallographic orientation including Pd(1 1 1) [570,575–592], Pd(1 0 0) [585–589,592–596], Pd(1 1 0) [586,597–600], Pd(1 1 2) [582,583,601–605], Pd(3 2 0) [448,600] and Pd(3 1 1) [589,606]. In addition, some adsorption and reaction studies have been performed on supported Pd model catalysts (see, e.g. [585,592,607–611]). The adsorbate structures and sites occupied by NO on the different single crystal facets will be discussed in more detail in Section 8.3. As an important result from the experimental work on single crystals, it was found that, in general, NO remains molecularly adsorbed on the Pd(1 1 1) facet up to elevated temperatures, whereas more open and in particular stepped surfaces have a significantly higher activity toward NO dissociation. N_2 and N_2O were identified as the possible products of NO reduction, but the selectivity toward N_2 was found to be the higher in most surface science studies (see, e.g. [448,582,589,598,600]). In the high pressure region, Goodman and coworkers observed an increasing selectivity toward N_2O with increasing reaction temperature, which was explained by the increasing θ_{NO}/θ_{CO} ratio under these conditions [570,591]. NO adsorption and dissociation has been subject to intense theoretical investigations as well [612–620]. In particular, DFT calculations by Hammer [614,617] and recently also by Sautet and coworkers [620] confirmed the enhanced dissociation activity of stepped Pd surfaces. Goodman and coworkers showed in a comparative study that the Pd(1 1 1) surface is more active for NO reduction by CO than the more open (1 0 0) and (1 1 0) facets ([588,610,611,621], see also [570,592]). The result is somewhat surprising in view of the enhanced dissociation activity of stepped and open surfaces, but was explained by the presence of strongly bound N species, leading to a poisoning and deactivation of the surface. Such more strongly bound species were experimentally observed in several cases (see, e.g. [600,610]). In summary, it has to be pointed out, however, that the structure and size dependence of the kinetics of NO dissociation and reduction is not well-understood yet. In particular, the role of co-adsorbates, which in case of oxygen and nitrogen may be present up to high reaction temperatures, remains largely unclear.

In addition to the size and structure dependences observed for the active particles, the support plays an important role. Besides the capture zone effects discussed in Section 5.1, chemical reactions with the support may become important in the mechanism of NO_x reduction on supported catalysts. The latter effect is receiving increasing attention in studies on real catalysts (see, e.g. [22,23,622]), but has hardly been subject to fundamental studies on supported model systems yet.

In the following, we summarize the MB work on Pd model catalysts primarily addressing the following issues: (a) the mechanism and kinetics of NO adsorption and reaction with the support (Section 8.2) [235,236], (b) the adsorption on supported Pd nanoparticles (Section 8.3) [201,202,235,238], (c) the dissociation on supported Pd nanoparticles (Section 8.4) [201,202,234,238]] and recently on Cu particles as well [242], (d) the kinetics of the CO–NO reaction [178,202,204,205,623] (Section 8.5) and (e) approaches toward the development of microkinetic models (Section 8.6) [624,625]. Similar to the previous sections we primarily discuss the effects which may potentially lead to particle size and structure dependent effects in the kinetics, including, e.g. support effects, the presence of different adsorption and reaction sites, or the modified adsorption behavior of small metal aggregates.

8.2. NO interaction with the model support

Recently, the interaction of NO with the Al_2O_3/NiAl(1 1 0) model support was studied using a MB of NO and TR-IRAS (see Fig. 51) [235,236]. A rather complex behavior was found, involving a variety of absorption bands in the frequency range between 1300 and 1900 cm^{-1}, appearing successively as a function of NO exposure. The relatively large exposures in the order of 10^2 L required before the appearance of any absorption band and the simultaneous disappearance of the LEED pattern of the oxide film was interpreted in terms of a slow reaction of the NO with the support, involving a restructuring of the oxide film and the loss of its long-range order (see also [626]). To some extent, the NO derived bands could be assigned on the basis of previous work on NO adsorption on different oxide and metal surfaces, such as, e.g. on oxidized and bare Mo(1 1 0) substrates [627–630], on weakly interacting metal surfaces such as Ag(1 1 1) [631,632], Cu(1 1 1)[633] and Cu(1 1 0) [634], on oxide surfaces [635,636] as well as on pure alumina [637–639] and mixed oxides containing alumina [23,622], the latter under ambient conditions. The various NO derived species observed in vibrational spectroscopy have been reviewed recently [640]. Based on this data the species formed initially on the Al_2O_3/NiAl(1 1 0) support was assigned to a strongly bound NO entity (1620 cm^{-1}). For NO/alumina at ambient pressures absorption bands in the corresponding frequency region are typically assigned to surface nitrates, nitro or nitrito species [23,637,640]. The slow formation kinetics and the loss of the diffraction pattern is compatible with a restructuring process, which, as discussed later, preferentially takes place at defects sites on the oxide film. The second NO derived species (1690 cm^{-1}) is formed after substantial surface reconstruction of the support only and is followed by an emerging high frequency band at 1880 cm^{-1}. Absorption signals in this range have previously been

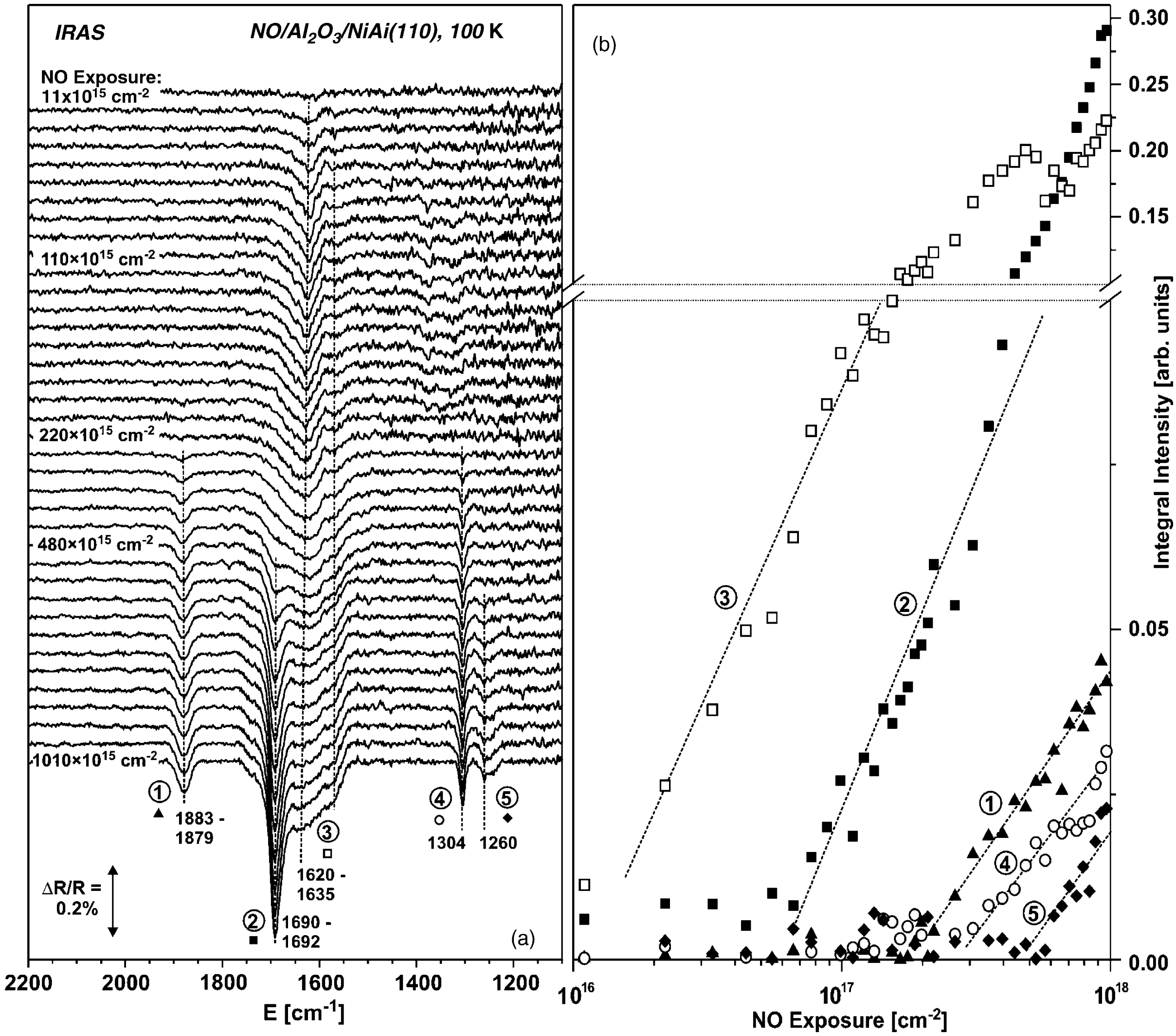

Fig. 51. (a) IR spectra acquired during exposure of the pristine Al_2O_3/NiAl(1 1 0) model support to a molecular beam of NO and (b) integral absorption of the different IR bands indicated in (a) as a function of NO exposure, from [236].

assigned to the formation of NO dimers [627,631,632,634]. Such dimer formation has been identified as an important pathway for NO decomposition at low temperature. On many surfaces, the NO dimer has been shown to decompose via N_2O and oxygen [630,632–634,641]. It should be noted, however, that the N_2O formed via $(NO)_2$ decomposition, could not be identified yet, possibly suggesting rapid desorption under the experimental conditions applied. In any case, NO decomposition toward N_2O would provide a pathway to formation of surface oxygen and, thus, toward the formation of NO species in higher oxidized states. Many of such entities have been observed on alumina powders at higher pressure, such as. e.g. linear, bridging and chelating nitro and nitrito species, different types of bridging and chelating nitrates as well as hyponitrites [23,622,637,638,640]. Although their exact identification remains controversial in many cases, typically, these species give rise to a variety of bands between 1000 and 1600 cm^{-1}. Thus, the features appearing at highest NO exposure on Al_2O_3/NiAl(1 1 0) may be tentatively attributed to such oxo-surface compounds of nitrogen.

Of special interest is the investigation of the interaction of NO with the alumina film after the growth of Pd particles (see Fig. 52, from [235]). As compared to the pristine film, a completely different behavior was observed in this case. Whereas in the range of low NO exposure no absorption signals were observed on the pristine film, the spectrum of the Pd-covered system has already reached its full absorption level. The individual bands could be assigned to NO molecularly adsorbed on the Pd particles only. The exact origin of the bands is discussed in Section 8.3. The rapid saturation at low exposure is of course expected in view of the high sticking coefficient on the metal surface, which is additionally enhanced by the capture zone effect at low adsorption temperature. As usual, it should be noted that the relative intensities of the bands do not reflect the relative concentrations of the corresponding species (see, e.g. Sections 2.1 and 7.2 [125,565]).

Comparing the spectra of the Pd-covered and Pd-free support, the most surprising observation was the absence of several bands which were found to be characteristic for the NO decomposition process on the alumina support [235,236]. This becomes particularly evident, if the IR spectra for the pristine and Pd-covered alumina film are compared in the regime of large NO exposures (Fig. 52). The above observation suggests that the low temperature NO decomposition processes are strongly inhibited on the Pd-covered oxide film. Based on the growth behavior of the Pd particles (see Section 3.2), it was proposed that the support restructuring and NO decomposition process would require specific support defect sites, such as antiphase boundaries or point defects to be initiated. With the Pd particles efficiently covering these defects, they could also prevent the initial step of the decomposition sequence, leading to the observed inertness of the oxide after metal deposition.

8.3. NO adsorption on supported model catalysts

In the next step, we consider MB studies on the adsorption on supported model catalyst [201,202,235,238,242]. As discussed in Section 5, the first step in adsorption is in many cases trapping of the reactant molecule in a weakly bound precursor state, either on the support or on the active particle itself. Trapping on the support, leading to an enhanced flux of adsorbates to the particles, i.e. the capture zone effect, has been discussed in Section 5.1. Possible implications for the kinetics of the CO–NO reaction will be considered in Section 8.6. For adsorption experiments at low temperature, trapping on both, on the support, and on the particles simply decreases the exposures required to establish a given coverage on the particles.

Corresponding IR spectra acquired during exposure of a Pd/Al_2O_3/NiAl(1 1 0) model catalyst to a molecular beam of NO are displayed in Fig. 53, from [235]. In the exposure range considered, no absorption signals are observed on the pristine alumina film. In the spectrum of the Pd-covered system three principal spectral regions are identified with bands around 1750 cm^{-1}, at 1600–1700 cm^{-1} and below 1600 cm^{-1}. As seen in Fig. 52, the absorption features are subject to slow changes at very high coverage, possibly due to contaminations or slow restructuring processes. In the following, we focus on the assignment of the spectral features at lower exposure (Fig. 53). Here, bands at 1525, 1640 and 1735 cm^{-1} are observed initially. The bands blue-shift and develop low frequency shoulders (1620, 1548 cm^{-1}) of increasing intensity at higher exposure. In addition to the adsorption studies at low temperature, more detailed IR studies were performed as a function of sample temperature [235,238].

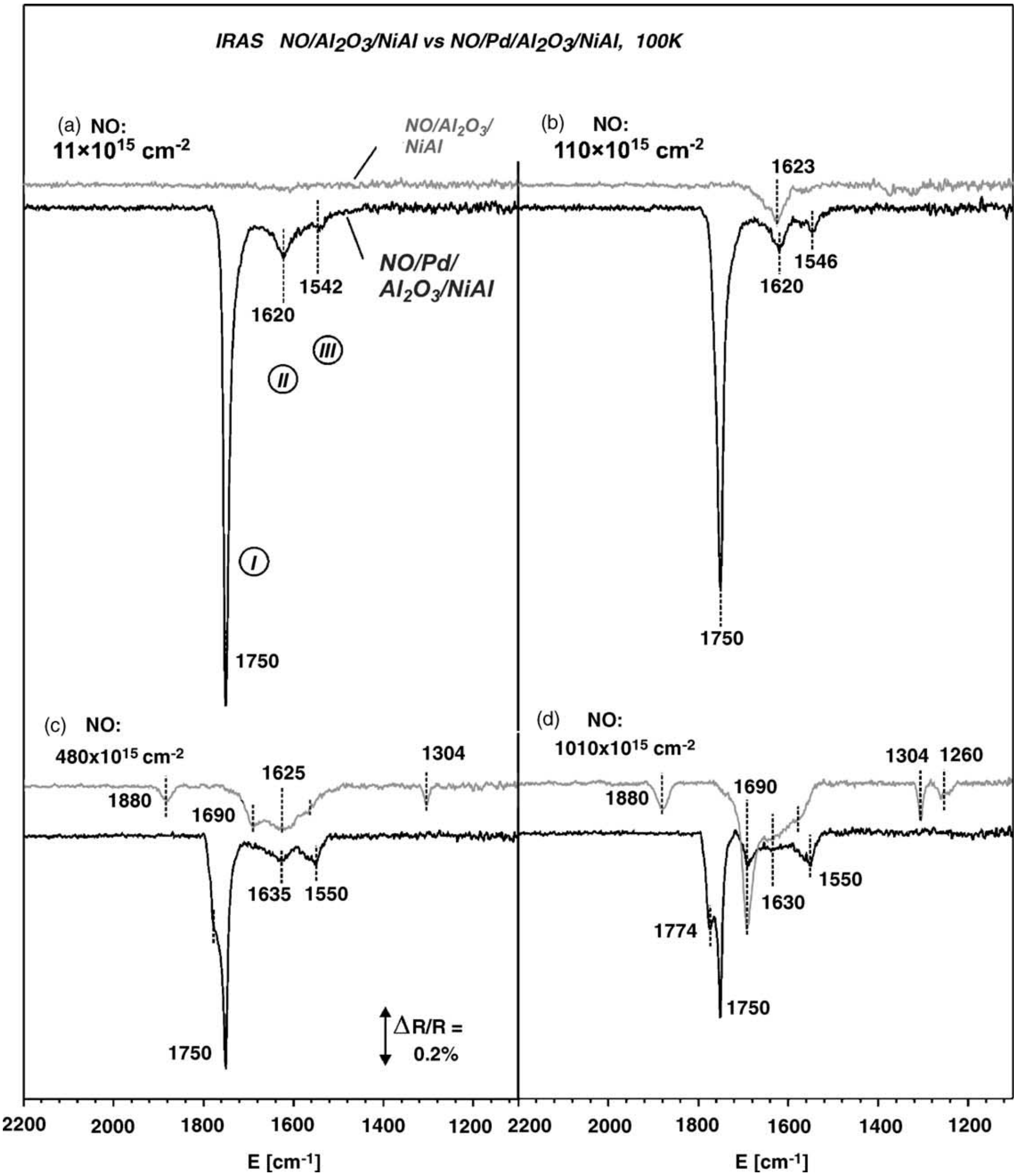

Fig. 52. Comparison of IR spectra acquired during exposure of the pristine Al_2O_3/NiAl(1 1 0) model support (gray traces) and a Pd/Al_2O_3/NiAl(1 1 0) model catalyst (6 nm particles, black traces) to a molecular beam of NO, from [235].

The assignment of the spectral features observed for the Pd particle system is an important prerequisite for further investigations on the role of specific reaction sites. Here, important information can be obtained on the basis of a comparison with previous studies on Pd single crystals, the results of which can be briefly summarized as follows.

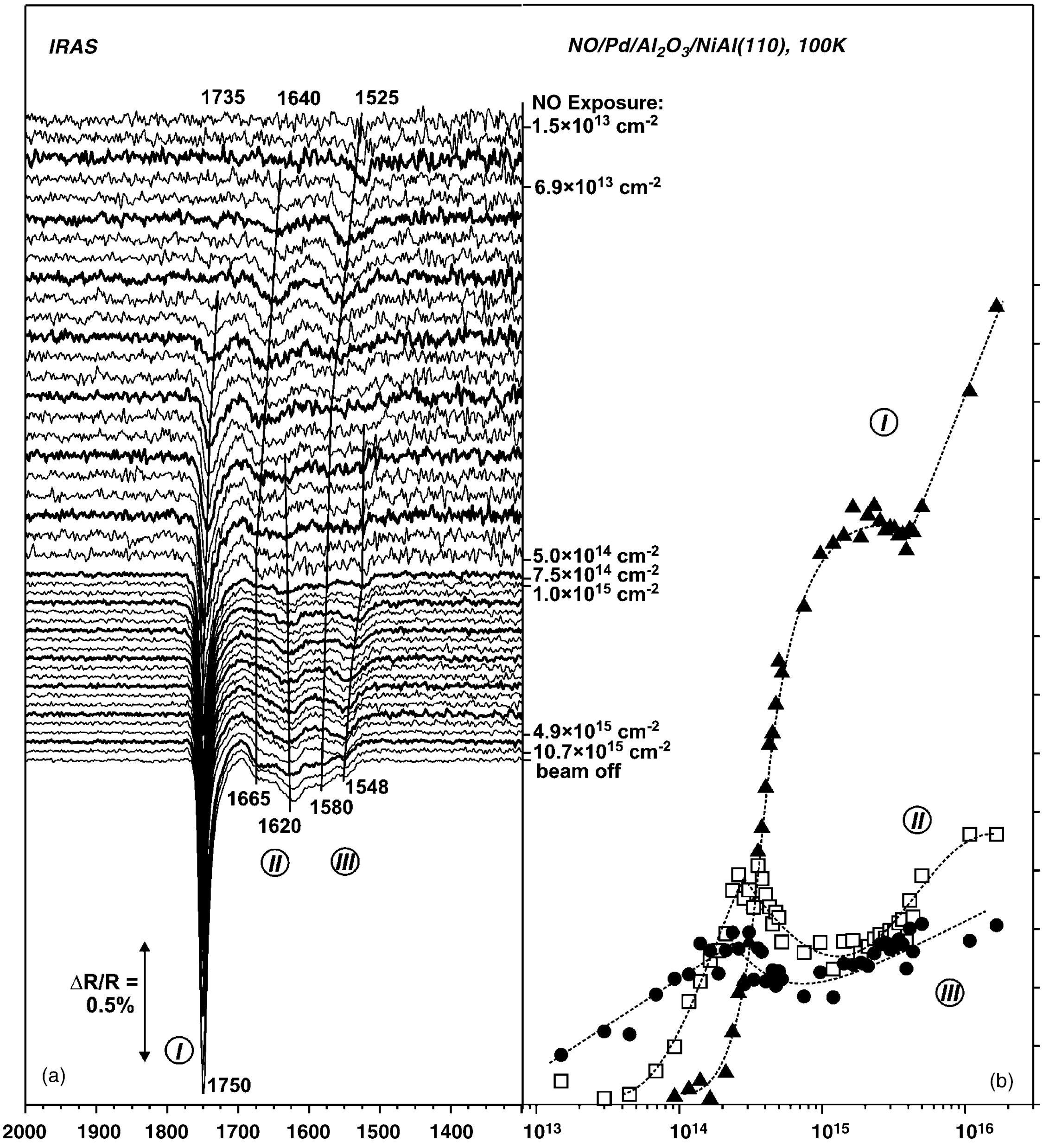

Fig. 53. IR spectra acquired during exposure of the Pd/Al_2O_3/NiAl(1 1 0) model catalyst to a molecular beam of NO and (b) integral absorption of the different IR bands in the three frequency regions indicated in (a), from [235].

On Pd(1 1 1), TPD studies showed three main desorption features at 257, 285 and 510 K [575,577]. The high temperature desorption is connected to a disordered adsorbate phase at an NO coverage of up to $\theta = 0.33$ [577,578]. Vibrational studies of NO adsorption in this temperature range have been preformed by Ramsier et al. [582,583], who observed at 373 K a single band shifting from 1540 to 1590 cm^{-1} with increasing coverage, and Bertolo et al. [577,578] who found after NO saturation at 300 K a single band at 1589 cm^{-1}. Under UHV conditions, higher coverages can be obtained at lower surface temperature only [584]. Here, several ordered adsorbate structures have been identified: an ordered c(2 × 4)-2NO phase gives rise to an absorption band around 1620 cm^{-1} at $\theta = 0.50$ [570,577,578,580,581,584], and at the highest coverage ($\theta = 0.75$) at 100 K a p(2 × 2)-3NO structure is observed which is characterized by bands around 1548 and 1758 cm^{-1} [570,577,578,580,582,584]. In an intermediate coverage region ($\theta = 0.625$) between these phases, a c(8 × 2)-5NO structure was reported (1736, 1586 cm^{-1}) [570,581,584]. The situation is further complicated by the fact that the different structures may coexist over a substantial coverage region [584]. The local sites occupied by NO in these adsorbate structures have recently been investigated theoretically [615,616,618] and experimentally [584]. It was concluded that NO occupies fcc hollow sites at low coverage, a mixture of fcc and hcp sites at $\theta = 0.50$, and on-top sites in addition to a mixture of fcc and hcp sites for the higher coverage structures at 100 K up to $\theta = 0.75$. At even lower temperature, indications for the formation of NO dimers have been observed [578]. The misassignments of NO adsorption sites, which in older studies arose from the interpretation of vibrational spectra on the basis of nitrosyl compounds, have recently been reviewed by Brown and King [642].

On Pd(1 0 0), the vibrational spectra of adsorbed NO have been investigated by Nyberg and Uvdal [593]. At elevated temperature (420 K) a p(4 × 2) superstructure is formed, which corresponds to a coverage of $\theta = 0.25$ and gives rise to a vibrational spectrum showing a single signal at 1492 cm^{-1}. At temperatures of 400 K and below a second band at 1653 cm^{-1} emerges and at 250 K ($\theta = 0.50$) a $(2\sqrt{2} \times 2\sqrt{2})R45^\circ$ superstructure is obtained, which is finally characterized by a single band at 1678 cm^{-1}. The saturation coverage at 80 K was estimated as $\theta = 0.65$ [594]. In a similar manner as for Pd(1 1 1), the site occupation was reinterpreted recently, concluding that four-fold hollow sites are occupied in the case of the low coverage structure ($\theta = 0.25$–0.30), whereas at higher coverage ($\theta = 0.50$) NO adsorbs on bridge sites [595].

In addition to the close-packed single crystal planes, adsorption on open and stepped Pd surfaces is of high relevance for the present case of NO adsorption on supported particles. An extensive comparative study was performed by Ramsier et al. on Pd(1 1 2) and Pd(1 1 1) [582,583]. Briefly it was observed that upon adsorption on Pd(1 1 2) at 373 K, an additional band appears in the spectral region between 1655 and 1670 cm^{-1}, which was assigned to NO adsorption at edge sites. Similar results were recently obtained by Nakamura et al. in a comparative investigation on Pd(1 1 1), Pd(1 0 0) and Pd(3 1 1) [589].

On the basis of these results, the spectra in the low frequency region were assigned to NO adsorbed on hollow sites, predominately on Pd(1 1 1) facets of the Pd nanoparticles [235]. Some weak indications for NO on four-fold hollow sites of (1 0 0) facets were reported as well. In contrast to the low frequency region, strong deviations from the single crystal behavior were observed for the absorption bands at higher frequency. For example, the presence of on-top NO up to 300 K was found, in sharp contrast to the single crystal behavior, both on Pd(1 1 1) and Pd(1 0 0). The corresponding band, which was red-shifted with respect to the single-crystals, was assigned to NO adsorption at particle defect sites such as, e.g. edges, corners and steps. The most drastic deviation from the Pd(1 1 1) single crystal was identified in the spectral range between 1600 and 1700 cm^{-1}. On Pd(1 1 1) a band at 1620 cm^{-1} can be observed at coverages exceeding $\theta = 0.50$ only, which, however, cannot be reached at 300 K in UHV. On the Pd particles, on the other hand, strong bands in this frequency region are preserved up to high temperatures [234,235,238]. Similar, as previously discussed, to the case of CO adsorption (Section 7.4), there are two possible assignments which can be discussed. First, there can be a contribution due to NO adsorption at defect sites such as particle edges, defects or steps, similar to the species observed on stepped Pd surfaces (see, e.g. [582,583,589]). Some moderate enhancement of the binding energy at steps was indeed predicted in theoretical calculations as well [617]. In addition to the edge sites, a contribution due to (1 0 0) facets is expected, which would give rise to an absorption bands in the same region [589,593]. Similar to the arguments used in connection with CO adsorption (see Section 7.4), it was suggested that the large intensity of the corresponding bands could not be accounted for by the small fraction of (1 0 0) facets exposed by the particles (in addition, these facets are tilted with respect to the surface normal, which should further reduce the perpendicular component of the dynamic dipole moment). Thus, the spectral region between 1600 and 1700 cm^{-1} was predominately assigned to defect, step and edge sites on the particles.

As a final remark it should be noted that – as remarked before – the relative intensities of the NO bands do not reflect the relative concentrations of the corresponding species, which is, for example, illustrated by the strong dominance of the on-top NO (1750 cm^{-1}) in the IR spectrum. Such effects can, e.g. be due to differences of the dynamic dipole moment (which vary as a function of the local adsorption geometry and as a result of coupling to the metal), due to different molecular orientation in combination with the MSSR and due to intensity transfer between neighboring bands due to dipole coupling (see, e.g. [565]). Such intensity borrowing is illustrated Fig. 53b, which shows the integral intensities of the bands in the three frequency regions (from [235]), where, e.g. the appearance of the on-top NO band at the highest frequency is directly correlated to an attenuation of the other absorption features. However, it should again be noted that other effects such as the electronic coupling between the adsorbate and the particle may also change as a function of coverage and, therefore, a more exhaustive analysis would require a detailed theoretical studies.

In addition to adsorption of pure NO, the effect of co-adsorbed oxygen and CO on the NO adsorption on Pd/Al_2O_3/NiAl(1 1 0) was studied as well (see Fig. 54, from [235]).

For the case of oxygen co-adsorption, the sample was pre-dosed with O_2 at 300 K and subsequently exposed to an NO beam at a sample temperature of 100 K (Fig. 54a). Characteristic changes were observed with respect to both the intensity ratios and the frequency of all NO derived bands. Specifically, it was found that all NO bands exhibited a pronounced blue-shift, the size of which depended on the specific type of adsorption sites. Moreover, the appearance of the on-top NO signal was found to be strongly preferred as compared to the clean Pd particle and the edge, step and defect signal was suppressed. The exact assignment of the co-adsorption bands is somewhat complicated by the limited amount of single crystal reference data for O and NO co-adsoption on Pd single crystals. Some experimental results are available on Pd(1 0 0), where Nyberg and Uvdal observed a blue-shift of bridge-bonded NO of approximately 20–30 cm^{-1} on Pd(1 0 0)-p(2 × 2)O [596]. Similar shifts and redistribution effects between sites were observed on other transition metal surfaces as well (see, e.g. [643,644]). Typically, the blue-shift is interpreted in terms of a strengthening of the NO bond due to the electronegative oxygen co-adsorbate, reducing the NO $2\pi^*$ electron density. In co-adsorption studies using oxygen and NO on Pd(1 1 2) using TPD by Ramsier et al. [602], a reduced NO uptake and a weakening of the Pd–NO bond was interpreted along the same lines. On the basis of these results, it is apparent that the co-adsorption data for the supported Pd particles point to the formation a mixed NO–O overlayer. In fact, on the basis of a more detailed analysis, it was found that the spectral shifts and changes of adsorption site could be interpreted in detail by assuming the initial formation of an O-p(2 × 2) superstructure and subsequent NO co-adsorption on this layer [235]. The additional suppression of the

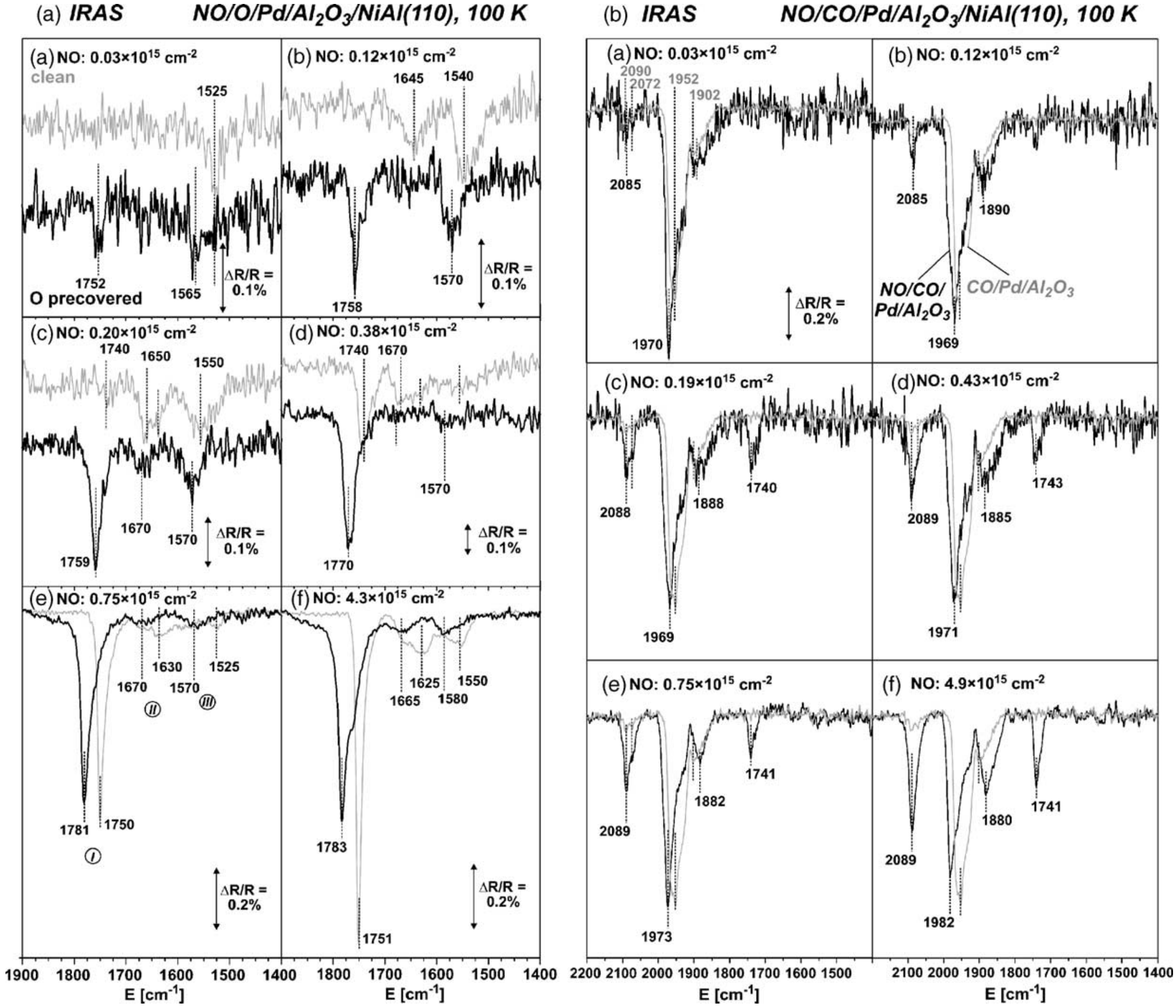

Fig. 54. Co-adsorption on a Pd/Al_2O_3/NiAl(1 1 0) model catalyst: (a) IR spectra acquired during exposure of the pristine Pd particles (gray traces) and the oxygen pre-covered Pd particles (black traces) to a molecular beam of NO and (b) IR spectra acquired after saturation of the Pd particles by CO at 300 K and after subsequent exposure to a molecular beam of NO (black traces) at 100 K, from [235].

NO band assigned to NO at particle defect, steps and edges points to an enhanced interaction of oxygen with these sites as, e.g. has also been suggested in a recent STM study [607].

IR spectra for NO co-adsorption on a CO pre-covered Pd/Al_2O_3/NiAl(1 1 0) sample were obtained by pre-dosing CO at 300 K and subsequent exposure to a NO beam at a sample temperature of 100 K (Fig. 54b).

Focusing on the NO region, the absence of the characteristic on-top band indicated initial occupation of higher coordinated sites by NO. Only at higher exposures, an additional occupation of on-top sites occurs; a behavior, which is consistent with the Pd(1 1 1) single crystal results [585], showing on-top NO at low temperature and high coverage only (see [618,645] for theoretical investigations of CO–NO co-adsorption on Pd(1 1 1)). Shifting the focus to the CO stretching frequency region, the corresponding reference spectra for $Pd/Al_2O_3/NiAl(1\,1\,0)$ were discussed in detail in Section 6.1. Upon NO co-adsorption, all parts of the CO spectrum were found to be subject to strong changes, including an increase in intensity in the CO on-top region (2090 cm^{-1}) and a blue-shift for the particle defect, step and (1 0 0) derived band around 1952 cm^{-1} (see Sections 6.2 and 7.4). The latter effect can be interpreted to result from a compression of the CO adsorbate layer by NO, similar to the behavior observed upon increasing the CO coverage [60]. Moreover, the strong increase of the on-top CO band indicates a partial change of the adsorption sites of CO from higher coordinated sites to on-top positions. A similar behavior has not yet been reported for single crystal surfaces. A possible explanation for this effect is related to the presence of defects and steps, which – in comparison with the low index Pd single crystal planes – have been shown to exhibit an enhanced tendency for binding CO in on-top geometry [46,60] and thus may facilitate the CO site change as a function of NO coverage.

8.4. NO dissociation

The first MB studies on NO adsorption and dissociation on model catalysts were performed by Henry and coworkers [201,204,205]. In these experiments, the NO sticking coefficient and the product spectrum was analyzed applying a modulated NO beam to Pd/MgO(1 0 0) model catalysts with particle sizes between approximately 3 and 15 nm in a temperature range between 440 and 700 K. There were several remarkable results found in this work. Firstly, the transient NO uptake was observed to always exceed NO desorption, indicating a substantial probability for NO dissociation and reduction. As the main product, N_2 was found, with a negligible rate of N_2O formation. Secondly, there were indications for the presence of different types of adsorbed nitrogen species. The latter was concluded from the fact that: (i) the N_2 desorption kinetics were characterized by different time constants and (ii) from the observation that strongly adsorbed nitrogen remained on the surface under reaction conditions (as identified via CO titration experiments). Both observations are compatible with the simultaneous presence of more weakly and more strongly bound atomic nitrogen species, as have been discussed previously on single crystal surfaces (see Section 8.1). Moreover, the diffusion of oxygen into subsurface regions was invoked in order to explain the stabilization of the dissociation capacity in pulsed experiments [201]. This effect was later investigated in titration experiments using a CO beam, showing that indeed the oxygen coverage on the Pd particles rapidly decreases as a function of time at reaction temperatures above 500 K [205]. In addition to these general effects, clear particle size and structure dependencies were observed [201]. For example, the NO equilibrium coverage was found to be significantly enhanced on smaller particles. In addition, to the dissociation kinetics, the NO adsorption and desorption kinetics was investigated in the same work. The corresponding results were summarized in Sections 5.1 and 5.2.

In our group, we have recently studied the NO adsorption and dissociation on $Pd/Al_2O_3/NiAl(1\,1\,0)$ model catalysts using TR-IRAS and MB techniques, mainly focusing on the possible role of the different reaction sites available on the Pd particles [234,238]. Here, the NO dissociation is of special interest considering the pronounced structure dependence observed for single crystal surfaces and supported particle systems (see Section 8.1).

In order to investigate the dissociation kinetics, the Pd model catalyst was exposed to an NO beam and IR spectra were recorded as a function of time and surface temperature. As discussed in the previous section, the different bands in the NO stretching frequency region can be assigned to a majority of (1 1 1) facets and other sites such as (1 0 0) minority facets, steps, edges or other defects. The important point with respect to kinetic studies is that the various sites are occupied up to elevated temperatures and, therefore, allow monitoring of the occupation of the corresponding adsorption and reaction sites under reaction conditions. With increasing reaction time, the corresponding band intensities decrease, indicating the accumulation of the dissociation products, i.e. atomic nitrogen and oxygen, which block the NO adsorption sites on the Pd particles. Some selected spectra taken under reaction conditions are reproduced in Fig. 55a (from [238]). In general, it was observed that at elevated temperatures a complete loss of the adsorption capacity occurred. At low reaction temperatures around 300 K, however, the NO signal was found to approach a constant residual value, indicating a partial poisoning by atomic nitrogen and oxygen, only [238].

The analysis of the corresponding spectra as a function of temperature showed that the three spectral NO stretching frequency regions exhibit an entirely different dependence on exposure. Specifically, it was found that the bands in those regions primarily assigned to NO in on-top and bridge sites on (1 0 0) facets, steps and edges (I and II in Fig. 55a) decrease in intensity immediately after admission of the beam, whereas the band assigned to (1 1 1) facets (III in Fig. 55a) remains unaffected initially [238]. From this, it was concluded that the atomic dissociation products of NO preferentially occupy particle edges, defects and (1 0 0) sites, whereas the (1 1 1) facets are initially affected to a lesser extent. A similar observation was made in an STM study of oxygen adsorption on the same Pd model catalyst, showing preferential adsorption at particle edges [607]. Also, this effect is comparable to the behavior of atomic carbon discussed in Section 7.4.

It should be pointed out, however, that the preferential occupation of specific sites on the Pd particles does not automatically imply that these sites are also most active for NO dissociation. Instead, the step, edge and (1 0 0) sites may also represent energetically preferred chemisorption sites at which the atomic co-adsorbates are accumulated, provided that their surface mobility is sufficiently high. Such a preference would, e.g. be compatible with theoretical investigations for atomic nitrogen adsorption, in which some energetic preference for (1 0 0) sites and steps over (1 1 1) facets was found [617].

The situation can be clarified by comparing the NO dissociation behavior as a function of temperature. Assuming that in accordance with the structure sensitivity for NO dissociation (Section 8.1) only specific sites on the particles are responsible for NO dissociation, the fact that the particles eventually lose their full absorption capacity implies that there is diffusion of atomic adsorbates over the particle surface. The fact that particle edge, steps and (1 0 0) facets are preferentially occupied indeed suggests an energetic preference of these sites. The observation that at low temperature only the particle edges, steps and (1 0 0) sites are modified and that the reaction stops before the (1 1 1) facets are affected points to the fact that no or only very little dissociation occurs on the (1 1 1) facets of the particles and that the limited mobility of atomic nitrogen and oxygen at low temperature prevents diffusion of these species onto the (1 1 1) facets [238].

Spectroscopically, this hypothesis was verified by a detailed analysis of the spectral shifts of the NO stretching frequency bands during NO dissociation (see Fig. 55a, from [238]). At elevated sample temperatures a pronounced blue-shift was observed for all bands in the NO stretching frequency region upon accumulation of the atomic reaction products. This effect was interpreted on the basis of co-adsorption studies discussed in Section 8.3 (see [235]). The blue-shifts observed upon oxygen co-adsorption (compare, e.g. [596,643]) are typically attributed to a strengthening of the N–O bond due to the electronegative oxygen co-adsorbate, reducing the NO $2\pi^*$ electron density. Similar effects are expected for co-adsorbed nitrogen. As a result, the blue-shift of the NO spectral features was interpreted to be due to the presence of co-adsorbed atomic nitrogen and oxygen in the direct vicinity of the

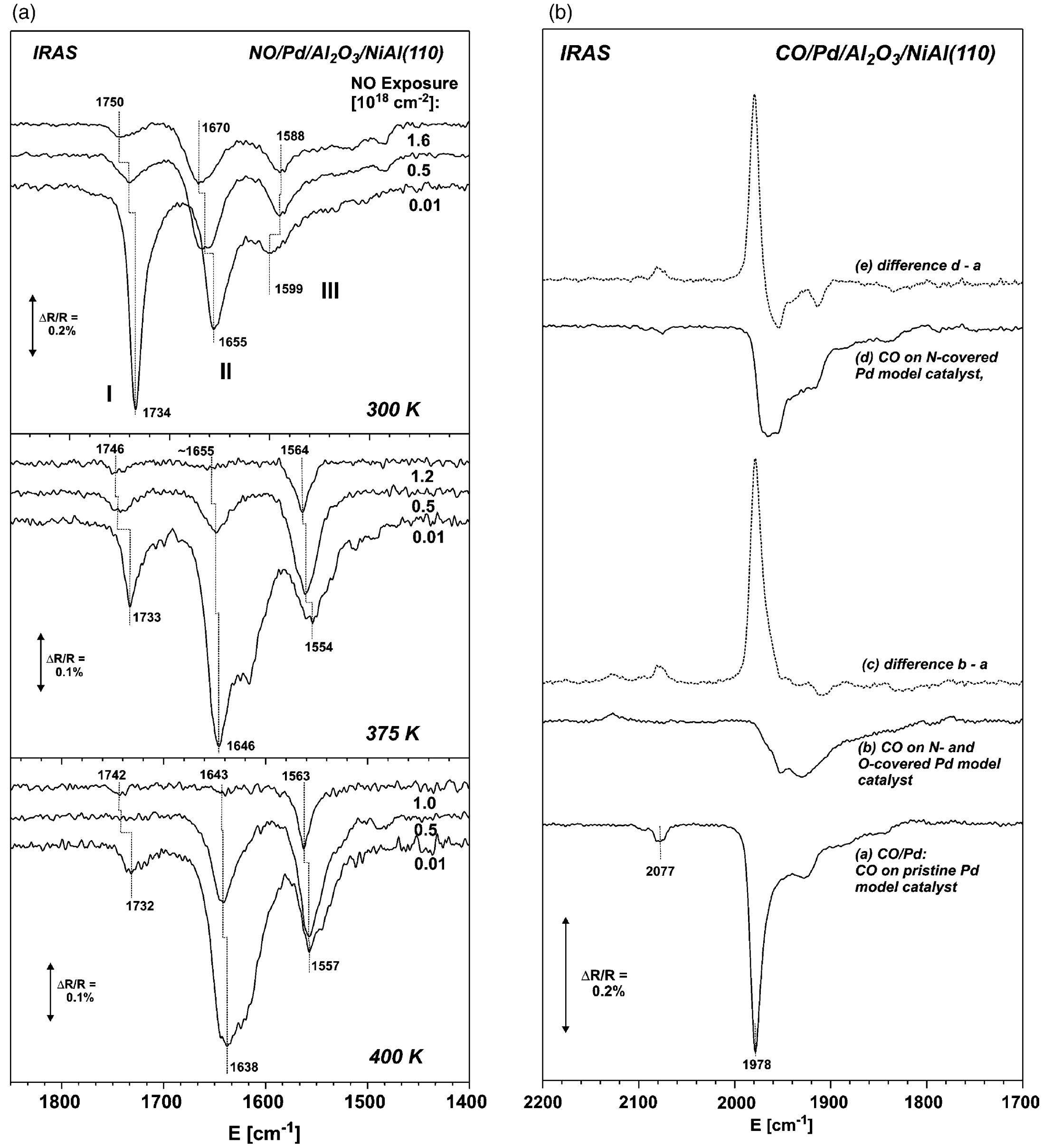

Fig. 55. Identification of adsorption sites on a Pd/Al_2O_3/NiAl(1 1 0) model catalyst occupied by atomic co-adsorbates: (a) IR spectra of the NO stretching frequency region recorded at different surface temperatures during exposure to a molecular beam of NO and (b) CO used as a probe molecule. IR spectra of the CO stretching frequency region were recorded after CO saturation of the pristine Pd model catalyst. The O pre-covered and N pre-covered Pd particles were prepared by exposure to NO, and for the N pre-covered particles by exposure to NO and subsequent removal of oxygen by CO oxidation, from [238].

corresponding NO species. Accordingly, the fact that for elevated reaction temperatures similar shifts were observed for all spectral regions implies the presence of the atomic reaction products on all particle sites. At low sample temperature, on the other hand, only the spectral regions attributed to particle edges, steps and (1 0 0) facets (I and II in Fig. 55a) were found to be subject to a blue-shift, whereas the feature related to (1 1 1) facets (III in Fig. 55a) was observed to undergo a weak red-shift instead. According to the above arguments, this observation was interpreted as due to the absence of atomic dissociation products on the particle facets, indicating suppressed diffusion of the atomic species from the active dissociation sites onto the (1 1 1) facets and a suppression of NO dissociation after occupation of these active sites.

An alternative method for the assignment of specific reaction sites on the catalyst particles, is the use of CO as a probe molecule, as was discussed in Section 7.4. In order to further verify the above results on the assignment of sites, corresponding experiments were performed for the NO dissociation reaction on Pd/Al_2O_3/NiAl(1 1 0) (see Fig. 55b, from [238]). Following the spectroscopic assignment for adsorbed CO on the supported Pd model catalyst discussed in Sections 6.3 and 7.4, CO can be used as a probe for the occupation of particle sites by strongly bound atomic species. For this purpose, a partially nitrogen and oxygen-covered surface was prepared by NO exposure at elevated temperature, followed by CO saturation below the reaction temperature for CO oxidation. Similarly, purely nitrogen-covered particles can be prepared by selectively removing oxygen through applying a pulse of CO above the reaction temperature for CO oxidation (before CO saturation below reaction temperature in order to use CO as a probe). The corresponding CO IR spectra are displayed in Fig. 55b. In all cases, it was observed that only weak changes occurred in the spectral region assigned to the particle (1 1 1) facets, whereas the frequency region assigned to bridge-bonded CO on the particle edges, steps, defects and (1 0 0) facets was strongly attenuated. This effect was most pronounced for the partially nitrogen and oxygen-covered particles, but still rather strong in the case in which only nitrogen was present. In line with the results obtained from the IR spectra of NO adsorption, this behavior indicates that the adsorption of both nitrogen and oxygen preferentially occurs at or near the particle steps, edges and defects and (1 0 0) facets, leading to a modification of the adsorption properties of these sites.

This result emphasizes the value of IR spectroscopy of adsorbed CO used as a sensitive probe molecule even in the case of relatively complex surfaces. There is a second aspect, which is noteworthy, however, which is the observation that CO IR spectra exhibit some chemical specifity to the nature of the co-adsorbed species. For example, it was found that carbon co-adsorption results in a strong population of on-top sites by CO under the experimental conditions applied here (see Section 7.4, also [237]), whereas the nitrogen and oxygen co-adsorbates apparently do not show this effect (compare also [454]). Such differences arise from the fact that not all CO adsorption sites are affected in a similar manner by all co-adsorbates. Possible explanations for these dissimilarities in CO adsorption as a function of co-adsorbate species include different influences of the co-adsorbate on the electronic structure of the surrounding metal atoms, but also the occupation of different sites such as, e.g. the possible formation of subsurface species, which has been suggested in the case of co-adsorbed carbon [566].

The development of experimental procedures, which allow the monitoring and manipulation of site occupation on the active particles, opens up the possibility to investigate the influence of specific co-adsorbates on the catalytic activity of the related sites. A corresponding experiment is briefly illustrated in Fig. 56 (from [234]), in which the effect of atomic oxygen and nitrogen on the NO dissociation was probed. According to the above discussion, the two NO stretching frequency bands observed could be assigned to NO adsorbed at (1 1 1) facets on the one hand and defects, steps, edges and (1 0 0) sites on the

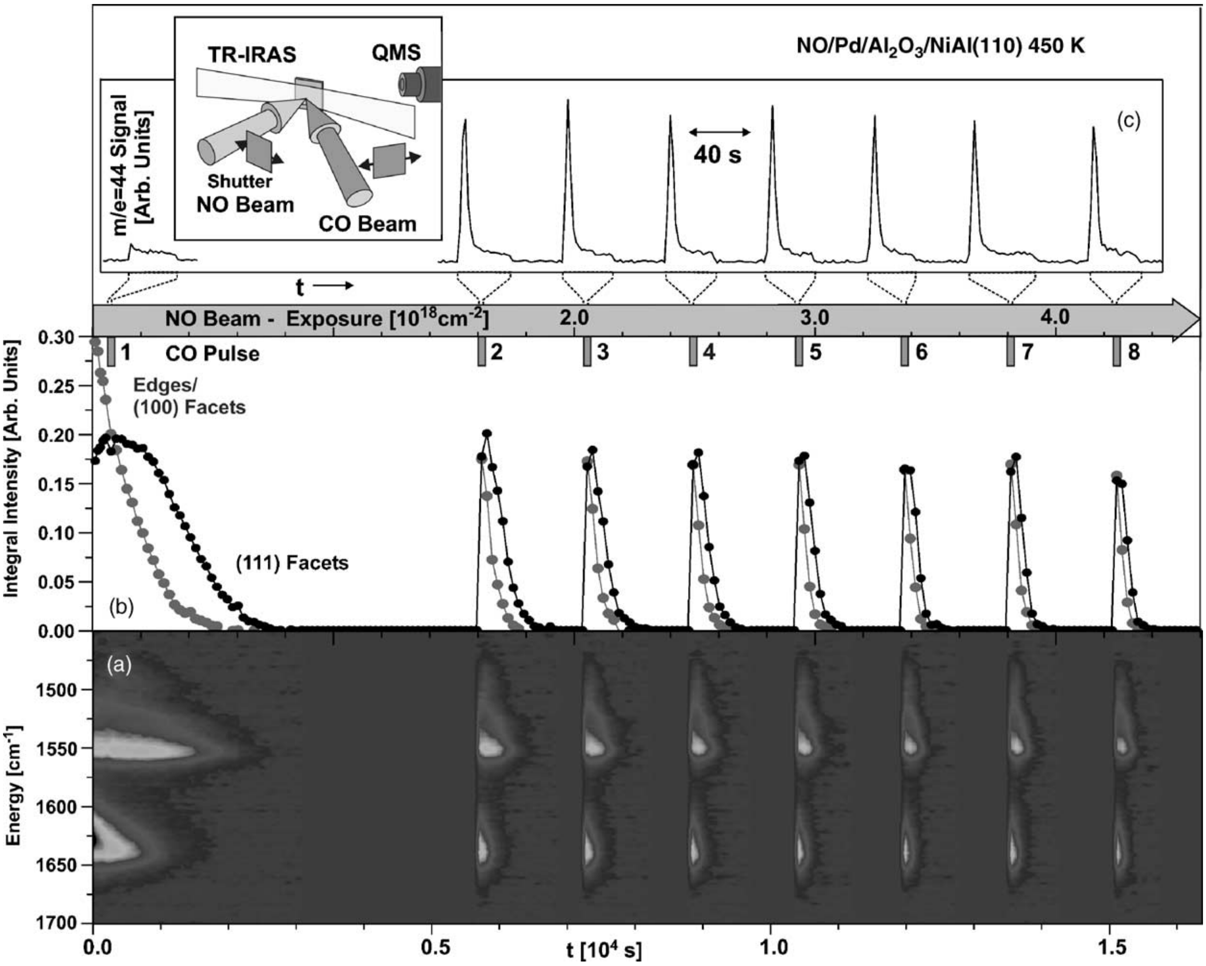

Fig. 56. TR-IRAS experiment monitoring the site-occupation during NO dissociation on a Pd/Al_2O_3/NiAl(1 1 0) model catalyst (6 nm particle size): (a) development of the NO absorption bands as a function of NO exposure and CO pulsing; (b) integral intensity of the two absorption bands in the NO stretching frequency region; (c) CO_2 evolution during CO pulsing, from [234].

other. As described before, the latter was observed to vanish first as a result of preferential adsorption of atomic nitrogen and oxygen in the vicinity of edge, step and (1 0 0) sites. Finally, the particles become fully covered by the atomic dissociation products leading to a complete loss of the NO adsorption capacity. Again, a CO pulse could be used to completely remove atomic oxygen from the particles via oxidation to CO_2. The process is fast on the time-scale of NO dissociation and thus makes it possible to differentiate between the effect of adsorbed atomic oxygen and nitrogen on the dissociation activity. The corresponding experiment (see Fig. 56) showed a full recovery of the NO band from (1 1 1) facets, whereas the edge, step and (1 0 0) band was found to be partially restored only. In line with previous discussions in this section and in Section 8.1, this observation was interpreted in terms of the existence of a strongly bound nitrogen species, which remains adsorbed on the particles under the reaction conditions applied and which is located preferentially in the vicinity of edge and step sites. Beyond the nitrogen coverage level, defined by this strongly adsorbed species, there is no further accumulation of nitrogen as indicated by the constant CO_2 yield in successive titration experiments. Another important observation in these experiments is the fact that the rate of NO dissociation was found to be significantly enhanced after NO initial exposure and oxygen removal, i.e. on the partially nitrogen pre-covered surface. Although the microscopic origin of this effect is not fully understood yet, this observation shows that the presence of the atomic co-adsorbate species, which are preferentially located in the vicinity of the most active sites including steps, edges, defects and (1 0 0) domains, critically control the dissociation activity. Different effects have been discussed which might contribute to the observed effect on the dissociation rate, including, e.g. a reduced site blocking in the regime of high NO coverage or the influence of the co-adsorbate on the electronic structure of the metal and, therefore, on the activation barrier for NO dissociation [234].

Finally, it should be noted that in addition to the work on Pd model catalysts, the adsorption and dissociation of NO has recently been studied on Cu particles on Al_2O_3/NiAl(1 1 0) by Raval and coworkers [242]. The most remarkable aspect from this work is that it illustrates that NO decomposition can proceed via an alternative mechanism at low reaction temperature. The behavior, which is similar to the one observed for NO on Cu single crystal surfaces [634], involves NO chemisorption via a precursor mechanism, producing NO adsorbed in bridge and hollow sites, followed by the conversion to NO dimers. The $(NO)_2$ was then found to decompose to N_2O, which can either dissociate to form N_2 and adsorbed oxygen or – at higher coverages – can desorb molecularly.

8.5. NO–CO reaction

The first MB study on the NO–CO reaction on a supported catalyst system was reported by Valden et al. [623]. This work is also unique in a second respect, which is that the authors used a conventional γ-alumina based Pd catalyst, prepared by wet impregnation, as a coating of a thin metal foil. Of course, the chemical composition and structure of this system is much less well-defined as the UHV-prepared model catalyst used in later studies [42,178,202,204,205].

Henry and coworkers investigated the CO–NO reaction systematically as a function of NO and CO pressure, sample temperature and particle size [202,204,205], using Pd/MgO(1 0 0) model catalysts with particle sizes between approximately 3 and 15 nm. A typical product spectrum as a function of sample temperature is reproduced in Fig. 57a (from [204]). It was reported that the main product was N_2 with only a very small fraction of N_2O being produced. From this result and the observation that NO reduction was only observed at temperatures at which NO dissociation occurs, it was concluded that NO reduction occurred via dissociative adsorption of NO only. At temperatures at which NO dissociation is negligible, NO exposure was found to lead to CO displacement only, without CO_2 production [205]. It should be noted at this point that at low reaction temperatures other reaction pathways were suggested or observed including, e.g. a direct reaction of NO and CO (see, e.g. discussion below [178]) or NO decomposition via dimer formation (see Sections 8.4 and 8.2).

Experiments under both steady-state and transient conditions were performed. In Fig. 57a, summary of the steady-state results is given. In general, it was found that the reaction rate goes through a maximum located at temperatures around 500–550 K, depending on the reactant pressure and structural properties of the model catalyst. At low temperature, NO dissociation was generally identified as a critical step in the reaction sequence, which is hindered if the NO and CO coverages are high. Evidence for the rate-limiting character of NO dissociation was also derived from transient experiments [204]. At high

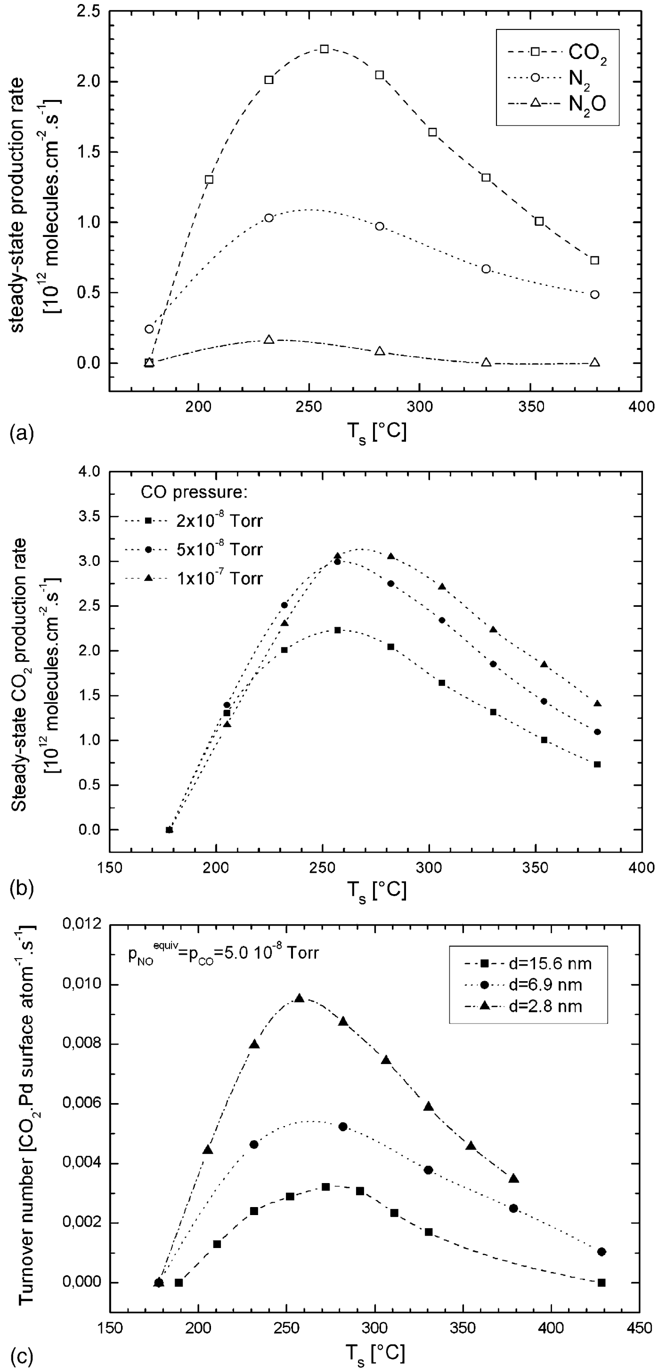

Fig. 57. (a) Steady-state production of CO_2, N_2 and N_2O during the CO–NO reaction from on a Pd/MgO(1 0 0) model catalyst (2.8 nm particle size) as a function of temperature, from [204]; (b) steady-state production of CO_2 from a Pd/MgO(1 0 0) model catalyst (2.8 nm particle size) as a function of CO partial pressure, from [204]; (c) CO_2 TOF as a function of particle size and temperature, from [202].

temperatures, the desorption of both NO and CO becomes fast and leads to a decreasing reaction rate with increasing temperature. The identification of the RDS at high temperature is more complex and depends on the reactant fluxes or pressures, similar as in the case of CO oxidation (see, e.g. in Sections 5.1 and 6.2). Under conditions of high NO flux leading to high steady-state oxygen coverage and moderately high temperatures, the RDS can be CO adsorption as suggested by Piccolo and Henry [204], but in general the other steps including nitrogen recombination may have a substantial DRC as well (see, e.g. [465–469] for a definition and discussion of the terms RDS and DRC).

In addition to the steady-state experiments, additional kinetic information can be derived from transient experiments. Experiments using both modulated CO and NO beams have recently been performed by Henry and coworkers, some of which are summarized in Fig. 58 [205]. Starting from the Pd catalyst immediately after preparation, it was found that the NO dissociation probability was initially very large, but part of the nitrogen was forming a strongly bound species, not taking part in further reactions. After several NO pulses, the adsorption–desorption process showed a reversible component

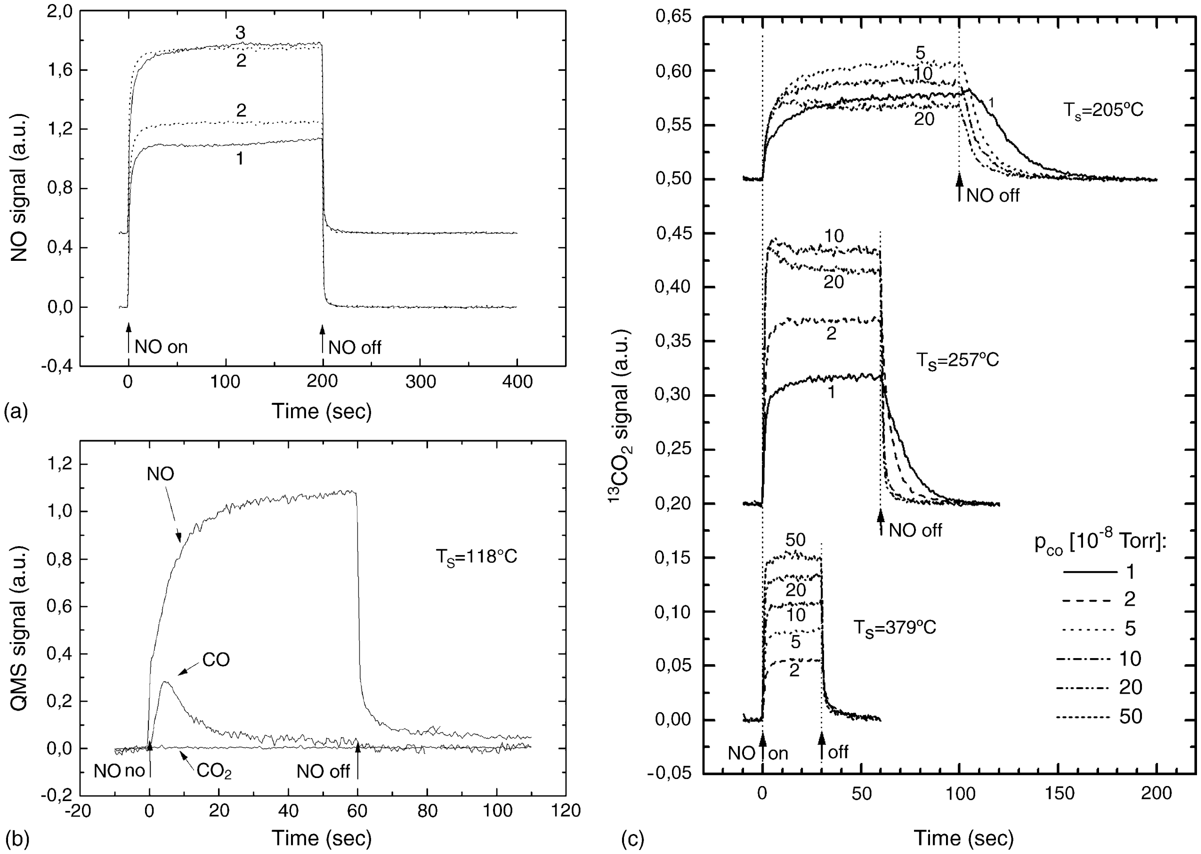

Fig. 58. (a) NO adsorption–desorption transients on a Pd/MgO(1 0 0) model catalyst at 330 °C, (1) on the clean sample, (2) under steady-state conditions and (3) after exposure to CO; (b) NO and adsorption–desorption transients and CO desorption during exposure of the CO pre-covered model catalyst to NO (118 °C); (c) systematic study of the transient CO_2 production rate as a function of CO partial pressure and surface temperature, from [205].

only (see Fig. 58a). Removal of atomic oxygen by CO titration did not restore the original dissociation rate, indicating the presence of the strongly bound nitrogen species. Another remarkable observation in this work was that the coverage of surface oxygen was found to rapidly decrease as a function of time. The effect was attributed to a subsurface and bulk diffusion process, as discussed previously (see, e.g. Sections 3.1, 6.1 and 6.2). A transient experiment demonstrating the replacement of pre-adsorbed CO by NO is shown in Fig. 58b. Moreover, it was shown from residence time measurements that the adsorption energy of NO was slightly larger on the Pd particles that the adsorption energy of CO, leading to a significantly higher NO coverage at typical reaction temperatures [205] (see also Section 5.2). Results of a first systematic MB study of the transient kinetics of the CO–NO reaction are reproduced in Fig. 58c (from [205]). This type of data is essential in microkinetic modeling of the reaction (see Section 8.6).

The transient kinetics were investigated at different sample temperatures using a modulated NO beam and varying the CO background pressure. Qualitatively, the results can be understood as follows: at low reaction temperature the reaction is mainly controlled by NO dissociation. The CO and oxygen surface coverage, however, strongly depend on the CO pressure. At low CO pressure a large oxygen coverage is built up, leading to the slow transient response. At high CO pressure, the steady-state oxygen coverage is lower and, consequently, is built up more rapidly. In addition, the higher CO steady-state coverage at high CO pressure can lead to a further inhibition of NO dissociation and decrease in the steady-state rate. With increasing temperature the CO steady-state coverage decreases rapidly and, as a result, the maximum in the rate as a function of CO pressure shifts toward higher values. The transient behavior upon termination of the NO beam is indicative of the steady-state NO coverage. The decrease is slow for low CO pressures and low temperatures, indicating high steady-state NO coverage. For highest steady-state coverages, an transient increase in reaction rate was observed upon termination of the NO beam, which was attributed to a transient maximum in the dissociation rate occurring as a result of decreasing site blocking after partial desorption or reaction.

In addition to the quite detailed information on the general kinetics of the NO–CO reaction, the most remarkable result from the above studies is, however, the observed dependence on particle size and structure. In their first study, Piccolo and Henry reported strong differences of the TOF as a function of particle size, with the largest values observed for the smallest particles [202] (see Fig. 57c). The authors rescaled these results in order to account for the capture zone effect by calculating an effective reaction probability. The reaction probability takes into account the NO flux toward the active particle both via the gas phase and via trapping and diffusion on the support [204]. As discussed in Section 5.1, this approach is valid if the NO adsorption is the RDS, i.e. if the reaction probability for NO is high (so that the largest fraction of NO reaching the particles is immediately consumed in the reaction). Under conditions in which the reaction probability is low, however, i.e. at low or very high reaction temperature or at high NO flux, the capture zone has no kinetic relevance and direct comparison of the effective reaction probabilities including fluxes via the capture zone would not be appropriate.

The particle size dependence could, at least to some extent, be rationalized on the basis of morphological differences as a function of particle size [202,204,205]. In particular, it was found that the larger particle exhibited a larger fraction of (1 0 0) facets as a result of coalescence processes which occur during the growth. In contrast, the smaller particles expose a larger fraction of (1 1 1) facets. According to the discussion in Section 8.1, these (1 0 0) facets as well as stepped or open parts of the particle surface are expected to be subject to a partial deactivation due to the formation of strongly bound atomic nitrogen species [588,610,611,621], see also [570,592], whereas this effect is less pronounced on the (1 1 1) facets. For this reason, the latter remain more active under reaction conditions. In this sense, the particle size dependence of the reaction rate observed for the NO–CO reaction on the Pd model catalysts would be closely related to the morphology of the particles, rather than their simple size.

In addition to the studies on relatively large Pd nanoparticles discussed above, MB experiments on the kinetics of the NO–CO reaction on small size-selected Pd_n clusters with $1 \leq n \leq 30$ deposited on MgO(1 0 0)/Mo were recently performed by Heiz and coworkers [42,178]. There were several remarkable results derived from these experiments. Firstly, it was found that clusters up to Pd_4 were inert with respect to the NO–CO reaction, whereas a non-monotonical increase of CO_2 production was observed with increasing cluster size for the larger Pd aggregates. Furthermore, TPD experiments revealed two CO_2 desorption features around 145 and 300 K. On the basis of IR data, the authors attributed the low temperature CO_2 production to a LH reaction channel involving molecularly adsorbed CO and NO, whereas the second channel was assigned to the conventional mechanism starting by dissociation of molecularly adsorbed NO, followed by a LH reaction step involving O and CO. The negligible low temperature CO_2 production for $n < 20$ was attributed to the higher dissociation efficiency of these clusters.

In a second experiment, Heiz and coworkers investigated the kinetics of the high temperature reaction channel as a function of cluster size and temperature, dosing CO from the background pressure and NO via a pulsed MB source [42,178] (see Fig. 59). As already discussed in connection with the CO oxidation

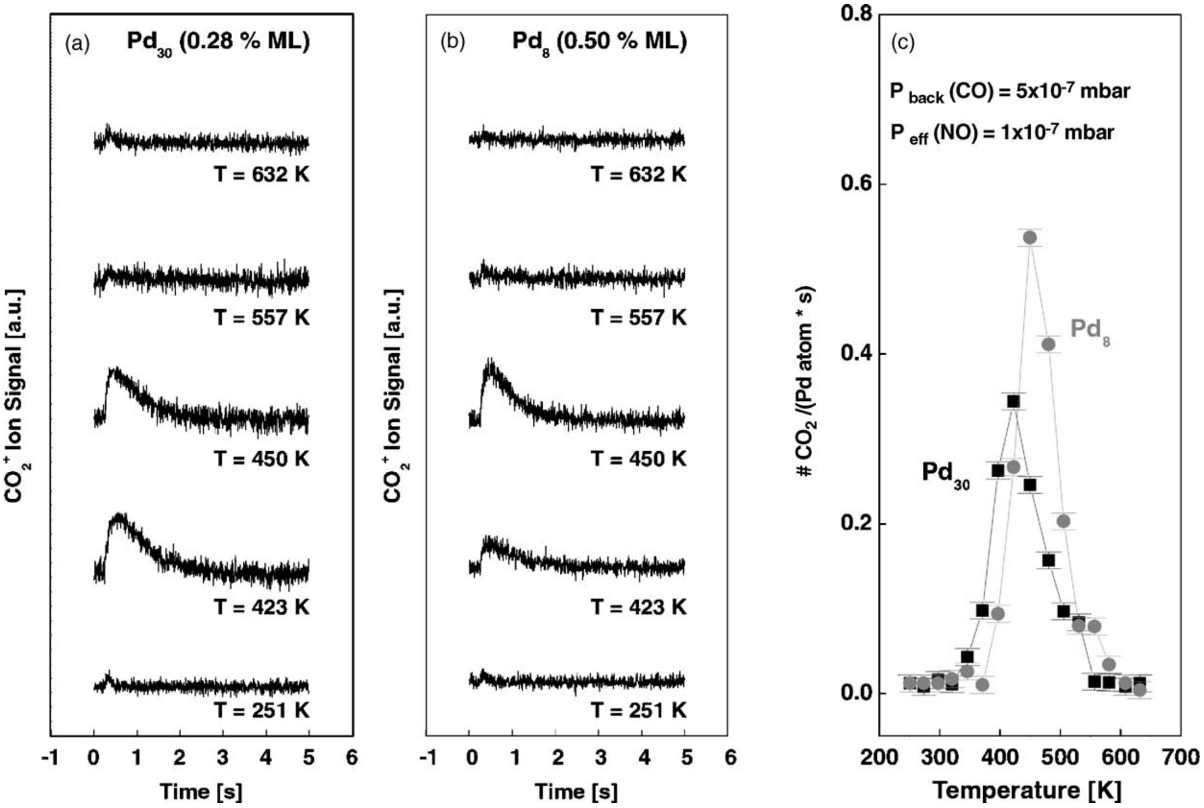

Fig. 59. (a and b) CO_2 formation rates measured for mass-selected Pd_{30} and Pd_8 clusters deposited on MgO(1 0 0). CO was dosed from the gas background and NO pulses were applied via a pulsed nozzle MB source; (c) TOFs as calculated from the experiments displayed in (a) and (b), from [178].

experiments (see Section 6.2), it is very difficult to quantitatively compare the TOF and reaction probabilities calculated in this study to other work on supported particle systems, due to the fact that the measurements were performed in a transient mode and under experimental conditions, which strongly differ from those used in previous work. Nevertheless, some remarkable observations can be made considering the temperature dependence of the maximum TOF (see Fig. 59c). It was found that the rate maximum appeared at temperatures substantially below the values observed for single crystal surfaces. In addition, the value strongly depended on cluster size. The authors, tentatively related these differences to differences in the adsorption energy of reactants and intermediates as a function of cluster size: desorption of CO and NO as well as nitrogen recombination was observed to occur at lower temperature as compared to single crystal surfaces and larger particles. This effect is also expected to shift the maximum rate for CO–NO dissociation to lower temperatures.

8.6. Microkinetic simulations

The experimental work and microkinetic models for the NO–CO reaction on Rh catalysts have recently been reviewed by Zhdanov and Kasemo [574]. For Pd based catalysts, kinetic models are more rare, but recently some attempts have been made to reproduce the MB experiments discussed in the previous section on the basis of detailed MF [624] and MC [625] models.

Schematically, some reaction steps are summarized in Fig. 60, which might be of relevance, according to the discussion in the previous sections. The initial step is the adsorption of NO, which can occur on the support and on the active particles. Depending on the reaction probability or (in other words, on the reversibility of the adsorption step) surface diffusion processes between the support and the particles, i.e. capture zone effects, have to be taken into account. Prevot and Henry included the capture zone for NO in their model via a scaling factor of the NO flux, which according to the previous discussion is appropriate,

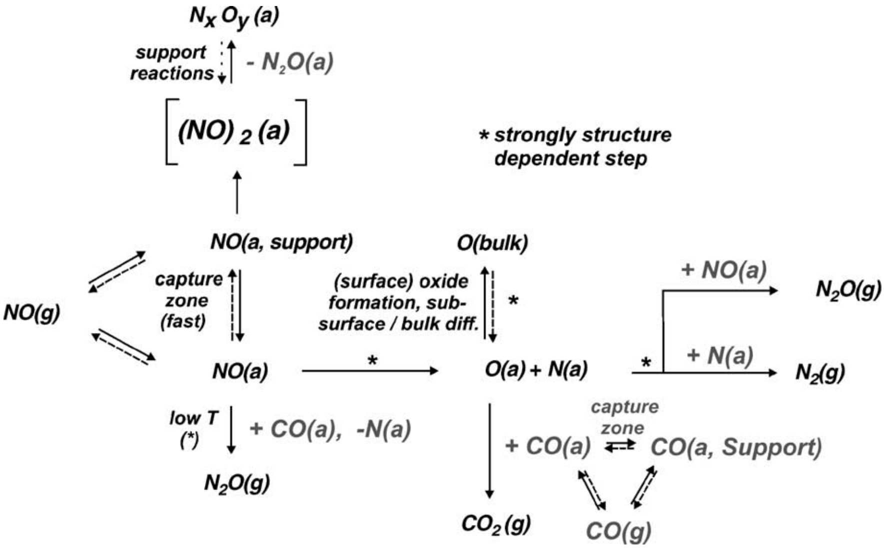

Fig. 60. Schematic representation of various microscopic reaction steps involved in the CO–NO reaction and their possible relation to structure and size dependencies of the reaction kinetics.

however, only in the limit of high NO reaction probability (i.e. NO adsorption is the RDS, see Section 5.1) [624]. Moreover, a complete description would have to take into account the CO capture zone as well under reaction conditions in which CO adsorption has a substantial DRC.

In addition to the main reaction pathway involving NO dissociation, support reactions (Section 8.2) and molecular pathways (Section 8.5) could play a role on some supports, but so far little is known about these alternative pathways and their kinetics on well-defined model catalysts. In particular, the investigation of the kinetics of support reactions and transfer processes between the support and the active particles will represent an important challenge for future kinetic studies.

The NO dissociation as well as the nitrogen recombination represents two important reaction steps, both of which are known to show pronounced structure dependences. Some information on the activation barriers and kinetic parameters of these steps can be derived from single crystal data (see Section 8.1), but the main problem, associated with the kinetics of these elementary steps is the description of their coverage dependence. In particular, NO dissociation is strongly inhibited in the presence of any type of adsorbate or co-adsobate (e.g. NO and CO at low temperature or strongly bound N at high temperature). In their MF model, Prevot and Henry included rather simple dependences of the activation energy for NO dissociation and NO desorption on the total adsorbate coverage [624]. Using this type of model, they managed to reproduce semi-quantitatively the steady-state reaction rates as a function of NO and CO pressure and temperature as well as most of the features observed in the transient kinetics. As for any complex microkinetic model, its accuracy remains a matter of discussion, as long as there is no in situ verification of the coverage and reaction rates of all surface species under reaction conditions. With the development of time-resolved in situ spectroscopies (e.g. vibrational spectroscopy or photoelectron spectroscopy) in combination with the MB experiments described above. This type of verification or refinement, however, may become feasible in future studies.

As pointed out in connection with the discussion of CO oxidation (Section 6.2), the reaction kinetics on supported particle systems is substantially more complicated in the presence of different reaction sites, such as different crystallographic facets, steps, edges or interface sites. As discussed in Section 6.2, such effects can in principle be included in a MF description. In view of the limited knowledge on the numerous kinetics parameters even for the case of a homogeneous surface, the description of particle size and structure dependent kinetic effects for the CO–NO reaction on the basis of a microscopically motivated heterogeneous MF model, similar as for the CO oxidation, appear rather problematic at the present state of knowledge. Still, some attempts have been made recently to qualitatively reproduce the size and structure dependencies on the basis of MC simulations [625]. For these simulations, models were constructed, which reproduced the particles sizes and (1 1 1) to (1 0 0) facet ratios used in the experimental studies. The particle size dependent effects found in these simulations, were mainly related to the different ratios of crystallographic facets as well as to finite size effects on small facets due to the large fraction of facet edge sites.

Another point, which is quite poorly understood is the role of adsorbed atomic oxygen, produced during NO dissociation. In their MB experiments, Prevot et al. have observed oxygen depletion of the surface at reaction temperatures and have attributed this effect to a bulk diffusion process [205]. Accordingly, the bulk diffusion channel was taken into account in their MF model for the CO–NO reaction [624]. The exact nature of the oxygen species on Pd remains rather unclear, however. As pointed out in previous discussions there has been a large number of experimental and theoretical investigation on the interaction of oxygen with Pd surfaces suggesting the formation of various adsorbate structures, surface oxides, subsurface and bulk oxygen species and oxide formation [274–298]. If is, e.g. not clear, whether surface oxide structures are formed under the reaction conditions applied in these experiments and what could be the possible role of Pd surface oxides and subsurface and bulk oxygen in the reaction kinetics. For the supported particle system, the situation is further complicated by the simultaneous presence of different crystallographic facets and defect sites with different oxidation behavior (compare, e.g. [289,292]).

In conclusion, it should be pointed out that with respect to its kinetic behavior, the CO–NO reaction systems turns out to be a rather complex process and the kinetics of several of the elementary processes remain very poorly understood. The situation is further complicated by the presence of molecular and atomic adsorbates on the active particles under reaction conditions, which critically control the rate of several elementary steps. Although it is known from many experiments that these adsorbates give rise to coverage dependencies, which play a key role in the kinetics (see Section 8.1 or 8.4), very little quantitative data is available which could serve as a basis for kinetic modeling at this point. As a result, present microkinetic descriptions are rather crude and involve a large number of unknown parameters. On supported particle systems the situation is further complicated by the coexistence and coupling of different active sites with strongly different activity.

As pointed out before, the experimental information required at this point is in principle within reach. In particular, quantitative kinetics studies which focus on systematic kinetic experiments and quantitative time-resolved spectroscopy of surface species could provide the necessary database for detailed microkinetic models. In addition, theoretical investigations may become increasingly helpful in kinetic modeling, providing accurate information on rate constants of specific elementary steps (see, e.g. [510]).

9. Summary and outlook

In this review, we have summarized the present state of MB experiments, aiming at an understanding of reaction kinetics on complex model catalysts at the microscopic level.

We have briefly summarized the experimental pre-requisites and foundations of MB work on complex surfaces, pointing out that the development of TR surface spectroscopies is one of main challenges in future studies. The principle advantages of MB based kinetic experiments are related to the extremely well-controlled conditions under which the measurements are performed. The single scattering conditions of the experiments allow, for example, the precise quantification of reaction probabilities, quantitative and systematic steady-state measurements under isothermal condition, investigations of the transient kinetics via accurate flux modulation, investigations of the adsorption and desorption dynamics or angle-resolved product detection in order to identify specific reaction sites.

On single crystal surfaces, MB techniques are well-established among the major tools that provide detailed insight into the kinetics and dynamics of surface reactions. Applied to more complex surfaces such as supported model catalysts, the kinetic behavior of these systems can be compared in detail to what is experimentally known or expected on single crystal surfaces. In this fashion, specific kinetic effects on model catalysts can be identified. There is a long list of such effects ranging from the role of the catalyst support in the adsorption process or reaction kinetics, via the role of specific reactive sites or different crystallographic facets on the catalyst nanoparticles, the modification of the adsorption or reaction properties of the particle sites by co-adsorbates, poisons or as a result of the modified electronic structure of the particles. Moreover, there are specific nanoscale kinetic effects arising as a result of surface diffusion between different surface areas, coverage fluctuations or restructuring processes of nanometer scale particles. Little is known on such processes at the microscopic scale yet, but there are several examples already, which show that such effects can indeed be related to the catalytic reaction kinetics at the microscopic level. In addition to the quality of the kinetic experiments, an essential prerequisite for such studies is a detailed structural and chemical characterization of the model surfaces. Here, planar supported model catalysts, prepared on the basis of well-defined oxide films or oxide single crystals provide the advantage that very detailed investigations can be performed by applying surface science techniques. In addition, the chemical and structural complexity of the model surfaces is substantially reduced in comparison to real catalysts, which largely simplifies the interpretation and modeling of the kinetic data.

So far, MB experiments on model catalysts have been performed mainly on three types of reaction systems: the CO oxidation, the methanol oxidation and the CO–NO reaction, primarily on Pd model catalysts supported on MgO and Al_2O_3 surfaces and some other systems. In addition, the adsorption kinetics on supported model catalysts has been studied in detail.

A large fraction of the studies on the adsorption and desorption kinetics has focused on the role of the support and the influence of the so-called capture zone on adsorption processes. For several reactants including CO, O_2 and NO, it was shown that the capture zone can indeed dominate the adsorption kinetics, in particular at low reaction temperature. Also, capture zone effects were included in kinetic modeling.

The CO oxidation on metal surfaces is one of best studied and best understood reaction in surface science. Starting from this information, different kinetic effects on supported article systems could be identified by means of MB experiments under transient and steady-state conditions. Here, one rather general issue is the presence of different adsorption and reaction sites on the catalyst nanoparticles. This heterogeneity of the surface and its role in the reaction kinetics has been addressed in detail and the results have been subject to microkinetic simulations. Other phenomena including the diffusion of reactants on the catalyst particles and the occurrence of coverage fluctuations on small particles have also been investigated experimentally and have been interpreted on the basis of detailed models.

The second reaction system, the methanol oxidation, is significantly more complex than the CO oxidation, but with respect to the microkinetic description provides the advantage that it contains several elementary steps, which are well-understood from studies on the CO oxidation system. Here, one of the most interesting aspects is the fact that there are different reaction pathways, i.e. dehydrogenation and CO bond scission, which compete under reaction condition and offer the possibility to study selectivity effects in a simple model system. Based on combined MB/spectroscopy experiments, information on the local selectivity of specific sites on the Pd catalyst particles could be obtained.

The final group of studies has been performed on the CO–NO reaction. What is most interesting about this reaction system is the strong structure dependent effects, which are observed in single crystal studies. Consequently, pronounced kinetic effects are expected to arise on supported nanoparticles as well. Such effects were indeed observed and interpreted on the basis of the microscopic particle morphology. Another critical point for the kinetics of the CO–NO reaction, as well as many other reaction system, is the role of co-adsorbates and their influence on specific reactive sites during reaction. Such effects were identified by MB experiments and surface spectroscopy under reaction conditions, showing a preferential occupation of specific sites by certain adsorbates and experimentally demonstrating their important role in the kinetics.

Eventually, the question remains whether it will be possible to understand reaction kinetics on complex surfaces, such as supported catalysts, at the microscopic level. This goal is particularly challenging in view of the fact that even for single crystal surfaces, there are only very few reaction systems for which a well-founded microkinetic description exists. At the present state of knowledge, the primary goal is the development of basic concepts, which provide a microscopically well-founded description of the reaction kinetics on complex surfaces, rather than a quantitative modeling of all steps involved. Here, the most important point is that the type of experiments described in this review are in principle capable of provide sufficiently detailed data in order to identify the phenomena of interest and allow a experimental verification of kinetic models and concepts.

In comparison to MB experiments on the dynamics and kinetics of surface reactions on single crystal surfaces, it is clear that corresponding work on more complex model catalysts is still in its infancy. As pointed out in Section 1, there are two sides of what is sometimes called the complexity gap between real catalytic reactions on the one side and simple model systems on the other. The first aspect is the structural and compositional complexity of the surfaces, the second aspect is the chemical complexity of the reaction systems. There have been developments along both directions. Nevertheless, it is rather obvious that the model surfaces and model reaction, which from the point of view of surface science appear rather complex, are still simplistic when compared to real catalytic processes. Among the chemical and structural features of catalyst surfaces which have not or rarely been modeled yet are, for example, modified and mixed oxide surfaces, mixed metal particles, promoted and poisoned catalysts or surface oxidation. From the point of view of complexity of the chemical reaction systems, very little or no work has been performed on multiple-reactant or multiple-pathway reaction systems so far.

If and how fast this complexity gap can be closed will depend on the progress made in the development of experimental techniques. One aspect contributing in this field may be an rigorously quantitative approach toward surface chemistry: until now, the majority of reaction studies at surfaces mainly focus on qualitative issues. If we would like to address particle size and support effects or selectivity issues, however, efforts must be made to establish quantitative and systematic methods of experimentation under well-controlled conditions. Here, the MB reactor is at least one approach, which allows easy and systematic variation of reaction conditions, easy automation providing access to large databases and a broad range of detailed kinetic experiments. In addition, detailed microscopic information on the reactive state of the surface is required. Therefore, the development of in situ spectroscopies and microscopies plays a crucial role from an experimental point of view. In addition, theory has been making fast progress, providing additional and reliable information on the mechanisms, energetics and kinetics of specific elementary steps. Combining these different sources of information, a quantitative kinetic modeling of surface reactions even on relatively complex surfaces may become a realistic aim in the near future.

Acknowledgements

We would like to thank the authors of the original articles for the providing articles, artwork and the permission to use their figures in this review. Helpful discussions and fruitful collaborations are acknowledged with M. Bäumer (Bremen, Germany), C.T. Campbell (Seattle, USA), N. Rösch (Munich, Germany), K. Neyman (Barcelona, Spain), C.R. Henry (Marseille, France), B. Kasemo, A.W. Grant (Göteborg, Sweden), V. Zhdanov (Novosibirsk, Russia and Göteborg, Sweden), C.S. Gopinath (Pune, India), G. Scoles (Princeton, USA) and G. Rupprechter, H. Kuhlenbeck, Sh. S. Shaikhudinov and G. Weinberg at the FHI, Berlin. We are grateful to G. Kresse for communicating the results of reference [259] prior to publication.

Concerning the experimental work performed at the FHI, we would in particular like to thank the Ph.D. students, postdocs and other coworkers involved. Here, essential contributions were made by Ingo Meusel, Jens Hartmann, Jens Hoffmann, Swetlana Schauermann, Viktor Johanek, Mathias Laurin and Tobias Schalow. The FHI projects were financially supported by the Deutsche Forschungsgemeinschaft, the Volkswagen Foundation and the Fonds der Chemischen Industrie.

References

[1] J.M. Thomas, W.J. Thomas, Principle and Practice of Heterogeneous Catalysis, VCH, Weinheim, 1997.
[2] H. Heinemann, in: G. Ertl, H. Knözinger, J. Weitkamp (Eds.), Handbook of Heterogeneous Catalysis, vol. 1, Wiley/VCH, 1997, pp. 35–48.
[3] E.K. Rideal, Concepts in Catalysis, Academic Press, London, 1968.
[4] G. Ertl, H. Knoezinger, J. Weitkamp (Eds.), Handbook of Heterogeneous Catalysis, VCH, Weinheim, 1997.
[5] J.A. Dumesic, D.F. Rudd, L.M. Aparicio, J.E. Rekoske, A.A. Trevino, The Microkinetics of Heterogeneous Catalysis, American Chemical Society, Washington, DC, 1993.
[6] P. Stoltze, Prog. Surf. Sci. 65 (2000) 65.
[7] V.P. Zhdanov, Surf. Sci. Rep. 45 (2002) 233.
[8] E.S.J. Lox, B.H. Engler, in: G. Ertl, H. Knözinger, J. Weitkamp (Eds.), Environmental Catalysis, Wiley/VCH, Weinheim, 1999, pp. 1–117.
[9] E.S.J. Lox, B.H. Engler, in: G. Ertl, H. Knözinger, J. Weitkamp (Eds.), Handbook of Heterogeneous Catalysis, vol. 4, Wiley/VCH, Weinheim, 1997, pp. 1559–1633.
[10] T. Engel, G. Ertl, in: D.A. King, D.P. Woodruff (Eds.), The Chemical Physics of Solid Surfaces and Heterogeneous Catalysis, vol. 4, Elsevier, 1982, p. 73.
[11] T. Kreuzer, S.E. Lox, D. Lindner, J. Leyrer, Catal. Today 29 (1996) 17.
[12] R.J. Farrauto, R.M. Heck, Catal. Today 55 (2000) 179.
[13] J.B. Hansen, in: G. Ertl, H. Knözinger, J. Weitkamp (Eds.), Handbook of Heterogeneous Catalysis, vol. 4, Wiley/VCH, Weinheim, 1997, pp. 1856–1876.
[14] M.L. Poutsma, L.F. Elek, P.A. Ibarbia, A.P. Risch, J.A. Rabo, J. Catal. 52 (1978) 157.
[15] J.P. Hindermann, G.J. Hutchings, A. Kiennemann, Catal. Rev. Sci. Eng. 35 (1993) 1.
[16] A. Gotti, R. Prins, J. Catal. 175 (1998) 302.
[17] M. Che, C.O. Bennett, Adv. Catal. 20 (1989) 153.
[18] B.C. Bond, Surf. Sci. 156 (1985) 966.
[19] C.R. Henry, Surf. Sci. Rep. 31 (1998) 231.
[20] V.P. Zhdanov, B. Kasemo, Surf. Sci. Rep. 39 (2000) 25.
[21] N. Takahashi, H. Shinjoh, T. Iijima, T. Suzuki, K. Yamazaki, K. Yokota, H. Suzuki, N. Miyoshi, S. Matsumoto, T. Tanizawa, T. Tanaka, S. Tateishi, K. Kasahara, Catal. Today 27 (1996) 63.
[22] E. Fridell, H. Persson, L. Olsson, B. Westerberg, A. Amberntsson, M. Skoglundh, Top. Catal. 16 (2001) 133.
[23] C. Sedlmair, K. Seshan, A. Jentys, J.A. Lercher, J. Catal. 214 (2003) 308.
[24] W.C. Conner, J.L. Falconer, Chem. Rev. 95 (1995) 759.
[25] G.M. Pajonk, in: G. Ertl, H. Knözinger, J. Weitkamp (Eds.), Handbook of Heterogeneous Catalysis, vol. 3, Wiley/VCH, Weinheim, 1997, pp. 1064–1077.
[26] E. Gillet, S. Channakhone, V. Matolin, M. Gillet, Surf. Sci. 152/153 (1985) 603.
[27] V.P. Zhdanov, B. Kasemo, Phys. Rev. B 55 (1997) 4105.
[28] U. Diebold, Surf. Sci. Rep. 48 (2003) 53.
[29] G. Pacchioni, N. Rösch, Surf. Sci. 306 (1994) 169.
[30] S. Shaikhutdinov, R. Meyer, D. Lahav, M. Bäumer, T. Klüner, H.-J. Freund, Phys. Rev. Lett. 91 (2003) 076102.
[31] R. Meyer, M. Bäumer, S.K. Shaikhutdinov, H.-J. Freund, Surf. Sci. Lett. 546 (2003) L813.
[32] T.W. Hansen, J.B. Wagner, P.L. Hansen, S. Dahl, H. Topsoe, C.J.H. Jacobsen, Science 294 (2001) 1508.
[33] K. Hayek, R. Kramer, Z. Paál, Appl. Catal. A Gen. 162 (1997) 1.

[34] V.P. Zhdanov, B. Kasemo, J. Catal. 170 (1997) 377.
[35] V.P. Zhdanov, B. Kasemo, Surf. Sci. 405 (1998) 27.
[36] A.M. Doyle, S.K. Shaikhutdinov, S.D. Jackson, H.-J. Freund, Angew. Chem. Int. Ed. 42 (2003) 5240.
[37] K.A. Fichthorn, E. Gulari, R.M. Ziff, Phys. Rev. Lett. 63 (1989) 1527.
[38] Y. Suchorski, J. Beben, E.W. James, J. Evans, R. Imbihl, Phys. Rev. Lett. 82 (1999) 1907.
[39] V.P. Zhdanov, B. Kasemo, Surf. Sci. 496 (2002) 251.
[40] H. Graoui, S. Giorgio, C.R. Henry, Surf. Sci. 417 (1998) 350.
[41] A. Berko, F. Solymosi, J. Catal. 183 (1999) 91.
[42] U. Heiz, E.L. Bullock, J. Mater. Chem. 14 (2004) 564.
[43] D.W. Goodman, Surf. Rev. Lett. 2 (1995) 9.
[44] H.-J. Freund, M. Bäumer, H. Kuhlenbeck, Adv. Catal. 45 (2000) 333.
[45] M. Bäumer, J. Libuda, H.-J. Freund, in: R.M. Lambert, G. Pacchioni (Eds.), Chemisorption and Reactivity on Supported Clusters and Thin Films, Kluwer Academic Press, Dordrecht, 1997, p. 61.
[46] M. Bäumer, H.-J. Freund, Prog. Surf. Sci. 61 (1999) 127.
[47] C.T. Campbell, A.W. Grant, D.E. Starr, S.C. Parker, V.A. Bondzie, Top. Catal. 14 (2001) 43.
[48] T.P. St. Clair, D.W. Goodman, Top. Catal. 13 (2000) 5.
[49] T. Hrncir, V. Matolin, V. Nehasil, Surf. Sci. 482–485 (2001) 260.
[50] C.R. Henry, in: A. Wieckowski, E.R. Savinova, C.G. Vayenas (Eds.), Catalysis and Electrocatalysis at Nanoparticle Surfaces, Marcel Dekker, New York, Basel, 2003.
[51] C.R. Henry, C. Chapon, C. Duriez, S. Giorgio, Surf. Sci. 253 (1991) 177.
[52] V. Nehasil, T. Hrncir, S. Zafeiratos, S. Ladas, V. Matolin, Surf. Sci. 454 (2000) 289.
[53] D.R. Rainer, D.W. Goodman, J. Mol. Catal. A 131 (1998) 259.
[54] M. Bäumer, J. Libuda, A. Sandell, H.-J. Freund, G. Graw, T. Bertrams, H. Neddermeyer, Ber. Bunsenges. Phys. Chem. 99 (1995) 1381.
[55] J. Libuda, M. Frank, A. Sandell, S. Andersson, P.A. Brühwiler, M. Bäumer, N. Martensson, H.-J. Freund, Surf. Sci. 384 (1997) 106.
[56] A. Sandell, J. Libuda, P.A. Brühwiler, S. Andersson, M. Bäumer, A.J. Maxwell, N. Mårtensson, H.-J. Freund, Phys. Rev. B 55 (1997) 7233.
[57] K. Wolter, O. Seiferth, J. Libuda, H. Kuhlenbeck, M. Bäumer, H.-J. Freund, Surf. Sci. 402–404 (1998) 428.
[58] K. Wolter, O. Seiferth, H. Kuhlenbeck, M. Bäumer, H.-J. Freund, Surf. Sci. 399 (1998) 190.
[59] K.H. Hansen, T. Worren, S. Stempel, E. Laegsgaard, M. Bäumer, H.-J. Freund, F. Besenbacher, I. Stensgaard, Phys. Rev. Lett. 83 (1999) 4120.
[60] M. Frank, M. Bäumer, Phys. Chem. Chem. Phys. 2 (2000) 3723.
[61] I. Meusel, J. Hoffmann, J. Hartmann, M. Heemeier, M. Bäumer, J. Libuda, H.-J. Freund, Catal. Lett. 71 (2001) 5.
[62] S. Shaikhutdinov, M. Heemeier, J. Hoffmann, I. Meusel, B. Richter, M. Bäumer, H. Kuhlenbeck, J. Libuda, H.-J. Freund, R. Oldman, S.D. Jackson, C. Konvicka, M. Schmid, P. Varga, Surf. Sci. 501 (2002) 270.
[63] M.P. D'Evelyn, R.J. Madix, Surf. Sci. Rep. 3 (1984) 413.
[64] J.A. Barker, D.J. Auerbach, Surf. Sci. Rep. 4 (1985) 1.
[65] M. Asscher, G.A. Somorjai, in: G. Scoles (Ed.), Atomic and Molecular Beam Methods, vol. 2, Oxford University Press, 1988, p. 489.
[66] M.L. Yu, L.A. DeLouise, Surf. Sci. Rep. 19 (1994) 285.
[67] C.T. Rettner, D.J. Auerbach, J.C. Tully, A.W. Kleyn, J. Phys. Chem. 100 (1996) 13021.
[68] A.W. Kleyn, Chem. Soc. Rev. 32 (2003) 87.
[69] A.W. Kleyn, in: D.P. Woodruff (Ed.), The Chemical Physics of Solid Surfaces (Surface Dynamics), vol. 11, Elsevier, Amsterdam, 2003.
[70] A. Hodgson, in: D.P. Woodruff (Ed.), The Chemical Physics of Solid Surfaces (Surface Dynamics), vol. 11, Elsevier, Amsterdam, 2003.
[71] J. Libuda, H.-J. Freund, J. Phys. Chem. B 106 (2002) 4901.
[72] J. Libuda, Chem. Phys. Chem. 5 (2004) 625.
[73] J. Libuda, S. Schauermann, M. Laurin, T. Schalow, J. Hartmann, H.-J. Freund, Monatshefte für Chemie, Chem. Monthly 136 (2005) 59.

[74] J. Libuda, Surf. Sci., in press.
[75] C.R. Henry, in: D.P. Woodruff (Ed.), The Chemical Physics of Solid Surfaces (Surface Dynamics), vol. 11, Elsevier, Amsterdam, 2003.
[76] G. Scoles, Atomic and Molecular Beam Methods, Oxford University Press, Oxford, 1988.
[77] R. Campargue (Ed.), Atomic and Molecular Beams—The State of the Art 2000, Springer, Berlin and Heidelberg, 2001.
[78] S.T. Ceyer, W.J. Siekhaus, G.A. Somorjai, J. Vac. Sci. Technol. 19 (1981) 726.
[79] C. Duriez, C.R. Henry, C. Chapon, Surf. Sci. 253 (1991) 190.
[80] L.A. DeLouise, J. Chem. Phys. 94 (1991) 1528.
[81] M. Rocca, U. Valbusa, A. Gussoni, G. Maloberti, L. Racca, Rev. Sci. Instrum. 62 (1991) 2172.
[82] P.M. Holmblad, J. Wambach, I. Chorkendorff, J. Chem. Phys. 102 (1995) 1.
[83] M. Bowker, P.D.A. Pudney, C.J. Barnes, J. Vac. Sci. Technol. A 8 (1990) 816.
[84] B.N. Eldridge, M.L. Yu, Rev. Sci. Instrum. 58 (1987) 1014.
[85] M. Balooch, W.J. Siekhaus, D.R. Olander, J. Phys. Chem. 88 (1984) 3521.
[86] M.E.M. Spruit, E.W. Kuipers, M.G. Tenner, J. Kimman, A.W. Kleyn, J. Vac. Sci. Technol. A 5 (1987) 496.
[87] F. Pradere, M. Chateau, M. Benslimane, M. Bierry, M. Chatelet, D. Clement, A. Guilbaud, J.C. Jeannot, A.D. Martino, H. Vach, Rev. Sci. Instrum. 65 (1994) 161.
[88] M.G. Tenner, E.W. Kuipers, W.Y. Langhout, A.W. Kleyn, G. Nicolasen, S. Stolte, Surf. Sci. 236 (1990) 151.
[89] K.D. Gibson, S.J. Sibener, J. Chem. Phys. 88 (1988) 791.
[90] L.S. Brown, S.J. Sibener, J. Chem. Phys. 89 (1988) 1163.
[91] J. Liu, M. Xu, T. Nordmeyer, F. Zaera, J. Phys. Chem. 99 (1995) 6167.
[92] S.M. Wetterer, D.J. Lavrich, T. Cummings, S.L. Bernasek, G. Scoles, J. Phys. Chem. B 102 (1998) 9266.
[93] K. Hayek, M. Fuchs, B. Klötzer, W. Reichl, G. Rupprechter, Top. Catal. 13 (2000) 55.
[94] I. Stara, V. Matolin, Surf. Sci. 313 (1994) 99.
[95] R. Denecke, M. Kinne, C.M. Whelan, H.-P. Steinrück, Surf. Rev. Lett. 9 (2002) 797.
[96] J. Häger, H. Walther, Annu. Rev. Mater. Sci. 19 (1989) 265.
[97] J. Libuda, I. Meusel, J. Hartmann, H.-J. Freund, Rev. Sci. Instrum. 71 (2000) 4395.
[98] D.F. Padowitz, K.A. Peterlinz, S.J. Sibener, Langmuir 7 (1991) 2566.
[99] D.A. King, M.G. Wells, Surf. Sci. 29 (1972) 454.
[100] X.C. Guo, D.A. King, Surf. Sci. 302 (1994) L251.
[101] B. Berenbak, D.A. Butler, B. Riedmüller, D.C. Papageorgopoulos, S. Stolte, A.W. Kleyn, Surf. Sci. 414 (1998) 271.
[102] A.M. Efstathiou, X.E. Verykios, Appl. Catal. A 151 (1997) 109.
[103] C.T. Foxon, M.R. Boudry, B.A. Joyce, Surf. Sci. 44 (1974) 69.
[104] H.H. Sawin, R.P. Merrill, J. Vac. Sci. Technol. 19 (1981) 40.
[105] R.H. Jones, D.R. Olander, W.J. Siekhaus, J.A. Schwarz, J. Vac. Sci. Technol. 9 (1972) 1429.
[106] J.A. Schwarz, R.J. Madix, Surf. Sci. 46 (1974) 317.
[107] H.-C. Chang, W.H. Weinberg, J. Chem. Phys. 66 (1977) 4176.
[108] B.J. Hinch, L.H. Dubois, Chem. Phys. Lett. 171 (1990) 131.
[109] D.C. Jacobs, J. Phys. Condens. Matter 7 (1995) 1023.
[110] M. Bonn, A.W. Kleyn, G.J. Kroes, Surf. Sci. 500 (2002) 475.
[111] G. Comsa, R. David, Surf. Sci. Rep. 5 (1985) 145.
[112] M.G. Moula, S. Wako, Y. Ohno, M.U. Kislyuk, I. Kobal, T. Matsushima, Phys. Chem. Chem. Phys. 2 (2000) 2773.
[113] M.G. Moula, S. Wako, G. Cao, K. Kimura, Y. Ohno, I. Kobal, T. Matsushima, Phys. Chem. Chem. Phys. 1 (1999) 3677.
[114] M.G. Moula, S. Wako, G. Cao, I. Kobal, Y. Ohno, T. Matsushima, Appl. Surf. Sci. 169–170 (2001) 268.
[115] M.G. Moula, A.B.P. Mishra, I. Rzeznicka, M.U. Kislyuk, S. Liu, Y. Ohno, T. Matsushima, Chem. Phys. Lett. 341 (2001) 225.
[116] T. Matsushima, Surf. Sci. Rep. 52 (2003) 1.
[117] S.L. Tang, J.D. Beckerle, M.B. Lee, S.T. Ceyer, J. Chem. Phys. 84 (1986) 6488.
[118] J.A. Serri, M.J. Cardillo, G.E. Becker, J. Chem. Phys. 77 (1982) 2175.
[119] M. Bowker, S. Haq, R.P. Holroyd, P.M. Parlett, S. Poulston, N. Richardson, J. Chem. Soc. Faraday Trans. 92 (1996) 4683.
[120] T. Fuhrmann, M. Kinne, C.M. Whelan, J.F. Zhu, R. Denecke, H.-P. Steinrück, Chem. Phys. Lett. 390 (2004) 208.
[121] M. Kinne, T. Fuhrmann, J.F. Zhu, C. Whelan, R. Denecke, H.-P. Steinrück, J. Chem. Phys. 120 (2004) 7113.

[122] J.F. Zhu, M. Kinne, T. Fuhrmann, B. Trankenschuh, R. Denecke, H.-P. Steinrück, Surf. Sci. 547 (2003) 410.

[123] M. Kinne, T. Fuhrmann, C.M. Whelan, J.F. Zhu, J. Pantförder, M. Probst, G. Held, R. Denecke, H.-P. Steinrück, J. Chem. Phys. 117 (2003) 10852.

[124] J.T. Yates, T.E. Madey (Eds.), Vibrational Spectroscopy of Molecules on Surfaces, Plenum, New York, 1987.

[125] F.M. Hoffmann, Surf. Sci. Rep. 3 (1983) 107.

[126] J. Ryczkowsky, Catal. Today 68 (2001) 263.

[127] C. Goyhenex, M. Croci, C. Claeys, C.R. Henry, Surf. Sci. 352–354 (1996) 475.

[128] O. Krauth, G. Fahsold, A. Pucci, J. Chem. Phys. 110 (1999) 3113.

[129] X. Xu, D.W. Goodman, J. Phys. Chem. 97 (1993) 7711.

[130] J. Evans, B.E. Hayden, F. Mosselmans, A. Murray, Surf. Sci. 301 (1994) 61.

[131] J. Evans, G. Lu, B.E. Hayden, Surf. Sci. 360 (1996) 61.

[132] B.E. Hayden, in: J.T. Yates, Jr., T.E. Madey (Eds.), Methods of Surface Characterization, vol. 1, Plenum Press, New York, 1987, p. 267.

[133] G.E. Caledonia, B.D. Green, R.M. Murphy, J. Chem. Phys. 71 (1979) 4369.

[134] P.M. Aker, J.J. Sloan, J. Chem. Phys. 85 (1986) 1412.

[135] R. Fletcher, S.R. Leone, J. Chem. Phys. 88 (1988) 4720.

[136] G.V. Hartland, W. Xie, H.-L. Dai, A. Simon, M.J. Anderson, Rev. Sci. Instrum. 63 (1992) 3261.

[137] L.T. Letendre, H.-L. Dai, I.A. McLaren, T.J. Johnson, Rev. Sci. Instrum. 70 (1999) 18.

[138] D.R. Miller, in: G. Scoles (Ed.), Atomic and Molecular Beam Methods, Oxford University Press, Oxford, 1988.

[139] H. Pauly, in: G. Scoles (Ed.), Atomic and Molecular Beam Methods, Oxford University Press, Oxford, 1988.

[140] M. Izawa, S. Kita, H. Inouye, J. Appl. Phys. 53 (1982) 4688.

[141] L. Abad, D. Bermejo, V.J. Herrero, J. Santos, I. Tanarro, Rev. Sci. Instrum. 66 (1995) 3826.

[142] P.U. Andersson, M.B. Nagard, K. Bolton, M. Svanberg, J.B.C. Pettersson, J. Phys. Chem. A 104 (2000) 2681.

[143] P. Clausing, Z. Phys. 66 (1930) 471.

[144] H.C.W. Beijerinck, N.F. Verster, Physica B&C 111 (1981) 327.

[145] R.H. Jones, D.R. Olander, V.R. Kruger, J. Appl. Phys. 40 (1970) 4641.

[146] D.R. Olander, J. Appl. Phys. 40 (1970) 4650.

[147] D.R. Olander, V.R. Kruger, J. Appl. Phys. 41 (1970) 2769.

[148] D.R. Olander, R.H. Jones, W.J. Siekhaus, J. Appl. Phys. 41 (1970) 4388.

[149] W.J. Siekhaus, R.H. Jones, D.R. Olander, J. Appl. Phys. 41 (1970) 4392.

[150] C.T. Campbell, S.M. Valone, J. Vac. Sci. Technol. A 3 (1985) 408.

[151] H.-P. Steinrück, K.D. Rendulic, Vacuum 36 (1986) 213.

[152] A. Winkler, J.T. Yates Jr., J. Vac. Sci. Technol. A 6 (1988) 2929.

[153] D.M. Murphy, J. Vac. Sci. Technol. A 7 (1989) 3075.

[154] D.E. Kuhl, R.G. Tobin, Rev. Sci. Instrum. 66 (1995) 3016.

[155] J.M. Guevremont, S. Sheldon, F. Zaera, Rev. Sci. Instrum. 71 (2000) 3869.

[156] K. Hayek, B. Jenewein, B. Klötzer, W. Reichl, Top. Catal. 14 (2001) 25.

[157] C.T. Campbell, Surf. Sci. Rep. 27 (1997) 1.

[158] P.L.J. Gunter, J.W. Niemantsverdriet, G.A. Somorjai, Catal. Rev. Sci. Eng. 39 (1997) 77.

[159] H.-J. Freund, J. Libuda, M. Bäumer, T. Risse, A. Carlsson, Chem. Rec. 3 (2003) 181.

[160] H.-J. Freund, Surf. Sci. 500 (2002) 271.

[161] T. Engel, G. Ertl, J. Chem. Phys. 69 (1978) 1267.

[162] G. Ertl, Angew. Chem. Int. Ed. Engl. 29 (1990) 1219.

[163] J.G. Chen, J.E. Crowell, J.T. Yates Jr., Surf. Sci. 185 (1987) 373.

[164] D.N. Belton, S.J. Schmieg, Surf. Sci. 199 (1988) 518.

[165] C.A. Leighton, A.J. Swift, J.C. Vickerman, Surf. Sci. 253 (1991) 220.

[166] R.M. Jaeger, H. Kuhlenbeck, H.-J. Freund, M. Wuttig, W. Hoffmann, R. Franchy, H. Ibach, Surf. Sci. 259 (1991) 235.

[167] T. Schröder, M. Adelt, B. Richter, N. Naschitzki, M. Bäumer, H.-J. Freund, Surf. Rev. Lett. 7 (2000) 7.

[168] M.C. Wu, J.S. Corneille, C.A. Estrada, J.W. He, D.W. Goodman, Chem. Phys. Lett. 182 (1991) 472.

[169] H. Kuhlenbeck, C. Xu, B. Dillmann, M. Hassel, B. Adam, D. Ehrlich, S. Wohlrab, H.-J. Freund, U.A. Ditzinger, H. Neddermeyer, M. Neuber, M. Neumann, Ber. Bunsenges. Phys. Chem. 96 (1992) 15.

[170] W. Weiss, W. Ranke, Prog. Surf. Sci. 70 (2002) 1.
[171] C.C. Chusuei, X. Lai, K. Luo, D.W. Goodman, Top. Catal. 14 (2001) 71.
[172] D. Cappus, C. Xu, D. Ehrlich, B. Dillmann, C.A. Ventrice, K. Al-Shamery, H. Kuhlenbeck, H.-J. Freund, Chem. Phys. 177 (1993) 533.
[173] H.-J. Freund, B. Dillmann, D. Ehrlich, M. Hassel, R.M. Jaeger, H. Kuhlenbeck, C.A. Ventrice, F. Winkelmann, S. Wohlrab, C. Xu, T. Bertrams, H. Brodde, H. Neddermeyer, J. Mol. Catal. 82 (1993) 143.
[174] J. Libuda, F. Winkelmann, M. Bäumer, H.-J. Freund, T. Bertrams, H. Neddermeyer, K. Müller, Surf. Sci. 318 (1994) 61.
[175] D.R. Rainer, M.C. Wu, D.I. Mahon, D.W. Goodman, J. Vac. Sci. Technol. A 14 (1996) 1184.
[176] J. Evans, B.E. Hayden, M.A. Newton, Surf. Sci. 462 (2000) 169.
[177] A.M. Argo, B.C. Gates, J. Phys. Chem. B 107 (2003) 5519.
[178] K. Judai, S. Abbet, A.S. Worz, U. Heiz, C.R. Henry, J. Am. Chem. Soc. 126 (2004) 2732.
[179] M. Melzer, J. Urban, H. Sack-Kongehl, K. Weiss, H.-J. Freund, R. Schlögl, Catal. Lett. 81 (2002) 219.
[180] J.P. Spatz, A. Roescher, M. Möller, Adv. Mater. 8 (1996) 337.
[181] R. Glass, M. Möller, J.P. Spatz, Nanotechnology 14 (2003) 1153.
[182] C. Werdinius, L. Österlund, B. Kasemo, Langmuir 19 (2003) 458.
[183] M. Gustavsson, H. Fredriksson, B. Kasemo, Z. Jusys, J. Kaiser, C. Jun, R.J. Behm, J. Electroanal. Chem. 568 (2004) 371.
[184] B. Kasemo, S. Johansson, H. Persson, P. Thormählen, V.P. Zhdanov, Top. Catal. 13 (2000) 43.
[185] K. Wong, S. Johansson, B. Kasemo, Faraday Discuss. 105 (1996) 237.
[186] A.S. Eppler, G. Rupprechter, L. Guczi, G.A. Somorjai, J. Phys. Chem. B 101 (1997) 9973.
[187] A.S. Eppler, J. Zhu, E.A. Anderson, G.A. Somorjai, Top. Catal. 13 (2000) 33.
[188] J. Grunes, J.F. Zhu, E.A. Anderson, G.A. Somorjai, J. Phys. Chem. B 106 (2002) 11463.
[189] N. Magg, S. Giorgio, M. Frank, B. Immaraporn, T. Schröder, M. Bäumer, H.-J. Freund, J. Am. Chem. Soc. 126 (2004) 3616.
[190] C. Xu, W.S. Oh, D.W. Goodman, J. Phys. Chem. B 104 (2000) 10310.
[191] A. Carlsson, N. Naschitzki, M. Bäumer, H.-J. Freund, J. Chem. Phys. 119 (2003) 10885.
[192] M. Heemeier, A.F. Carlsson, N. Naschitzki, M. Schmal, M. Bäumer, H.-J. Freund, Angew. Chem. Int. Ed. 41 (2002) 4073.
[193] S. Shaikhutdinov, M. Frank, M. Bäumer, S.D. Jackson, R. Oldman, J.C. Hemminger, H.-J. Freund, Catal. Lett. 80 (2002) 115.
[194] C.R. Henry, C. Chapon, C. Duriez, Z. Phys. D 19 (1991) 347.
[195] C.R. Henry, C. Chapon, C. Duriez, J. Chem. Phys. 95 (1991) 700.
[196] C.R. Henry, C. Chapon, C. Goyhenex, R. Monot, Surf. Sci. 272 (1992) 283.
[197] C. Becker, C.R. Henry, Surf. Sci. 352–354 (1996) 457.
[198] C. Becker, C.R. Henry, Catal. Lett. 43 (1997) 55.
[199] L. Piccolo, C. Becker, C.R. Henry, Eur. Phys. J. D 9 (1999) 415.
[200] L. Piccolo, C. Becker, C.R. Henry, Appl. Surf. Sci. 164 (2000) 156.
[201] L. Piccolo, C.R. Henry, Surf. Sci. 452 (2000) 198.
[202] L. Piccolo, C.R. Henry, Appl. Surf. Sci. 162–163 (2000) 670.
[203] C.R. Henry, Appl. Surf. Sci. 164 (2000) 252.
[204] L. Piccolo, C.R. Henry, J. Mol. Catal. A 167 (2001) 181.
[205] G. Prevot, O. Meerson, L. Piccolo, C.R. Henry, J. Phys. Condens. Matter 14 (2002) 4251.
[206] M. Meunier, C.R. Henry, Surf. Sci. 309 (1994) 514.
[207] C.R. Henry, M. Meunier, Mater. Sci. Eng. A 217 (1996) 239.
[208] C.R. Henry, Cryst. Res. Technol. 33 (1998) 1119.
[209] H. Graoui, S. Giorgio, C.R. Henry, Phil. Mag. B 81 (2001) 1649.
[210] I. Stara, V. Nehasil, V. Matolin, Surf. Sci. 365 (1996) 69.
[211] I. Jungwirthova, I. Stara, V. Matolin, Surf. Sci. 377 (1997) 644.
[212] I. Stara, V. Matolin, Surf. Rev. Lett. 4 (1997) 1353.
[213] V. Matolin, I. Stara, Surf. Sci. 398 (1998) 117.
[214] I. Stará, V. Gonzales, I. Jungwirthova, K. Masek, V. Matolin, Surf. Rev. Lett. 5 (1998) 397.
[215] I. Stara, E. Tomkova, V. Matolin, Czech. J. Phys. 43 (1993) 1023.
[216] I. Stara, V. Nehasil, V. Matolin, Surf. Sci. 331–333 (1995) 173.

[217] V. Nehasil, I. Stara, V. Matolin, Surf. Sci. 352 (1996) 305.
[218] V. Nehasil, I. Stara, V. Matolin, Surf. Sci. 377 (1997) 813.
[219] I. Stara, D. Zeze, V. Matolin, J. Pavluch, B. Gruzza, Appl. Surf. Sci. 115 (1997) 46.
[220] M. Bowker, P. Stone, R. Bennett, N. Perkins, Surf. Sci. 497 (2002) 155.
[221] M. Bowker, P. Stone, R. Bennett, N. Perkins, Surf. Sci. 511 (2002) 435.
[222] P. Stone, S. Poulston, R.A. Bennett, M. Bowker, Chem. Commun. (1998) 1369.
[223] R.A. Bennett, C.L. Pang, N. Perkins, R.D. Smith, P. Morrall, R.I. Kvon, M. Bowker, J. Phys. Chem. B 106 (2002) 4688.
[224] T. Dellwig, J. Hartmann, J. Libuda, I. Meusel, G. Rupprechter, H. Unterhalt, H.-J. Freund, J. Mol. Catal. A 162 (2000) 51.
[225] J. Hoffmann, I. Meusel, J. Hartmann, J. Libuda, H.-J. Freund, J. Catal. 204 (2001) 378.
[226] J. Libuda, I. Meusel, J. Hoffmann, J. Hartmann, L. Piccolo, C.R. Henry, H.-J. Freund, J. Chem. Phys. 114 (2001) 4669.
[227] J. Libuda, I. Meusel, J. Hoffmann, J. Hartmann, H.-J. Freund, J. Vac. Sci. Technol. A 19 (2001) 1516.
[228] I. Meusel, J. Hoffmann, J. Hartmann, J. Libuda, H.-J. Freund, J. Phys. Chem. B 105 (2001) 3567.
[229] J. Hoffmann, S. Schauermann, J. Hartmann, V.P. Zhdanov, B. Kasemo, J. Libuda, H.-J. Freund, Chem. Phys. Lett. 354 (2002) 403.
[230] S. Schauermann, J. Hoffmann, V. Johánek, J. Hartmann, J. Libuda, Phys. Chem. Chem. Phys. 4 (2002) 3909.
[231] S. Schauermann, J. Hoffmann, V. Johánek, J. Hartmann, J. Libuda, H.-J. Freund, Angew. Chem. Int. Ed. 41 (2002) 2532.
[232] S. Schauermann, J. Hoffmann, V. Johánek, J. Hartmann, J. Libuda, H.-J. Freund, Catal. Lett. 84 (2002) 209.
[233] J. Hoffmann, S. Schauermann, V. Johánek, J. Hartmann, J. Libuda, J. Catal. 213 (2003) 176.
[234] V. Johanek, S. Schauermann, M. Laurin, J. Libuda, H.-J. Freund, Angew. Chem. Int. Ed. 42 (2003) 3035.
[235] S. Schauermann, V. Johánek, M. Laurin, J. Libuda, H.-J. Freund, Phys. Chem. Chem. Phys. 6 (2003) 5139.
[236] S. Schauermann, V. Johánek, M. Laurin, J. Libuda, H.-J. Freund, Chem. Phys. Lett. 381 (2003) 298.
[237] I.V. Yudanov, R. Sahnoun, K.M. Neyman, N. Rösch, J. Hoffmann, S. Schauermann, V. Johánek, H. Unterhalt, G. Rupprechter, J. Libuda, H.-J. Freund, J. Phys. Chem. B 107 (2003) 255.
[238] l. Johánek, S. Schauermann, M. Laurin, C.S. Gopinath, J. Libuda, H.-J. Freund, J. Phys. Chem. B 108 (2004) 14244.
[239] V. Johánek, M. Laurin, A.W. Grant, B. Kasemo, C.R. Henry, J. Libuda, Science 304 (2004) 5677.
[240] M. Laurin, V. Johanek, A.W. Grant, B. Kasemo, J. Libuda, H.-J. Freund, in press.
[241] C. Winkler, A.J. Carew, S. Haq, R. Raval, Langmuir 19 (2003) 717.
[242] S. Haq, A. Carew, R. Raval, J. Catal. 221 (2004) 2004.
[243] C. Winkler, A. Carew, R. Raval, J. Ledieu, R. McGrath, Surf. Rev. Lett. 8 (2001) 693.
[244] K. Müller, H. Lindner, D.M. Zehner, G. Ownby, Verh. Dtsch. Phys. Ges. 25 (1990) 1130, private communication.
[245] J.E. Crowell, J.G. Chen, J.T. Yates, Surf. Sci. 165 (1986) 37.
[246] R.L. Strong, J.L. Erskine, J. Vac. Sci. Technol. A 3 (1985) 1428.
[247] J.G. Chen, J.E. Crowell, J.T. Yates, Phys. Rev. B 35 (1987) 5299.
[248] R.M. Jaeger, J. Libuda, M. Bäumer, K. Homann, H. Kulenbeck, H.-J. Freund, J. Electron Spectrosc. Relat. Phenom. 64/65 (1993) 217.
[249] J.-P. Jacobs, S. Reijne, R.J.M. Elfrink, S.N. Mikhailov, H.H. Brongersma, M. Wuttig, J. Vac. Sci. Technol. A 12 (1994) 2308.
[250] M. Klimenkov, S. Nepijko, H. Kuhlenbeck, H.-J. Freund, Surf. Sci. 385 (1997) 66.
[251] H. Isern, G.R. Castro, Surf. Sci. 211/212 (1989) 865.
[252] A. Sandell, J. Libuda, P.A. Brühwiler, S. Andersson, M. Bäumer, A.J. Maxwell, N. Martensson, H.-J. Freund, J. Electron Spectrosc. Relat. Phenom. 76 (1995) 301.
[253] A. Stierle, F. Renner, R. Streitel, H. Dosch, W. Drube, B.C. Cowie, Science 303 (2004) 1652.
[254] N. Nilius, M. Kulawik, H.-P. Rust, H.-J. Freund, Phys. Rev. B 6912 (2004) 1401.
[255] M. Kulawik, N. Nilius, H.-P. Rust, H.-J. Freund, Phys. Rev. Lett. 91 (2003) 256101.
[256] G. Ceballos, Z. Song, J.I. Pascual, H.-P. Rust, H. Conrad, M. Bäumer, H.-J. Freund, Chem. Phys. Lett. 359 (2002) 41.
[257] J. Libuda, M. Bäumer, H.-J. Freund, J. Vac. Sci. Technol. A 12 (1994) 2259.
[258] D.R. Jennison, C. Verdozzi, P.A. Schultz, M.P. Sears, Phys. Rev. B 59 (1999) 15605.
[259] G. Kresse, M. Schmid, E. Napetschnig, M. Shishkin, L. Köhler, P. Varga, submitted for publication.
[260] G. Renaud, B. Vilette, I. Vilfan, A. Bourret, Phys. Rev. Lett. 73 (1994) 1825.
[261] C. Barth, M. Reichling, Nature 414 (2001) 54.

[262] A. Sandell, J. Libuda, P.A. Brühwiler, S. Andersson, A.J. Maxwell, M. Bäumer, N. Mårtensson, H.-J. Freund, J. Vac. Sci. Technol. A 14 (1996) 1546.

[263] A. Sandell, A. Beutler, R. Nyholm, J.N. Andersson, P.A. Brühwiler, N. Martensson, J. Libuda, K. Wolter, O. Seiferth, M. Bäumer, H. Kuhlenbeck, H.-J. Freund, Phys. Rev. B 57 (1998) 13199.

[264] M. Bäumer, M. Frank, unpublished.

[265] N. Magg, J.B. Giorgi, M.M. Frank, B. Immaraporn, T. Schroeder, M. Bäumer, H.-J. Freund, J. Am. Chem. Soc. 126 (2004) 3616.

[266] A. Carlsson, N. Naschitzki, M. Bäumer, H.-J. Freund, J. Phys. Chem. B 107 (2003) 778.

[267] S. Shaikhutdinov, M. Heemeier, M. Bäumer, T. Lear, D. Lennon, R.J. Oldman, S.D. Jackson, H.-J. Freund, J. Catal. 200 (2001) 330.

[268] M. Frank, R. Kühnemuth, M. Bäumer, H.-J. Freund, Surf. Sci. 454–456 (2000) 968.

[269] M. Frank, M. Bäumer, R. Kühnemuth, H.-J. Freund, J. Vac. Sci. Technol. A 19 (2001) 1497.

[270] C.T. Campbell, S.C. Parker, D.E. Starr, Science 298 (2002) 811.

[271] R. Imbihl, J.E. Demuth, Surf. Sci. 173 (1986) 395.

[272] X. Guo, A. Hoffman, J.T. Yates Jr., J. Chem. Phys. 90 (1989) 5787.

[273] M.K. Rose, A. Borg, J.C. Dunphy, T. Mitsui, D.F. Ogletree, M. Salmeron, Surf. Sci. 547 (2003) 162.

[274] H. Conrad, G. Ertl, J. Küppers, E.E. Latta, Surf. Sci. 65 (1977) 254.

[275] D.L. Weissman, M.L. Shek, W.E. Spicer, Surf. Sci. 92 (1980) L59.

[276] D.L. Weissman-Wenicur, M.L. Shek, P.M. Stefan, I. Lindau, W.E. Spicer, Surf. Sci. 127 (1983) 513.

[277] L. Surnev, G. Bliznakov, M. Kiskinova, Surf. Sci. 140 (1984) 249.

[278] M. Milun, P. Pervan, M. Vacjic, K. Wandelt, Surf. Sci. 211–212 (1989) 887.

[279] B.A. Banse, B.E. Koel, Surf. Sci. 232 (1990) 275.

[280] V.A. Bondzie, P. Kleban, D.J. Dwyer, Surf. Sci. 347 (1996) 319.

[281] E.H. Voogt, A.J.M. Mens, O.L.J. Gijzeman, J.W. Geus, Surf. Sci. 373 (1997) 210.

[282] W. Huang, R. Zhai, X. Bao, Surf. Sci. 439 (1999) L803.

[283] F.P. Leisenberger, G. Koller, M. Sock, S. Surnev, M.G. Ramsey, F.P. Netzer, B. Klötzer, K. Hayek, Surf. Sci. 445 (2000) 380.

[284] V.A. Bondzie, P.H. Kleban, D.J. Dwyer, Surf. Sci. 465 (2000) 266.

[285] V.A. Bondzie, P. Kleban, D.J. Dwyer, J. Vac. Sci. Technol. A 11 (1993) 1946.

[286] S. Ladas, R. Imbihl, G. Ertl, Surf. Sci. 219 (1989) 88.

[287] M.R. Basset, R. Imbihl, J. Chem. Phys. 93 (1990) 811.

[288] J. Hartmann, R. Imbihl, W. Vogel, Catal. Lett. 28 (1994) 373.

[289] G. Zheng, E.I. Altman, Surf. Sci. 462 (2000) 151.

[290] M.K. Rose, A. Borg, T. Mitsui, D.F. Ogletree, M. Salmeron, J. Chem. Phys. 115 (2001) 10927.

[291] B. Klötzer, K. Hayek, C. Konvicka, E. Lundgren, P. Varga, Surf. Sci. 482 (2001) 237.

[292] G. Zheng, E.I. Altman, Surf. Sci. 504 (2002) 253.

[293] E. Lundgren, G. Kresse, C. Klein, M. Borg, J.N. Andersen, M. De Santis, Y. Gauthier, C. Konvicka, M. Schmid, P. Varga, Phys. Rev. Lett. 88 (2002) 246103.

[294] B.L.M. Hendriksen, S.C. Bobaru, J.W.M. Frenken, Surf. Sci. 552 (2004) 229.

[295] M. Saidy, O.L. Warren, P.A. Thiel, K.A.R. Mitchell, Surf. Sci. 494 (2001) L799.

[296] M. Todorova, E. Lundgren, V. Blum, A. Mikkelsen, S. Gray, J. Gustafson, M. Borg, J. Rogal, K. Reuter, J.N. Andersen, M. Scheffler, Surf. Sci. 541 (2003) 101.

[297] E. Lundgren, J. Gustafson, A. Mikkelsen, J.N. Andersen, A. Stierle, H. Dosch, M. Todorova, J. Rogal, K. Reuter, M. Scheffler, Phys. Rev. Lett. 92 (2004) 046101.

[298] M. Todorova, K. Reuter, M. Scheffler, J. Phys. Chem. 108 (2004) 14477.

[299] M. Bäumer, J. Biener, R.J. Madix, Surf. Sci. 432 (1999) 189.

[300] L. Osterlund, S. Kielbassa, C. Werdinius, B. Kasemo, J. Catal. 215 (2003) 95.

[301] S. Johansson, L. Österlund, B. Kasemo, J. Catal. 201 (2001) 275.

[302] S. Johansson, E. Fridell, B. Kasemo, J. Catal. 200 (2001) 370.

[303] S. Johansson, E. Fridell, B. Kasemo, J. Vac. Sci. Technol. A 18 (2000) 1514.

[304] S. Johansson, K. Wong, V.P. Zhdanov, B. Kasemo, J. Vac. Sci. Technol. A 17 (1999) 297.

[305] J. Grunes, J. Zhu, M.C. Yang, G.A. Somorjai, Catal. Lett. 86 (2003) 157.
[306] T. Tsirlin, J. Zhu, J. Grunes, G.A. Somorjai, Top. Catal. 19 (2002) 165.
[307] S. Baldelli, A.S. Eppler, E. Anderson, Y.R. Shen, G.A. Somorjai, J. Chem. Phys. 113 (2000) 5432.
[308] A.S. Eppler, G. Rupprechter, E.A. Anderson, G.A. Somorjai, J. Phys. Chem. B 104 (2000) 7286.
[309] A. Avoyan, G. Rupprechter, A.S. Eppler, G.A. Somorjai, Top. Catal. 10 (2000) 107.
[310] M.X. Yang, D.H. Gracias, P.W. Jacobs, G.A. Somorjai, Langmuir 14 (1998) 1458.
[311] P.W. Jacobs, S.J. Wind, F.H. Ribeiro, G.A. Somorjai, Surf. Sci. 372 (1997) L249.
[312] X.C. Su, J. Jansen, M.X. Yang, M.B. Salmeron, Y.R. Shen, G.A. Somorjai, Faraday Discuss. 105 (1996) 263.
[313] P.W. Jacobs, F.H. Ribeiro, G.A. Somorjai, S.J. Wind, Catal. Lett. 37 (1996) 131.
[314] V. Johanek, M. Laurin, J. Hoffmann, S. Schauermann, A.W. Grant, B. Kasemo, J. Libuda, H.-J. Freund, Surf. Sci. Lett. 561 (2004) L218.
[315] M. Laurin, V. Johanek, A.W. Grant, B. Kasemo, J. Libuda, H.-J. Freund, J. Chem. Phys. 122 (2005) 084713.
[316] J. Schoiswohl, G. Kresse, L. Surnev, M. Sock, M.G. Ramsey, F.P. Netzer, Phys. Rev. Lett. 9220 (2004) 6103.
[317] J. Schoiswohl, M. Sock, S. Eck, L. Surnev, M.G. Ramsey, F.P. Netzer, Phys. Rev. B 6915 (2004) 5403.
[318] J. Schoiswohl, M. Sock, L. Surnev, M.G. Ramsey, F.P. Netzer, G. Kresse, J.N. Andersen, Surf. Sci. 555 (2004) 101.
[319] C. Klein, G. Kresse, S. Surnev, F.P. Netzer, M. Schmid, P. Varga, Phys. Rev. B 6823 (2003) 5416.
[320] S. Eck, C. Castellarin-Cudia, S. Surnev, K.C. Prince, M.G. Ramsey, F.P. Netzer, Surf. Sci. 536 (2003) 166.
[321] S. Surnev, M. Sock, G. Kresse, J.N. Andersen, M.G. Ramsey, F.P. Netzer, J. Phys. Chem. B 107 (2003) 4777.
[322] S. Surnev, M. Sock, M.G. Ramsey, F.P. Netzer, B. Klotzer, W. Unterberger, K. Hayek, Surf. Sci. 511 (2002) 392.
[323] L. Surnev, G. Kresse, M. Sock, M.G. Ramsey, F.P. Netzer, Surf. Sci. 496 (2001) 91.
[324] S. Surnev, L. Vitali, M.G. Ramsey, F.P. Netzer, G. Kresse, J. Hafner, Phys. Rev. B 61 (2000) 13945.
[325] K. Judai, S. Abbet, A.S. Wörz, M.A. Röttgen, U. Heiz, Int. J. Mass Spectrom. 229 (2003) 99.
[326] U. Heiz, W.D. Schneider, Crit. Rev. Solid State Mater. Sci. 26 (2000) 251.
[327] S. Abbet, A. Sanchez, U. Heiz, W.D. Schneider, A.M. Ferrari, G. Paccioni, N. Rösch, J. Am. Chem. Soc. 122 (2000) 3453.
[328] H. Häkkinen, S. Abbet, A. Sanchez, U. Heiz, U. Landman, Angew. Chem. Int. Ed. 42 (2003) 1297.
[329] A.S. Wörz, K. Judai, S. Abbet, U. Heiz, J. Am. Chem. Soc. 125 (2003) 7964.
[330] U. Heiz, F. Vanolli, L. Trento, W.D. Schneider, Rev. Sci. Instrum. 68 (1997) 1986.
[331] C.R. Helms, R.J. Madix, Surf. Sci. 52 (1975) 677.
[332] T. Engel, J. Chem. Phys. 69 (1978) 373.
[333] C.T. Campbell, G. Ertl, H. Kuipers, J. Segner, Surf. Sci. 107 (1981) 207.
[334] T.H. Lin, G.A. Somorjai, Surf. Sci. 107 (1981) 573.
[335] S.T. Ceyer, J.D. Beckerle, M.B. Lee, S.L. Tang, Q.Y. Yang, M.A. Hines, J. Vac. Sci. Technol. A 5 (1987) 501.
[336] M.B. Lee, J.D. Beckerle, S.L. Tang, S.T. Ceyer, J. Chem. Phys. 87 (1987) 723.
[337] M.E.M. Spruit, P.J. Vandenhoek, E.W. Kuipers, F.H. Geuzebroek, A.W. Kleyn, Surf. Sci. 214 (1989) 591.
[338] B.E. Hayden, D.C. Godfrey, Surf. Sci. 232 (1990) 24.
[339] K.A. Peterlinz, T.J. Curtiss, S.J. Sibener, J. Chem. Phys. 95 (1991) 6972.
[340] Y.W. Yang, J.C. Lin, T. Engel, Surf. Sci. 289 (1993) 267.
[341] P.M. Holmblad, J.H. Larsen, I. Chorkendorff, J. Chem. Phys. 104 (1996) 7289.
[342] J. Liu, M. Xu, F. Zaera, Catal. Lett. 37 (1996) 9.
[343] C.T. Rettner, D.J. Auerbach, J. Chem. Phys. 105 (1996) 8842.
[344] Y.Y. Yeo, L. Vattuone, D.A. King, J. Chem. Phys. 106 (1997) 392.
[345] T. Ali, B. Klotzer, A.V. Walker, D.A. King, J. Chem. Phys. 109 (1998) 10996.
[346] M. Beutl, J. Lesnik, K.D. Rendulic, Surf. Sci. 429 (1999) 71.
[347] T. Becker, C. Boas, U. Burghaus, C. Woll, J. Vac. Sci. Technol. A 18 (2000) 1089.
[348] T. Becker, M. Kunat, C. Boas, U. Burghaus, C. Woll, J. Chem. Phys. 113 (2000) 6334.
[349] Z. Dohnalek, G.A. Kimmel, S.A. Joyce, P. Ayotte, R.S. Smith, B.D. Kay, J. Phys. Chem. B 105 (2001) 3747.
[350] M. Kunat, C. Boas, T. Becker, U. Burghaus, C. Woll, Surf. Sci. 474 (2001) 114.
[351] R. Denecke, B. Trankenschuh, M.P. Engelhardt, H.P. Steinruck, Surf. Sci. 532 (2003) 173.
[352] C.T. Campbell, G. Ertl, H. Kuipers, J. Segner, Surf. Sci. 107 (1981) 220.
[353] C.T. Rettner, L.A. Delouise, D.J. Auerbach, J. Vac. Sci. Technol. A 4 (1986) 1491.
[354] C.B. Mullins, Y. Wang, W.H. Weinberg, J. Vac. Sci. Technol. A 7 (1989) 2125.

[355] C.T. Rettner, C.B. Mullins, J. Chem. Phys. 94 (1991) 1626.
[356] A.E. Wiskerke, F.H. Geuzebroek, A.W. Kleyn, B.E. Hayden, Surf. Sci. 272 (1992) 256.
[357] J. Hall, O. Saksager, I. Chorkendorff, Chem. Phys. Lett. 216 (1993) 413.
[358] R.W. Verhoef, D. Kelly, W.H. Weinberg, J. Vac. Sci. Technol. A 11 (1993) 1926.
[359] X.C. Guo, J.M. Bradley, A. Hopkinson, D.A. King, Surf. Sci. 310 (1994) 163.
[360] L. Vattuone, M. Rocca, C. Boragno, U. Valbusa, J. Chem. Phys. 101 (1994) 713.
[361] L. Vattuone, M. Rocca, C. Boragno, U. Valbusa, J. Chem. Phys. 101 (1994) 726.
[362] R.W. Verhoef, D. Kelly, W.H. Weinberg, Surf. Sci. 306 (1994) L513.
[363] D. Kelly, R.W. Verhoef, W.H. Weinberg, J. Chem. Phys. 102 (1995) 3440.
[364] R.W. Verhoef, D. Kelly, W.H. Weinberg, Surf. Sci. 328 (1995) 1.
[365] J.M. Bradley, X.C. Guo, A. Hopkinson, D.A. King, J. Chem. Phys. 104 (1996) 4283.
[366] F.B. deMongeot, M. Rocca, U. Valbusa, Surf. Sci. 363 (1996) 68.
[367] M.C. Wheeler, D.C. Seets, C.B. Mullins, J. Chem. Phys. 105 (1996) 1572.
[368] P. Brault, H. Range, J.P. Toennies, J. Chem. Phys. 106 (1997) 8876.
[369] P.D. Nolan, B.R. Lutz, P.L. Tanaka, J.E. Davis, C.B. Mullins, Phys. Rev. Lett. 81 (1998) 3179.
[370] P.D. Nolan, B.R. Lutz, P.L. Tanaka, C.B. Mullins, Surf. Sci. 419 (1998) L107.
[371] P.D. Nolan, M.C. Wheeler, J.E. Davis, C.B. Mullins, Acc. Chem. Res. 31 (1998) 798.
[372] U. Valbusa, F.B. De Mongeot, M. Rocca, L. Vattuone, Vacuum 50 (1998) 445.
[373] A.V. Walker, B. Klotzer, D.A. King, J. Chem. Phys. 109 (1998) 6879.
[374] P.D. Nolan, B.R. Lutz, P.L. Tanaka, J.E. Davis, C.B. Mullins, J. Chem. Phys. 111 (1999) 3696.
[375] A. Böttcher, H. Conrad, H. Niehus, J. Chem. Phys. 112 (2000) 4779.
[376] A.T. Gee, B.E. Hayden, J. Chem. Phys. 113 (2000) 10333.
[377] A.V. Walker, B. Klotzer, D.A. King, J. Chem. Phys. 112 (2000) 8631.
[378] L. Savio, L. Vattuone, M. Rocca, Phys. Rev. Lett. 87 (2001) 276101.
[379] L. Savio, L. Vattuone, M. Rocca, J. Phys. Condens. Matter 14 (2002) 6065.
[380] O. Weisse, C. Wesenberg, M. Binetti, E. Hasselbrink, C. Corriol, G.R. Darling, S. Holloway, J. Chem. Phys. 118 (2003) 8010.
[381] R.L. Palmer, J.N. Smith, J. Vac. Sci. Technol. 11 (1974) 243.
[382] R.L. Palmer, J.N. Smith, J. Chem. Phys. 60 (1974) 1453.
[383] C.T. Campbell, G. Ertl, H. Kuipers, J. Segner, J. Chem. Phys. 73 (1980) 5862.
[384] J.A. Fair, R.J. Madix, J. Chem. Phys. 73 (1980) 3486.
[385] L.S. Brown, S.J. Sibener, J. Chem. Phys. 90 (1989) 2807.
[386] Q. Guo, R.W. Joyner, M. Bowker, J. Phys. Condens. Matter 3 (1991) S55.
[387] C.B. Mullins, C.T. Rettner, D.J. Auerbach, J. Chem. Phys. 95 (1991) 8649.
[388] M. Bowker, Q.M. Guo, Y.X. Li, R.W. Joyner, Catal. Lett. 18 (1993) 119.
[389] U. Burghaus, H. Conrad, Surf. Sci. 338 (1995) L869.
[390] J.I. Colonell, K.D. Gibson, S.J. Sibener, J. Chem. Phys. 103 (1995) 6677.
[391] U. Burghaus, H. Conrad, Surf. Sci. 364 (1996) 109.
[392] A. Böttcher, H. Niehus, S. Schwegmann, H. Over, G. Ertl, J. Phys. Chem. B 101 (1997) 11185.
[393] U. Burghaus, H. Conrad, Surf. Sci. 370 (1997) 17.
[394] M. Bowker, I.Z. Jones, R.A. Bennett, S. Poulston, Stud. Surf. Sci. Catal. 116 (1998) 431.
[395] U. Burghaus, J.Q. Ding, W.H. Weinberg, J. Vac. Sci. Technol. A 16 (1998) 1010.
[396] U. Burghaus, J.Q. Ding, W.H. Weinberg, Surf. Sci. 396 (1998) 273.
[397] J.Y. Kim, J. Lee, J. Chem. Phys. 109 (1998) 869.
[398] M.C. Wheeler, C.T. Reeves, D.C. Seets, C.B. Mullins, J. Chem. Phys. 108 (1998) 3057.
[399] I.Z. Jones, R.A. Bennett, M. Bowker, Surf. Sci. 439 (1999) 235.
[400] U. Burghaus, I.Z. Jones, M. Bowker, Surf. Sci. 454 (2000) 326.
[401] M.A. Weibel, K.M. Backstrand, T.J. Curtiss, Surf. Sci. 444 (2000) 66.
[402] M. Hirsimaki, P. Nieminen, M. Valden, Surf. Sci. 482 (2001) 147.
[403] M. Bowker, R.A. Bennett, I.Z. Jones, Top. Catal. 28 (2004) 25.
[404] C. Barnes, P. Pudney, Q.M. Guo, M. Bowker, J. Chem. Soc. Faraday Trans. 86 (1990) 2693.

[405] P.D.A. Pudney, M. Bowker, R.W. Joyner, Surf. Sci. 251 (1991) 1106.
[406] M.A. Newton, M. Bowker, Catal. Lett. 21 (1993) 139.
[407] S.M. Francis, F.M. Leibsle, S. Haq, N. Xiang, M. Bowker, Surf. Sci. 315 (1994) 284.
[408] M. Bowker, Top. Catal. 3 (1996) 461.
[409] R.P. Holroyd, M. Bowker, Surf. Sci. 377 (1997) 786.
[410] L. Diekhoner, D.A. Butler, A. Baurichter, A.C. Luntz, Surf. Sci. 409 (1998) 384.
[411] M.A. Newton, J. Catal. 182 (1999) 357.
[412] A.M. De Asha, J.T.S. Critchley, A.E. Siokou, R.M. Nix, Phys. Chem. Chem. Phys. 2 (2000) 4758.
[413] R. Schennach, A. Eichler, K.D. Rendulic, J. Phys. Chem. B 107 (2003) 2552.
[414] R. Schennach, G. Krenn, K.D. Rendulic, Vacuum 71 (2003) 89.
[415] G. Krenn, R. Schennach, J. Chem. Phys. 120 (2004) 5729.
[416] A.W. Kleyn, A.C. Luntz, D.J. Auerbach, Phys. Rev. Lett. 47 (1981) 1169.
[417] C.T. Campbell, G. Ertl, J. Segner, Surf. Sci. 115 (1982) 309.
[418] A.C. Luntz, A.W. Kleyn, D.J. Auerbach, J. Chem. Phys. 76 (1982) 737.
[419] J.A. Serri, M.J. Cardillo, G.E. Becker, J. Vac. Sci. Technol. 20 (1982) 604.
[420] A.W. Kleyn, A.C. Luntz, D.J. Auerbach, Surf. Sci. 152 (1985) 99.
[421] A.W. Kleyn, E.W. Kuipers, M.G. Tenner, S. Stolte, J. Chem. Soc. Faraday Trans. 85 (1989) 1337.
[422] E.W. Kuipers, M.G. Tenner, A.W. Kleyn, S. Stolte, Phys. Rev. Lett. 62 (1989) 2152.
[423] G.H. Fecher, N. Bowering, M. Volkmer, B. Pawlitzky, U. Heinzmann, Surf. Sci. 230 (1990) L169.
[424] M.G. Tenner, F.H. Geuzebroek, E.W. Kuipers, A.E. Wiskerke, A.W. Kleyn, S. Stolte, A. Namiki, Chem. Phys. Lett. 168 (1990) 45.
[425] M. Bowker, Q. Guo, R.W. Joyner, Surf. Sci. 257 (1991) 33.
[426] F.H. Geuzebroek, A.E. Wiskerke, A.W. Kleyn, S. Stolte, Nucl. Instrum. Methods Phys. Res. Sect. B Beam Interact. Mater. Atoms 58 (1991) 354.
[427] C.T. Rettner, J. Kimman, D.J. Auerbach, J. Chem. Phys. 94 (1991) 734.
[428] M.G. Tenner, E.W. Kuipers, A.W. Kleyn, S. Stolte, J. Chem. Phys. 94 (1991) 5197.
[429] A. Hopkinson, D.A. King, Chem. Phys. 177 (1993) 433.
[430] A.E. Wiskerke, C.A. Taatjes, A.W. Kleyn, R.J.W.E. Lahaye, S. Stolte, D.K. Bronnikov, B.E. Hayden, Faraday Discussions 96 (1993) 297.
[431] H. Muller, B. Dierks, G.H. Fecher, N. Bowering, U. Heinzmann, J. Chem. Phys. 101 (1994) 7154.
[432] H. Muller, G. Zagatta, N. Bowering, U. Heinzmann, Chem. Phys. Lett. 223 (1994) 197.
[433] M. Brandt, H. Muller, G. Zagatta, O. Wehmeyer, N. Bowering, U. Heinzmann, Surf. Sci. 333 (1995) 30.
[434] A.E. Wiskerke, C.A. Taatjes, A.W. Kleyn, R. Lahaye, S. Stolte, D.K. Bronnikov, B.E. Hayden, J. Chem. Phys. 102 (1995) 3835.
[435] W.A. Brown, R.K. Sharma, D.A. King, S. Haq, J. Phys. Chem. 100 (1996) 12559.
[436] J.I. Colonell, K.D. Gibson, S.J. Sibener, J. Chem. Phys. 104 (1996) 6822.
[437] J.E. Davis, S.G. Karseboom, P.D. Nolan, C.B. Mullins, J. Chem. Phys. 105 (1996) 8362.
[438] U. Heinzmann, S. Holloway, A.W. Kleyn, R.E. Palmer, K.J. Snowdon, J. Phys. Condens. Matter 8 (1996) 3245.
[439] R. Lahaye, S. Stolte, S. Holloway, A.W. Kleyn, J. Chem. Phys. 104 (1996) 8301.
[440] M.K. Ainsworth, J. McCombie, M.R.S. McCoustra, M.A. Chesters, J. Chem. Phys. 112 (2000) 6031.
[441] B. Berenbak, B. Riedmuller, D.A. Butler, C.T. Rettner, D.J. Auerbach, S. Stolte, A.W. Kleyn, Phys. Chem. Chem. Phys. 2 (2000) 919–923.
[442] Y. Huang, A.M. Wodtke, H. Hou, C.T. Rettner, D.J. Auerbach, Phys. Rev. Lett. 84 (2000) 2985.
[443] A.J. Komrowski, K. Ternow, B. Razaznejad, B. Berenbak, J.Z. Sexton, I. Zoric, B. Kasemo, B.I. Lundqvist, S. Stolte, A.W. Kleyn, A.C. Kummel, J. Chem. Phys. 117 (2002) 8185.
[444] B. Berenbak, B. Riedmuller, S. Stolte, A.W. Kleyn, Chem. Phys. 301 (2004) 309.
[445] M. Bowker, Q.M. Guo, Y.X. Li, R.W. Joyner, J. Chem. Soc. Faraday Trans. 91 (1995) 3663.
[446] M. Brandt, H. Muller, G. Zagatta, N. Bowering, U. Heinzmann, Surf. Sci. 352 (1996) 290.
[447] M. Brandt, G. Zagatta, N. Bowering, U. Heinzmann, Surf. Sci. 385 (1997) 346.
[448] M. Hirsimaki, S. Suhonen, J. Pere, M. Valden, M. Pessa, Surf. Sci. 404 (1998) 187.
[449] C.S. Gopinath, F. Zaera, J. Catal. 186 (1999) 387.

[450] C.S. Gopinath, F. Zaera, J. Catal. 200 (2001) 270.
[451] S. Bertarione, D. Scarano, A. Zecchina, V. Johanek, J. Hoffmann, S. Schauermann, J. Libuda, G. Rupprechter, H.-J. Freund, J. Catal. 223 (2004) 64.
[452] I. Stará, V. Nehasil, V. Matolín, Surf. Sci. 331–333 (1995) 173.
[453] I. Stará, V. Nehasil, V. Matolín, Surf. Sci. 365 (1996) 69.
[454] S. Bertarione, D. Scarano, A. Zecchina, V. Johanek, J. Hoffmann, S. Schauermann, M.M. Frank, J. Libuda, G. Rupprechter, H.-J. Freund, J. Phys. Chem. B 108 (2004) 3603.
[455] H.-J. Freund, H. Kuhlenbeck, J. Libuda, G. Rupprechter, M. Bäumer, H. Hamann, Top. Catal. 15 (2001) 201.
[456] H.-J. Freund, M. Bäumer, J. Libuda, T. Risse, G. Rupprechter, S. Shaikhutdinov, J. Catal. 216 (2003) 223.
[457] V. Matolin, E. Gillet, Surf. Sci. 166 (1986) L115.
[458] S. Ladas, H. Poppa, M. Boudart, Surf. Sci. 102 (1981) 151.
[459] F. Rumpf, H. Poppa, M. Boudart, Langmuir 4 (1988) 722.
[460] C.R. Henry, Surf. Sci. 223 (1989) 519.
[461] H. Taylor, Actes du Deuxieme Congres International de Catalyse, vol. 1, Paris, 1961, p. 159.
[462] K. Tsu, M. Boudart, Actes du Deuxieme Congres International de Catalyse, vol. 1, Paris, 1961, p. 593.
[463] P. Kisliuk, J. Phys. Chem. Solids 3 (1957) 95.
[464] J.F. Weaver, A.F. Carlsson, R.J. Madix, Surf. Sci. Rep. 50 (2003) 107.
[465] M. Boudart, K. Tamaru, Catal. Lett. 9 (1991) 15.
[466] C.T. Campbell, Top. Catal. 1 (1994) 353.
[467] J.A. Dumesic, J. Catal. 185 (1999) 496.
[468] M. Boudart, Top. Catal. 14 (2001) 181.
[469] C.T. Campbell, J. Catal. 204 (2001) 520.
[470] T. Becker, C. Boas, U. Burghaus, C. Wöll, Phys. Rev. B 61 (2000) 4538.
[471] C. Duriez, C. Chapon, C.R. Henry, J.M. Rickard, Surf. Sci. 230 (1990) 123.
[472] J.L. Davis, M.A. Barteau, Surf. Sci. 235 (1990) 235.
[473] A.K. Bhattacharya, M.A. Chesters, M.E. Pemble, N. Sheppard, Surf. Sci. 206 (1988) L845.
[474] K. Christmann, J.E. Demuth, J. Chem. Phys. 76 (1982) 6318.
[475] K. Christmann, J.E. Demuth, J. Chem. Phys. 76 (1982) 6308.
[476] R. Aris, J. Catal. 22 (1971) 282.
[477] D.-J. Kuan, H.T. Davis, R. Aris, Chem. Eng. Sci. 38 (1983) 719.
[478] C.R. Henry, C. Chapon, Surf. Sci. 156 (1985) 952.
[479] V.P. Zhdanov, Surf. Sci. Rep. 12 (1991) 183.
[480] E. Poehlmann, M. Schmitt, H. Hoinkes, H. Wilsch, Surf. Rev. Lett. 2 (1995) 741.
[481] T. Engel, G. Ertl, Chem. Phys. Lett. 54 (1978) 95.
[482] G. Ertl, in: J.R. Anderson, M. Boudart (Eds.), Catalysis—Science and Technology, vol. 4, Springer, 1983, p. 209.
[483] V.P. Zhdanov, B. Kasemo, Surf. Sci. Rep. 20 (1994) 111.
[484] V.V. Kaichev, M. Morkel, H. Unterhalt, I.P. Prosvirin, V.I. Bukhtiyarov, G. Rupprechter, H.-J. Freund, Surf. Sci. 566–568 (2004) 1024.
[485] D.L. Doering, H. Poppa, J.T. Dickinson, J. Catal. 73 (1982) 104.
[486] V. Matolin, E. Gillet, Surf. Sci. 238 (1990) 75.
[487] E. Ozensoy, B.K. Min, A.K. Santra, D.W. Goodman, J. Phys. Chem. B 108 (2004) 4351.
[488] D.W. Goodman, Chem. Rev. 95 (1995) 523.
[489] J. Szanyi, W.K. Kuhn, D.W. Goodman, J. Phys. Chem. 98 (1994) 2978.
[490] J. Szanyi, D.W. Goodman, J. Phys. Chem. 98 (1994) 2972.
[491] X. Xu, J. Szanyi, Q. Xu, D.W. Goodman, Catal. Today 21 (1994) 57.
[492] R. Meyer, M. Bäumer, S.K. Shaikhutdinov, H.-J. Freund, Surf. Sci. 546 (2003) L813.
[493] A.M. Bradshaw, F.M. Hoffman, Surf. Sci. 72 (1978) 513.
[494] H. Conrad, G. Ertl, J. Küppers, Surf. Sci. 76 (1978) 323.
[495] H. Ohtani, M.A. van Hove, G. Sormorjai, Surf. Sci. 187 (1987) 372.
[496] X. Guo, J.J.T. Yates, J. Chem. Phys. 90 (1989) 6761.
[497] M. Tüshaus, W. Berndt, H. Conrad, A.M. Bradshaw, B. Persson, Appl. Phys. A 51 (1990) 91.

[498] W.K. Kuhn, J. Szanyi, D.W. Goodman, Surf. Sci. 274 (1992) L611.
[499] T. Gießel, O. Schaff, C.J. Hirschmugl, V. Fernandez, K.-M. Schindler, A. Theobald, S. Bao, R. Lindsay, W. Berndt, A.M. Bradshaw, C. Baddeley, A.F. Lee, R.M. Lambert, D.P. Woodruff, Surf. Sci. 406 (1998) 90.
[500] D. Loffreda, D. Simon, P. Sautet, Surf. Sci. 425 (1999) 68.
[501] L. Surnev, M. Sock, M.G. Ramsey, F.P. Netzer, M. Wiklund, A. Borg, J.N. Andersen, Surf. Sci. 470 (2000) 171.
[502] M.K. Rose, T. Mitsui, J.C. Dunphy, A. Borg, D.F. Ogletree, M. Salmeron, P. Sautet, Surf. Sci. 512 (2002) 48.
[503] A. Ortega, Ph.D. Thesis, Technische Universität Berlin, Berlin, 1980.
[504] M. Tüshaus, Ph.D. Thesis, Freie Universität Berlin, Berlin, 1990.
[505] J. Szanyi, W.K. Kuhn, D.W. Goodman, J. Vac. Sci. Technol. A 11 (1993) 1969.
[506] G. Zheng, E.I. Altmann, J. Phys. Chem. B 2002 (2002) 1048.
[507] V.P. Zhdanov, Surf. Sci. Rep. 45 (2002) 231.
[508] T. Matsushima, H. Asada, J. Chem. Phys. 85 (1986) 1658.
[509] E.G. Seebauer, C.E. Allen, Prog. Surf. Sci. 49 (1995) 265.
[510] K. Reuter, D. Frenkel, M. Scheffler, Phys. Rev. Lett. 93 (2004) 116105.
[511] M. Snabl, O. Borusik, V. Chab, M. Ondrejcek, W. Stenzel, H. Conrad, A.M. Bradshaw, Surf. Sci. 385 (1997) L1016.
[512] K. Honkala, K. Laasonen, J. Chem. Phys. 115 (2001) 2297.
[513] C.W. Gardiner, Handbook of Stochastic Methods for Physics, Chemistry and the Natural Sciences, Springer, Berlin, 1983.
[514] N. Pavlenko, J.W. Evans, D.-J. Liu, R. Imbihl, Phys. Rev. E 65 (2002) 016121.
[515] E.S. Kurkina, N.L. Semendyaeva, Surf. Sci. 558 (2004) 122.
[516] Y. Suchorski, J. Beben, R. Imbihl, Surf. Sci. 405 (1998) L477.
[517] Y. Suchorski, J. Beben, R. Imbihl, Prog. Surf. Sci. 59 (1998) 343.
[518] Y. Suchorski, J. Beben, R. Imbihl, Surf. Sci. 454 (2000) 331.
[519] Y. Suchorski, J. Beben, R. Imbihl, E.W. James, D.-J. Liu, J.W. Evans, Phys. Rev. B 63 (2001) 165417.
[520] R. Imbihl, G. Ertl, Chem. Rev. 95 (1995) 697.
[521] S. Jakubith, H.H. Rotermund, W. Engel, A.V. Oertzen, G. Ertl, Phys. Rev. Lett. 65 (1990) 3013.
[522] S. Wehner, F. Baumann, J. Küppers, Chem. Phys. Lett. 370 (2003) 126.
[523] D. Hua, Y. Ma, Phys. Rev. E 66 (2002) 066103.
[524] D.-J. Liu, J.W. Evans, J. Chem. Phys. 117 (2002) 7319.
[525] Z. Hou, L. Yang, H. Xin, Surf. Sci. 399 (1998) L332.
[526] A.V. Zhdanova, Phys. Rev. E 63 (2001) 153410.
[527] E.M. Cordi, J.L. Falconer, J. Catal. 162 (1996) 104.
[528] M.L. Cubeiro, J.L.G. Fierro, J. Catal. 179 (1998) 150.
[529] R. Shiozaki, T. Hayakawa, Y.Y. Liu, T. Ishii, M. Kumagai, S. Hamakawa, K. Suzuki, T. Itoh, T. Shishido, K. Takehira, Catal. Lett. 58 (1999) 131.
[530] W.J. Shen, M. Okumura, Y. Matsumura, M. Haruta, Appl. Catal. A Gen. 213 (2001) 225.
[531] G.C. Cabilla, A.L. Bonivardi, M.A. Baltanas, Catal. Lett. 55 (1998) 147.
[532] F. Fajula, R.G. Anthony, J.H. Lunsford, J. Catal. 73 (1982) 237.
[533] V.L. Kirillov, Y.A. Ryndin, React. Kinet. Catal. Lett. 59 (1996) 351.
[534] J.M. Driessen, E.K. Poels, J.P. Hindermann, V. Ponec, J. Catal. 82 (1983) 26.
[535] K.P. Kelly, T. Tatsumi, T. Uematsu, D.J. Driscoll, J.H. Lunsford, J. Catal. 101 (1986) 396.
[536] O. Rodriguez de la Fuente, M. Borasio, P. Galetto, G. Rupprechter, H.-J. Freund, Surf. Sci. 566–568 (2004) 740.
[537] M. Morkel, V.V. Kaichev, G. Rupprechter, H.-J. Freund, I.P. Prosvirin, V.I. Bukhtiyarov, J. Phys. Chem. B 108 (2004) 12955.
[538] J.-J. Chen, Z.-C. Jiang, Y. Zhou, B.R. Chakraborty, N. Winograd, Surf. Sci. 328 (1995) 248.
[539] F. Solymosi, A. Berko, Z. Toth, Surf. Sci. 285 (1993) 197.
[540] M. Rebholz, V. Matolin, R. Prins, N. Kruse, Surf. Sci. 251 (1991) 1117.
[541] M. Rebholz, N. Kruse, J. Chem. Phys. 95 (1991) 7745.
[542] N. Kruse, M. Rebholz, V. Matolin, G.K. Chuah, J.H. Block, Surf. Sci. Lett. 238 (1990) L457.
[543] X. Guo, L. Hanley, J.T. Yates Jr., J. Am. Chem. Soc. 111 (1989) 3155.
[544] R.J. Levis, Z.C. Jiang, N. Winograd, J. Am. Chem. Soc. 111 (1989) 4605.
[545] R.J. Levis, Z.C. Jiang, N. Winograd, J. Am. Chem. Soc. 110 (1988) 4431.

[546] G.A. Kok, A. Noordermeer, B.E. Nieuwenhuys, Surf. Sci. 135 (1983) 65.
[547] S.M. Francis, J. Corneille, D.W. Goodman, M. Bowker, Surf. Sci. 364 (1996) 30.
[548] M. Neurock, Top. Catal. 9 (1999) 135.
[549] C.J. Zhang, P. Hu, J. Chem. Phys. 115 (2001) 7182.
[550] J.G. Chen, K.H. Lim, K.M. Neyman, N. Rösch, Phys. Chem. Chem. Phys. 6 (2004) 4499.
[551] M. Mavrikakis, M.A. Barteau, J. Mol. Catal. A 131 (1998) 135.
[552] J.L. Davis, M.A. Barteau, Surf. Sci. 197 (1988) 123.
[553] J.L. Davis, M.A. Barteau, Surf. Sci. 268 (1992) 11.
[554] J.L. Davis, M.A. Barteau, J. Am. Chem. Soc. 111 (1989) 1782.
[555] S.Y. Nishimura, R.F. Gibbons, N.J. Tro, J. Phys. Chem. B 102 (1998) 6831.
[556] B.G. Frederick, G. Apai, T.N. Rhodin, Surf. Sci. 277 (1992) 337.
[557] J.S. Huberty, R.J. Madix, Surf. Sci. 360 (1996) 144.
[558] M.C. Wu, C.M. Truong, D.W. Goodman, J. Phys. Chem. 97 (1993) 9425.
[559] P. Uvdal, M.K. Weldon, C.M. Friend, Phys. Rev. B 50 (1994) 12258.
[560] R. Ryberg, Phys. Rev. B 31 (1985) 2545.
[561] R. Zenobi, J.Z. Xu, J.T. Yates Jr., B.N.J. Persson, A.I. Volokitin, Chem. Phys. Lett. 208 (1993) 414.
[562] K.T. Queeney, C.M. Friend, J. Chem. Phys. 109 (1998) 6067.
[563] V. Matolin, M. Rebholz, N. Kruse, Surf. Sci. 245 (1991) 233.
[564] M. Frank, Ph.D. Thesis, Berlin, 2000.
[565] P. Hollins, Surf. Sci. Rep. 16 (1992) 51.
[566] I.V. Yudanov, K.M. Neyman, N. Rösch, Phys. Chem. Chem. Phys. 6 (2004) 116.
[567] S. Völkening, J. Wintterlin, J. Chem. Phys. 114 (2001) 6382.
[568] H. Berndt, F.W. Schutze, M. Richter, T. Sowade, W. Grunert, Appl. Catal. B Environ. 40 (2003) 51.
[569] P.A.J. Bagot, Mater. Sci. Technol. 20 (2004) 679.
[570] E. Ozensoy, C. Hess, D.W. Goodman, Top. Catal. 28 (2004) 13.
[571] S. Salasc, M. Skoglundh, E. Fridell, Appl. Catal. B Environ. 36 (2002) 145.
[572] J.H. Holles, R.J. Davis, T.M. Murray, J.M. Howe, J. Catal. 195 (2000) 193.
[573] A. Martinez-Arias, M. Fernandez-Garcia, A.B. Hungria, A. Iglesias-Juez, K. Duncan, R. Smith, J.A. Anderson, J.C. Conesa, J. Soria, J. Catal. 204 (2001) 238.
[574] V.P. Zhdanov, B. Kasemo, Surf. Sci. Rep. 29 (1997) 31.
[575] H. Conrad, G. Ertl, J. Küppers, E.E. Latta, Surf. Sci. 65 (1977) 235.
[576] H.-D. Schmick, H.-W. Wassmuth, Surf. Sci. 123 (1982) 417.
[577] M. Bertolo, K. Jacobi, S. Nettesheim, Vacuum 41 (1990) 76.
[578] M. Bertolo, K. Jacobi, Surf. Sci. 226 (1990) 207.
[579] M. Bertolo, K. Jacobi, Surf. Sci. 236 (1990) 143.
[580] D.T. Wickham, B.A. Banse, B.E. Koel, Surf. Sci. 243 (1991) 83.
[581] P.J. Chen, D.W. Goodman, Surf. Sci. 297 (1993) L93.
[582] R.D. Ramsier, Q. Gao, H. Neergaard Waltenburg, K.-W. Lee, O.W. Nooij, L. Lefferts, J.T. Yates Jr., Surf. Sci. 320 (1994) 209.
[583] R.D. Ramsier, Q. Gao, H. Neergaard Waltenburg, J.T. Yates Jr., J. Chem. Phys. 100 (1994) 6837.
[584] K.H. Hansen, Z. Sljivancanin, B. Hammer, E. Laegsgaard, F. Besenbacher, I. Stensgaard, Surf. Sci. 496 (2002) 1.
[585] X. Xu, P. Chen, D.W. Goodman, J. Phys. Chem. 98 (1994) 9242.
[586] S. Sugai, H. Watanabe, T. Kioka, H. Miki, K. Kawasaki, Surf. Sci. 259 (1991) 109.
[587] S. Sugai, H. Watanabe, H. Miki, T. Kioka, K. Kawasaki, Vacuum 41 (1990) 90.
[588] S.M. Vesecky, D.R. Rainer, D.W. Goodman, J. Vac. Sci. Technol. A 14 (1996) 1457.
[589] I. Nakamura, T. Fujitani, H. Hamada, Surf. Sci. 514 (2002) 409.
[590] E. Ozensoy, C. Hess, D.W. Goodman, J. Am. Chem. Soc. 124 (2002) 8524.
[591] C. Hess, E. Ozensoy, D.W. Goodman, J. Phys. Chem. B 107 (2003) 2759.
[592] E. Ozensoy, D.W. Goodman, Phys. Chem. Chem. Phys. 6 (2004) 3765.
[593] C. Nyberg, P. Uvdal, Surf. Sci. 204 (1988) 517.
[594] S.W. Jorgensen, N.D.S. Canning, R.J. Madix, Surf. Sci. 179 (1987) 322.

[595] A.J. Jaworowski, R. Asmundsson, P. Uvdal, A. Sandell, Surf. Sci. 501 (2002) 74.
[596] C. Nyberg, P. Uvdal, Surf. Sci. 256 (1991) 42.
[597] R. Raval, M.A. Harrison, S. Haq, D.A. King, Surf. Sci. 294 (1993) 10.
[598] R.G. Sharpe, M. Bowker, Surf. Sci. 360 (1996) 21.
[599] M. Ikai, T. Tanaka, J. Phys. Chem. B 103 (1999) 8277.
[600] M. Hirsimaki, M. Valden, J. Chem. Phys. 114 (2001) 2345.
[601] Q. Gao, R.D. Ramsier, H.N. Waltenburg, J.T. Yates Jr., J. Am. Chem. Soc. 116 (1994) 3901.
[602] R.D. Ramsier, K.-W. Lee, J.T. Yates Jr., Langmuir 11 (1995) 169.
[603] M. Ikai, T. Tanaka, J. Chem. Phys. 110 (1999) 1999.
[604] K. Irokawa, S. Ito, K. Toshihide, H. Miki, Surf. Sci. 433 (1999) 297.
[605] R.D. Ramsier, K.-W. Lee, J.T. Yates Jr., J. Vac. Sci. Technol. A 13 (1995) 188.
[606] P.W. Davies, R.M. Lambert, Surf. Sci. 110 (1981) 227.
[607] K.H. Hansen, Z. Sljivancanin, E. Laegsgaard, F. Besenbacher, I. Stensgaard, Surf. Sci. 505 (2002) 25.
[608] X.P. Xu, Catal. Lett. 24 (1994) 31.
[609] H. Cordatos, T. Bunluesin, R.J. Gorte, Surf. Sci. 323 (1995) 219.
[610] D.R. Rainer, S.M. Vesecky, M. Koranne, W.S. Oh, D.W. Goodman, J. Catal. 167 (1997) 234.
[611] D.R. Rainer, M. Koranne, S.M. Vesecky, D.W. Goodman, J. Phys. Chem. B 101 (1997) 10769.
[612] B. Hammer, J.K. Norskov, Phys. Rev. Lett. 79 (1997) 4441.
[613] M.P. Jigato, K. Somasundram, V. Termath, N.C. Handy, D.A. King, Surf. Sci. 380 (1997) 83.
[614] B. Hammer, Faraday Discuss. 110 (1998) 323.
[615] D. Loffreda, D. Simon, P. Sautet, Chem. Phys. Lett. 291 (1998) 15.
[616] D. Loffreda, D. Simon, P. Sautet, J. Chem. Phys. 108 (1998) 6447.
[617] B. Hammer, J. Catal. 199 (2001) 171.
[618] K. Honkala, P. Pirilä, K. Laasonen, Surf. Sci. 489 (2001) 72.
[619] B. Hammer, Phys. Rev. Lett. 89 (2002) 016102.
[620] D. Loffreda, D. Simon, P. Sautet, J. Catal. 213 (2003) 211.
[621] S.M. Vesecky, P.J. Chen, X.P. Xu, D.W. Goodman, J. Vac. Sci. Technol. A 13 (1995) 1539.
[622] B. Westerberg, E. Fridell, J. Mol. Catal. A Chem. 165 (2001) 249.
[623] M. Valden, J. Aaltonen, E. Kuusisto, M. Pessa, C.J. Barnes, Surf. Sci. 307 (1994) 193.
[624] G. Prevot, C.R. Henry, J. Phys. Chem. B 106 (2002) 12191.
[625] V. Bustos, R.O. Unac, G. Zgrablich, C.R. Henry, Phys. Chem. Chem. Phys. 5 (2003) 2906.
[626] R.M. Jaeger, Ph.D. Thesis, Bochum, 1992.
[627] K.T. Queeney, S. Pang, C.M. Friend, J. Chem. Phys. 109 (1998) 8058.
[628] K.T. Queeney, C.M. Friend, Surf. Sci. 414 (1998) L957.
[629] K.T. Queeney, C.M. Friend, J. Phys. Chem. B 102 (1998) 9251.
[630] K.T. Queeney, C.M. Friend, J. Chem. Phys. 107 (1997) 6432.
[631] W.A. Brown, P. Gardner, M.P. Jigato, D.A. King, J. Chem. Phys. 102 (1995) 7277.
[632] W.A. Brown, P. Gardner, D.A. King, J. Phys. Chem. 99 (1995) 7065.
[633] P. Dumas, M. Suhren, Y.J. Chabal, C.J. Hirschmugl, G.P. Williams, Surf. Sci. 371 (1997) 200.
[634] W.A. Brown, R.K. Sharma, D.A. King, J. Phys. Chem. 100 (1996) 12559.
[635] M. Schönnenbeck, D. Cappus, J. Klinkmann, H.-J. Freund, L.G.M. Pettersson, P.S. Bagus, Surf. Sci. 347 (1996) 337.
[636] M. Wilde, O. Seiferth, K. Al-Shamery, H.-J. Freund, J. Chem. Phys. 111 (1999) 1158.
[637] T. Venkov, K. Hadjiivanov, D. Klissurski, Phys. Chem. Chem. Phys. 4 (2002) 2443.
[638] T.E. Hoost, K. Otto, K.A. Laframboise, J. Catal. 155 (1995) 303.
[639] D.K. Paul, B.W. Smith, C.D. Marten, J. Burchett, J. Mol. Catal. A Chem. 167 (2001) 67.
[640] K.I. Hadjiivanov, Catal. Rev. Sci. Eng. 42 (2000) 71.
[641] C.D. Valentin, G. Pacchioni, S. Abbet, U. Heiz, J. Phys. Chem. B 106 (2002) 7666.
[642] W.S. Brown, D.A. King, J. Phys. Chem. B 104 (2000) 2578.
[643] J.G. Chen, W. Erley, H. Ibach, Vacuum 41 (1990) 74.
[644] G. Odörfer, R. Jaeger, G. Illing, H. Kulenbeck, H.-J. Freund, Surf. Sci. 233 (1990) 44.
[645] K. Honkala, P. Pirilä, K. Laasonen, Phys. Rev. Lett. 86 (2001) 5942.